

The Aerosol Limb Imager: Limb Scattered Polarized Radiance Images Using an Acousto-Optic Filter for Stratospheric Aerosol Profiling from a Stratospheric Balloon

A Thesis Submitted to the
College of Graduate Studies and Research
In Partial Fulfillment of the Requirements
for the Degree of Doctor of Philosophy

In the Department of Physics and Engineering Physics
University of Saskatchewan
Saskatoon

By

Brenden J. Elash

© Copyright Brenden John Elash, December, 2016. All rights reserved.

Permission to Use

In presenting this thesis in partial fulfilment of the requirements for a Postgraduate degree from the University of Saskatchewan, I agree that the Libraries of this University may make it freely available for inspection. I further agree that permission for copying of this thesis in any manner, in whole or in part, for scholarly purposes may be granted by the professor or professors who supervised my thesis work or, in their absence, by the Head of the Department or the Dean of the College in which my thesis work was done. It is understood that any copying or publication or use of this thesis or parts thereof for financial gain shall not be allowed without my written permission. It is also understood that due recognition shall be given to me and to the University of Saskatchewan in any scholarly use which may be made of any material in my thesis.

Requests for permission to copy or to make other use of material in this thesis in whole or part should be addressed to:

Head of the Department of Physics and Engineering Physics

University of Saskatchewan

Saskatoon, Saskatchewan S7N 5E2

ABSTRACT

Stratospheric aerosol has been measured extensively from satellite platforms over the past three decades and is an important factor in the climate change discussion. Instruments capable of measuring vertically resolved aerosol extinction profiles are in decline with few future endeavours, if any, are planned to fill the hole left by the loss of current instruments. The Aerosol Limb Imager (ALI) is an optical remote sensing instrument designed to image scattered solar irradiance from the atmospheric limb. These measurements are used to retrieve spatially resolved information of the stratospheric aerosol distribution, including spectral extinction coefficient and particle size. Here we present the design, development and test results of an ALI prototype instrument. The instrument design uses a large aperture Acousto-Optic Tunable Filter (AOTF) to image the sunlit stratospheric limb in a selectable narrow wavelength band ranging from the visible to the near infrared. Additionally, through the nature of the AOTF, ALI is a polarized instrument recording the polarized limb radiance which is a relatively new concept as current techniques measure the total radiance. A study to address if there are any major advantages or concerns to measuring the linear polarization for aerosol is also addressed within this work.

The long term goal of this work is the eventual realization of ALI on a satellite platform in low earth orbit, where it can provide high spatial resolution observations, both in the vertical and cross-track. The ALI prototype was tested on a stratospheric balloon flight from the Canadian Space Agency (CSA) launch facility in Timmins, Canada, in September 2014. Preliminary analysis of the hyperspectral images indicate that the radiance measurements are of high quality, and we have used these to retrieve vertical profiles of stratospheric aerosol extinction coefficient from 650–950 nm, along with one moment of the particle size distribution..

ACKNOWLEDGMENTS

The work presented here would not be possible with the contributions of many people and organizations. Without these people and organizations I would not have been able to partake in this education journey through optics and atmospheric science. I would like to thank the Institute for Space and Atmospheric Studies, the University of Saskatchewan, the Natural Sciences and Engineering Research Council, the Centre National d'Etudes Spatiales, and the Canadian Space Agency for their financial support.

Members of my research team have been monumental to assisting in the completion of this project. Thanks to Paul Loewen for building and testing the electronics for ALI; Seth Dueck creating the polarized version of SASKTRAN-HR as well as the guidance given using the polarized model; Landon Rieger for help and advice in using the retrieval package; Dr. Nick Lloyd for his assistance in the designing and testing the flight software; and Dr. Douglas Degenstein for overall advice and knowledge during the project.

To my supervisor, Dr. Adam Bourassa, I would extend a sincere thanks for the wonderful opportunity to work alongside him in this endeavor. Without his guidance, knowledge, and enthusiasm this project would not be what it became.

Finally, I would like to thank my family and friends for their support throughout this work

To my family: Johanna, Amy, Kaitlyn, and Chris

TABLE OF CONTENTS

	<u>page</u>
ABSTRACT.....	iii
ACKNOWLEDGMENTS	iv
LIST OF TABLES	x
LIST OF FIGURES	xi
LIST OF ABBREVIATIONS	xix
1 INTRODUCTION.....	1
2 BACKGROUND	4
2.1 Introduction.....	4
2.2 Stratospheric Aerosol.....	7
2.2.1 Aerosol Sources and Microphysics.....	8
2.2.2 Climate Effects.....	11
2.3 Aerosol Measurements.....	12
2.3.1 In-Situ Measurements	12
2.3.2 Occultation	13
2.3.3 Lidar	15
2.3.4 Limb Scatter	16
2.4 Radiative Transfer.....	19
2.4.1 Scalar Radiative Transfer.....	19
2.4.2 Vector Radiative Transfer	23
2.4.3 Rayleigh Scattering	24
2.4.4 Mie Scattering	25
2.4.5 SASKTRAN Radiative Transfer Model	27
2.5 ALI Prototype and Stratospheric Balloon Flight	28
3 OPTICAL DESIGN AND CALIBRATIONS	31
3.1 AOTF Theory and Background	31
3.1.1 Solution to the Acoustic Equation	31
3.1.2 Diffraction Efficiency	35
3.1.3 Diffraction Angle	37
3.1.4 Tuning Curve	39
3.2 AOTF Calibration and Operation	41
3.2.1 Operation.....	42
3.2.2 Tuning Curve Analysis	44
3.2.3 Point Spread Function	47
3.2.4 Diffraction Efficiency	48
3.3 Optical Chain Development.....	48
3.3.1 Telecentric System Prototype	49

3.3.2 Telescopic System Prototype	57
3.3.3 ALI Optical Design	62
3.3.4 Correction to the Optical Design.....	67
3.4 Opto-Mechanical Design and Thermal Balancing.....	68
3.4.1 Opto-Mechanical Design	68
3.4.2 Baffle Design	74
3.4.3 Light Tight Case.....	79
3.4.4 Thermal Considerations	80
3.5 Control Software	82
3.6 ALI Calibrations and System Test.....	86
3.6.1 Exposure Time Determination	86
3.6.2 DC Offset Removal.....	88
3.6.3 Dark Current Correction	89
3.6.4 Stray Light Calibration.....	90
3.6.5 Relative Flat-Fielding Correction	92
3.6.6 Integrated Testing.....	95
4 THE SENSITIVITY TO POLARIZATION IN STRATOSPHERIC AEROSOL RETRIEVALS FROM LIMB SCATTERED MEASUREMENTS	97
4.1 Introduction.....	97
4.2 Background and Forward Model	99
4.2.1 Polarized Scattered Sunlight and Stratospheric Aerosols	99
4.2.2 SASKTRAN-HR Model	104
4.2.3 Model Scenarios.....	104
4.3 Methodology	107
4.4 Analysis.....	111
4.4.1 Difference in Scalar Retrievals using a Scalar or Vector Model	111
4.4.2 Fraction of Limb Signal due to Aerosol.....	113
4.4.3 Potential for Retrieval Bias	118
4.4.4 Precision analysis	120
4.5 Conclusions.....	125
5 STRATOSPHERIC BALLOON FLIGHT AND AEROSOL RETRIEVALS	127
5.1 Stratospheric Balloon Flight	127
5.1.1 Preflight Preparations.....	127
5.1.2 Balloon Flight	131
5.2 Limb Measurements.....	135
5.3 Aerosol Retrievals.....	141
5.3.1 Aerosol Extinction Retrieval Methodology	142
5.3.2 Aerosol Extinction Retrievals	146
5.3.3 Particle Size Retrieval Methodology	151
5.3.4 A Sample Particle Size Retrieval	155
5.4 Results and Future Improvements	157
6 CONCLUSION	159

LIST OF REFERENCES	163
A ALI HARDWARE COMPONENTS.....	175
A.1 Optical Components.....	175
A.1.1 Optical Lenses	175
A.1.2 Polarizers	175
A.1.3 AOTF	176
A.2 Opto-Mechanical and Electrical Components	177
A.2.1 RF Driver	177
A.2.2 QSI CCD Camera.....	177
A.2.3 OCELOT Computer	177
A.2.4 Opto-Mechanical Pieces.....	178
B ALI SOFTWARE COMMANDS	179
B.1 List of Commands for ALI Software	179
B.1.1 EnableScience.....	180
B.1.2 DisableScience	180
B.1.3 EnableRF	180
B.1.4 DisableRF	181
B.1.5 EnableAutoSendStats	181
B.1.6 DisableAutoSendStats	181
B.1.7 SetScienceMode	181
B.1.8 ReloadConfig.....	182
B.1.9 LdCusCnf	182
B.1.10 LdCusExp	182
B.1.11 GetFile	183
B.1.12 EndCurrentScienceCycle.....	183
B.1.13 SetExposureScaleFactor	183
B.1.14 UpdateExposureTimeCurve	183
B.1.15 EnableCheckRfTemps	184
B.1.16 DisableCheckRfTemps.....	184
B.1.17 ResetHousekeeping	184
B.1.18 DumpConfig	184
B.1.19 SetBitsPerSecond	184
B.1.20 EnableAutomation.....	185
B.1.21 DisableAutomation.....	185
B.1.22 SetAutomationTimeout	185
B.1.23 EnableGps	185
B.1.24 DisableGps	185
B.1.25 EnablePulse	185
B.1.26 DisablePulse	185
B.2 List of ALI Science Modes	186
B.2.1 Invalid Mode	186
B.2.2 Calibration Mode.....	186
B.2.3 Aerosol Mode	187

B.2.4 H ₂ O Mode.....	187
B.2.5 O ₂ Mode	188
B.2.6 Custom Mode	189
B.2.7 Aerosol Constant Exposure Time Mode	189
B.3 List of ALI Exposure Modes.....	189
B.3.1 Invalid Mode	189
B.3.2 Calibrated Exposure Mode	190
B.3.3 Custom Exposure Mode	190

LIST OF TABLES

<u>Table</u>	<u>page</u>
Table 3-1: Telecentric Test System Optical specifications	51
Table 3-2: Telescopic Prototype System Optical Parameters	58
Table 3-3: Final ALI optical specifications.....	65
Table 3-4: Revised ALI optical specifications	68
Table 3-5: Location of ALI temperature sensors.	84
Table 3-6: Estimated balloon flight exposure times.	88
Table 4-1: Different particle size distributions used to test the sensitivity of the aerosol retrieval.	107
Table 4-2: The SSA dependence of the normalized co-variance for the horizontal and vertical polarization retrievals. The given numbers are the mean with the standard deviation for each geometry across all wavelengths. Note that the SSA of 90° for the vertical polarization has been removed due to the poor signal in this region.....	123
Table A-1: Lens used in ALI and their specifications.	175
Table A-2: AOTF Specifications.	176
Table A-3: QSI CCD camera specifications.	177
Table A-4: Opto-mechanical components used in ALI	178
Table B-1: ALI operational science modes.....	186
Table B-2: ALI calibration science mode specifications.	187
Table B-3: ALI aerosol science mode specifications.....	187
Table B-4: ALI H ₂ O science mode specifications.	188
Table B-5: ALI O ₂ science mode specifications.....	188
Table B-6: ALI operational exposure time modes.....	189

LIST OF FIGURES

<u>Figure</u>	<u>page</u>
Figure 2-1: Log-normal distribution for non-volcanic background aerosol layer.	9
Figure 2-2: Bimodal particle size distributions fits from OPC. (a) Distributions from a volcanic period after the Mount Pinatubo eruption recorded in 1993. (b) Distributions from a background aerosol period recorded in 1999. Both of the aerosol distribution measurement are from 20 km altitude with the solid line being the fine mode and the dashed line is the coarse mode. Figure is recreated from Figure 5 of <i>Deshler et al.</i> (2003).	10
Figure 2-3: An occultation instrument monitoring the atmosphere by scanning the atmosphere by looking directly at the sun.	14
Figure 2-4: Lidar instrument showing a measurements in both the nadir and off-nadir lines of sight.	16
Figure 2-5: Limb scattering geometry measurement for an instrument where single and multiple scattering events occur.....	17
Figure 3-1: Geometry for the AOTF wave derivation assuming the acousto wave is along the x-axis and the AO interaction occurs along the z axis over a interaction length, L . The parameters ri , ki , and θi are the position vector, wave vector, and angle of the incident electric field and similarly for the diffracted electric field. Figure recreated from <i>Xu and Stroud</i> (1992)	33
Figure 3-2: A standard non-collinear AOTF experiential set up. The crystal is assumed to infinitely long in the y direction. Figure recreated after <i>Guenther</i> (1990) number 14B-1.....	38
Figure 3-3: General Layout of an AOTF. A randomly polarized incoming light source hits the front surface of the birefringent crystal. The black bar below the crystal is the piezoelectric transducer that produces the RF signal and forms the acousto wave represented by the grey arrow. The momentum matching Bragg diffraction occurs and monochromatic polarized light (-1 order) exits the AOTF at a constant angle with the 0th order and +1 order being blocked by an optical stop.....	39
Figure 3-4: The wave vectors generated by the AOTF experiment set up in Figure 3-2. From the above figure ke and ko are the wave vectors of the extraordinary and ordinary axis of the AOTF crystal.	40
Figure 3-5: (a) An AOTF undergoing Bragg diffraction with an unpolarized input incident wave with a RF wave applied represented by the arrow. After the diffraction event four output signals are formed: the zeroth order and first order ordinary (o) and extraordinary (e) signals. However the only optical path that remains at a constant angle no matter the applied RF wavelength is the first order extraordinary diffracted	

signal. (b) Two linear polarizers are added to the system, the first linear polarizer removes the ordinary polarization from the outputs with the dotted lines and the second linear polarizer removes undiffracted extraordinary light shown by the dashed line. This configuration is the “AOTF-on” state. (c) The system in (b) without a RF wave so no Bragg diffraction is occurring. Once again the first linear polarizer removes the ordinary polarization represented by the dotted line and the second linear polarizer removes the extraordinary light shown by the dashed line. This configuration is the “AOTF-off” state..... 43

Figure 3-6: Telecentric test experiential setup for AOTF parameter determination. All lenses and apertures are represented by the same symbol..... 45

Figure 3-7: (a) A row averaged image taken from the AOTF of the point spread function when the tuning frequency of the AOTF was at 124.96 MHz. (b) The FWHM for each of the determined wavelengths for the AOTF. The FWHM at 600 nm is 1.5 nm and as the wavelengths get longer the FWHM increases to 4.9 nm at 1080 nm. (c) The calibration curves for the AOTF RF versus the diffracted wavelength which contains the data points recorded and fit curves. (d) The percent error with respect to the measured frequency for the two best fit curves in the previous panel..... 47

Figure 3-8: A standard paraxial ray tracing diagram. The aperture is located to make the system telecentric in the image plane and f is the focal length of the lens..... 49

Figure 3-9: Ray Tracing diagram simulation of the telecentric lens system preformed using Code V. The elements in the system are the following: (1) Optical Stop and telecentric aperture. (2) 100 mm focal length plano-convex lens. (3) Brimrose AOTF characterized in section 3.2. (4) 100 mm focal length plano-convex lens. (5) Telecentric Aperture. (6) 75.6 mm focal length plano-convex lens. (7) Imaging plane. It should be noted that the x and y scales are not the same in this image. Also, in the lab a polarizer is added in front and behind the AOTF as well as prisms after the AOTF..... 50

Figure 3-10: Quantum efficiency of the Kodak KAF-1603ME contained within the QSI CCD camera is represented by blue curve. Quantum efficiency provided by QSI Scientific..... 52

Figure 3-11: The effect on the optical path of converging light bundles as they pass through a material of index of refraction $n(\lambda)$. When the index of refraction strongly depends on wavelength, as in the AOTF, the optical path length can experience great changes that will alter the focal point of the system..... 53

Figure 3-12: Code V simulation of the spot size for the telecentric system at focus at 800 nm. The spots are shown for 0.0, 1.5 and 2.6 degree fields of view at 600 nm (blue) and 800 nm (green). The full spot sizes for the 600 nm spots are 0.16, 0.22, and 0.25 mm for 0.0, 1.5, and 2.6 degrees fields respectively, with the corresponding 800 nm spot sizes being 0.024, 0.053, 0.094 mm. The black circles represent the Airy disk for each specific wavelength and FOV. 55

Figure 3-13: The top left is the original test image used for the experiment. The top right, bottom left, and bottom right are the images recorded through the telecentric system at 650, 750, and 850 nm. The system is focused at 800 nm.....	57
Figure 3-14: Ray Tracing diagram of the telescopic lens system simulated by Code V. The elements in the system are the following: (1) 100 mm focal length plano-convex lens. (2) Location where field stop will be located to limit stray light (3) 100 mm focal length plano-convex lens. (4) Brimrose AOTF characterized in section 3.2. (5) 75.6 mm focal length plano-convex lens. (6) Imaging plane. It should be noted that the x and y scales are not the same as Figure 3-9. Also, in the lab a polarizer is added in front and behind the AOTF as well as prisms behind the AOTF.....	58
Figure 3-15: Vertical displacement of a collimated bundle of light cause by a material of index of refraction $n(\lambda)$	60
Figure 3-16: Code V simulation of the spot size for the telescopic system. The spots are shown for 0.0, 1.5 and 3.0° fields of view at 600 nm (blue) and 800 nm (green). The full spot sizes for the 600 nm spots are 0.004, 0.045, and 0.122 mm for 0.0, 1.5, and 3.0° fields respectively, with the corresponding 800 nm spot sizes being 0.096, 0.081, 0.047 mm. The black circles represent the Airy disk for 600 nm wavelength and each FOV.	60
Figure 3-17: The top left is the original test image used for the experiment. The top right, bottom left, and bottom right are the images recorded through the telescopic system at 650, 750, and 850 nm. The system is focused at 800 nm.....	62
Figure 3-18: Final optical design for ALI with a Code V ray tracing diagram. The elements in the system are: (1) 150 mm focal length plano-convex lens. (2) Field stop. (3) 100 mm focal length plano-convex lens. (4) Vertical (extraordinary) linear polarizer. (5) Brimrose AOTF. (6) Horizontal (ordinary) linear polarizer. (7) 50.4 mm focal length bi-convex lens. (8) Imaging plane.	63
Figure 3-19: MTF analysis performed by Code V for the final ALI design used in campaign. The 7 pixel running average corresponds to a spatial frequency of 15.5 cycles/mm.	65
Figure 3-20: The final optical layout of ALI's optical chain from the top and profile perspectives with the components being the following: (1) 150 mm plano-convex lens with 25.4 mm diameter. (2) Field Stop. (3) 100 mm plano-convex lens with 50.8 mm diameter. (4) Optical rail system. (5) Vertical (extraordinary) linear polarizer. (6) Brimrose AOTF. (7) Rotation Stage. (8) Horizontal (ordinary) linear polarizer. (9) 50 mm bi-convex lens with 25.4 mm diameter. (10) QSI 616s CCD camera. (11) Optical rail.	70
Figure 3-21: The custom mounting hardware design to mount the AOTF and QSI CCD camera into ALI's opto-mechanical design. Left: Custom AOTF mounting hardware. Right: The five piece QSI CCD camera mounting hardware.	72

Figure 3-22: ALI opto-mechanical system with three degree horizontal tilt and designed baffle discussed in section 3.4.2.	73
Figure 3-23: (a) Start of the optical baffle geometry method. The red lines are the marginal rays and the green line is the first ray that can enter the system without encountering at least three surfaces. (b) The first internal vane has been added and the location of the next vane is being determined. (c) The second internal baffle has been added and since the green line intersects with the critical baffle no more baffle are required. (d) Additional interior vanes and an external vane have been added to ensure a height to pitch ratio of 0.5 to improve the baffle's capabilities to reduce stray light.	76
Figure 3-24: A cross-section view of the ALI baffle system. All dimensions on the drawing are in millimeters and the sloped black lines show the 6 degree field of view.....	77
Figure 3-25: ALI baffle vain profile. Dimensions are in millimeters.....	78
Figure 3-26: Final ALI optical and opto-mechanical assembly.....	79
Figure 3-27: ALI optical system with light tight case attached. Three degree horizontal tilt not present in this image.	80
Figure 3-28: A complete flow diagram showing interaction between all the of ALI software modules on the on board ALI flight computer.....	83
Figure 3-29: Simulated scalar radiances from the SASKTRAN-HR in blue and red with the radiance on the left side and the scaling factor in black with the value on the right side.....	87
Figure 3-30: The DC offset curve (Equation 3.42) is seen in black where the lab and flight calibration data is shown in blue. The counts on the vertical axis are the counts that need to be removed to account for the DC offset.	89
Figure 3-31: The dark current from the calibration images over a series of camera temperatures and exposure times.	90
Figure 3-32: A calibration image after stray light removal has been performed where the measured wavelength is 750 nm with a 1 second exposure time. Vignetting can be seen as moving away from center of the image. Additionally the last 1° of the horizontal field of view is on the right side is lost due to strong contamination from reflections within the system.	91
Figure 3-33: The blackbody emittance curve from Equation 3.43 normalized to 775 nm.	93
Figure 3-34: The flat fielding coefficients for 750 nm.	94
Figure 4-1: (Top) The fraction of a linear polarization (left is horizontal and right is vertical) over the total radiance for molecular air density. (Bottom) The change in	

linear polarization between an atmosphere that contains aerosol and one with only molecular air density..... 103

Figure 4-2: The two aerosol profiles used in this study. The blue is a background aerosol extinction levels, and the red curve is a representative aerosol profile after the Nabro eruption 106

Figure 4-3: Percent differences between the vector retrieved aerosol extinction profiles and the scalar retrieval from simulated total radiance measurements. Each column represents a different particle size distribution (see Table 4-1)..... 112

Figure 4-4: (Top) For a horizontal (left) or vertical (right) linear polarization the percent of the signal that is attributed to aerosol. (Bottom) The change in the fraction of the limb signal due to aerosol when compared to the total radiance for the horizontal (left) and vertical (right) polarization. The simulation uses a geometry of SZA=45° and SSA=60°, with the albedo being 0 and the aerosol state the background profile with particle size distribution #1..... 114

Figure 4-5: Dependence of the fraction of the limb spectra due to aerosol on solar scattering angle (left panels) for total radiance (top), horizontal polarization (middle) and vertical polarization (bottom), and the magnitude of the radiance for each case (right panels). Note the low signal near SSA of 90 degrees for the vertical polarization which would be problematic for terminator orbits. 115

Figure 4-6: The ratio of the linearly polarized radiance to the total radiance for horizontal (left) and vertical (right) orientations. Note that the scale for each plot is different. The simulation was performed with a SSA of 60 degrees with volcanic aerosol loading for a tangent altitude of 20 km..... 117

Figure 4-7: The mean percent difference between the retrieved aerosol extinction profile with an assumed particle size distribution and the true state corresponding to the indicated particle size distribution (see Table 4-1). Error bars represent one standard deviation of the variability across all viewing geometries. Results shown are for 750 nm and 20 km altitude..... 120

Figure 4-8: The wavelength dependence of the co-variance for the horizontal and vertical polarization retrievals normalized to the total radiance case. The faded line represent one standard deviation of the variability encountered across all input parameters. The top panel is for an instrument design and/or operation that compensates for changing signal levels with polarization and viewing geometry, and the bottom panel is for uncompensated measurements..... 122

Figure 5-1: Side of the QSI CCD with the panel that contains the vacuum seal opened. The orange o-ring seen in the cavity is removed from the chamber to open the vacuum seal to the camera's CCD chip. 129

Figure 5-2: The ALI instrument is mounted on board the CARMEN-2 gondola (top shelf on the right). ALI located next to SHOW, another Canadian instrument with

collaboration between ABB, York University, and the University of Saskatchewan. ALI has its red tag cover over the optical entrance to protect the instrument from dust and other contaminates. Thermal insulation has been added to the instrument and during the flight sun side will be on the side of SHOW. Some of the reflective layer was blacked out to not cause additional stray light into SHOW optical path..... 131

Figure 5-3: (a) The GPS data from ALI during the Nimbus 7 mission generated via Google Earth. The colour of the line represents the absolute speed of the gondola during the mission and the blue, green, red colours represent speeds of approximately 10, 70, and 140 km/h.. Important landmarks are noted on the image. The end of mission represents the end of the primary aerosol mission. No GPS data was collected from ALI after power down. The location of image 208 is the red label. (b) The temperature and altitude profiles from the Nimbus 7 flight. The time of image 208 is shown by the cyan vertical line and first light measured by ALI is occurs at the magenta vertical line..... 133

Figure 5-4: During the flight the calibrated exposure times was updated. The blue curve represents the exposure times from the ground calibration and the red curve is the recalibration during the flight. The black curve is the percent change in between the pre-flight calibrated results and the during flight calibration. 134

Figure 5-5: Stray light removal technique is performed using image 208 which is a 750 nm measurement. The top panel is the image after the DC offset has been removed from the measurement. The middle panel is the associated AOTF-off image and stray light features are seen in the upper right of the image as well as light being registered in the entire right side of the image. The final panel is the first panel minus the second panel and the abnormal gradient has been removed from the final image, leaving a cleaner radiance profile. 137

Figure 5-6: (a) Final calibrated 750 nm image, taken at 13:57 UTC located at 48.55°N, 80.00°W with a SZA and SSA of 63° and 98° respectively. (b) The same 750 nm image with the mean of the profile removed from the image leaving the residual signal that shows thin clouds in the troposphere. 138

Figure 5-7: Averaged ALI relative radiance vectors from 12 of the 13 wavelengths from the Nimbus 7 flight. Each panel presents the radiance vectors from a different wavelength measured which is denoted in the top right corner. The dashed lines are radiance profiles where the SZA is greater than 90° and solid lines are profile where the SZA is less than 90°. 140

Figure 5-8: Relative radiances spectrally from 650 nm to 950 nm as measured from ALI at approximately 14:20 UTC consisting of images number 204 to 216 looking 90° in the azimuth from the sun facing southwards. These spectral profiles are presented at several tangent altitudes with a horizontal look direction of 0°. The shading represents the error on the radiances..... 141

Figure 5-9: (a) The black, blue, red curves represent the measurement vector, first term of Equation 5.6, and second term of Equation 5.6 using image 208 (b) A collection of all of the measurement vectors at 750 nm during the mission with a SZA greater than 90° . (c) Image 208 measurement vector with associated error represented by the shading 143

Figure 5-10: An example of three aerosol retrievals from images 206, 208, and 214, with center wavelengths of 750, 850, and 950 nm respectively are vertically displayed in the figure from top to bottom. The left column shows the measurement vector, \mathbf{y} , in black with the retrieved forward model, \mathbf{F} , in blue. The center column shows the ratio of the measurement vector over forward model known as α and is the convergence factor between the ALI measurement and the forward model. For both of the first two columns, the black line is barely visible due to the very good agreement of the forward model. The final column is ALI aerosol extinction in blue with the associated error represented by the light blue shading. 148

Figure 5-11: Left is the retrieved aerosol extinction profiles from the last complete imaging cycle consisting of images 205 to 216 from the 0.0° horizontal line-of-sight. Right is the 750 nm ALI aerosol extinction in blue with its error represented by the shading compared to the 750 nm extinction measured by OSIRIS in red with its error represented by the shading. 149

Figure 5-12: (a) Image 208 (750 nm) re-retrieved using an albedo of 0 and 1 compared to the original albedo used from OSIRIS. (b) Using the determined zenith pointing error from section 5.2, image 208 is retrieved again using the maximum possible pointing error compared to the original. 150

Figure 5-13: Reproduced from Figure 4 of *Rieger et al.* (2014). For OSIRIS scan 6432001 aerosol measurement vectors were calculated at 22.5 km. (A) The three size distributions used in the study. (B) The measurement vectors calculated via the SASKTRAN simulation (C) The relative percent difference of the fine and representative distributions with respect to the bimodal distribution. A 1% error is the radiance yields an uncertainty in the bimodal measurement vector shown by the grey shading. 152

Figure 5-14: Computed with the optical properties of the SASKTRAN engine. This variation of the cross section with respect to the mode radius and width allows for some determination of the particle size distribution through the Angström exponent. 153

Figure 5-15: The top panel shows the convergence of two sample particle size retrievals, blue and red represent an initial state of 0.08 and $0.12 \mu\text{m}$ mode radius respectively. Both initial states converge to the same value over approximately 3 iterations in the particle size retrieval method. The middle panel shows the final Angström exponents determined from images 204-216. The shading represents the error associated with the least squares fit. The bottom panel shows a typical least squares

fit of the retrieved extinction values over wavelength to determine the Angström exponent at model altitude of 14.5 km..... 156

Figure A-1: The transmission and extinction ratios of the LPVIS100 used in ALI. 176

LIST OF ABBREVIATIONS

ALI	Aerosol Limb Imager
ALTIUS	Atmospheric Limb Tracker for the Investigation of the Upcoming Stratosphere
AMON	Absorption par les Minoritaires Ozone et NO _x
AO	Acousto-Optic
AOTF	Acousto-Optical Tunable Filter
BEO	Back End Optics
CALIPSO	Cloud-Aerosol Lidar and Infrared Path_nder Satellite Observations
CATS	Cloud Aerosol Transport System
CCD	Charged-Coupled Device
CNES	Centre National d'Etudes Spatiales
CSA	Canadian Space Agency
DC	Direct Current
FEO	Front End Optics
FOV	Field of View
FWHM	Full Width Half Max
GPS	Global Positioning System
ICESat	Ice, Cloud, and land Elevation Satellite
IR	InfraRed
LS	Lower Stratosphere
MART	Multiplicative Algebraic Reconstruction Technique
MIPAS	Michelson Interferometer for Passive Atmospheric Sounding
MLS	Microwave Limb Sounder
MTF	Modular Transfer Function
NASA	National Aeronautics and Space Administration
NIR	Near InfraRed
OMPS	Ozone Mapping and Pro_le Suite
OPC	Optical Particle Counter
OSIRIS	Optical Spectrograph and Infra-Red Imaging System
RF	Radio Frequency
SAGE	Stratospheric Aerosol and Gas Experiments
SALOMON-N2	Spectroscopie dAbsorption Lunaire pour lObservation des Minoritaires Ozone et NO _x - Nacelle 2
SAM	Stratospheric Aerosol Measurements
SCIAMACHY	SCanning Imaging Absorption spectroMeter for Atmospheric CHartographY
SNR	Signal to Noise Ratio
UT	Upper Troposphere
UTLS	Upper Troposphere and Lower Stratosphere

CHAPTER 1

INTRODUCTION

The atmosphere of the Earth is a dynamic, evolving system dependent upon its composition. The concentration of various atmospheric species is dependent upon altitude, geographical location, and time of day. These species interact with the incoming sunlight to absorb, scatter, and emit the incoming radiance. Using spectroscopy, concentrations of different species can be determined to discover the composition of the atmosphere. Over a period of time, changes to the composition caused by natural and anthropogenic sources can be used to infer climate change effects. One important species in determining the radiative forcing effect is stratospheric sulfuric aerosol. Aerosols are submicron droplets that scatter incoming irradiance away from earth and assist in the formation of clouds causing a cooling effect to the surface temperature. The source of these aerosols come from the burning of fossil fuels, biomass burning, marine processes and form the background aerosol layer. A large unpredictable perturbation of this layer occurs after large volcanic eruptions that can inject large quantities of sulfur directly into the stratosphere.

Instrumentation has been deployed over the past decades to monitor the atmospheric state from the ground, sky, and in space using many different methods. Some of these instruments have had the capability to measure aerosols however, many of these instruments are no longer operational or are operating well past their expected lifetimes. The evolution of the atmosphere will need to be monitored in the future and new instrumentation is required. Using new technologies the capabilities of future generations can be surpassed and used to monitor the earth with greater efficiency and higher resolution measurements allowing for a more detailed glimpse of the atmosphere and its dynamic processes. Without future techniques to continue the aerosol and other atmospheric species datasets the long term effect of human production and policy cannot be observed to monitor the effects of climate change.

In this work, a proposal for a new passive remote sensing instrument, named the Aerosol Limb Imager (ALI), will be discussed, which images the polarized limb radiance of the atmosphere to determine stratospheric aerosol profiles using a novel filtering technology. ALI measures the atmosphere using two dimensional imaging to acquire cross-track and vertical profiles giving additional measurement resolution and depth. Current limb instruments do not measure the cross-track profile and only the vertical. The addition of the cross track will allow for more localized measurement points which will allow better determination of atmospheric species such as aerosol and how it dynamically interacts with its environment. This instrument, although a prototype for a satellite instrument, will be tested on a stratospheric balloon flight and has been designed for this platform. Slight alterations would be needed to convert the instrument to a satellite platform mission.

In this work, Chapter 2 will outline the background of the atmosphere on which this project is based including an overview of the stratospheric aerosol. The background includes its discovery and discussion about the importance of aerosol in the atmosphere, effect on climate change, sources of aerosol, and microphysical properties. Following that will be an overview of the different techniques used to measure aerosols. This includes techniques used in in-situ measurements like optical particle counters and nephelometers and satellite based methods such as occultation and limb scatter. Then a brief overview of radiative transfer theory will be covered starting with a scalar representation and moving into the more complicated polarized theory needed for this work. Lastly is a brief discussion of the SASKTRAN-HR model used within this work.

Chapter 3 starts with an overview of Acousto-Optics Tunable Filters (AOTF), since this device is at the core of the ALI system. Background and practical application of this device will be covered with focus on the advantages and disadvantages to using this filter in a remote sensing

applications. Continuing will be a discussion of the possible optical layouts for ALI and the testing and underling choice for the optical system. With a selected optical layout of the ALI instrument and a finalized design, a discussion of calibration, testing, and creation of the operation software will be presented. Since ALI is a linear polarized instrument, a study was underwent to determine the best polarization to achieve the highest possible aerosol sensitivity, accuracy, and precision possible. Furthermore, the optimal geometry for a limb scatter polarized instrument was also determined in this same study. This was done by probing the solution space and the results of this study will be the focus of Chapter 4. The final discussion section, Chapter 5, is a presentation of the ALI test flight on a stratospheric balloon in Timmins, Ontario. The results from the measurements recorded from the flights are also presented including calibrated images, retrieved aerosol profiles, precision estimates, and particle size estimation. These results are compared to current satellite measurements and a discussion about the quality of the ALI retrievals is underwent.

CHAPTER 2

BACKGROUND

2.1 Introduction

Stratospheric aerosol plays an important role in the global radiative forcing balance by scattering solar irradiation and causing an overall cooling effect that depends on the particle size distribution and the concentration (*Kiehl and Briegleb*, 1993; *Stocker et al.*, 2013). These climate effects are an important and recent focus of research due to the potential contribution of stratospheric aerosol to the so-called global warming hiatus (*Solomon et al.*, 2011; *Haywood et al.*, 2014; *Fyfe et al.*, 2013) and efforts to quantify the variability and trends in the global stratospheric aerosol load are underway with various ground-based and satellite data sets (*Rieger et al.*, 2015; *Ridley et al.*, 2014).

Since its discovery with stratospheric balloon observations (*Junge et al.*, 1961), stratospheric aerosol has been measured with various techniques, although due to the variability of physical composition and particle size, the observations are always limited to some degree and no single measurement technique can fully determine the full range of aerosol properties unambiguously. In-situ balloon observations continue to be used and have provided highly valuable data sets, including most notably the long time series of Optical Particle Counter (OPC) measurements from Laramie, WY (*Deshler et al.*, 2003; 2008; *Kovilakam et al.*, 2015). Aircraft-borne nephelometers (*Beuttell and Brewer*, 1949; *Charlson et al.*, 1969) acquire detailed in-situ measurements, providing, for example, plume composition (*Murphy et al.*, 2014), but are spatially limited to the aircraft track. Ground based lidars have been used to do detailed studies of the extent of volcanic aerosol plumes (*Chazette et al.*, 1995; *Sawamura et al.*, 2012) and provide valuable insight into long term local variability and trends in the aerosol layer. For example, lidar observations were used by *Hofmann et al.* (2009) to first report the observed increase in stratospheric aerosol over

approximately the last decade. However, the global distribution, which can only really be obtained with satellite observations, provides invaluable insight into aerosol processes and variability. A good example of this is the use of satellite observations by *Vernier et al.* (2011b) to determine that the increased stratospheric aerosol load reported by *Hofmann et al.* (2009) was in fact due to a series of relatively minor, mostly tropical, volcanic eruptions.

Several recent studies have highlighted the requirement for continued global stratospheric aerosol observations and especially the need to resolve, both vertically and horizontally, aerosol in the lowermost stratosphere and the upper troposphere. This is the case for tracking the evolution of aerosol from volcanic eruptions, which can have a substantial effect on the aerosol optical depth in the lowermost stratosphere (*Ridley et al.*, 2014; *Andersson et al.*, 2015). Furthering the understanding of the transport of aerosol near and across the tropopause would also benefit from higher spatial and temporal resolution observations. This is evident in the case of volcanic plumes, such as that from Nabro in 2011, the transport and origin of which has been studied extensively and the conclusions are somewhat controversial (*Bourassa et al.*, 2012c; 2013; *Vernier et al.*, 2013; *Fromm et al.*, 2013; 2014; *Fairlie et al.*, 2014; *Clarisso et al.*, 2014). However, this is also the case for the formation of background-level aerosol, particularly in the region of the Asian and North American monsoons, which have been identified as a source of substantial, seasonal and highly structured aerosol formation from precursor tropospheric source gases (*Vernier et al.*, 2011a; *Neely et al.*, 2014; *Thomason and Vernier*, 2013).

Continued stratospheric aerosol observations from space are drastically needed though few, if any, planned missions with such capability are underway. In this work, we present the design and test of a prototype instrument for potential future satellite-based stratospheric aerosol observation. The Aerosol Limb Imager (ALI) concept is a relatively small, low-cost, low-power, passive

instrument, suitable for microsatellite deployment with the capability to provide high spatial resolution measurements, both vertically and horizontally, of the visible/NIR aerosol extinction coefficient. The basic idea is to leverage the clear advantages of the limb scatter technique as a passive, and therefore low mass and low power, means to obtain daily global coverage, with a two dimensional hyperspectral imager for filling cross-track observation.

The ALI instrument concept is built around the use of an Acousto-Optic Tunable Filter (AOTF), which is a novel filtering technology that provides the ability to rapidly select the central wavelength of an image with no moving parts. These filters, which have recently been developed as large aperture imaging quality devices, operate very efficiently in the red and near infrared spectral range, which is a well matched spectral range for limb scatter sensitivity to aerosol and cloud (*Rieger et al.*, 2014). Additionally, the spectral bandpass of the AOTF, which is typically between 3-6 nm at these wavelengths, is very suitable for the broadband scattering characteristics of the aerosol limb signal. The two dimensional imaging nature of the design provides the capability to achieve at least sub-kilometer resolution at the tangent point, which is on the order of the scale size of the upper troposphere and lower stratosphere (UTLS) aerosol features mentioned above.

It should be noted that the basic instrument design concept of ALI is very similar to that of the Atmospheric Limb Tracker for the Investigation of the Upcoming Stratosphere (ALTIUS) (*Dekemper et al.*, 2012), which is a Belgian instrument concept from the Belgian Institute for Space Aeronomy (BIRA). ALTIUS is designed to measure limb scattered sunlight; however, it also has solar, stellar, and planetary occultation modes and is scientifically focused on trace gas measurements, particularly for ozone, whereas ALI is optimized for aerosol observation.

2.2 Stratospheric Aerosol

The atmosphere of earth is a complex and complicated system and is effected by human activities. In the late 18th century, it was known that atmospheric temperature decreased with altitude and a theory had been raised that at specific altitude the temperature must eventually go to absolute zero. This lead to a series of balloon campaigns, which were noisy and unreliable due to the technology available, to discover this mysterious altitude in the atmosphere,. However, in the late 19th century the technology used in these sounding balloons had improved to a point where the atmospheric temperature could be accurately measured and it was found that at approximately 12 km an inversion point was discovered where the temperature started to increase and thus the tropopause, which separates troposphere and the stratosphere, was discovered (*Hoinka*, 1997). The stratosphere is the region of the atmosphere above the temperature inversion of the troposphere, where atmospheric temperature increases and the lower bound of the stratosphere is in-between 10 and 16 km from the high latitude to the tropics (*Andrews*, 1987). The stratosphere, which extends up to approximately 50 km, is thermodynamically stable and fairly dry (*Boucher*, 2015). The characteristic stability of the region limits vertical transport of the stratosphere, leading to long lifetimes, spanning from months to years, for non-volatile species (*Volk et al*, 1997; *Brasseur and Solomon*, 2005)

The stratosphere undergoes exchange of air with the troposphere though a series of dynamical processes including tropical convection, polar vortex, and tropopause folding (*Holton et al.*, 1995) and circulation within the stratosphere is dominated by the slow Brewer-Dobson circulation (*Plumb and Eluszkiewicz*, 1999). Some chemicals can cross the tropopause thermal barrier into the stratosphere which allows for chemicals reactions to occur. One such reaction forms stratospheric sulfate aerosol, discovered by *Junge et al* (1961) though stratospheric balloon sondes. Sulfate aerosols are droplets of hydrated sulfuric acid (H_2SO_4) formed from the oxidation

of sulfate compounds, primary OCS and SO₂ (*Brock et al.*, 1995). This stable layer of aerosol exists in the stratosphere from the altitude of the tropopause to approximately 30 km.

2.2.1 Aerosol Sources and Microphysics

The sources for sulfate aerosol are primarily produced in the troposphere and formed through both natural and anthropogenic processes. One primary source of this sulfur is OCS which originates from marine processes, biomass burnings, and industry (*Kettle et al.*, 2002; *Notholt et al.*, 2003). OCS has a long lifetime in the troposphere and low solubility allowing for a significant portion to reach the stratosphere and some of it oxidizes and hydrates to form sulfate aerosol (H₂SO₄) and adds to the background aerosol layer (*Crutzen*, 1976).

Another source of sulfur is SO₂, which originates in the troposphere through industry from the burning of fossil fuels. Sulfur dioxide (SO₂) has a short lifetime in the troposphere, its concentration varies regionally, and also hydrates into sulfate aerosol (*Thomason and Peter*, 2006). A second source of SO₂ is from volcanic eruptions which are highly variable in location and time and can inject a large amount of sulfur directly into the stratosphere. Volcanos can inject such large amounts of sulfur that they in fact dominate the stratospheric aerosol layer perturbing the background levels. Examples of this perturbation of the aerosol layer were noted during the volcanic eruptions of El Chichon in 1982 (12-20 Tg of sulfur) (*McCormick and Swissler*, 1983; *Hofmann and Rosen*, 1983) and Mount Pinatubo in 1991 (20-30 Tg of sulfur) (*McCormick and Veiga*, 1992). However, after the Mount Pinatubo eruption a volcanically quiescent period occurred where aerosol layers returned to background. Following this period, a series of smaller volcanic eruptions have increased the background aerosol layer in the amount of 4-7% per year from 2000 to 2009 (*Vernier et al.*, 2011).

These sulfur sources undergo a series of reactions to be converted into H₂SO₄ and have been found to form droplets of aerosol that consists of approximately 25% H₂O and 75% H₂SO₄

(Rossen, 1971; Wang *et al.*, 1989). These aerosol particles form droplets of various sizes on the order of 0.05 to 1.0 μm depending on the processes of nucleation, evaporation and condensation that is underwent (Junge *et al.* 1961; Brock *et al.*, 1995; Bingen *et al.*, 2004). A log-normal distribution has been used to approximate the particle size of aerosol in the form of

$$\frac{dn(r)}{dr} = \frac{n_0}{r \ln(\sigma_g) (2\pi)^{1/2}} \exp\left(-\frac{\ln^2(r/r_g)}{2 \ln^2(\sigma_g)}\right) \quad (2.1)$$

where n_0 is the aerosol number density, r_g is the mode radius, and σ_g is the mode width (Jäger and Hofmann, 1991; Hamill *et al.* 1997). The particles are distributed normally over the logarithm of the radius. To fully describe aerosol for a single log-normal distribution the number density, mode radius and mode width is required and for a non-volcanic background aerosol layer an approximate mode radius and mode width of 0.08 μm and 1.6 respectively have been determined (Thomason, 1991) shown in Figure 2-1.

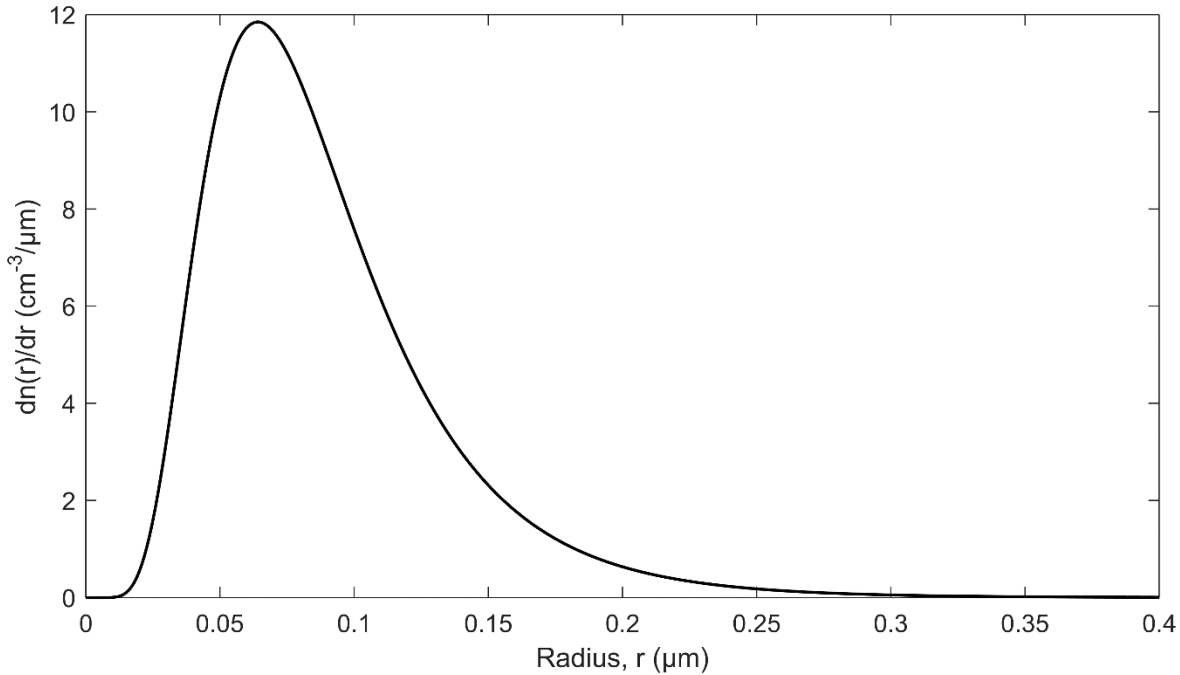


Figure 2-1: Log-normal distribution for non-volcanic background aerosol layer.

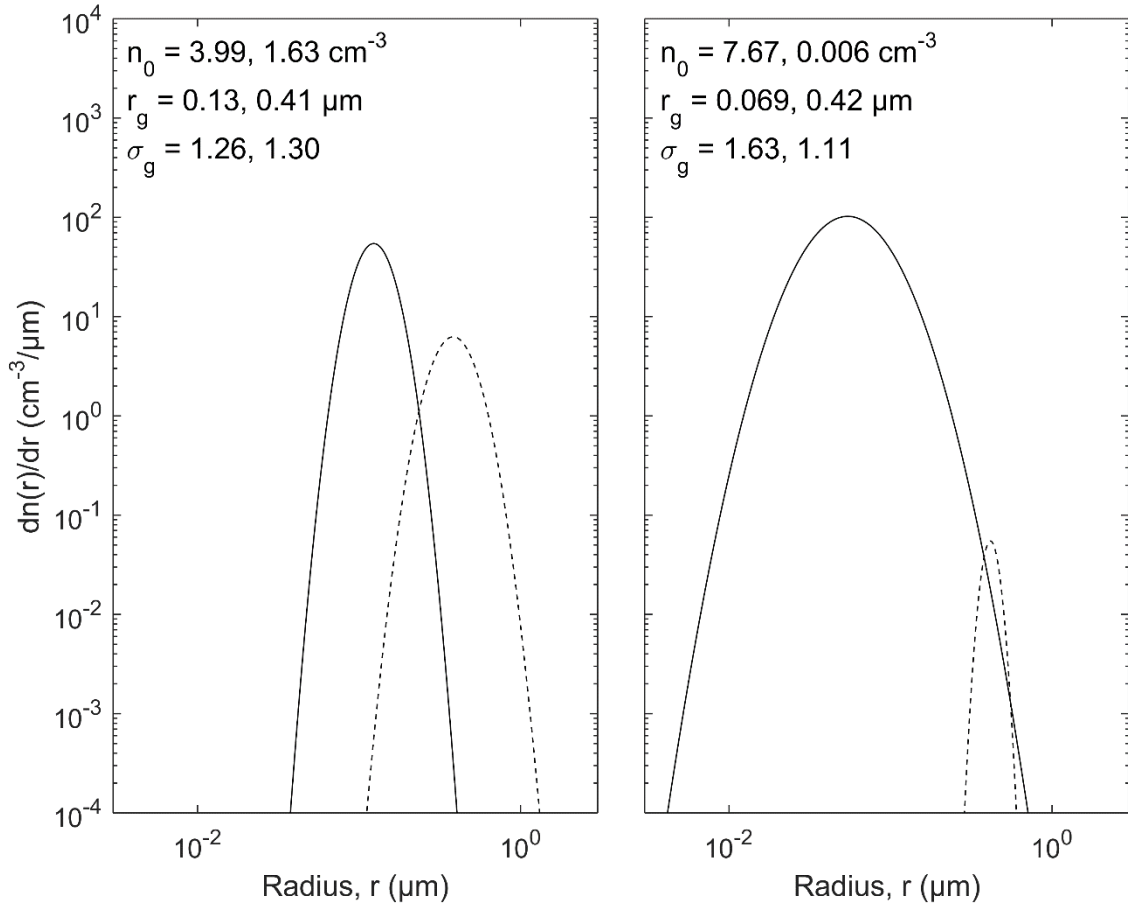


Figure 2-2: Bimodal particle size distributions fits from OPC. (a) Distributions from a volcanic period after the Mount Pinatubo eruption recorded in 1993. (b) Distributions from a background aerosol period recorded in 1999. Both of the aerosol distribution measurement are from 20 km altitude with the solid line being the fine mode and the dashed line is the coarse mode. Figure is recreated from Figure 5 of *Deshler et al. (2003)*.

OPC have been used on board sondes from Laramie, Wyoming over the past 40 years to measure particle sizes in bins between 0.15 to 2.0 μm . The composition of the particle size distributions have been primarily unimodal, known as a fine mode, over non-volcanic periods and can be used as an acceptable distribution to approximate background periods. But during volcanic episodes, a bimodal log-normal distribution of aerosol particles is more representative of the stratospheric aerosol with the addition of a coarse mode (*Deshler et al., 2003; 2008; Kovilakam et al., 2015*). The coarse mode has larger particles than the fine mode and complicates determining full aerosol microphysical parameters since the number of required parameters has increased to

six: a number density for both the fine and coarse mode, two mode radii, and two mode widths. Figure 5 from *Deshler et al.* (2003), recreated in Figure 2-2, demonstrated two bimodal particle size distributions from balloon OPC. The first distribution is from a volcanic period in 1993 after the Mount Pinatubo eruption and another from a background period in 1999.

2.2.2 Climate Effects

Aerosol have several effects on the climate of the planet with a large amount of uncertainty to the overall effect (*Solomon et al.*, 2007). Through a direct effect, aerosol particles scatter incoming visible solar radiation away from earth increasing the albedo causing a cooling effect on the surface of the planet (*Lacis et al.*, 1992). The albedo is the amount of incoming irradiance that is reflected by the earth. A secondary effect from aerosols, that is dependent on aerosol particle size distributions, is a greenhouse effect that is caused by infrared radiation from the planet being scattered by aerosols (*Kiehl and Briegleb*, 1993). Aerosol also introduces an indirect effect to a radiative balance known as the cloud albedo effect. This is caused by condensation on existing aerosol particles forming cloud condensation nuclei which leads to an increase of the albedo for short wavelengths which also contributes to cooling the planet's surface. These types of cloud forming particles tend to increase the overall lifetime of the cloud increasing the cloud coverage of the planet and thus increasing the albedo (*Charlson et al.*, 1992). Overall, the cooling effect of the aerosol particles dominates the warming effect and cools the surface of the planet (*Solomon et al.*, 2011).

Background aerosol periods result in nominal cooling from stratospheric aerosols but this can greatly change during periods of volcanic activity where the layer can be greatly perturbed. After the eruption of Mount Pinatubo in 1991 the sulfate aerosol load was increased by large quantities causing cooling of the lower atmosphere by 0.5°C (*McCormick et al.* 1995; *Soden et al.*, 2002) and 0.1 to 0.3°C on the surface (*Thompson et al.*, 2009; *Canty et al.*, 2013). And the surface

temperatures did not return to pre-Pinatubo level until approximately three years after the eruption as the atmosphere filtered out the additional aerosol (*Hansen et al.*, 1996). More recently, a series of small to moderate volcanic eruptions have increased the background stratospheric aerosol layer (*Vernier et al.*, 2011b). The additional volcanic aerosol load has been proposed to be linked to a larger cooling effect, known as the global warming hiatus, when compared to background levels (*Solomon et al.*, 2011; *Haywood et al.*, 2014; *Fyfe et al.*, 2013). In order to fully quantify this effect, long term time series with microphysics information are required to fully understand the aerosol forcing effect on climate modeling and change.

2.3 Aerosol Measurements

Two fundamental methods are used to measure aerosol concentrations within the atmosphere. The first of these methods are ground based and in-situ measurements which give good detail and information about a specific localized area. However, these measurements are limited in scope as they do not have global coverage that is inherent in satellite instrumentation. Both ground-based instruments and satellites have important roles in monitoring the planet's aerosol content and each of these methods have inherent advantages and disadvantages. An overview will be given on some of the common methods to determine aerosol extinction and why using different methods helps to increase the overall accuracy and precision of merged data sets.

2.3.1 In-Situ Measurements

In-situ measurement have occurred on balloon based platforms and aircrafts. Balloon instruments that use particle counters during the ascent directly count the aerosol particles and can determine the particle size distributions. The OPC is an active instrument that uses light source internal to the device to optically count aerosol particles. This instrument has been launched from Laramie, Wyoming since 1971 and have successfully measured aerosol extinction and particle size distributions (*Deshler et al.*, 2003; 2008; *Kovilakam et al.*, 2015). Another type of balloon

instrument uses a passive light source, such as the sun, moon, or stars, to determine aerosol extinctions. Some instruments that use this type of technology are the Absorption par les Minoritaires Ozone et NO_x (AMON) from 1992 to 2003 and Spectroscopie d’Absorption Lunaire pour l’Observation des Minoritaires Ozone et NO_x - Nacelle 2 (SALOMON-N2) from 2007 onwards which use starlight and moon light respectively (*Berthet et al.*, 2002). Furthermore, aircrafts have been used to carry nephelometers to acquire detailed in-situ measurements (*Beuttell and Brewer*, 1949; *Charlson et al.*, 1969) including plume composition (*Murphy et al.*, 2014) but are limited spatially to the aircraft track.

In-situ measurements of aerosol extinction give direct measurement of scattered light from the altitude that the instrument is currently situated and allows for direct measurements of aerosol extinction and cross-section unlike remote sensing applications from satellites. However, these types of instruments do not achieve global coverage and only give aerosol extinction from a very localized region, like the Laramie, Wyoming OPC, or have very few flights, for example AMON which had a total of six stratospheric balloon flights, three mid-latitude northern and three high-latitude northern flights. In order to achieve full global coverage satellite remote sensing instruments are needed to fill the spatial gap.

2.3.2 Occultation

Satellite instrumentation capable of remote sensing stratospheric aerosol has been in use since the 1970s, beginning with limb sounding solar occultation measurements, and its operational geometry can be seen in Figure 2-3. Solar occultation measurements have provided a reliable, accurate and essentially continuous long term record of vertically resolved aerosol extinction coefficient measurements, mostly from the series of Stratospheric Aerosol and Gas Experiment (SAGE) instruments (*Russell and McCormick*, 1989; *Thomason and Taha*, 2003). These SAGE measurements, which have a vertical resolution of approximately 1 km, have generally compared

well with ground-based and in-situ measurements, although there are challenges associated with determining microphysical parameters and comparison between instruments can be challenging (*Russell and McCormick, 1989; Kovilakam et al., 2015*). However, solar occultation is generally a robust and stable technique as it directly measures atmospheric optical depth, along with the exo-atmospheric solar spectrum with each scan, allowing for straightforward retrieval of aerosol extinction coefficients (*Damadeo et al, 2013*). The major drawback to occultation instruments is that a sunrise or sunset event is required to perform a measurement limiting is the number of scans per day to 16-48 measurements depending on the orbit.

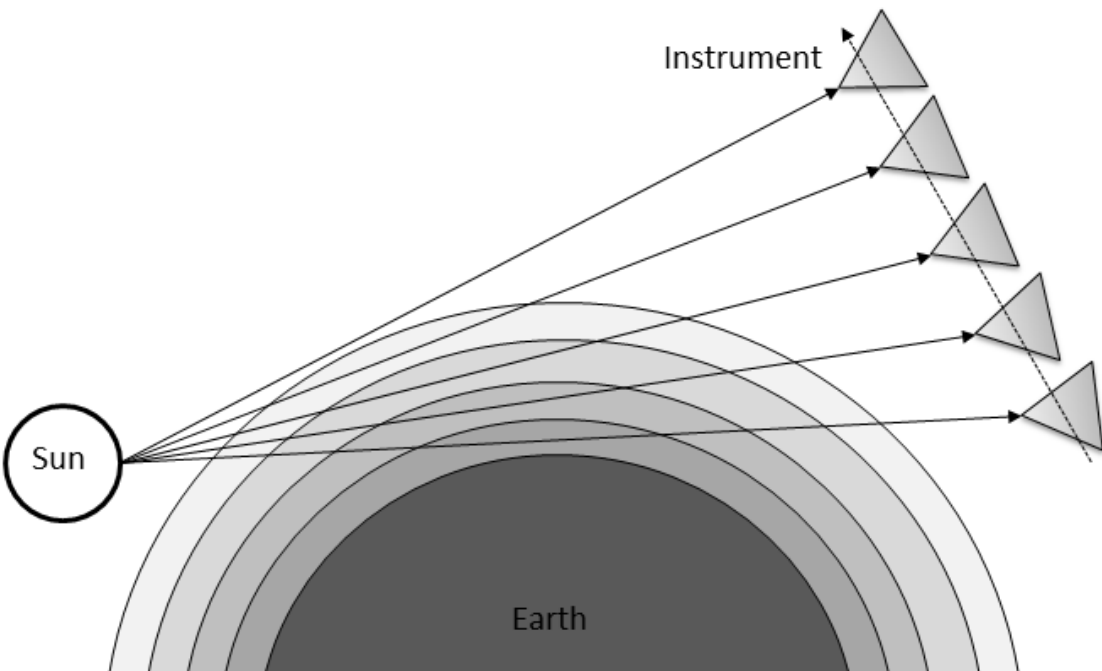


Figure 2-3: An occultation instrument monitoring the atmosphere by scanning the atmosphere by looking directly at the sun.

The SAGE III mission came to an end in 2006 and the occultation measurements have continued from the currently operational MAESTRO and ACE-Imager instruments on SciSat (*McElroy et al., 2007; Gilbert et al., 2007*) and have had some success producing stratospheric aerosol extinction products (*Vanhellemon et al., 2008; Sioris et al., 2010*). Furthermore, a

manifestation of SAGE III is planned for deployment on the International Space Station in 2016 (*Cisewski et al.*, 2014).

2.3.3 Lidar

A method known as lidar can determine atmospheric parameters through the pulsing of a laser and measuring of the intensity of the backscattered laser light at different wavelengths and polarizations. Lidar has been used at ground based facilities to measure aerosol layers dating back to the 1960s (*Fiocco and Grams*, 1964) and are still used today. More recently lidar instruments have been used on satellite missions including the Ice, Cloud, and land Elevation Satellite (ICESat) from 2002 to 2010 (*Schutz et al.*, 2005) and Cloud-Aerosol Lidar and Infrared Pathfinder Satellite Observations (CALIPSO) which launched in 2006 (*Winker et al.*, 2007). More recently Cloud Aerosol Transport System (CATS) (*Chuang et al.*, 2013) has been mounted on the international space station in 2015 with a three year planned mission. Traditional lidar instruments have looked in the nadir direction (either straight down or up) however some instruments have looked slightly off-nadir, both can be seen in Figure 2-4. Lidar measurements have been used to determine aerosol plumes from volcanos (*Chazette et al.*, 1995; *Sawamura et al.*, 2012) and long term trends (*Hofmann et al.*, 2009).

CALIPSO is a joint mission developed between the National Aeronautics and Space Administration (NASA) and the Centre National d'Etudes Spatiales (CNES) of the United States and France respectively. It uses a two wavelength polarized lidar system to achieve high resolution aerosol and cloud retrievals along the satellite's orbital track with global coverage from 82°S to 82°N (*Young and Vaughan*, 2009). CALIPSO nominally measures backscatter profiles approximately every 300 m along track with approximately 200 m vertical resolution. However, the stratospheric backscatter signal is weak and requires averaging of only the night time measurements over several days and typically yielding resolutions of 0.5 km vertically and 500 km

horizontally (*Vernier et al.*, 2011b). Additionally, the uncertainty in the calibration with respect to the molecular background is on the order of the stratospheric aerosol signal and leads to a potential bias in the stratospheric measurements (*Rogers et al.*, 2011). CALIPSO was launched in 2006 and although it is presently still operational, it is also operating beyond its design lifetime.

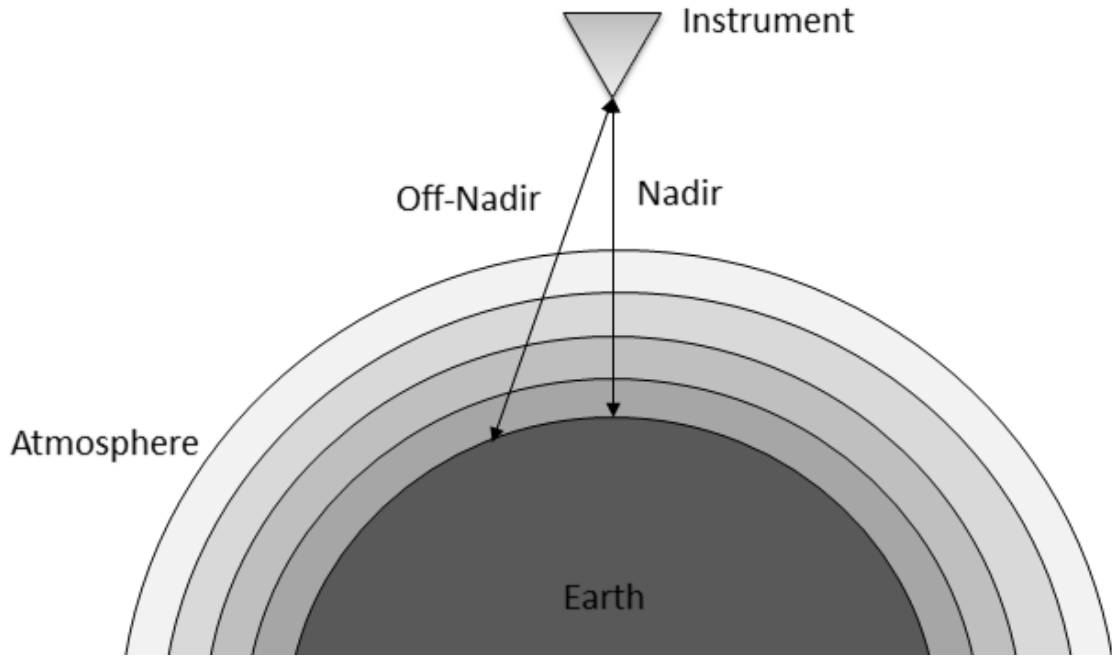


Figure 2-4: Lidar instrument showing a measurements in both the nadir and off-nadir lines of sight.

2.3.4 Limb Scatter

The limb scatter technique measures light that is scattered into the line of sight of the instrument from atmospheric interactions. These scattering interactions can undergo either single or multiple scattering events. Single scatter is when light from the sun interacts with a particle in the atmosphere and scatters it directly into the line of sight of the instrument. Multiple scatter is when the photon of light undergoes several scattering events before entering the line of sight including scattering off of multiple particles in the atmosphere or scattering off of the ground. These events can occur any number of times before entering the instrument. The geometry for the limb scatter

technique can be seen in Figure 2-5 and demonstrates the defining angles for this method. All angles are defined from the tangent point, which is the point where the distance between the line of sight and the surface of the earth is minimized, represented by the black dot. The Solar Zenith Angle (SZA) is the angle between the local vertical and the direction of the sun; the Solar Scattering Angle (SSA) is the defined to be between the direction of the sun and the line of sight and the Solar Azimuth Angle (SAA) is the angle between the projection of the sun on the plane of the line of sight and the line of sight. These angles can also be seen on Figure 2-5.

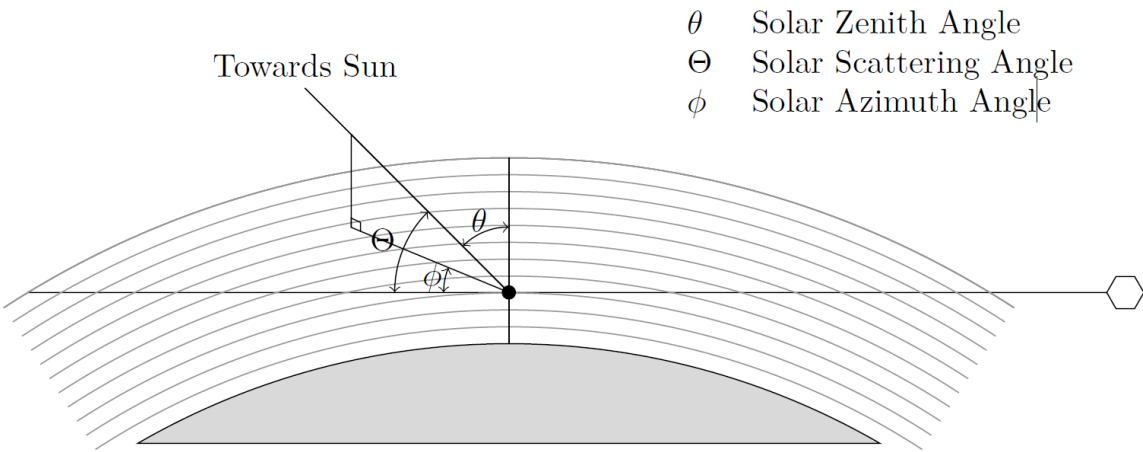


Figure 2-5: Limb scattering geometry measurement for an instrument where single and multiple scattering events occur.

The limb scatter method yields vertical resolution and allows for measurements to be taken during any daylight period with good Signal to Noise Ratio (SNR), however it requires the use of a complex forward model to calculate the scattering events along with some a priori knowledge of the aerosol scattering cross section in order to retrieve the extinction coefficient profile. The model needs to accurately determine the effect of multiple scatter since it consists of 10-50% of the measured signal depending of the specific geometry and wavelength (*Oikarinen et al., 1999*). Furthermore, due to the complex nature of the problem; a large amount of computational time and memory is required for an accurate calculation.

The first use of limb scatter was on the Solar Mesosphere Explorer (SME) (*Barth et al.*, 1983) to measure mesospheric ozone profiles in 1981. Much later, other limb scatter instruments were launched into low earth orbit that had the capability to determine aerosol extinctions including the Optical Spectrograph and InfraRed Imaging System (OSIRIS) launched on the Odin satellite in 2001 (*Llewellyn et al.*, 2004) and the SCanning Imaging Absorption spectroMeter for Atmospheric CHartographY (SCIAMACHY) on Envisat launched in 2002 (*Bovensmann et al.*, 1999). Both of these instruments are scanning grating spectrometers which can gather a single tangent point and scans the atmosphere to complete a vertical profile.

The OSIRIS version 5.07 data product provides 750 nm extinction profiles at approximately 2 km vertical resolution (*Bourassa et al.*, 2007) and has been shown to agree relatively well, generally within 15%, with SAGE II and SAGE III occultation measurements (*Bourassa et al.*, 2012b; *Rieger et al.*, 2015). The SCIAMACHY instrument uses a retrieval technique essentially similar to OSIRIS to retrieve aerosol profiles at 750 nm with approximately 3 km vertical resolution (*Ernst et al.*, 2012; *von Savigny et al.*, 2015). However SCIAMACHY observations ceased with the demise of Envisat in 2012 and although OSIRIS continues to operate, it is now in the fourteenth year of a mission designed for two years.

The most recently launched limb scatter instrument is the Ozone Mapping Profiler Suite Limb Profiler (OMPS-LP) on the Suomi-NPP satellite in 2011. Although similar in spectral range and vertical resolution to OSIRIS, OMPS-LP is an imaging spectrometer that vertically images the limb in a single measurement. The imaging capability of OMPS-LP provides a decrease in the time required to obtain a limb profile and so increases the along track sampling. Recent work on the feasibility of aerosol retrieval from OMPS-LP measurements show promising results (*Rault and Loughman*, 2013).

An instrument that is currently under development is ALTIUS (*Dekemper et al.*, 2012), which is a Belgian instrument concept from the Belgium Institute for Space Aeronomy. ALTIUS is designed to image limb scattered sunlight, both vertically and horizontally across the track through the use of the AOTF technology (see section 3.1) and additionally has solar, stellar, and planetary occultation modes. ALTIUS is scientifically focused on trace gas measurements, particularly for ozone and the instrument has three channels, each channel with a separate AOTF, measuring wavelengths from 250-2000 nm which could eventually be used for aerosol extinction measurements.

2.4 Radiative Transfer

To use the limb scatter technique to determine aerosol extinction and particle size information, an understanding of radiative transfer is required. However, modeling the complex scattering interactions of light within the atmosphere is difficult. In this section, an overview of scalar radiative transfer will be performed followed by the necessary modifications to form polarized radiative transfer equations. A description of scattering interactions important to aerosols will be undertaken. Finally, an overview of the SASKTRAN radiative transfer model used within this work will be introduced.

2.4.1 Scalar Radiative Transfer

The scattering and absorption processes in the atmosphere are non-trivial and an adequate method to model this interaction is needed. The following will present a derivation of radiative transfer equations for the atmosphere with scalar radiance which does not account for polarization. In order to accurately discuss radiative transfer, a coordinate system must first be defined. If we assume that a ray of light, I , is propagating in a given direction, $\widehat{\Omega}$, and starts at a location, s_0 , with the initial position of r_0 , then the position of the ray along the path direction can be completely

defined by its path length, s . The basis of path length will be used to define the radiative transfer equations.

The fundamental theory for radiative transfer is known as Beer-Lamberts law. The law describes the change in intensity or radiance of light, dI , as it interacts with a thin layer of space or atmosphere, ds . The thin layer has particles which affect the attenuation of the light which is dependent on the number of particles, n , and the particle cross section, σ . If there are several different particles, the attenuation is a summation of the number densities and cross sections. The Beer-Lambert Law gives the following form

$$\frac{dI(s)}{ds} = -I(s) \sum_i n_i(s) \sigma_i(s). \quad (2.2)$$

The extinction of the particles is a measure of the loss of light over a given distance and is defined as

$$k(s) = \sum_i n_i(s) \sigma_i(s). \quad (2.3)$$

Integrating Equation 2.2 forms the following result

$$I(s_1) = I(s_0) e^{-\int_{s_0}^{s_1} k(s') ds'}. \quad (2.4)$$

The optical depth, $\tau(s)$, is defined as the extinction over the path length simplifying Equation 2.4 to

$$I(s_1) = I(s_0) e^{-\tau(s)}. \quad (2.5)$$

The above gives the radiance at point s_1 after it has gone through attenuation from s_0 .

Although this form of the Beer-Lambert's Law is useful for describing the loss of light through scattering or absorbing from an initial source though a medium, the atmosphere also has incoming

light that is scattered into the line of sight from other directions or emitted from particles. To account for this additional source of light a source term, J , is added to Equation 2.2 to yield

$$\frac{dI(s)}{ds} = k(s)(J(s) - I(s)). \quad (2.6)$$

Using the fact that the change in optical depth is defined as

$$d\tau = -k(s)ds \quad (2.7)$$

Equation 2.6 is rearrange to

$$\frac{dI(\tau)}{d\tau} = I(\tau) - J(\tau). \quad (2.8)$$

Using the following derivative

$$\frac{d}{d\tau}(I(\tau)e^{-\tau}) = \frac{dI(\tau)}{d\tau}e^{-\tau} - I(\tau)e^{-\tau} \quad (2.9)$$

and substituting it into Equation 2.8 yields

$$\frac{d}{d\tau}(I(\tau)e^{-\tau}) = -J(s)e^{-\tau}. \quad (2.10)$$

This form can now be integrated over the optical depth giving

$$I(\tau)e^{-\tau} - I(\tau_0)e^{-\tau_0} = - \int_{\tau_0}^{\tau} J(\tau')d\tau'. \quad (2.11)$$

Selecting the reference point at the observer to be $\tau_0 = s_0 k(s_0) = 0$ and converting the equation back to path lengths yields

$$I(s_0) = I(s)e^{-\tau(s)} + \int_s^{s_0} k(s')J(s')ds' \quad (2.12)$$

which gives the radiance as seen from an observer at a point, s , along the line of sight.

With the full form of the radiative transfer equation, the source term must be determined. In the atmosphere there are three sources of additional radiation, blackbody emissions, photochemical reactions, and scattered light. For wavelengths from the visible to the near infrared (*i.e.*

wavelengths less than 2 μm) there is little contributions from blackbody emissions, also known as thermal emission. Furthermore, as long as wavelengths where photochemical reactions occur are avoided this source term can also be ignored. This leaves the only significant source of light to be added into the line of sight to be from scattered sunlight. The source term for scattered sunlight is given by

$$J(s, \hat{\Omega}) = \frac{k_{scat}(s)}{k(s)} \int_{4\pi} I(s, \hat{\Omega}') p(s, \Theta) d\hat{\Omega}'. \quad (2.13)$$

The diffuse radiance is given by $I(s, \hat{\Omega}')$ and is the radiation scattered into the line of sight from all directions. The phase function, $p(s, \Theta)$, described the probability that a ray of light will be scattered from a direction, $\hat{\Omega}'$, into the line of sight propagation direction, $\hat{\Omega}$. The scattering angle, Θ , is defined as

$$\cos(\Theta) = \hat{\Omega}' \cdot \hat{\Omega}. \quad (2.14)$$

Lastly, $k_{scat}(s)$ is the extinction only caused by scattering and not absorption. The term $\frac{k_{scat}(s)}{k(s)}$ only allows the fraction of particles that scatter radiation, and not absorb it, to contribute to the source term.

As a final note, the calculation of the diffuse radiance is what makes this a computationally heavy problem. To completely solve for the diffuse radiance, the radiance at every point in the atmosphere must be determined. Furthermore, the light can be scattered multiple times in the atmosphere, requiring a diffuse radiance for each order of scatter. Each successive scattering adds smaller contributions to the final radiance at the observer. Through this iterative process the full multiple scatter solution to the radiative transfer equation is

$$I(s_0) = \sum_{i=1}^{\infty} [I_i(s)] e^{-\tau(s)} + \int_s^0 k(s') \sum_{i=1}^{\infty} [J_i(s')] ds'. \quad (2.15)$$

The multiple scatter term is calculated until the contribution is sufficiently small to be negligible.

2.4.2 Vector Radiative Transfer

The scalar radiative transfer equation works well for systems that do not measure polarized light as the effect of polarization on the scalar radiance is small. However for instruments that measure polarized light, a vector radiative transfer equation is required. Before polarization can even be discussed, a method to quantify polarization must be defined which will be the Stokes vectors. The Stokes vectors are given as

$$\mathbf{I} = \begin{bmatrix} I \\ Q \\ U \\ V \end{bmatrix}, \quad (2.16)$$

where I is the scalar or total radiance, Q is the horizontally polarization, U is the diagonally ($+45^\circ$) polarization, and V is the counter clockwise circular polarization (*Bickel and Bailey, 1985*). Using a reference frame where the local x-axis is defined to be the horizontal polarization leads to the following definition for the Stokes vector

$$\begin{aligned} I &= \langle E_x \rangle^2 + \langle E_y \rangle^2 \\ Q &= \langle E_x \rangle^2 - \langle E_y \rangle^2 \\ U &= 2\text{Re}(\langle E_x \rangle \langle E_y^* \rangle) \\ V &= 2\text{Im}(\langle E_x \rangle \langle E_y^* \rangle) \end{aligned} \quad (2.17)$$

The electric field aligned with the x and y-axis are E_x and E_y respectively, the star is the complex conjugate, and Re and Im are the “real part of” and “imaginary part of” respectively. The degree of polarization can be determined with the Stokes vectors. If the equality $I^2 = Q^2 + U^2 + V^2$ holds true then the light is fully polarized, otherwise it is only partially polarized if $I^2 > Q^2 + U^2 + V^2$.

With the addition of polarization, the radiative transfer and source term equations (Equations 2.12 and 2.13) need to be rewritten with polarization state included. The polarized radiative transfer equation are

$$\mathbf{I}(s_0) = \mathbf{I}(s)e^{-\tau(s)} + \int_s^0 k(s')\mathbf{J}(s')ds' \quad (2.18)$$

$$\mathbf{J}(s, \hat{\Omega}) = \frac{k_{scat}(s)}{k(s)} \int_{4\pi} \bar{\mathbf{L}}(\alpha_2) \bar{\mathbf{p}}(s, \theta) \bar{\mathbf{L}}(\alpha_1) \mathbf{I}(s, \hat{\Omega}') d\hat{\Omega}', \quad (2.19)$$

which are the vector radiative transfer and source term equations respectively (*Mishchenko et al.*, 2002). With polarization a scattering reference frame is defined and incoming radiance is rotated into the scattering frame multiplied by the phase matrix then returned to the original propagation frame. The rotation matrix is defined as

$$\bar{\mathbf{L}}(\alpha) = \begin{bmatrix} 1 & 0 & 0 & 0 \\ 0 & \cos(2\alpha) & \sin(2\alpha) & 0 \\ 0 & -\sin(2\alpha) & \cos(2\alpha) & 0 \\ 0 & 0 & 0 & 1 \end{bmatrix} \quad (2.20)$$

where α is the angle between the propagation and polarization reference frame. The radiance and the source terms are now Stokes vectors in 4 by 1 matrices and the phase function is a 4 by 4 tensor that describes the probability of the incoming light to be scattered in the propagation direction with a specific polarization. The polarization equation adds extra computation and memory consumption since the polarization must be computed at each step in the interactive radiative transfer, which is nontrivial, and stored in memory, which is four times the size of a standard scalar radiance calculations.

With the complete vector polarized radiative transfer expression the two scattering interactions that pertain to determining aerosol will be described. The first interaction is Rayleigh scattering which defines the scattering of the background atmosphere, and Mie scattering which determines how incoming light will scatter off of aerosol particles.

2.4.3 Rayleigh Scattering

Rayleigh scatter is the scattering performed on the molecular background of the atmosphere. The first calculation of molecular atmospheric scattering cross sections was by Lord Rayleigh

where he assumed the molecules were dielectric spheres with radii much less than the wavelength of the light. Later, the King correction was added to the Rayleigh scattering cross section, σ_{ray} , to yield the following expression

$$\sigma_{ray} = \frac{128\pi^5 \alpha_0^2}{3\lambda^4} \frac{6 + 3\rho_n}{6 - 7\rho_n}, \quad (2.21)$$

which is highly dependent on wavelength, λ , which is in cm. The parameters α_0 and ρ_n are the volume polarizability, in cm^{-3} , and the depolarization ratio, which is unitless (*Sneep and Ubachs, 2005*).

The other important quantity for scattering is the phase function. For Rayleigh scattering, the vector model phase function is given by the Rayleigh-Gans approximation (*Mishchenko et al., 2002*)

$$\bar{p}(\theta) = \frac{3}{4} \begin{bmatrix} 1 + \cos^2 \theta & -\sin^2 \theta & 0 & 0 \\ -\sin^2 \theta & 1 + \cos^2 \theta & 0 & 0 \\ 0 & 0 & 2\cos\theta & 0 \\ 0 & 0 & 0 & 2\cos\theta \end{bmatrix}. \quad (2.22)$$

Each component of the phase matrix itself is smooth which allows for easy and accurate calculation for Rayleigh scattering.

2.4.4 Mie Scattering

For larger particles, like sulfate aerosol, Rayleigh scattering no longer holds since the wavelengths are on the order of the size of the particles and Mie scattering must be used. *Mie (1908)* solved Maxwell's equations in a general sense with a solution using spherical Bessel and Henkel functions. Only the fundamental Mie scatter equation will be presented here but a full derivation of Mie scatter can be found in *van de Hulst (1957)*. The scattering cross section from Mie theory is given by

$$\sigma_{mie} = \frac{2\pi}{k^2} \sum_{l=1}^{\infty} (2l+1) (|a_l|^2 + |b_l|^2), \quad (2.23)$$

where k is the wavenumber and the coefficients a_l and b_l are given by

$$a_l = \frac{\Psi'_l(nkr)\Psi_l(kr) - n\Psi_n(nkr)\Psi'_l(kr)}{\Psi'_l(nkr)\zeta_l(kr) - n\Psi_l(mkr)\zeta'_l(kr)}, \quad (2.24)$$

$$b_l = \frac{n\Psi'_l(nkr)\Psi_l(kr) - \Psi_n(nkr)\Psi'_l(kr)}{n\Psi'_l(nkr)\zeta_l(kr) - \Psi_l(mkr)\zeta'_l(kr)}. \quad (2.25)$$

With the radius of the particle given by r , n is the index of refraction of the particle, and Ψ_l and ζ_l are the normalized half-integer order Bessel functions of the first kind and Henkel functions of the second kind respectively. The phase function for Mie scatter for a vector solution has the following form (*Hansen and Travis, 1974*)

$$\bar{p}(\Theta) = \frac{2\pi}{k^2 \sigma_{mie}} \begin{bmatrix} S_1 S_1^* + S_2 S_2^* & S_1 S_1^* - S_2 S_2^* & 0 & 0 \\ S_1 S_1^* - S_2 S_2^* & S_1 S_1^* + S_2 S_2^* & 0 & 0 \\ 0 & 0 & S_1 S_2^* + S_2 S_1^* & i(S_1 S_2^* + S_2 S_1^*) \\ 0 & 0 & -i(S_1 S_2^* + S_2 S_1^*) & S_1 S_2^* + S_2 S_1^* \end{bmatrix}. \quad (2.26)$$

The terms in the phase matrix, S_1 and S_2 , are known as the amplitude functions and are given by

$$S_1(\Theta) = \sum_{l=1}^{\infty} \frac{2l+1}{l(l+1)} \left[a_l \frac{1}{\sin\Theta} + b_l \frac{d}{d\Theta} \right] P_l^1(\cos\Theta), \quad (2.27)$$

$$S_2(\Theta) = \sum_{l=1}^{\infty} \frac{2l+1}{l(l+1)} \left[b_l \frac{1}{\sin\Theta} + a_l \frac{d}{d\Theta} \right] P_l^1(\cos\Theta), \quad (2.28)$$

where P_l^1 are the Legendre polynomials.

In the atmosphere, various particle sizes occur and a log-normal distribution (Equation 2.1) is assumed for aerosols. In order to determine effective scattering cross-section, a weighted average over the particle radius is performed

$$\sigma_{eff} = \frac{\int_0^{\infty} \sigma_{mie}(r)n(r)dr}{\int_0^{\infty} n(r)dr}. \quad (2.29)$$

The weighted average is similarly performed to determine the effective phase function for a particle size distribution.

It should be noted that although the theory is well founded to calculate the Mie scattering cross sections and phase functions, in practice it is computationally intensive since the terms consist of infinite sums of Bessel functions. Work done by *Wiscombe* (1980) has allowed for effective computation of the Mie scattering coefficients, which has been implemented into the SASKTRAN radiative transfer engine.

2.4.5 SASKTRAN Radiative Transfer Model

The SASKTRAN radiative transfer was first developed to solve the scalar radiative transfer equation in a fully spherical atmosphere for both single and multiple scatter with a one dimensional atmosphere (*Bourassa et al.*, 2008). The first source term, J_1 , is from the radiance from the sun which is assumed to encounter the earth in parallel randomly polarized rays. Higher order source terms are based off of the scattering within the atmosphere to produce the diffuse radiance, however it is impractical to calculate the radiance at every point in the atmosphere. Instead, a series of diffuse radiance profiles are used to simulate the diffuse radiance term. Another important assumption in the SASKTRAN model is that the ground reflection is assumed to have a depolarizing Lambertian distribution when any radiance encounters the surface of the earth with the efficiency of the albedo.

Recent upgrades have been performed on SASKTRAN and have led to a new engine known as SASKTRAN High Resolution model or SASKTRAN-HR (*Zawada et al.*, 2015) which has expanded the model to be able to perform radiative transfer calculations with a fully three dimensional atmosphere. This update allows the model to vary the atmospheric concentrations in

the model not just in the vertical direction, like the original SASKTRAN, but in both of the horizontal geometries, allowing for true variances observed in the atmosphere.

The most important update to the SASKTRAN-HR model for this work is the addition of the ability to calculate the vector or polarized radiances (*Dueck et al.*, 2016). Using the vector model allows for SASKTRAN to compute the Stokes vectors in the reference frame of the model, which can be rotated into any desired frame of reference through the use of a provided basis by SASKTRAN-HR. The polarization output from SASKTRAN-HR only performs polarized calculations up to the third order scattering interaction and all subsequent orders are assumed to be scalar.

2.5 ALI Prototype and Stratospheric Balloon Flight

New satellite instrumentation will be necessary to continue the stratospheric aerosol data set, especially since the current generation of remote sensing instruments are aging and are operating well beyond their designed lifetimes. With current prospects for missions looking bleak these new instruments will need to supply higher quality and quantity of measurements. This will be achieved with the addition of new and improved technology as well as better techniques to perform analysis on the measurements to achieve high accuracy aerosol profiles. Furthermore, the state of climate change needs to be monitored in the future to determine if current policy's such as Paris Agreement has been successful in curbing the effect of climate change and aerosol loading is an important aspect in the radiative balancing. Additionally, the current range of effects from aerosol is relatively unknown and more detailed measurement with the ability to determine aerosol microphysical parameters and dynamical process that distribution and filter aerosol in the stratosphere will help to more precisely contribute the cooling effects from aerosol on climate change.

One such instrument proposed to fulfill this role is the Aerosol Limb Imager (ALI) which will collect spectral images the atmosphere using an AOTF as the filtering device. The measurements will be recorded in a limb scatter geometry and with the correct orbit be able to achieve daily global aerosol extinctions. The ability to measure cross-track and vertical profiles measured by ALI will achieve a second dimension to the aerosol profiles that can be used to assist in the determination of aerosol dynamical processes. Additionally the used of cross-track information can be used to help identify sources and sinks of aerosol that pass through the tropopause to better understand the process that contribute to aerosol loading. The possible wavelength range for ALI can range from the visible to the near infrared will allow information the collection of microphysical parameters of aerosol. This additional information of particle size distribution in combination with the extinction profile will help to understanding the radiative forcing effects that stratospheric aerosol contribute to the planet's atmosphere. The additional information that could be provided by an ALI instrument would be significant to the contributions of determining and monitoring the effects of global climate change.

In order to image the atmosphere an AOTF will be used which will complicate the optical design and has not been well tested in a space environment. However, before a satellite mission can be considered, a proof of concept or prototype missions need to be undergone to verify feasibility of the technology. This work will entail the designing, fabricating, building, and calibrating of a prototype ALI instrument. Another important aspect of ALI is that the measurements are inherently polarized due to the nature of the AOTF and a study to determine the best geometry and polarization for a future satellite or balloon missions is undergone. Once ALI was completed, it was packed and shipped to Timmins, Ontario and was flown on a stratospheric balloon in the fall of 2014, performing an engineering test of the technology. After the mission,

the radiance measurements were used to verify that this technology can retrieve aerosol profiles accurately.

CHAPTER 3

OPTICAL DESIGN AND CALIBRATIONS

This chapter will discuss ALI from the initial planning to a completed system including calibration and testing. First, a discussion of the Acousto-Optical Tunable Filter (AOTF) will occur that covers the solution of the wave equation, diffraction efficiency, output diffracted angle, and tuning curve. Following is a calibration of the specific AOTF used in ALI and with the complete characterization of the AOTF. Following is a discussion of the two primary optical layouts considered for the instrument. Then the final optical specifications will be presented. Next, will be the addition of the opto-mechanical and control systems required to support the ALI mission. Lastly, will be the calibrations for ALI and results from a full system test.

3.1 AOTF Theory and Background

The fundamental piece of technology that allows for the building of ALI is an AOTF which permits a signal to be passed through a band gap wavelength filter with two special directions. The use of AOTF technology for space based initiatives is only recently possible due to the recent advances in creating AOTFs with the ability to maintain imaging qualities over a wide acceptance angles. This section will discuss the theory behind the AOTF.

3.1.1 Solution to the Acoustic Equation

An AOTF is a device that through phonon-phonon interaction and Bragg diffraction allows a broadband light source to be filtered and the output can be captured as a spectral image. Two primary types of AOTFs exist, collinear (*i.e.* the acoustic wave is aligned with the incident beam, (*Harris and Wallace, 1969*)) and non-collinear (*i.e.* the acoustic wave and the optical beam do not propagate collinearly in the crystal, (*Chang, 1977*)) configurations, and both use an optically anisotropic medium (*Saito and Yano, 1976*). An anisotropic medium is a material that is transparent and has a different index of refraction based upon the polarization state of the incoming

light and its propagation direction, commonly called birefringence. For imaging purposes, a wide aperture is required for an AOTF and has been developed (*Gass and Sambles*, 1991) and are currently readily available. In order to fully understand the principles behind an AOTF a stress analysis through the acousto-wave will be used to solve the wave equation.

A derivation of the wave equation for the Acousto-Optic (AO) effect will be presented starting from two of Maxwell's equations, Amperes law and Faradays law, seen in the following

$$\nabla \times \mathbf{E} + \frac{\partial \mathbf{B}}{\partial t} = 0 \quad (3.1)$$

$$\nabla \times \frac{\mathbf{B}}{\mu} = \mathbf{J} + \frac{\partial(\epsilon \mathbf{E})}{\partial t} \quad (3.2)$$

where \mathbf{E} is an electric field, \mathbf{B} is the magnetic field, \mathbf{J} is the current density, μ is the permeability, and ϵ is the permittivity. By taking the curl of the Equation 3.1, combining it with Equation 3.2, and assuming that the AOTF crystal is non-conductive (*i.e.* $\mathbf{J} = 0$) along with the identity $\nabla \times (\nabla \times \mathbf{E}) = \nabla(\nabla \cdot \mathbf{E}) - \nabla^2 \mathbf{E}$ and assuming the crystal has no net charge (*i.e.* $\nabla \cdot \mathbf{E} = 0$) gives the simplified form

$$\nabla^2 \mathbf{E} = \mu_0 \frac{\partial^2(\epsilon \mathbf{E})}{\partial t^2}. \quad (3.3)$$

Since the dielectric is not a constant with time it induces a susceptibility yielding the following form

$$\nabla^2 \mathbf{E} - \mu_0 \epsilon \frac{\partial^2 \mathbf{E}}{\partial t^2} = \frac{\mu_0}{\epsilon_0} \frac{\partial^2 \mathbf{P}}{\partial t^2} \quad (3.4)$$

where \mathbf{P} is the induced polarization due to the stress in the AO medium given by $\mathbf{P} = \epsilon_0 \Delta \chi \mathbf{E}$ and the change is the susceptibility, $\Delta \chi$ is given by $\Delta \chi = -n_i^2 n_d^2 p \mathbf{S}$. In the previous definition n_i and n_d are the indices of refraction for the incident and diffracted electric fields and p is the elasto-optic coefficient which is dependent on medium and orientation of the crystal used and \mathbf{S} is the

strain wave induced by the acousto wave. A solution for this equation will be presented in the Bragg region meaning there will only be first order diffraction effects.

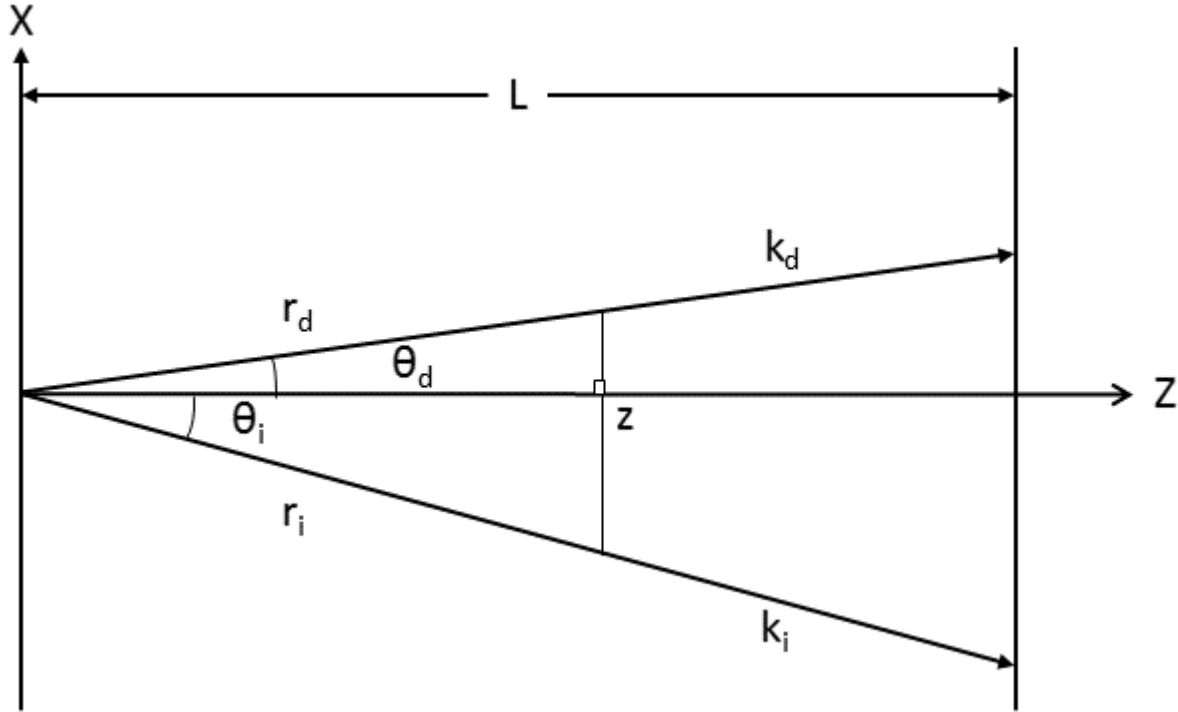


Figure 3-1: Geometry for the AOTF wave derivation assuming the acousto wave is along the x-axis and the AO interaction occurs along the z axis over a interaction length, L . The parameters r_i , k_i , and θ_i are the position vector, wave vector, and angle of the incident electric field and similarly for the diffracted electric field. Figure recreated from Xu and Stroud (1992)

Assuming the incoming electric field is a plane wave, the above differential equation can be solved. A standard acousto-optical geometry is used in the solution and is shown in Figure 3-1. The acoustic wave is propagating in the x direction of the crystal causing a stress wave which leads to the modulation of the index of refraction within the acoustic region of the crystal denoted by L . The system will be orientated such that the acousto interaction occurs along on the z axis and the electric field entering the device will be a plane wave described by

$$\mathbf{E}_i(\mathbf{r}, t) = \frac{1}{2} \mathbf{E}_i(z) \exp[j(\omega_i t - \mathbf{k}_i \cdot \mathbf{r}) + \text{c. c}] \quad (3.5)$$

and the diffracted electric field is described as

$$\mathbf{E}_d(\mathbf{r}, t) = \frac{1}{2} \mathbf{E}_d(z) \exp[j(\omega_d t - \mathbf{k}_d \cdot \mathbf{r}) + c.c.] \quad (3.6)$$

where ω and \mathbf{k} are the frequencies and wave vectors for the incident and diffracted beam and c.c. is the complex conjugate of the exponential term. The modulation caused by the acoustic wave is a strain on the crystal given as

$$\mathbf{S}(\mathbf{r}, t) = \frac{1}{2} \mathbf{S}(z) \exp[j(\Omega t - \boldsymbol{\kappa} \cdot \mathbf{r}) + c.c.] \quad (3.7)$$

where Ω is the frequency of the Radio Frequency (RF) wave, and $\boldsymbol{\kappa}$ is the acousto wave vector.

Equations 3.4 through 3.7 will be used to determine the coupled wave equations. The induced polarization is given by the incident wave and the strain wave interacting in the form of $\mathbf{P} = \epsilon_0 \Delta \chi \mathbf{E}$. The polarization wave will in turn stimulate the diffracted electric field yielding the first half of the coupled equations in the form

$$\frac{dE_d(z)}{dz} - j\Delta k E_d(z) = -j \frac{n_i^2 k_d}{4 \cos \theta_d} p S E_i(z) \quad (3.8)$$

$$\frac{dE_d(z)}{dz} - j\Delta k E_d(z) = j \frac{v_i}{2L} E_i(z)$$

where Δk is the difference between the group and phase wave vectors of the diffracted electric field, and L is the length of the AO interaction. However, once the interaction between the incident electric field forms the diffracted field, the diffracted field in turn interacts to form a polarization wave that stimulates the incident wave yielding the second coupled equation

$$\begin{aligned} \frac{dE_i(z)}{dz} &= -j \frac{n_d^2 k_i}{4 \cos \theta_i} p S^* E_d(z) \\ \frac{dE_i(z)}{dz} &= j \frac{v_d}{2L} E_d(z). \end{aligned} \quad (3.9)$$

For Bragg diffraction the geometry is set up such that the difference of the wave vectors for the incident electric field is zero. Finally, v_i and v_d is the optical phase shift and the effective optical phase shift is defined as $v^2 = v_i v_d$.

Solving the coupled wave equations yields the following solutions

$$E_i(z) = \exp\left(j \frac{\Delta k}{2} z\right) \left(A_1 \cos \frac{Tz}{L} + A_2 \sin \frac{Tz}{L} \right) \quad (3.10)$$

$$E_d(z) = \exp\left(j \frac{\Delta k}{2} z\right) \left(B_1 \cos \frac{Tz}{L} + B_2 \sin \frac{Tz}{L} \right) \quad (3.11)$$

where $T = (v_i v_d + \Delta k^2/4)^{\frac{1}{2}}$. It should be noted that the frequency of the diffracted wavelength will be $\omega_i + \Omega$ though the coupled interaction. To find the unknown coefficients, the boundary conditions of the system, are used

$$E_i(0) = E_i, \quad E'_i(0) = 0, \quad E_d(0) = 0, \quad E'_d(0) = \frac{v_i}{2L} E_i. \quad (3.12)$$

Solving for the coefficients yields

$$E_i(z) = E_i \exp\left(j \frac{\Delta k}{2} z\right) \left(\cos \frac{Tz}{L} - j \frac{\Delta k L}{2T} \sin \frac{Tz}{L} \right) \quad (3.13)$$

$$E_d(z) = E_i \exp\left(j \frac{\Delta k}{2} z\right) \left(\frac{v_i}{2T} \sin \frac{Tz}{L} \right). \quad (3.14)$$

3.1.2 Diffraction Efficiency

The diffraction efficiency, η , of the AOTF is ratio of the energy of the incident electric field compared to the energy of the diffracted electric field at the end of the acoustic interaction region given by

$$\eta = \frac{|E_d(L)|^2}{|E_i(0)|^2} = \left(\frac{v_i}{2}\right)^2 \left(\frac{\sin T}{T}\right)^2 \cong \left(\frac{v}{2}\right)^2 \left(\frac{\sin T}{T}\right)^2. \quad (3.15)$$

This form yields the common sinc function shape for the spectral Point Spread Function (PSF) of an AOTF. However, this form can be altered to better identify how to increase the diffraction

efficiency of an AOTF. The diffraction efficiency will be converted into a form that uses the RF driving power assuming exact momentum matching (*i.e.* $\Delta k = 0$) and that the interaction is occurring within a birefringent medium. The RF driving power is the amplitude at which the piezoelectric transducer pumps the RF signal into the AO medium. The average energy flow of the acoustic power is defined by

$$P_a = \frac{\rho v^3 S^2 H L}{2} \quad (3.16)$$

where ρ is mass density of the medium, v is the acoustic velocity in the crystal, H and L is the height and length of the acoustic wave interaction region. Another variable that will be defined is known as the acousto-optic figure of merit, M_2 , which is completely determined by the medium properties defined by

$$M_2 = \frac{n_i^3 n_d^3 p^2}{\rho v^3} \quad (3.17)$$

and is a measure of how efficient a medium can undergo the AO effect.

Using Equations 3.16 and 3.17 and rearranging Equation 3.15 yields the following for the diffraction efficiency

$$\eta = \sin^2 \left(\frac{\pi}{\lambda \sqrt{\cos \theta_i \cos \theta_d}} \sqrt{\frac{M_2 L P_a}{2H}} \right). \quad (3.18)$$

The efficiency of the diffraction at a wavelength, λ , can be increased through design considerations. First, a medium should be picked that yields the largest possible AO figure of merit. Second, the active region of the AO interaction should be narrow and long increasing the L/H ratio. And lastly, the driving power of RF wave should be large enough to equate the component inside of the sinusoid function in Equation 3.18 to π . It should be noted that increasing the RF power too high can have the possibility of decreasing the AOTF diffraction efficiency.

3.1.3 Diffraction Angle

Although the wave equations are useful in determining the diffraction efficiency and the form of the electric fields; it is not convenient to determine angle of the diffracted wave or the RF acousto wave to wavelength relation known as the tuning curve (covered in the section 3.1.4). A discussion on the diffraction angle will be analyzed using the interaction between the acoustic sound wave and the phonon light by

$$\mathbf{k}_i = \boldsymbol{\kappa} \pm \mathbf{k}_d \quad (3.19)$$

known as the momentum matching criteria. For this analysis, only the +1 order diffraction interaction will be performed although a similar analysis can be performed for the -1 case. The wave vectors are defined as

$$|\mathbf{k}_i| = \frac{2\pi n_i}{\lambda}, \quad (3.20)$$

$$|\mathbf{k}_d| = \frac{2\pi n_d}{\lambda}, \quad (3.21)$$

$$|\boldsymbol{\kappa}| = \frac{2\pi F}{v}. \quad (3.22)$$

It will be assumed that the extraordinary light undergoes the momentum matching through the device.

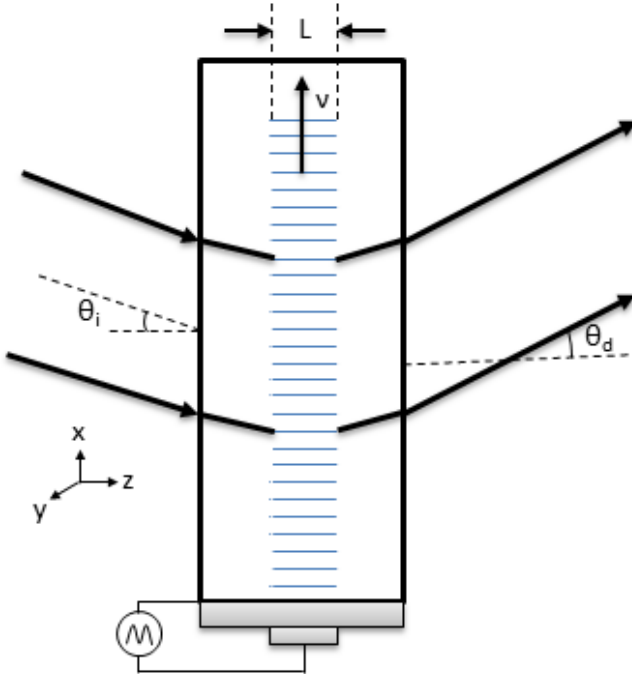


Figure 3-2: A standard non-collinear AOTF experiential set up. The crystal is assumed to infinitely long in the y direction. Figure recreated after *Guenther* (1990) number 14B-1.

A standard acousto optical experimental setup, which can be seen in Figure 3-2, will be used to determine the diffraction angle. Using Equation 3.19, the x component of the wave vector is

$$k_x = k_i \sin \theta_i = k_d \sin \theta_d + \kappa \quad (3.23)$$

and the magnitude of the diffracted wave vector is

$$k_d = \frac{\omega_d}{c} = \frac{\omega_i - \Omega}{c}. \quad (3.24)$$

Combining the results from Equation 3.23 and Equation 3.24 the angular deviation of the diffracted source is

$$\sin \theta_d = \frac{c(k_i \sin \theta_i - \kappa)}{\omega_i - \Omega}. \quad (3.25)$$

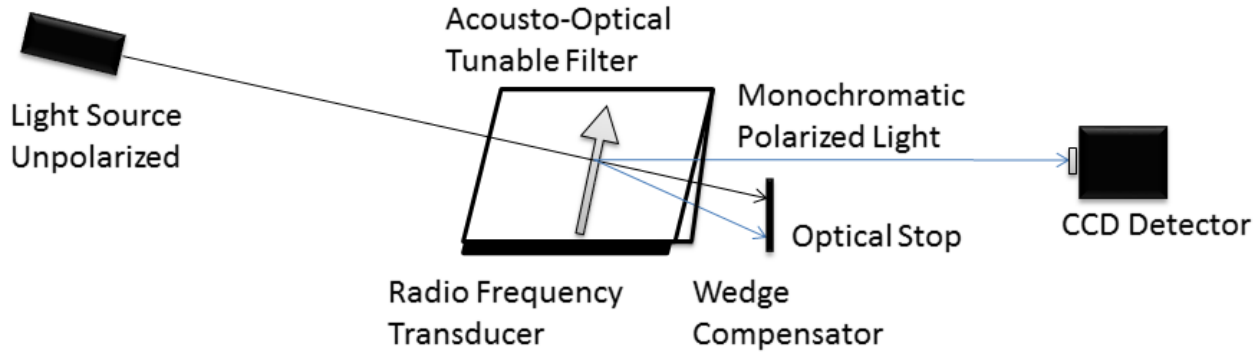


Figure 3-3: General Layout of an AOTF. A randomly polarized incoming light source hits the front surface of the birefringent crystal. The black bar below the crystal is the piezoelectric transducer that produces the RF signal and forms the acousto wave represented by the grey arrow. The momentum matching Bragg diffraction occurs and monochromatc polarized light (-1 order) exits the AOTF at a constant angle with the 0th order and +1 order being blocked by an optical stop.

The diffracted light will leave the AOTF at a different angles depending on the RF which translates to lateral movement of diffracted beam as the wavelength is scanned. In order for the device to be usable in an imaging optical system, the diffracted light must always leave the device following the same path no matter what wavelength is being filtered. Thus, a crystal wedge or compensator is fashioned to the back of the device to compensate for this effect using a correcting prism like effect causing the diffracted beam to always leave the device at the same angle. A general optical layout with the deflection in the optical path and an attached compensating wedge is shown in Figure 3-3.

3.1.4 Tuning Curve

The tuning curve is the AOTF relationship between the outputted diffracted wavelength and the acoustic sound wave frequency or RF. The analysis will be performed using the momentum matching criteria stated in Equation 3.19. **Error! Reference source not found.** shows the wave vectors in the orientation of a tellurium oxide (TeO_2) crystal in a birefringent orientation where α is the propagation angle of the acoustic wave with respect to the crystal orientation.

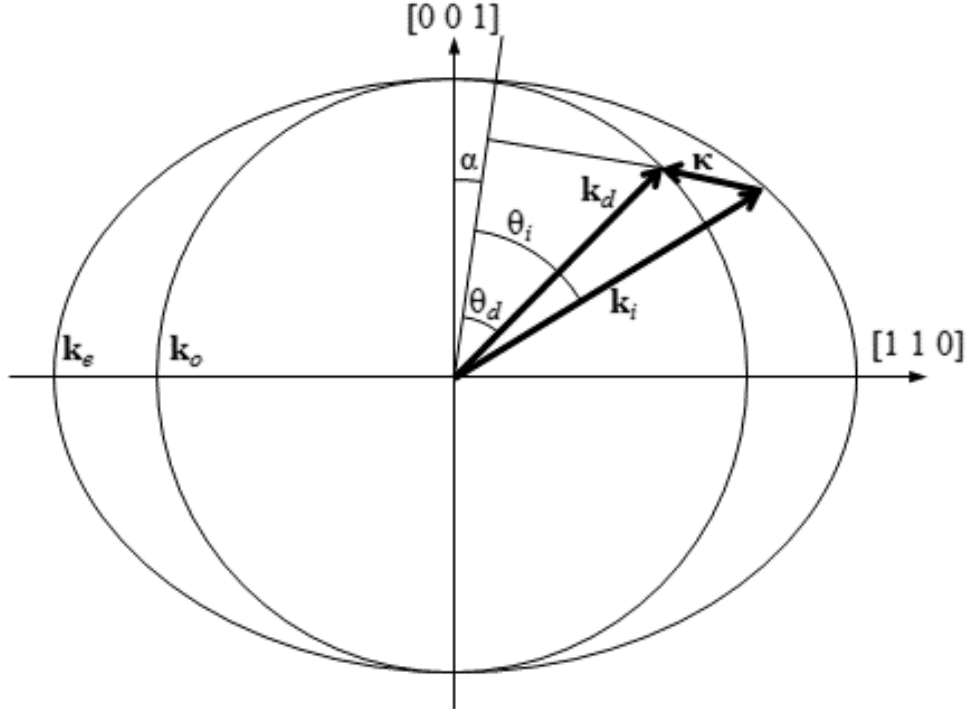


Figure 3-4: The wave vectors generated by the AOTF experiment set up in Figure 3-2. From the above figure k_e and k_o are the wave vectors of the extraordinary and ordinary axis of the AOTF crystal.

The wave vector diagram can be used to define the incident and diffracted indices of refraction in terms of the ordinary and extraordinary indices of refraction in the following

$$n_i = \left(\frac{\sin^2(\theta_i + \alpha)}{n_e^2} + \frac{\cos^2(\theta_i + \alpha)}{n_o^2} \right)^{-\frac{1}{2}}, \quad (3.26)$$

$$n_d = n_o. \quad (3.27)$$

If the difference in the index of refraction is small, as it is for TeO_2 , Equation 3.26 can be approximated as (*Voloshinov et al., 2007*)

$$n_i = n_o + \Delta n \sin^2(\theta_i + \alpha), \quad (3.28)$$

where Δn is the difference between the extraordinary and ordinary indices of refraction (*i.e.* $\Delta n = n_e - n_o$). The wave vectors, seen in **Error! Reference source not found.**, of the system need to follow the momentum matching criteria from Equation 3.19. Separating the wave vectors into their

directional components with respect to the propagation angle, α , the tangential and perpendicular directions respectively are

$$k_i \cos \theta_i = k_d \cos \theta_d \quad (3.29)$$

$$k_i \sin \theta_i - \kappa = k_d \sin \theta_d \quad (3.30)$$

The tangential and perpendicular directions of the wave vector can be used in combination with the wave vectors definitions (Equations 3.20-3.22) to yield

$$\lambda = \frac{\nu}{F} \left[n_i \sin \theta_i - (n_o^2 - n_i^2 \cos^2 \theta_i)^{\frac{1}{2}} \right]. \quad (3.31)$$

The above can be written as

$$\lambda = \frac{\Delta n \nu}{F} \frac{\sin^2(\theta_i + \alpha)}{\sin \theta_i} \quad (3.32)$$

assuming difference in indices of refraction is small (Equation 3.28) and the Taylor expansion approximation of the square root is used (*Voloshinov and Mosquera*, 2006). This equation has several implications to the operation of the device which affects the design possibilities in an imaging system. First, the wavelength diffracted by the AOTF is inversely related to frequency of the RF wave. Second, the wavelength of the diffracted signal is dependent on the angle of incidence of the incoming wave therefore passing a signal through the AOTF at different incident angles will result in different outgoing wavelengths. Also, through the described interaction, the diffracted light goes through a 90° rotation in polarization (*Voloshinov*, 1996).

3.2 AOTF Calibration and Operation

An AOTF was acquired from Brimrose of America (model number TEAFI10-0.6-1.0-MSD) with a Gooch and Housego driver (model number 64020-200-2ADMDFS-A). The AOTF has a large aperture that is of imaging quality. It is optically tuned for a range of 600 nm to 1200 nm and made from a tellurium dioxide (TeO_2) birefringent crystal. The extraordinary light is diffracted at

2.7° off of the optical axis of the device with a 10 mm by 10 mm optical aperture with a minimum separation angle of 6.4° between the zeroth and first order. A detailed overview of the AOTF specifications can be found in appendix A.1.3. First, a section on AOTF operation will be discussed and then calibration of the device will be performed. The AOTF needs to be fully calibrated to expand upon the factory specifications including:

- A tuning curve analysis
- A point spread function analysis
- Diffraction efficiency determination.

3.2.1 Operation

Some nomenclature with regards to the AOTF's operational states will be defined. This section will describe the two fundamental states used throughout the rest of this work but first will be the general operation of the AOTF itself. The general operation of the AOTF is shown in Figure 3-5a. In the general operation, with an RF wave applied, there is one input, the unpolarized chromatic incident ray, and four output signals. The birefringence of the crystal splits the zeroth order ordinary and extraordinary polarizations into two separate outputs. The RF wave interacts with the incoming radiance to form the first order extraordinary and ordinary diffracted beams with polarizations rotated by 90° . Further, only the first order extraordinary polarization remains at a consistent angle due to the compensation mentioned in section 3.1.3.

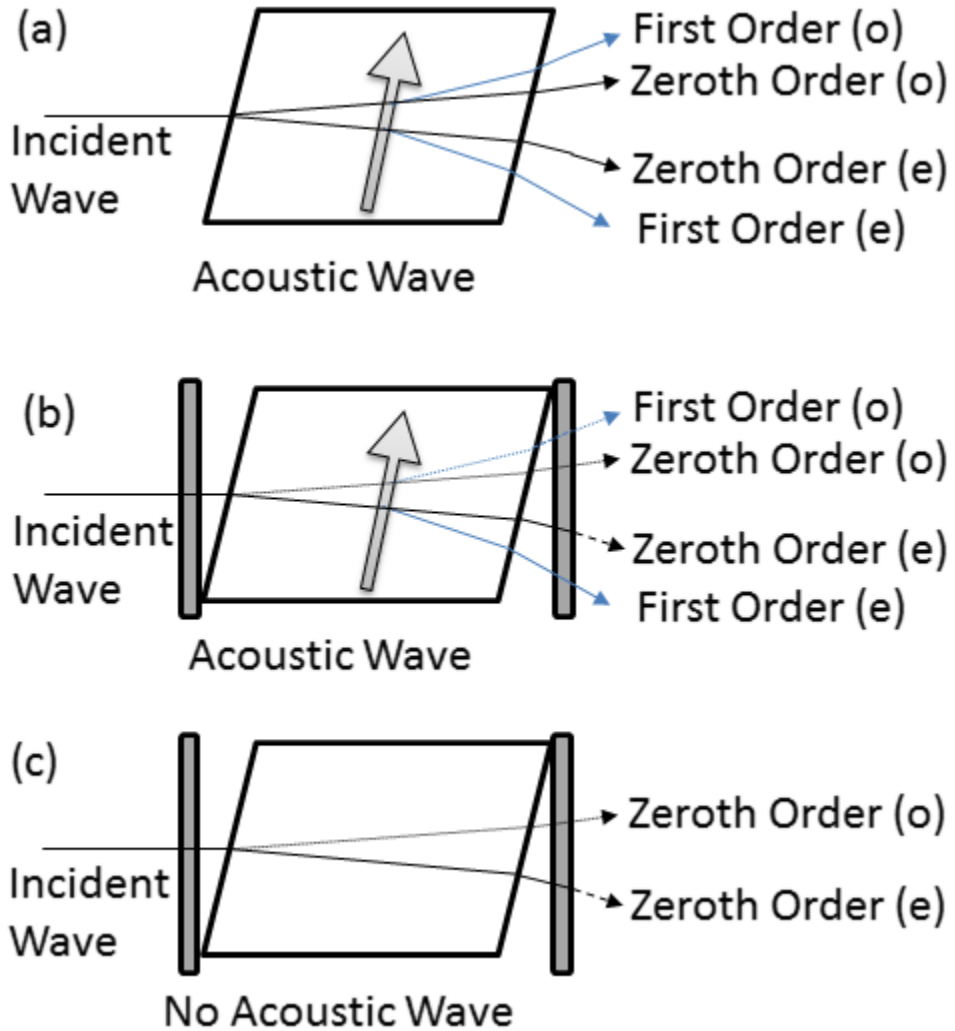


Figure 3-5: (a) An AOTF undergoing Bragg diffraction with an unpolarized input incident wave with a RF wave applied represented by the arrow. After the diffraction event four output signals are formed: the zeroth order and first order ordinary (o) and extraordinary (e) signals. However the only optical path that remains at a constant angle no matter the applied RF wavelength is the first order extraordinary diffracted signal. (b) Two linear polarizers are added to the system, the first linear polarizer removes the ordinary polarization from the outputs with the dotted lines and the second linear polarizer removes undiffracted extraordinary light shown by the dashed line. This configuration is the “AOTF-on” state. (c) The system in (b) without a RF wave so no Bragg diffraction is occurring. Once again the first linear polarizer removes the ordinary polarization represented by the dotted line and the second linear polarizer removes the extraordinary light shown by the dashed line. This configuration is the “AOTF-off” state.

When the AOTF is used in any experiments or design, the removal of the unwanted polarizations are desired to achieve high quality low contamination images. As such, a linear polarizer is always placed in front of the AOTF to remove the ordinary polarization and a linear

polarizer is place behind the AOTF to remove the zeroth border extraordinary polarization. When an RF wave is applied to the crystal with the polarizers, as seen in Figure 3-5b, the AOTF will be considered to be in the on or “AOTF-on” state. When an RF wave is not applied to the crystal and the polarizers are present, as seen in Figure 3-5c, the AOTF will be considered to be in the off or “AOTF-off” state. These two states, “AOTF-on” and “AOTF-off” will be used throughout the remainder of this work to describe these two fundamental states of the AOTF.

3.2.2 Tuning Curve Analysis

A test optical set up was devised in the lab to determine the output central wavelength with regards to the selected RF, known as the tuning curve, which was determined to know the accuracy and precision of the AOTF to select the central wavelength.

A telecentric test layout was used, which will be described in section 3.3.1. An advantage of the telecentric testing layout is that the wavelength dependence of the acousto effect from the incident angle, noted in Equation 3.32, is removed since all the lines of sight enter the AOTF with the same angular spread. The experimental set up consisted of the AOTF being located in the center of two 100 mm focal length lenses to optimally fill the AOTF aperture and linear polarizers were inserted before and after the AOTF to remove unwanted polarizations. An aperture was set up in front and behind the AOTF optical chain at the focal length of the front and back lenses respectively and opened to 5 mm to complete the telecentric experimental layout. The high front end f-number of 20 required long integration times to capture with sufficient signal but the light entering the spectrometer optics were well collimated and limited the amount of stray light. It also enabled the system to have a much higher degree of telecentricity. Two prisms were used to compensate for the 2.7° off axis bending to set the light parallel to the optical path. A standard 100 W tungsten halogen bulb was used as a light source. The front end optics had no magnification

and back optics were used to match the f-number of the spectrometer's input optics. The layout can be seen in Figure 3-6.

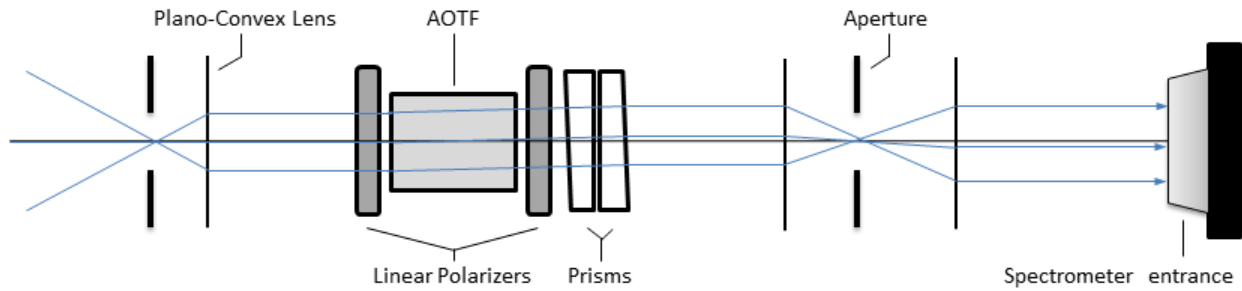


Figure 3-6: Telecentric test experiential setup for AOTF parameter determination. All lenses and apertures are represented by the same symbol.

The output is passed into a HORIBA iHR320 spectrometer with a 1200 lines/mm grating blazed at 750 nm and is imaged on a Synopse 354308 front-illuminated CCD detector with 1024x256 pixels. The CCD is thermoelectricity cooled to -75°C to reduce any significant dark current contributions to the measurements.

Images were taken at a set of RFs spaced every 150 kHz from 160 MHz to 75 MHz nominally corresponding to a 1 nm resolution. The spectral images were recorded with the spectrometer slit at 0.5 mm making the minimum Full Width Half Max (FWHM) of the spectrometer 1.175 nm, which is less than the factory specified resolution of 1.6 nm. At each RF two images were taken with a 15 second integration time: one with the AOTF in its on state and another with the AOTF in its off state. The stray light, dark current, and the DC bias are recorded in the image with the AOTF off and can be removed from the AOTF spectral image by taking the image with the AOTF on and subtracting the image with the AOTF off. Since the recorded spectra are vertical in nature all of the rows of the CCD are summed together to get the total count measurement at each wavelength. The maximum value of each image is taken to be the diffracted wavelength through

the AOTF at each respective RF. A typical spectral measurement result can be seen in Figure 3-7a.

The maximum values from each of the images were determined as well as the corresponding wavelengths. It was imperially noted that the curve appear to follow a power function of the form

$$F = a\lambda^b. \quad (3.33)$$

A linear least squares fit was performed in log space finding the coefficients a and b . The fit was performed and appeared to match the data quite well but a relative error analysis was preformed and it was seen that there was only an agreement better than 0.6% near the edges. A better fit was desired to characterize the AOTF's tuning curve so a modified power function was used in the form of

$$F = a\lambda^{b+c\log\lambda}. \quad (3.34)$$

The results of these fits can be seen in Figure 3-7c and Figure 3-7d. The agreement of this form is better than 0.1% throughout the whole wavelength range and the determined tuning curve is

$$F = \exp(19.793)\lambda^{-3.381+0.168\log\lambda} \quad (3.35)$$

where λ is in nanometers and F is in megahertz with a 0.1% error in the central wavelength. Even with considering the temperature change, the AOTF would experience a maximum wavelength drift of 2.5 nm during the mission which is acceptable for the slowly varying broadband scattering of aerosol. Furthermore, it should be noted that even though the AOTF optical range is 600 nm to 1200 nm, our analysis only measured wavelengths from 600 nm to 1080 nm due to the low quantum efficiency of the CCD beyond this range.

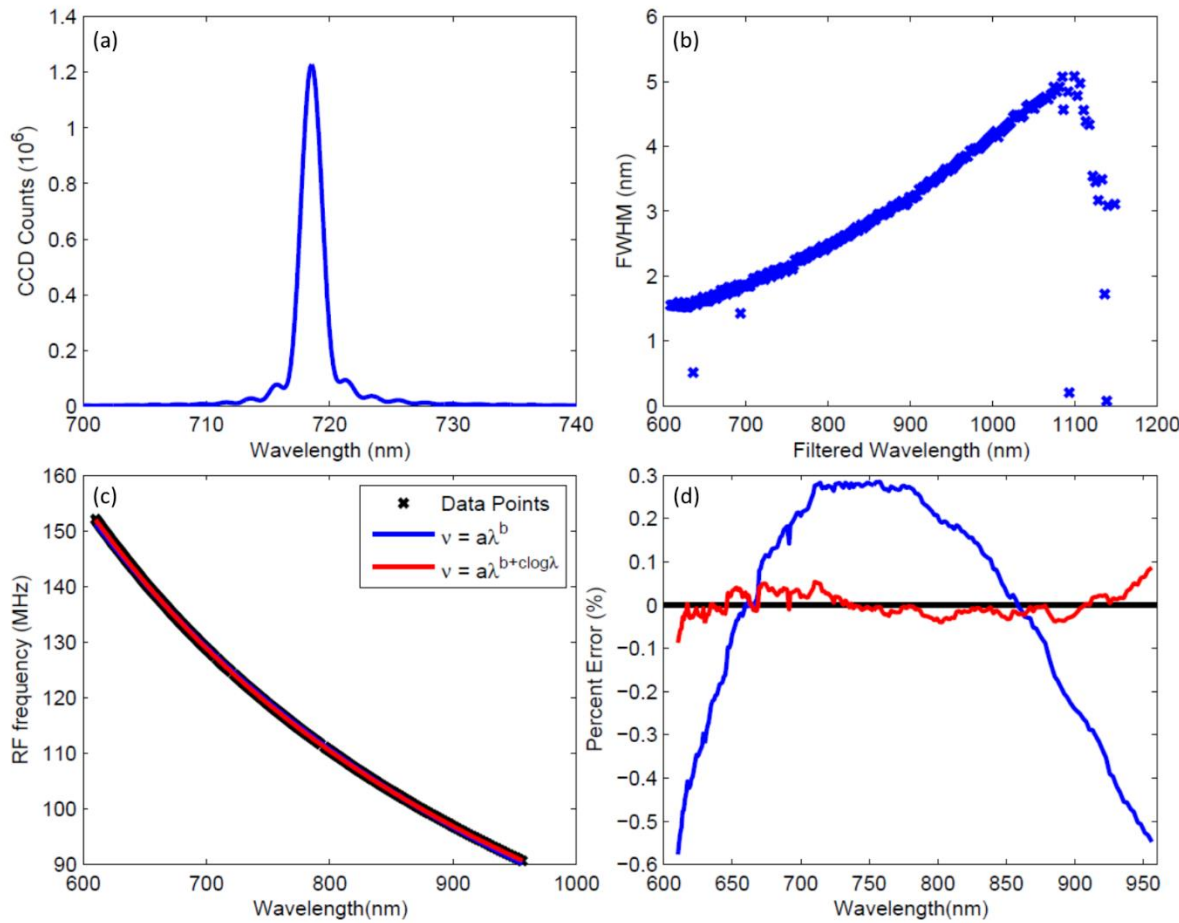


Figure 3-7: (a) A row averaged image taken from the AOTF of the point spread function when the tuning frequency of the AOTF was at 124.96 MHz. (b) The FWHM for each of the determined wavelengths for the AOTF. The FWHM at 600 nm is 1.5 nm and as the wavelengths get longer the FWHM increases to 4.9 nm at 1080 nm. (c) The calibration curves for the AOTF RF versus the diffracted wavelength which contains the data points recorded and fit curves. (d) The percent error with respect to the measured frequency for the two best fit curves in the previous panel

3.2.3 Point Spread Function

The spectral Point Spread Function (PSF) of the AOTF was also determined using the same set of data that was used to determine the tuning curve. The spectral PSF was found by determining the FWHM for each wavelength. These results are shown in Figure 3-7b. The fringes in Figure 3-7a are a known AO effect discussed in section 3.1.2 as a result of Equation 3.17 from the induced RF wave and for the Brimrose AOTF amounts to 8 to 14% of the total signal depending on

wavelength. The AOTF spectral resolution is well within the limits that are required in order to determine aerosol extinction in the upper troposphere and lower stratosphere since aerosol is a broadband scatterer.

3.2.4 Diffraction Efficiency

An experiment was performed on several wavelengths to determine the RF power that yielded the highest throughput through the AOTF using a collimated light source. For the AOTF in ALI, the maximum throughput occurred when the RF power was at the limit of the AOTF, which was 2 W. Following this, the diffraction efficiency of the AOTF was determined by using two sets measurements. The first is the experimental data used to perform the wavelength calibration, and the second is measurements of the intensity of the incident collimated light beam. The light in both experiments was linearly polarized and aligned with the polarization axis of the AOTF; for the second set the AOTF was simply removed from the optical chain. It should be noted that the attenuation of the AOTF crystal itself was not determined independently and is combined with the diffraction efficiency. We are more concerned about signal throughput of the device so the combination of the effects is acceptable. The incident light source was then measured with the same iHR320 spectrometer and Synapse CCD. By taking the ratio of the intensity at the diffracted wavelength to the incident intensity the diffraction efficiency was determined. It was found to vary between 54 and 64 % across the measured spectral range. It should be noted that the diffraction efficiency changes also with respect to incoming angle and this experimental determination only measured the diffraction efficiency at normal incidence (*Xu and Stroud, 1992*).

3.3 Optical Chain Development

ALI is a simple optical system that essentially images a single wavelength at a time through the use of an AOTF. The AOTF is a unique device that allows for filtering without any moving parts and relatively low power consumption. However, the AOTF operation requires important

instrument design considerations to account for its optical operation (*Suhre et al.*, 2004). For example, the diffractive qualities of the AOTF depend on the angle that light enters the device. Additionally, in practice the AOTF output is limited to a single linear polarization, which reduces the system throughput and causes potential internal stray light in the system through the rejection of the other linear polarization. The following sections provide a brief introduction to the two optical systems considered for ALI and an overview of the final ALI optical design. The final design images the atmosphere with a resolution on the order of 200 m for both vertical and cross-track special dimensions with a wavelength range of 600-1000 nm which corresponds to the usable range of the QSI CCD to be used in the system. Code V optical design software was used to assist in the designing and analyzing the performance of both of the optical designs and final optical system.

3.3.1 Telecentric System Prototype

The first optical system considered for ALI is a telecentric system which allows for the images without perspective. Before the telecentric prototype is discussed a basic description of a telecentric system will be described.

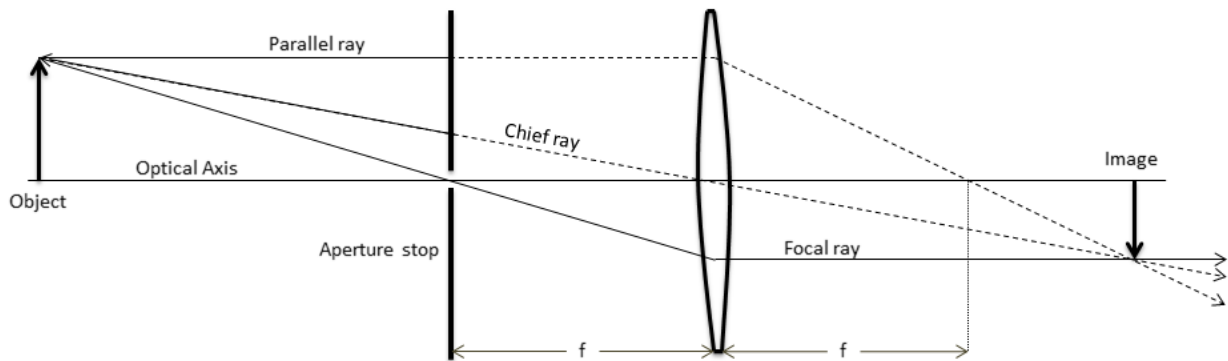


Figure 3-8: A standard paraxial ray tracing diagram. The aperture is located to make the system telecentric in the image plane and f is the focal length of the lens.

To describe the concept behind the telecentric system, a basic ray tracing image is shown in Figure 3-8 where three paraxial rays are drawn using a simple biconvex lens. To make this simple biconvex system telecentric in image space, an aperture is added to the system on the object side at the focal point of the lens. The theoretical idea is to have an aperture so small that only the focal ray can pass through it. All of the other rays, including the chief and parallel ray, are blocked from entering the system. Now the image is only defined by a single ray and it is in focus everywhere on the image side of the system, and therefore has an infinite depth of field. However, an aperture that is so small proposes a few problems in practice. First, a hole of such a small size would cause diffraction effects that would dominate the imaging qualities of the system. Second, such a small aperture would let so little signal through that very long exposure times would be needed or a low SNR would result. So in practice a larger aperture is used at the focal point. Now the system no longer has an infinite depth of field, but still retains a large depth of field and remains almost the same size no matter where the image plane is located. It should be noted that a telecentric system in object space can be created by putting the aperture on the image side of the lens causing the object to always be the same size in the image no matter where it is physically located.

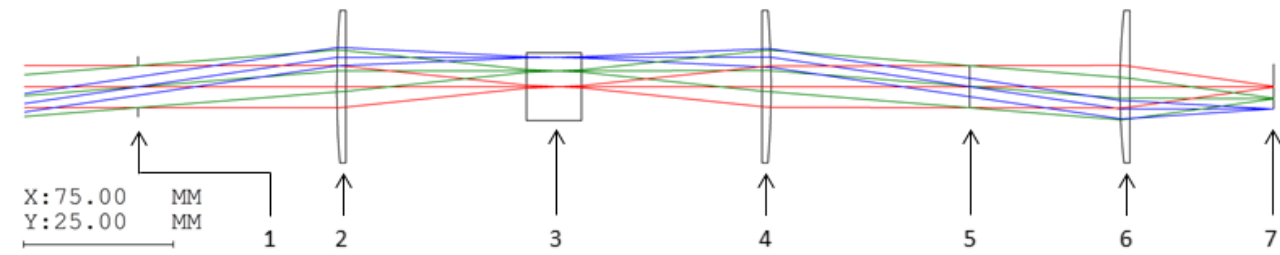


Figure 3-9: Ray Tracing diagram simulation of the telecentric lens system preformed using Code V. The elements in the system are the following: (1) Optical Stop and telecentric aperture. (2) 100 mm focal length plano-convex lens. (3) Brimrose AOTF characterized in section 3.2. (4) 100 mm focal length plano-convex lens. (5) Telecentric Aperture. (6) 75.6 mm focal length plano-convex lens. (7) Imaging plane. It should be noted that the x and y scales are not the same in this image. Also, in the lab a polarizer is added in front and behind the AOTF as well as prisms after the AOTF.

A telecentric layout in both image and object space has advantages and disadvantages for the imaging quality of the AOTF system. An advantage is since the wavelength filtered by the AOTF is dependent on the incident angle (Equation 3.32) and from the ray tracing diagram (Figure 3-9), all lines of sight enter with approximately the same angular spread so the filtered image has consistent wavelength and spectral point spread function. However, two problems are added to the system. First, a blurring effect is added to the final image dependent on wavelength, which will be discussed below in greater detail. As well, this method is sensitive to any surface defects of the crystal since the light enters the crystal in focused bundles.

A test optical system was designed with Front End Optics (FEO) to be telecentric in both object and image space with Back End Optics (BEO) to resize the image to fit on the CCD. A list of the specifications can be seen in Table 3-1 and a ray tracing diagram from a Code V simulation is shown in Figure 3-9. The AOTF has an optical aperture of 10 mm by 10 mm and is the field stop of the system. This is a physical limit of the device and causes the Field Of View (FOV) to be limited. In order to image the vertical limb from the ground to float altitude of a stratospheric balloon, typically 35 km, a 6° FOV is required. Also, with the current set up of 100 mm focal length lenses, the rays of light from each line of sight enter the AOTF at the maximum acceptance angle, which is 2°. The acceptance angle is the maximum angle that light can enter the AOTF aperture and still undergo efficient Bragg diffraction as measured from the normal to the face of the crystal (*Xu and Shroud, 1992*). This allows the maximum amount of light to enter the device to achieve highest possible throughput.

Table 3-1: Telecentric Test System Optical specifications

Parameter	Value
Effective focal length (mm)	75.6
Front End Optics Magnification	1.00
Back End Optics Magnification	0.756
Field Of View (°)	5.7 x 5.7

F-number	14.28
----------	-------

The image is focused on a 16-bit digital QSI 616 CCD with 1536x1024 pixels and a mechanical shutter that allows an integration time between 0.01 seconds to 240 minutes. The CCD chip itself is a Kodak KAF-1603ME with micro lenses to improve the quantum efficiency of the device and its spectral characteristics can be seen by the blue curve in Figure 3-10.

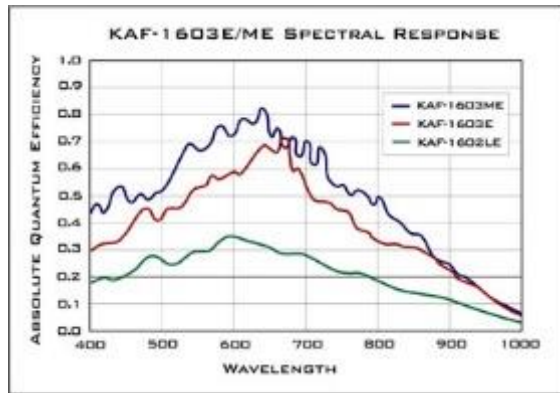


Figure 3-10: Quantum efficiency of the Kodak KAF-1603ME contained within the QSI CCD camera is represented by blue curve. Quantum efficiency provided by QSI Scientific.

The overall design has several aspects that make it a good system for imaging. First, all of the bundles of light entering the AOTF have the same angular spread. As seen in Equation 3.32, the diffracted wavelength depends on the incoming angle. With the telecentric layout all points of the imaging plane will have the same angular dependence so the entire image will be of the same center wavelength and have the similar spectral PSF.

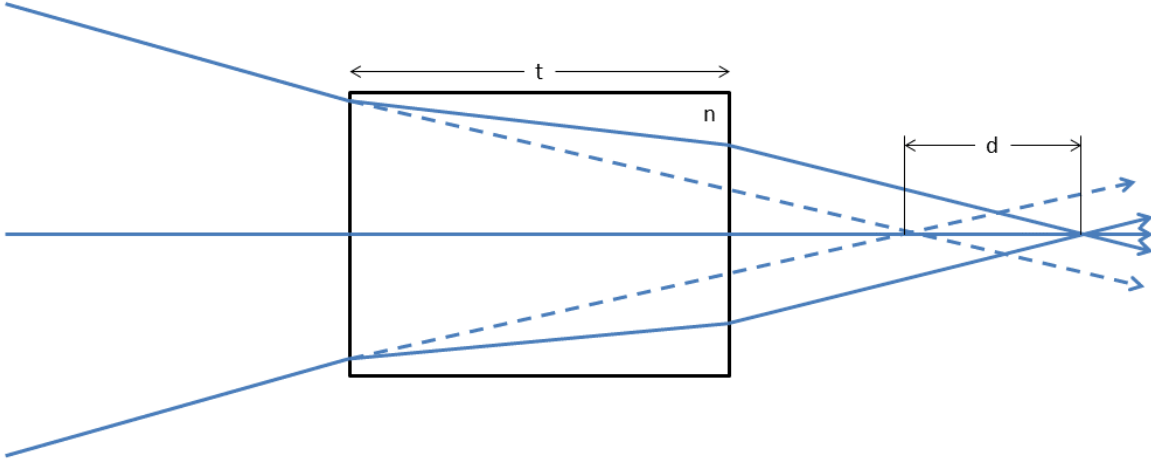


Figure 3-11: The effect on the optical path of converging light bundles as they pass through a material of index of refraction $n(\lambda)$. When the index of refraction strongly depends on wavelength, as in the AOTF, the optical path length can experience great changes that will alter the focal point of the system.

However, despite its benefits, there are a few drawbacks to consider in the design as well. First, the optical path between the two 100 mm focal length lenses is 200 mm in air for the prototype, however the AOTF is made of tellurium dioxide (TeO_2) or paratellurite and has a high index of refraction and dispersion given by (Uchida, 1971)

$$n_o^2 = 1 + \frac{2.584\lambda^2}{\lambda^2 - 0.1342^2} + \frac{1.157\lambda^2}{\lambda^2 - 0.2638^2}, \quad (3.36)$$

$$n_e^2 = 1 + \frac{2.823\lambda^2}{\lambda^2 - 0.1342^2} + \frac{1.542\lambda^2}{\lambda^2 - 0.2631^2}, \quad (3.37)$$

for the ordinary and extraordinary polarizations respectively. The high dispersive property, or Abbe number results in a change in the distance in the optical path, d , given by

$$d = \frac{n(\lambda) - 1}{n(\lambda)} t, \quad (3.38)$$

where $n(\lambda)$ is the index of refraction with a wavelength dependence and t is the thickness of the crystal. The AOTF crystal causes the optical path in air to be lengthened by d , as can be seen in Figure 3-11. In order to compensate, the length d must be added to the path to account for the

discrepancy, however the adjustment can only be compensated for a specific wavelength and thus a defocusing of the image plane will occur for other wavelengths. The severity of this problem can be seen in Figure 3-12 from a Code V simulation of the spot size of the optical system which was optimally focused for 800 nm. In this simulation, a grid of rays is passed through the system for each FOV and using ray tracing the final location for each FOV on the image plane are determined. The black circles represent the Airy disks, which are the minimum possible spot size possible due to diffraction for each wavelength of light. The spot sizes at 800 nm are on the order of 24 μm at the center, which is diffraction limited, and 94 μm at the edge of the FOV. However, for the same optical layout the 600 nm spot sizes are all greater than 160 μm which will cause a noticeable blurring in the recorded image. For a system using a telecentric system, this defocusing of the image plane would require additional compensating optics to correct the change in the path length or the detector of the system would need to be actively moved as wavelength is scanned. However, the f-number could be increased to increase the system's depth of field to reduce the defocusing effect caused by the AOTF, but the same effect causes a reduction in signal throughout leading to longer exposure times.

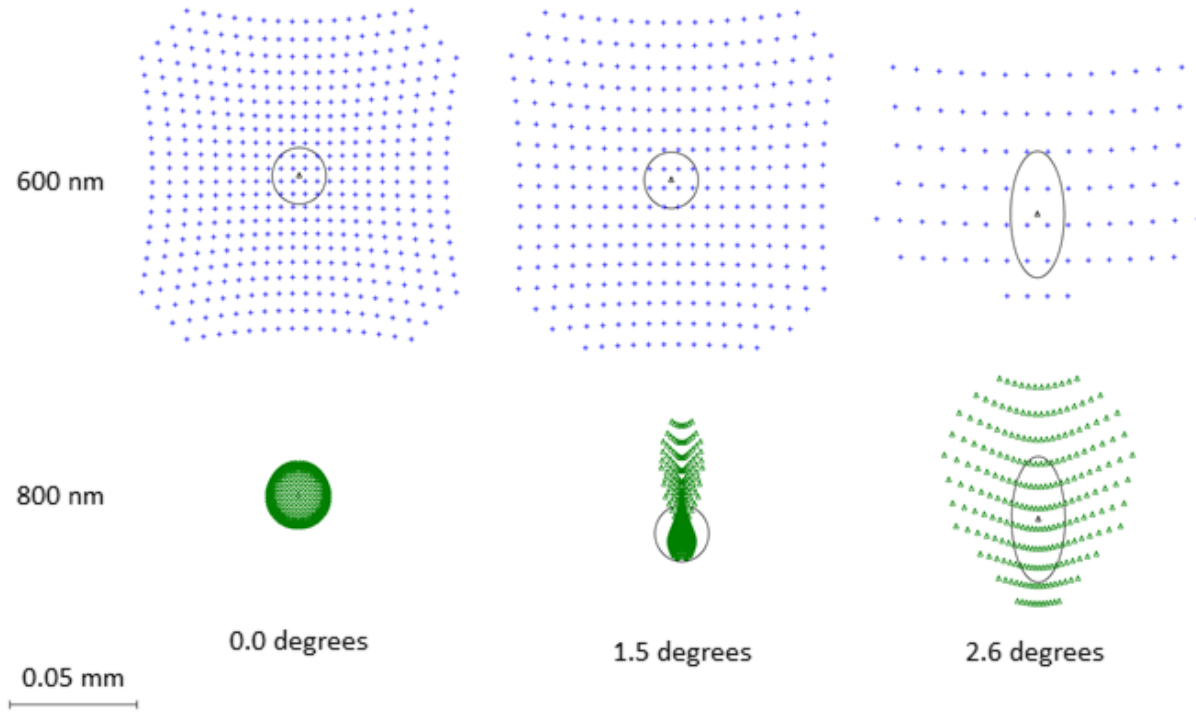


Figure 3-12: Code V simulation of the spot size for the telecentric system at focus at 800 nm. The spots are shown for 0.0, 1.5 and 2.6 degree fields of view at 600 nm (blue) and 800 nm (green). The full spot sizes for the 600 nm spots are 0.16, 0.22, and 0.25 mm for 0.0, 1.5, and 2.6 degrees fields respectively, with the corresponding 800 nm spot sizes being 0.024, 0.053, 0.094 mm. The black circles represent the Airy disk for each specific wavelength and FOV.

The telecentric system was breadboarded in the lab and used to image EIA 1956 standard resolution chart and the results of the test can be seen in Figure 3-13. The experimental set up is similar to the system in Figure 3-9 except for two fundamental differences. The Code V software can perform analysis for only one polarization and neglects the bend in the optical axis caused by the AOTF. However, these two issues can be dealt with sufficiently in the lab. The unwanted polarization is removed by adding a polarizer before and after the AOTF (Figure 3-5b and 3-5c). The light that is actively diffracted through the AOTF is the light that enters the AOTF crystal with extraordinary polarization. The polarizer before the device stops the ordinary polarization from entering the AOTF and the second polarizer, orientated 90° to the first, on the posterior of the AOTF is used to only let the diffracted extraordinary light through and removes the non-diffracted

extraordinary polarization light. As mentioned in section 3.1.4, the polarization of the diffraction beam is rotated by 90° (*Voloshinov*, 1996). The second issue to be handled is that the AOTF bends the optical path by 2.7°. Two prisms were added after the AOTF to straighten out the optical path; the optical path past the prisms is parallel to the original optical path and is offset by approximately a millimeter and obscures a part of the field of the view. The optical layout around the AOTF is similar to the optics around the AOTF in the characterization test shown in **Error! Reference source not found.**. The resolution chart was positioned so that the loss of the FOV due to the prism compensation was accounted for by a shift in the vertical location of the resolution chart.

The two images were taken, an “AOTF-off” and “AOTF-on” image, at every 25 nm at wavelengths between 600 and 1000 nm using a 30 second exposures imaged on the QSI CCD camera. The “AOTF-off” image was subtracted from the “AOTF-on” image to remove the dark current, DC offset, and stray light. Three sample images can be seen in Figure 3-13 with the optics in focused at 800 nm and the image blurring that was simulated in the spot size diagram can be easily noticed in the 650 nm wavelength image. The center lines of the resolution chart are unable to be resolved from each other compared to the 750 nm image. A unique line of sight can be resolved every 2 pixels in the center of the 750 nm image which corresponds to 150 m resolution at the tangent point from the balloon platform, and a 4-5 pixel resolution near the edge corresponding to about a 200 m resolution. Also due to the efficiencies of the CCD and the charts ability to reflect the longer wavelengths of light the SNR at the 850 nm image in the bottom right panel is rather low, and can be visibly seen by looking at the grainy quality of the image.

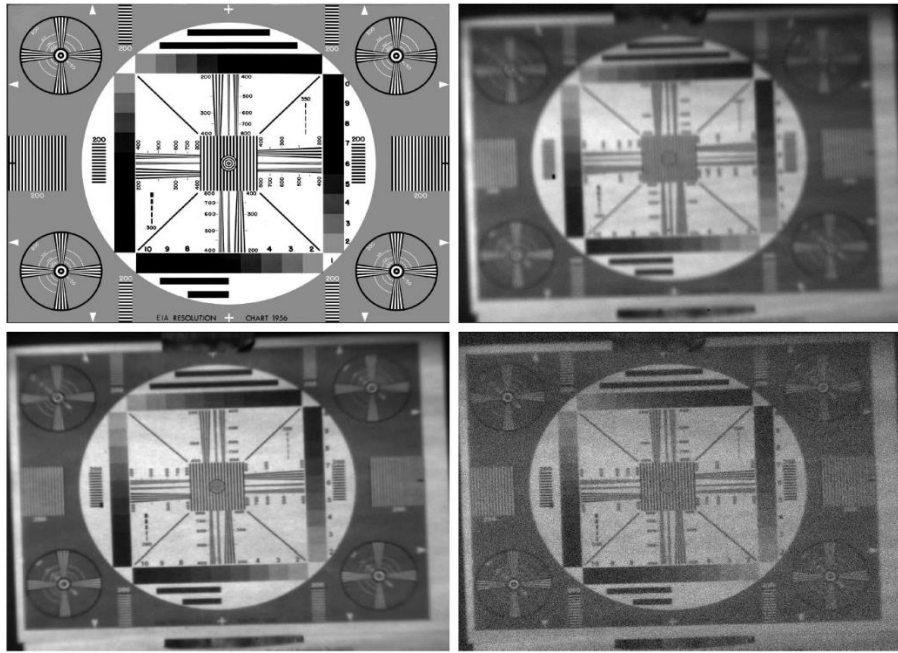


Figure 3-13: The top left is the original test image used for the experiment. The top right, bottom left, and bottom right are the images recorded through the telecentric system at 650, 750, and 850 nm. The system is focused at 800 nm.

3.3.2 Telescopic System Prototype

The second optical system in consideration is a telescopic optical system configuration consisting of a standard telescope for the FEO with a focusing lens. The front lens, known as the objective lens, is used to focus an object at infinity to the focal point of the lens, then a second lens, the eyepiece is used to increase the optical power of the system, that is to increase the angular size of the image with respect to the angular size of the object. The eyepiece lens is located at a combined distance of the focal lengths of both the objective and eyepiece and causes the image to be focused at infinity. However for our system the telescope is used to focus the light in order to enter the AOTF at an angle less than its acceptance angle as well as to reject light rays outside of the desired FOV. The light from each line of sight in the telescopic system enters the AOTF collimated and is focused though the BEO onto the QSI 616 CCD discussed in section 3.3.1. A

detailed simulation Code V layout and ray tracing of the optical design can be seen in Figure 3-14.

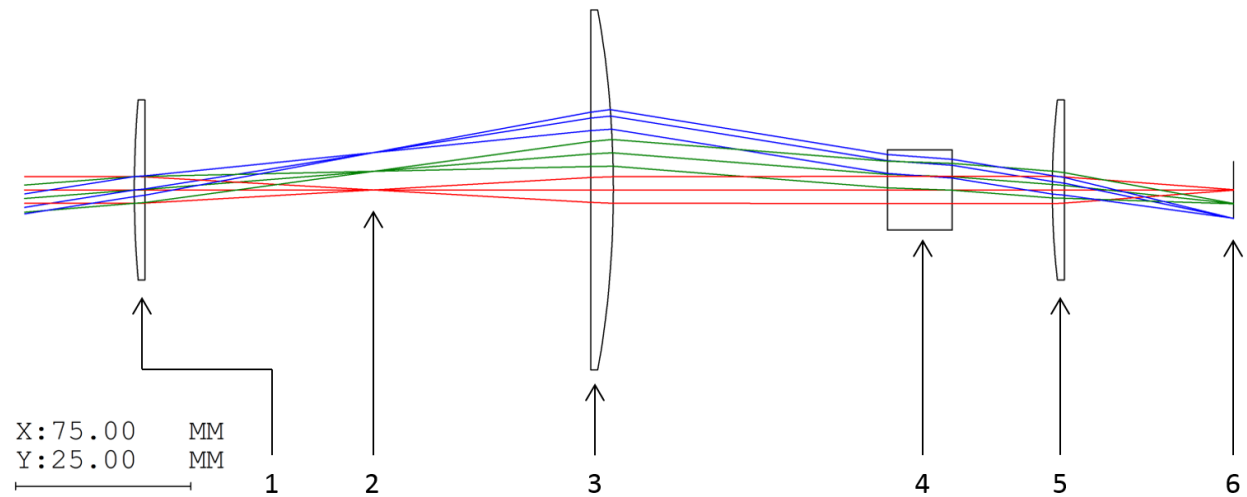


Figure 3-14: Ray Tracing diagram of the telescopic lens system simulated by Code V. The elements in the system are the following: (1) 100 mm focal length plano-convex lens. (2) Location where field stop will be located to limit stray light (3) 100 mm focal length plano-convex lens. (4) Brimrose AOTF characterized in section 3.2. (5) 75.6 mm focal length plano-convex lens. (6) Imaging plane. It should be noted that the x and y scales are not the same as Figure 3-9. Also, in the lab a polarizer is added in front and behind the AOTF as well as prisms behind the AOTF.

The telescopic prototype was designed with as many similar components and specifications as possible to the telecentric prototype in order to allow accurate comparisons of the systems without major optical effects and aberrations caused by using different materials, sizes, and focal length lenses. The optical specifications of this system are given in Table 3-2. However, there are a few fundamental differences. First, the aperture stop is located at the front lens which limits the rays of light that can enter the system, unlike the telecentric design that has a front aperture stop at the focal length of the first lens.

Table 3-2: Telescopic Prototype System Optical Parameters.

Parameter	Value
Effective focal length (mm)	75.6
Front End Optics Magnification	1.00

Back End Optics Magnification	0.756
Field Of View (°)	6.0 x 6.0
F-number	20

The second fundamental change to the optical system is that the AOTF now has collimated light passing through the device, unlike the telecentric system, and this has a few changes to improve and degrade the imaging quality of the system. First, the primary light passing through the AOTF from a single line of sight is entering the AOTF at the same angle, so the image will have a smaller spectral PSF than the telecentric counterpart; however, each line of sight will be diffracted with a different fundamental wavelength due to the angular dependence in the AOTF Bragg diffraction wavelength determination (Equation 3.32). The final image has a smaller spectral bandpass but there will be a wavelength gradient radiating out from the center of the image. Second, since the light now passes through the AOTF collimated, the focal point of the image no longer changes with wavelength. Instead, a lateral displacement of each line of sight occurs based on the angle of incidence and the diffracted wavelength which causes a slight magnification of the image. The lateral displacement that occurs is given by the following relation

$$\delta = n(\lambda) - 1 \frac{t\theta}{n(\lambda)} \quad (3.39)$$

where δ is the displacement from the original path; causing a slight magnification change based on the wavelength of the light being diffracted and θ is the incident angle on the crystal. However, this wavelength dependent change is less than a micrometer for the test configuration and is considered negligible. The effect can be seen in Figure 3-15. The last change to the system is the focusing power it possesses, as can be seen in the spot diagrams in Figure 3-16. The change in spot size due to wavelength is primarily due to the chromatic aberrations of the optical lenses. One option is to replace the lenses with mirrors in the flight version which will eliminate the chromatic aberration issue, the second is to use achromatic doublets to remove the chromatic aberrations.

Second, the system is diffraction limited for 600 nm for all lines of sight and for 800 nm at 3.0 degrees. Also the difference in location of the spot sizes is caused by the magnification effect discussed above.

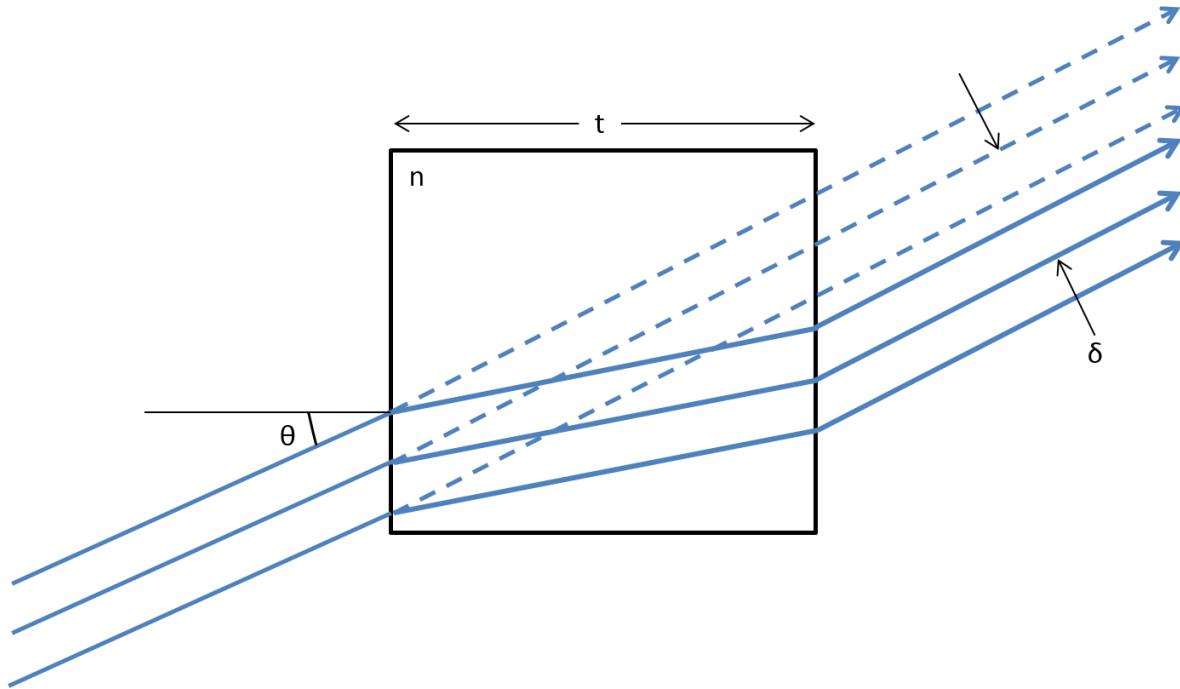


Figure 3-15: Vertical displacement of a collimated bundle of light cause by a material of index of refraction $n(\lambda)$.

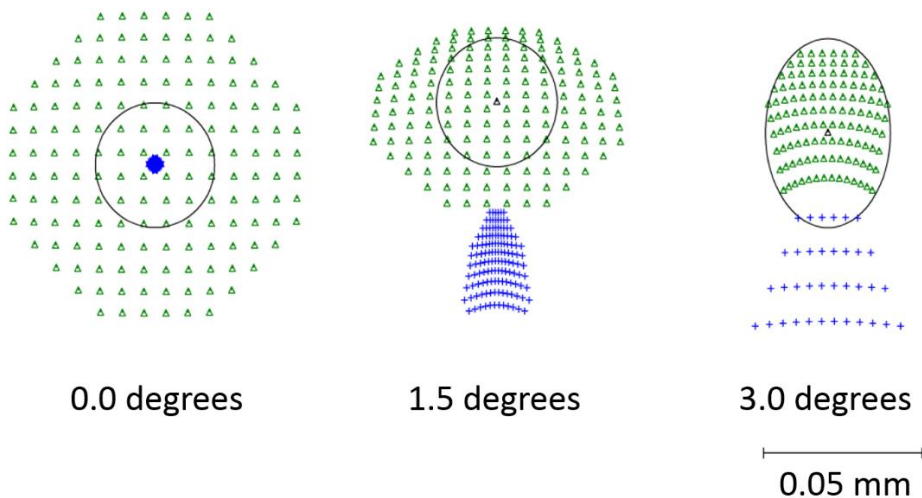


Figure 3-16: Code V simulation of the spot size for the telescopic system. The spots are shown for 0.0, 1.5 and 3.0° fields of view at 600 nm (blue) and 800 nm (green). The full spot sizes for the

600 nm spots are 0.004, 0.045, and 0.122 mm for 0.0, 1.5, and 3.0° fields respectively, with the corresponding 800 nm spot sizes being 0.096, 0.081, 0.047 mm. The black circles represent the Airy disk for 600 nm wavelength and each FOV.

An experimental resolution test was set up with the telescopic system with two polarizers and prisms added to the optical chain in the similar fashion to the section 3.3.1 experimental set up. The QSI CCD was also used with the same 30 second integration time. The results of this test can be seen in Figure 3-17. Once again the image at 750 nm is the sharpest of the three but the center lines of the EIA 1956 test chart are distinguishable at all of the wavelengths. The blurring of the 650 nm image is caused by the chromatic aberrations of the lens and the prisms. Furthermore the prisms will be removed in the final design reducing the aberrations. Also, the magnification issue discussed above is relatively insignificant in the test images and the small changes can be accounted for in the calibration of the final instrument. Lastly, the resolution target's poor ability to reflect NIR radiation of the light source causes the 850 nm image to also have a low SNR. This issue will not be a concern for the final system.

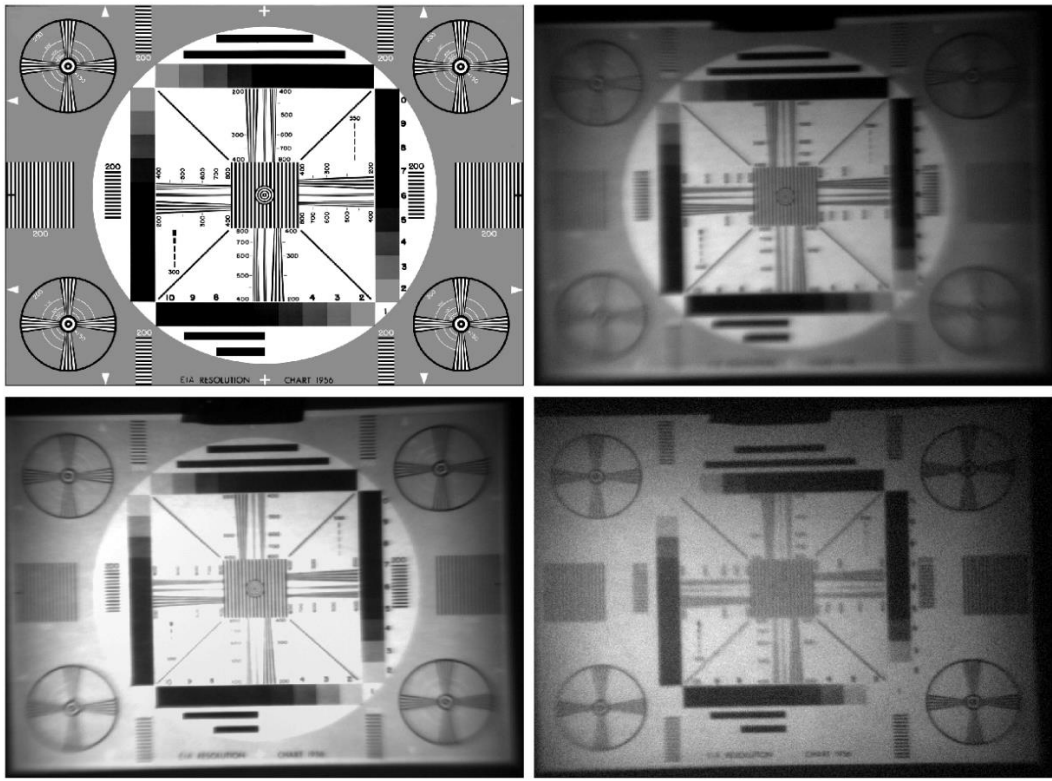


Figure 3-17: The top left is the original test image used for the experiment. The top right, bottom left, and bottom right are the images recorded through the telescopic system at 650, 750, and 850 nm. The system is focused at 800 nm.

3.3.3 ALI Optical Design

In light of the requirements for imaging aerosol, we have chosen a telescopic design for the ALI prototype. Since the wavelength gradient across the image is small compared to the slowly varying aerosol scattering cross section, the fixed image plane is preferable for the improvement it provides in spatial imaging, particularly as we desired to use as simple as possible an optical design.

We used a very simple three lens optical layout with commercial off-the-shelf components. Two lenses before the AOTF form a simple telescope for the Front End Optics (FEO), and a single focusing lens behind the AOTF comprises the Back End Optics (BEO). The AOTF is oriented such that the detected image is formed from the diffracted beam of the vertically polarized, i.e. extraordinary, light (defined at the entrance aperture). A linear polarizer with an extinction ratio

greater than 10^5 is placed at the back of the FEO to remove the incoming horizontal, or ordinary, polarized beam. The diffracted extraordinary beam undergoes a 90° rotation in polarization so a second linear polarizer, oriented at 90° to the first, is used after the AOTF but before the BEO to remove the undiffracted beam. This is shown schematically in Figure 3-5b. Note that even with the high extinction ratio of the polarizers, a not insignificant fraction of light that is intended to be blocked passes through the system. The diffracted extraordinary signal comprises at most a ~ 10 nm bandpass fraction of one polarization such that the unabsorbed broadband signal from the polarizers can be on the same order of intensity as the diffracted signal.

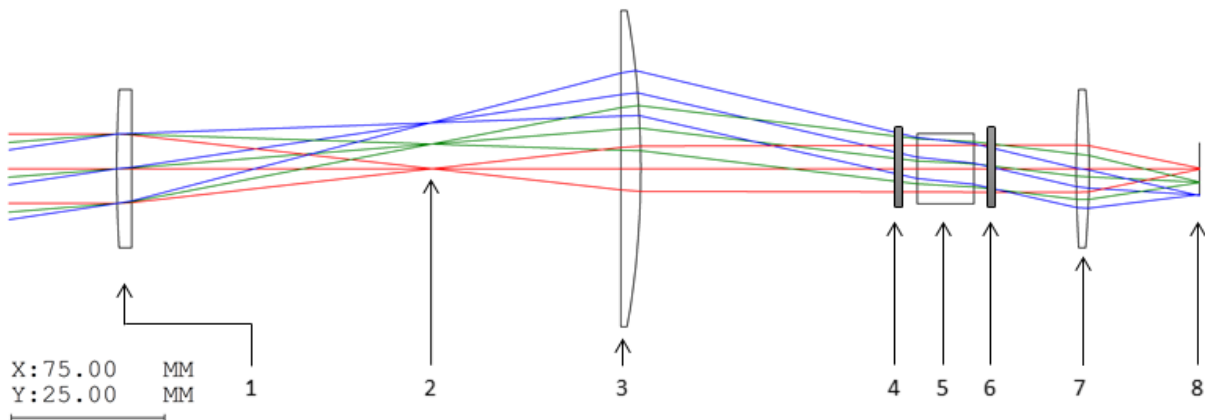


Figure 3-18: Final optical design for ALI with a Code V ray tracing diagram. The elements in the system are: (1) 150 mm focal length plano-convex lens. (2) Field stop. (3) 100 mm focal length plano-convex lens. (4) Vertical (extraordinary) linear polarizer. (5) Brimrose AOTF. (6) Horizontal (ordinary) linear polarizer. (7) 50.4 mm focal length bi-convex lens. (8) Imaging plane.

The extraordinary diffracted light is 2.7° from the optical axis and to compensate, the entire optical chain after the AOTF is mechanically aligned with this direction. The BEO forms the image of the signal on a QSI 616s 16 bit CCD with 1536 by 1024 pixels. A ray tracing diagram for ALI's optical system was created using the Code V optical design software and can be seen in Figure 3-18. No corrections were attempted to reduce chromatic or spherical aberrations within the system and the system exhibits coma due to a large field of view and the curvature of the lenses near the edge of the field of view. Analysis with Code V shows that the distortion due to these effects across

the center two degrees of the field of view is a change of less than 1% across the entire wavelength range. The final one degree shows a distortion of less than 4%.

An analysis was also performed to determine the minimum resolution required to achieve a Modular Transfer Function (MTF) of 0.3 across the entire field of view for all wavelengths (*Smith, 2000*). The MTF is an optical measure of the system's ability to resolve line pairs per millimeter where a line pair is a white line followed by a black line. Generally for increasing line pairs per millimeter the resolvability of an optical system will decrease. The MTF can be found computationally through

$$MTF(f) = \frac{I(f)_{max} - I(f)_{min}}{I(f)_{max} + I(f)_{min}}, \quad (3.40)$$

where the MTF is dependent on the frequency, f , of the line pairs, $I(f)_{max}$ is the maximum intensity of the measured pair, and $I(f)_{min}$ is the minimum. The MTF can vary differently with respect to tangential and radial directions of the optic system. To obtain a minimum MTF of 0.3 across the entire field, except for the 3° tangential or perpendicular FOV, a seven pixel running average is required, corresponding to a MTF frequency of 15.5 line pairs per millimeter. The 3° tangential field being below the detection threshold of 0.3 is not a large concern since the SNR is low at the edges of the FOV and primality results in a loss of cross-track resolution at the ground and float altitude tangent points which are not critical for analysis. Furthermore, when the FOV is 2.7° from the normal the tangential component is above the 0.3 MTF threshold. The MTF analysis of ALI can be seen in Figure 3-19. Overall, this corresponds to an average vertical and horizontal resolution of 210 m across the entire ALI field of view at the tangent point.

A tolerance study was also performed with Code V to assess the capability of the system within the tolerances of the mounting equipment. Through a Monte Carlo method, Code V perturbs the placement and shape of the optical components within the system and computes the change in the

MTF on the image plane. This analysis determines what optical misalignments or defects will degrade the performance of the system. Performing the analysis on ALI, it was determined that ALI was relatively insensitive to the tolerances of commercial off-the-shelf component used.

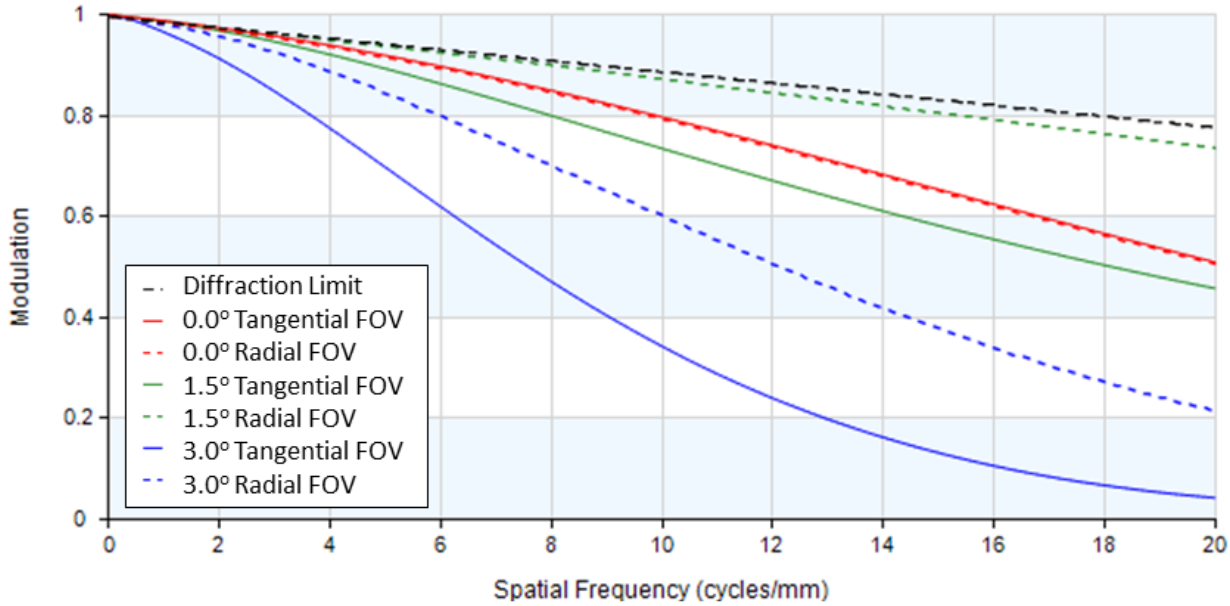


Figure 3-19: MTF analysis performed by Code V for the final ALI design used in campaign. The 7 pixel running average corresponds to a spatial frequency of 15.5 cycles/mm.

Table 3-3: Final ALI optical specifications

Parameter	Value
Effective focal length (mm)	74.3
Front end magnification	0.67
Back end magnification	1.27
Entrance Pupil (mm)	9.91
Field of view (°)	6.0 x 5.0
F-number	7.5
Image size (mm)	9 x 7.5
Image size (pixels)	1000 x 800
Resolved image size (averaged pixels)	143 x 114
Spectral range (nm)	650-950

An experiment to determine the exposure times and entrance pupil of ALI will be discussed in the calibrations section specifically in section 3.6.1 but the results of the experiment were that the ALI entrance pupil was selected at 9.91 mm to yield estimate flight exposure on the order of a second. Furthermore, a demagnification in the FEO and a magnification in the BEO was added to further increase the light throughput to help reduce the exposure times. A summary of the optical specification for the ALI prototype is given in Table 3-3.

It should be noted that our choice of a telescopic optical layout for ALI is actually the opposite choice of that made for the ALTIUS design, which uses a telecentric optical layout. For that instrument, the need for spectral resolution for trace gas retrieval makes the decision to use telecentric optics quite clear (*Dekemper et al.*, 2012). Given that basic design difference, the overall optical specifications are quite similar between the ALI and ALITUS prototype instruments (again see Table 3-3 for ALI specifications), although two key differences are noted. First, by using a telescopic layout the maximum field of view for ALI is determined by choosing lenses to ensure light enters ALI within the acceptance angle of the AOTF. This allows for a larger possible field of view than with a telecentric system where the field view is defined by the aperture of the AOTF. Second, the f-number for ALTIUS is 14.32 compared to 7.5 for ALI, which allows ALI to increase light throughput at the cost of slightly higher aberrations in the final image. *Dekemper et al.* (2012) reports that the visible channel of ALTIUS was breadboarded and tested by taking ground based measurements of a smoke stack plume. They used the measurements to retrieve NO₂ slant column density using 10 second exposure times; although, they note that an increase in measurement frequency would improve the instrument capabilities. This also factored into our decision to use telescopic optics to increase throughput for ALI. A final selection for the optical design of ALI was presented in this section as well the justifications used to determine the result.

For the final design of ALI, the telescopic system deemed to be the better option for our scientific purpose to determine aerosol extinction and engineering study to verify the capabilities of using an AOTF in space based remote sensing techniques.

3.3.4 Correction to the Optical Design

It should be noted a correction to the optical design is required that was discovered after the campaign of the instrument during the analysis. For the 3° FOV the light enters the AOTF at an angle of 2.2° from the normal and the acceptance angle of the AOTF is 2.0° . This results in a great loss of diffraction efficiency for the last approximately half degree of the field of view. This error was created when decreasing the f-number of the system to 7.5 to reduce the exposure times, remembering that lower f-numbers have higher light throughput, by adding a FEO magnification. However, this increase in throughput is overcompensated by the loss in diffraction efficiency of the AOTF overall resulting in a lower SNR. To rectify this problem a slight change to the optical system is suggested in this section while still using commercial off-the-shelf components.

The main issue results about the front end magnification and the suggestion resolves around keeping a similar optical layout with a smaller demagnification in the FEO, and a compensating demagnification with the BEO to maintain the same final image size. This is performed by replacing the first lens or objective lens of the telescope (element 1 in Figure 3-18) to a 125 mm focal length plano-convex lens and compensating the optics such that the distance between the first two lenses is the sum of the two focal lengths of the telescope. The back end lens is also replaced with a 62.9 mm bi-convex lens. This results in the 3° FOV entering the AOTF at 1.6° well within the acceptance angle of the AOTF. A table of the revised specifications can be found in Table 3-4.

This change results in several secondary changes to the system. First, the f-number is increased up to 8.0 which will reduce the throughput of the system over but the last half of a degree of the

field of view will become brighter helping to reduce the vignetting and SNR drop off near the edge of the measured images. Second, the size of the image on the CCD has reduced in size which should decrease the resolution of the instrument but the decrease is partially offset by the larger f-number reducing the system aberration resulting in a final average vertical horizontal resolution of 260 m.

Table 3-4: Revised ALI optical specifications

Parameter	Value
Effective focal length (mm)	78.9
Front end magnification	0.80
Back end magnification	0.98
Entrance Pupil (mm)	9.91
Field of view ($^{\circ}$)	6.0 x 5.0
F-number	8.0
Image size (mm)	8.5 x 7.1
Image size (pixels)	945 x 789
Resolved image size (averaged pixels)	135 x 114
Spectral range (nm)	650-950

3.4 Opto-Mechanical Design and Thermal Balancing

Upon the finalization of the optical design of the system, an opto-mechanical system was required for use of a stratospheric balloon. This section will give an overview of the hardware used to transform ALI from a laboratory breadboard to a flight model. The opto-mechanical design will discuss the optics component framing within the system, stray light reduction, as well as the addition of a light tight case. Following will be a brief overview of the thermal concerns of the system and how the system was designed to minimize the thermal risks.

3.4.1 Opto-Mechanical Design

After the optical system had been finalized, an opto-mechanic design to secure the optical components was required. The opto-mechanical system needed to be able to withstand the stresses

applied to the system during the launch of the stratospheric balloon and to withstand the large thermal changes that could be experienced during the flight to keep the optics in the system aligned and in focus. Furthermore, the system must also meet safety factors for torque and shock forces on the instrument so that it does not become detached from the gondola during the flight. This is to verify the safety of CNES workers who launch the balloon as well as citizens below the gondola during flight.

Consideration for thermal expansion and contraction of the opto-mechanical components also had to be considered when picking materials to house the optical lenses housing system in order to reduce the chance of any torques arising in the optical chain from thermal expansions. To reduce this effect, a consistent material was picked for the complete optical housing so all materials would have the same thermal response to the environment with which it is exposed. The chosen material was aluminum since it is commonly used in stratospheric balloon instruments and platforms because of its light weight and relatively inexpensive cost.

With a chosen material the next design parameter was what method to use to house the optics. Commonly, space based instrumentation uses a solid piece of material and is machined into the shape required to be able to house all the optical components. However, this method is relatively expensive and is generally used for finalized space instrumentation and not for design concept prototypes. These types of cases also have a long lead-times for the production and manufacturing components which would have been pressing our timeline for the launch date. The other option was to design an optical rail system primarily from off-the-shelf components from optical manufacturers, which would allow the flexibility to be able to make slight modifications to the design without having to commission a new one-piece case allowing for inexpensive alterations to the ALI optical chain without complete reconstruction. The drawback with only using off-the-shelf

components is it may be harder to maintain the alignment and resolution of the system. Considering the prototype nature of the project, the choice was made to go with off-the-shelf opto-mechanical and structural pieces for ALI with the possible limitation in alignment and resolution being classified as an acceptable trade-off.

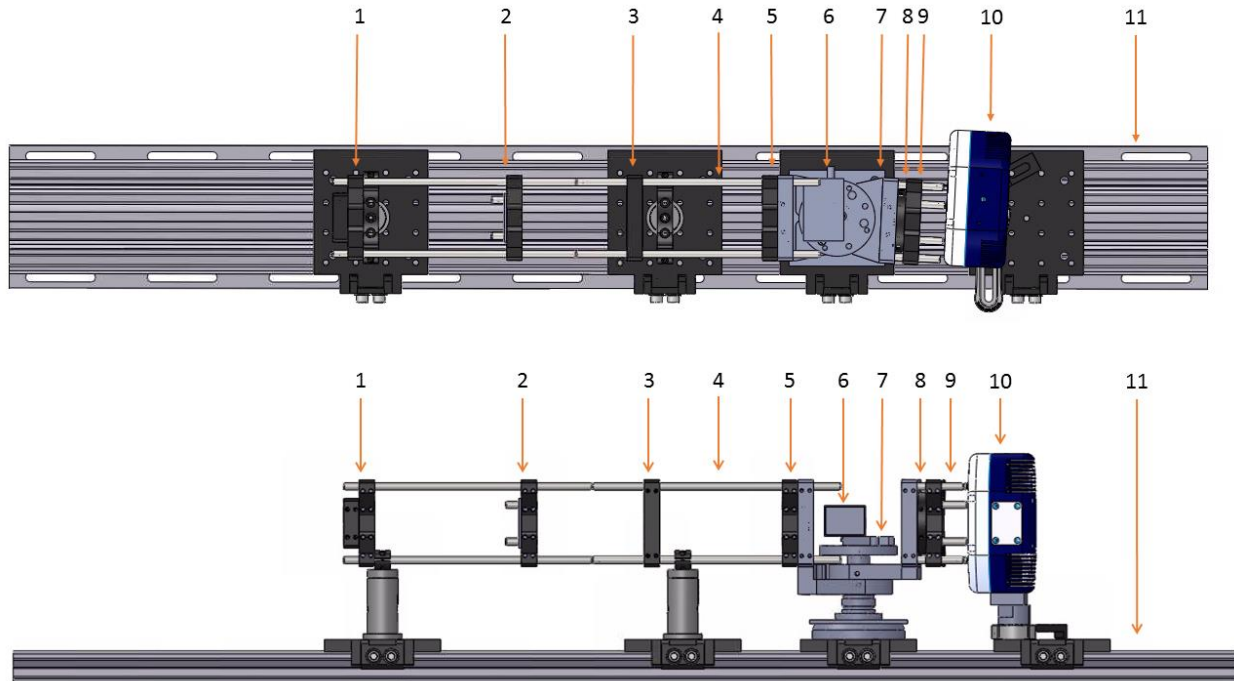


Figure 3-20: The final optical layout of ALI's optical chain from the top and profile perspectives with the components being the following: (1) 150 mm plano-convex lens with 25.4 mm diameter. (2) Field Stop. (3) 100 mm plano-convex lens with 50.8 mm diameter. (4) Optical rail system. (5) Vertical (extraordinary) linear polarizer. (6) Brimrose AOTF. (7) Rotation Stage. (8) Horizontal (ordinary) linear polarizer. (9) 50 mm bi-convex lens with 25.4 mm diameter. (10) QSI 616s CCD camera. (11) Optical rail.

Using components from ThorLabs, Edmund Optics, Newport, and McMaster-Carr, an opto-mechanical case was designed for ALI and can be seen in Figure 3-20. A single sturdy wide optical rail, element 11, was used as the system base since it has the whole optical chain plus a baffle (see section 3.4.2) mounted to it and would have a low suitability to torsion. This rail would serve as a base for all the optical mounting. The opto-mechanical chain was connected to the rail using rigid optical aluminum rods. For the optical chain, an optical cage system was used since the four rods

surrounding the optic mounts provided a rigid framework that would still allow for fine tuning of the optical elements. The optical cage is element 4 in Figure 3-20. Once the aligning of the optical system was completed, the components were glued into place to prevent slippage during transportation and flight.

During the testing of the breadboarded optical system in the lab, two prisms were used to account for the deviation in the optical chain caused the AOTF. These prisms were removed in the final design by bending the BEO of the optical chain by 2.7° through a rotation stage (element 7). The removal of the prisms further reduced distortions within the system.

It should be mentioned that optical lenses for ALI were repurchased for the final system with the addition of antireflection coatings. An antireflection coating would increase the systems efficiency. From ThorLabs, a B-type antireflection coating was ordered for the lenses which reduces reflection from each lens surface down to an average of less than 0.50% from 650 to 1050 nm instead of an approximately 8% loss per surface from an uncoated lenses. The lenses also had a 1% tolerance in the focal length and made from grade A NBK7 glass.

A selection of linear polarizers were considered for elements 5 and 8 in the opto-mechanical system. However, the wavelength range of ALI made standard polarizers difficult to find which limited the possible choices. A nanoparticle linear film polarizer from ThorLabs was eventually decided upon (model number LPVIS100) for ALI since it gave an extinction ratio better than 10^5 for 650 to 1200 nm completely covering ALI operating range. The extinction ratio is defined by the ratio between the maximum transmission when the polarizers axis is aligned with the signal to the minimum transmission after the polarizer has been rotated by 90° .

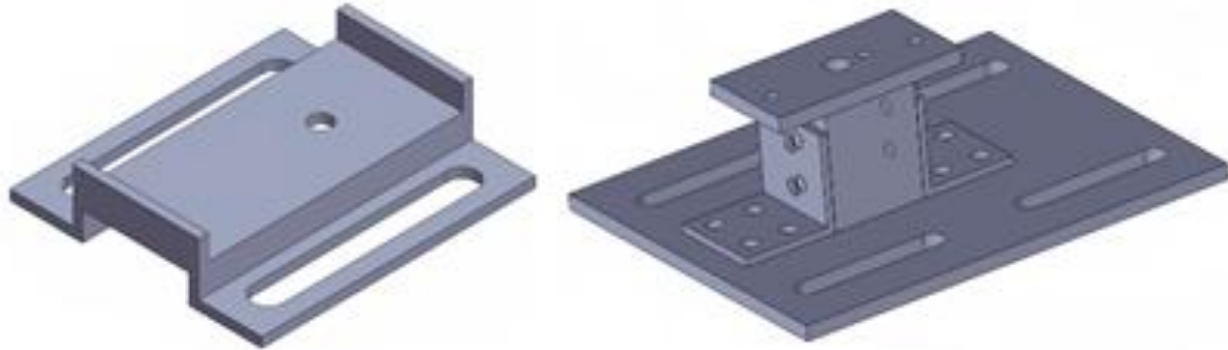


Figure 3-21: The custom mounting hardware design to mount the AOTF and QSI CCD camera into ALI's opto-mechanical design. Left: Custom AOTF mounting hardware. Right: The five piece QSI CCD camera mounting hardware.

For the opto-mechanical design special consideration had to be given to mounting the AOTF and CCD camera. Both of these elements are non-standard sizes in optics and no preexisting components could be purchased to mount these pieces. Therefore custom mounting pieces had to be used to rigidly mount these components. Both components were designed through the use of the SolidWorks design software.

The AOTF had one usable mounting hold on the bottom of the device to affix the device to the optical chain. However, directly mounting the device onto the rotation stage would result in the AOTF being offset downward from the optical path. Furthermore, with only one mounting point there was concern for rotation of the device rotating during the flight which would not be able to be mitigated. A single piece was designed that lightly clamped the AOTF onto the top of the mounting hardware to lock the AOTF's rotation axis. To mount the custom AOTF mount to the optical system four tapped screw holes were utilized on the top of the rotation stage. On the base of the AOTF mount two slot screw holes were used to be able to correctly align the AOTF within the optical chain when affixing it to the rotation stage which can be seen in the left side of Figure 3-21.

The mount for the CCD camera had a different set of requirements; mounting holes were available for use on the bottom of the camera but the camera mount needed to be able to securely hold the relatively heavy camera into place with very little available vertical space (~6 cm) between the base of the rail mount and the camera. A five piece mount was designed that would fit in the tight space and be sturdy to support the mass of the camera seen in the right side of Figure 3-21. The base plate perfectly fits onto the optical rail mount and the slotted holes allow for horizontal alignment of the camera with the optical axis. The vertical alignment to the optical axis is correctly set with the height of the camera mount. Also, the CCD sensor on the QSI camera is offset to one side and the mounting hardware accounts for this displacement.

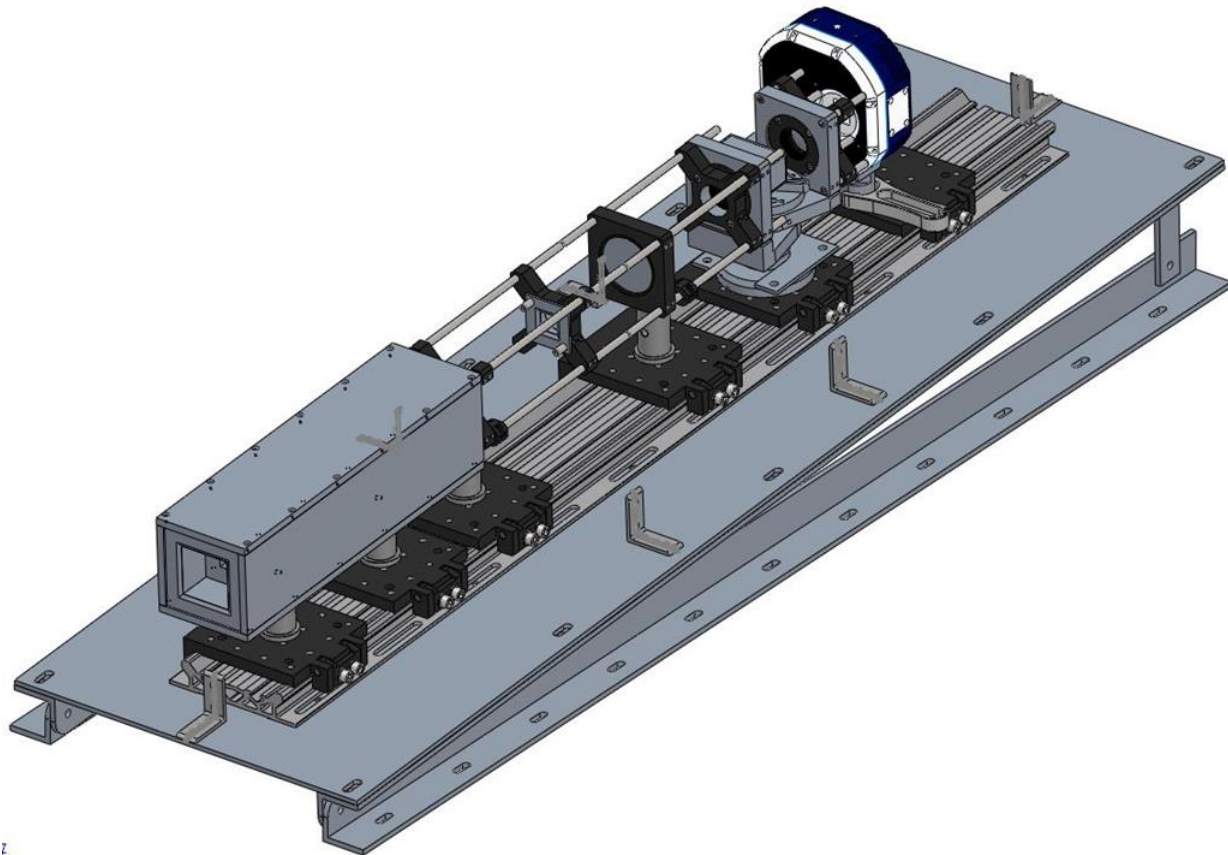


Figure 3-22: ALI opto-mechanical system with three degree horizontal tilt and designed baffle discussed in section 3.4.2.

The ALI system is tilted three degrees from the horizontal so that the FOV of the instrument from the balloon flight geometry would measure from the ground to the balloon float altitude. A SolidWorks rendition of ALI with the three degree tilt from the horizontal can be seen in Figure 3-22.

Finally, mounting hardware was tested through simulations done by the CSA to verify that the safety factor of the system was met, which it passed. The test was a stress analysis of the mounting points of the ALI system to the gondola and itself.

3.4.2 Baffle Design

A major concern with any optical instrument is the presence of unwanted or stray light. Two types of stray light are commonly defined: internal and out-of-field stray light. Internal stray light is unwanted light that passes through the system through scattering, reflections, or imperfections in optical elements. Out-of-field stray light is light that enters the optical path but originates from outside of the field of view. A long standing concern in the design of limb scatter instruments is the effective rejection of out-of-field stray light. This is due to the bright surface very near to the targeted limb in combination with the exponentially dropping limb signal with tangent altitude. For ALI test observations from the stratospheric balloon, a front end baffle was incorporated.

When designing a baffle several design aspects need to be considered. Consideration must be given to the length and width of the baffle as a larger, well-designed baffle will be able to better remove out-of-field light but will increase the size, mass, and cost of the instrument. Furthermore, the number of vanes in the baffle design must be considered. More vanes help to remove additional out-of-field light but each vane adds an edge that light can scatter off which may introduce more stray light into the system. A balance must be met with the size and number of vanes in the ALI baffle to best remove out-of-field stray light.

The first point of the discussion is the height and width of the baffle. In a baffle system, the larger the baffle is by cross-sectional area the better the baffle can be designed to reduce stray light. However, there is a limited amount of space to build the ALI instrument and the baffle must share space with optics, electronics and power systems; and as such, a size that fit these constraints had to be selected. An internal height and width of 70.00 mm was chosen since this was the size of the optical rails used to house the optical chain and the instrument could not be any taller than the height of the optical rail to meet size constraints.

The length is also limited by the space available, as well as the field of view and entrance aperture size. The baffle must be short enough so that the size of the field of view does not become larger than the cross-section of the baffle. To maximize the effectiveness of the baffle the longest possible length that could be accommodated was selected and was 300 mm in length.

Also, one always needs to make sure the optical stop located within the baffle is placed at the same location as the optical design. If the location of the optical stop is changed from the baffle design, it will affect the performance of the instrument itself. If the optical stop is moved further from the optical design specifications, the field of view remains the same but limits the amount of light that enters the system. Thus changing the overall f-number of the system either increases the exposure times or decreases the SNR. The other case is if the optical stop is moved closer to the optical system. The opposite problem occurs which is more light enters the system than the system was designed for causing an excess of stray light and rendering the baffle ineffective.

The baffle system is designed such that it minimizes the percentage of out-of-field stray light that enters the system without encountering at least three baffle surfaces. This method, the optimal baffle geometry, is standardly used in optics to minimize stray light (*Fischer, 2008*). In the system,

the baffles are spaced in such a way that little stray light can enter the system without coming into contact with at least three surfaces reducing the overall intensity of the light stray.

The optimal baffle geometry design method will be described. In Figure 3-23a the base baffle case is formed with the critical baffle vane at the entrance to the optical system (-250 mm) and a second vane is located closest to the optical chain. It should be noted that a reduction in the length of the baffle to 250 mm occurred so that an exterior baffle could be added to reduce surface reflections. The marginal rays of the optical system is represented by the red line.

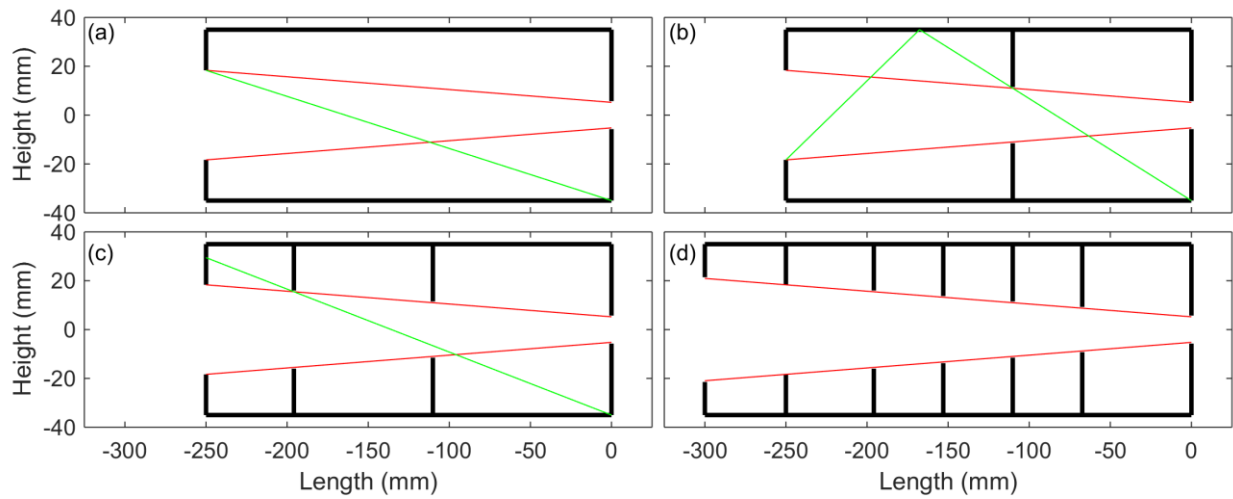


Figure 3-23: (a) Start of the optical baffle geometry method. The red lines are the marginal rays and the green line is the first ray that can enter the system without encountering at least three surfaces. (b) The first internal vane has been added and the location of the next vane is being determined. (c) The second internal baffle has been added and since the green line intersects with the critical baffle no more baffle are required. (d) Additional interior vanes and an external vane have been added to ensure a height to pitch ratio of 0.5 to improve the baffle's capabilities to reduce stray light.

Next, an indicator line is drawn from the bottom right corner of the baffle to the opposite tip of the critical baffle, represented by the green line. This line represents the first ray that can enter the system without coming into contact with at least three surfaces. The next vane is added where the indicator line and marginal ray intersect as can be seen in Figure 3-23b.

The next indicator line goes from the bottom corner to just passing the first vane and encounters the outer side of the baffle wall. The line goes through a reflection and passes just by the critical baffle once again. The intersection of the second segment of the indicator line and marginal ray is where the second vane is added as in Figure 3-23c.

The process is then repeated to determine the location of any additional vanes. For the ALI baffle, the indicator line no longer is able to reflect upon the top baffle surface and therefore the minimum level of baffles have been achieved. However, two extra internal baffles and one external baffle were added to the design (Figure 3-23d). The exterior baffle was added to help further reduce stray light from surface reflection by shielding the critical baffle from the direct ground reflections. The additional interior baffles were added to achieve a height to pitch ratio greater than 0.5. If the height to pitch ratio is less than 0.5, additional stray light enters the optical system due to the high amount of empty space within the baffle (*Fischner, 2008*).

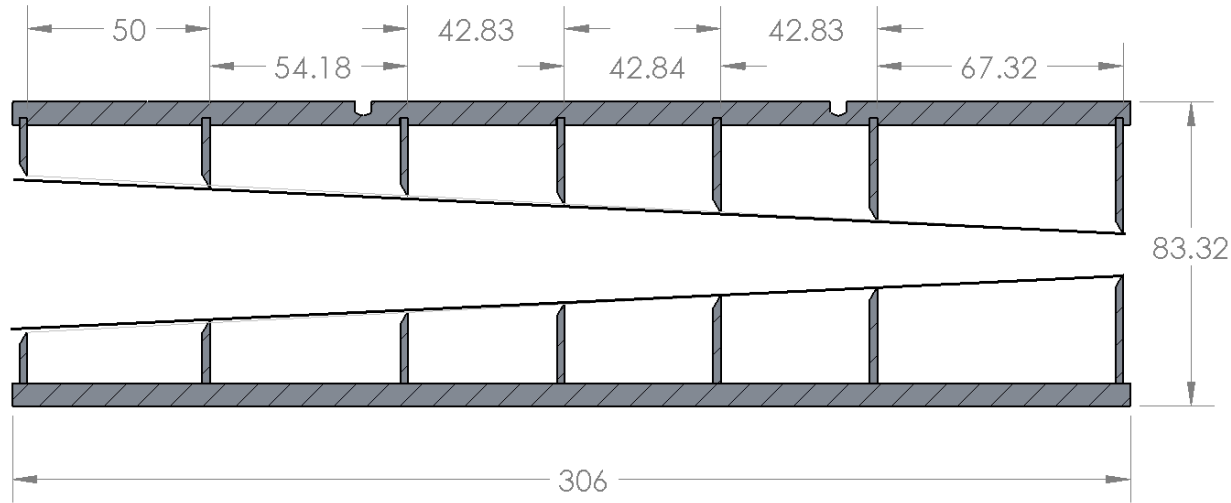


Figure 3-24: A cross-section view of the ALI baffle system. All dimensions on the drawing are in millimeters and the sloped black lines show the 6 degree field of view.

With the completed design, a drawing needed to be created to machine the baffle accounting for machining tolerances. With the exception of the critical baffle all of the edges of the vanes

were reduced in size by 0.5 mm so that they could be produced within possible machining tolerances and not limit the FOV by being too tall. A SolidWorks version of the baffle can be seen in Figure 3-24 which accounts for the thickness of the materials and machining tolerances.

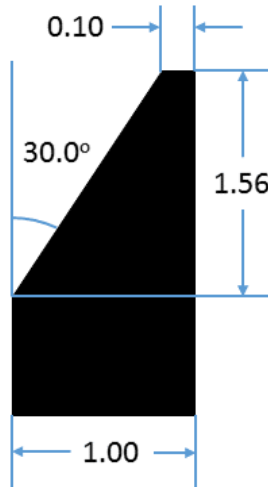


Figure 3-25: ALI baffle vain profile. Dimensions are in millimeters.

Ideally, the edges of the vanes would be machined to a fine blade. However, this is not practical for two reasons. First, the baffle's edges would be prone to damage causing dents or grooves in the vane cross-section possibly producing unwanted scattering effects. Second, it is only possible to machine the tips so fine with tolerances without reducing the height of the vane. Figure 3-25 shows the profile for the baffle vanes as they were machined. A final assembly of the optical system can be seen in Figure 3-26.

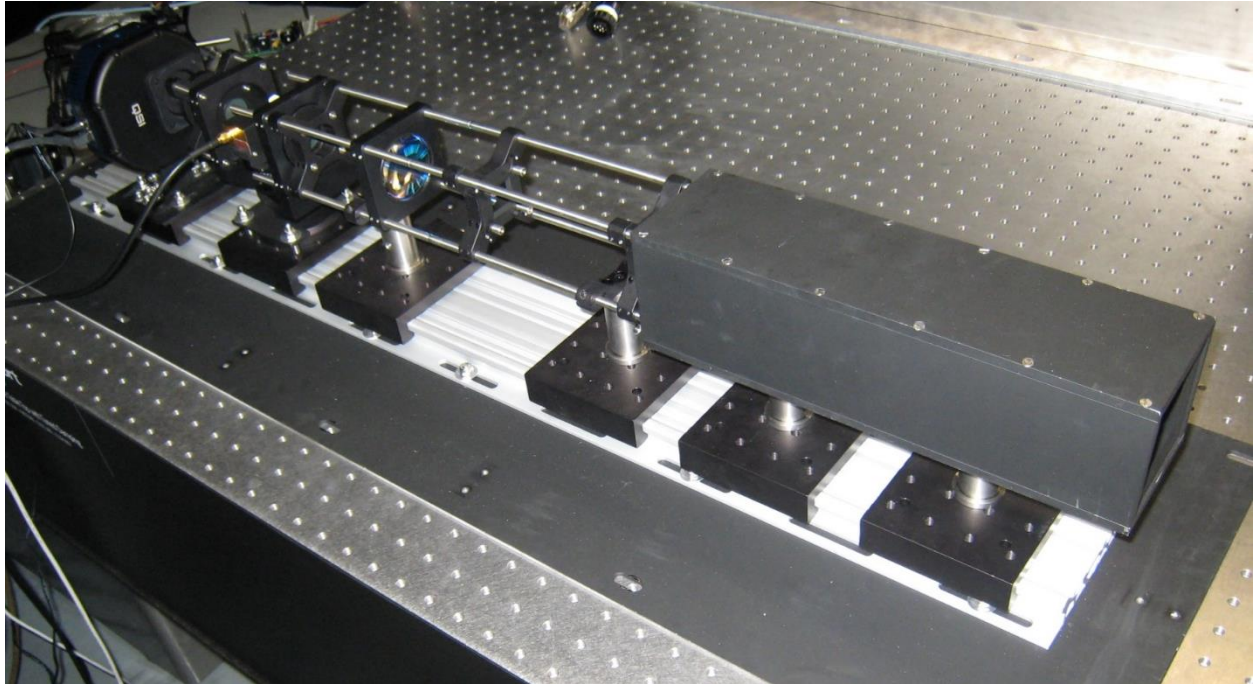


Figure 3-26: Final ALI optical and opto-mechanical assembly.

3.4.3 Light Tight Case

To complete the opto-mechanical design, a light tight case was required. The case was made out of aluminum and every connection point in the case was overlapped, through interlocking pieces, to verify the rejection of the light. The light tight case was clamped onto the base plate of ALI and a final rendition of ALI can be seen in Figure 3-27.

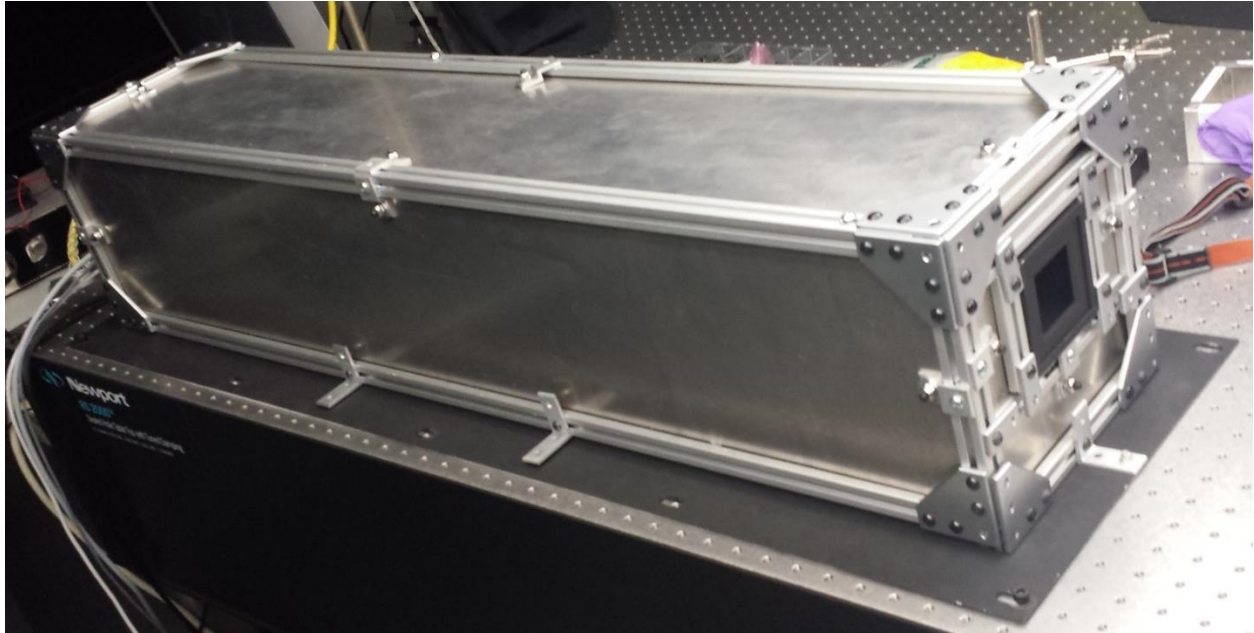


Figure 3-27: ALI optical system with light tight case attached. Three degree horizontal tilt not present in this image.

3.4.4 Thermal Considerations

An instrument, like ALI, has to survive the possibility of extreme temperatures during a flight on a stratospheric balloon. The extreme temperatures arise through various processes, first the instrument must survive the ascent through the tropopause where temperatures can reach -70°C and must survive the float temperatures which can be as cold as -50°C. Conversely, being exposed to direct sunlight causes heating that would result in instrument failure due to overheating. Furthermore, ALI using simple opto-mechanical design means there is no active thermal control and, with the reduced atmospheric density at approximately a float altitude of approximately 35 km convective cooling could not be relied on for thermal control. Following will be a discussion of various thermal concerns within ALI.

The electronics are stored within two aluminum cases, a computer case and power supply case. All components within the two cases are all rated for an extended thermal range (-40 to 85°C) except the RF driver which has an operational thermal range of 0 to 50°C. The extended range of

the all other electronic components reduces the concern since this case will not be exposed directly to the elements as they are sheltered via insulation and, from consultation with the CSA and CNES teams, the internal temperature of the electronics area from previous missions have reached a coldest temperature of approximately -20°C during normal flight operations.

However, the RF driver does not fall into the specified temperature range, which is a problem, and the driver also produces a large amount of heat that is convectively cooled on the surface which is not possible at float due to the reduced atmospheric pressure. Since the RF driver is a fundamental piece of hardware, failure in the component would result in a primary system failure.

To mitigate the risk, several considerations are made with regards to the RF driver. First, a RF driver with a cooling plate is purchased to better allow for conductive thermal control and without any method of cooling the driver on the gondola the driver would overheat and fail. So the driver is mounted to the aluminum case such that the cooling plate would be in direct contact with the surface of the case, and the case would be mounted on the gondola such that the surface of the case would be against the aluminum mounting surface on the gondola. This allows a large amount of heat to be dumped to the gondola to keep the RF driver within the operating range. Second, the driver freezing was not as large of a concern since the driver produced enough heat to sustain its temperature. However, the driver would be both on and off during the mission for different imaging modes which may result in freezing or overheating. A temperature sensor is used to monitor the driver and the control software on board ALI has a safety measure built in that would automatically turn the driver off if it reached 50°C or turn on if the temperature dipped below 0°C.

Another region of concern was the housing of the optical system which would be directly exposed to the elements. The optics would expand and contract based on the temperature and CCD camera had an operating temperature of -40 to 20°C. Furthermore, the CCD primarily used

convection to cool the camera; by recommendation from QSI, fans were disabled as they would rip apart due to the low atmospheric pressure since the rotation speed is based on air resistance. To mitigate the thermal risk, a twofold approach was taken. First, the optical housing was surrounded in foam to thermally insulate it from the cold experienced during darkness and ascent through the tropopause. Second, the foam insulation was covered in a reflective material to reduce direct warming from the radiation from the sun.

3.5 Control Software

During the stratospheric balloon flight, software will be needed in order to control the instrument from the ground and have it operate in the air. To accomplish the communication and control systems needed, two separate software packages were developed. First, a ground control platform that communicated to ALI and to receive diagnostic information, completed images, and to send commands to be processed. The second software package was the onboard system to control the instruments systems.

The ground control software contains the single module that is responsible for establishing communication with ALI, handling any loss of information during data transfer, decoding the data from the ALI flight software, as well as uploading commands to the instrument. The software onboard ALI is more complicated with different modules to handle the different aspects of the hardware and control systems. The onboard ALI computer system is a Debian Linux operating system with multi-threaded C++ based software that controls the hardware and science data collection operation. The onboard computer is a VersaLogic PC-104 OCELOT computer with fanless operation and a thermal operating range of -40 to 85°C. The flight software contains five different modules to handle different functions of the system. The five modules are the main module, communication module, diagnostics module, science module, and local storage represented in Figure 3-28 by blue, green, orange, purple, and yellow respectively.

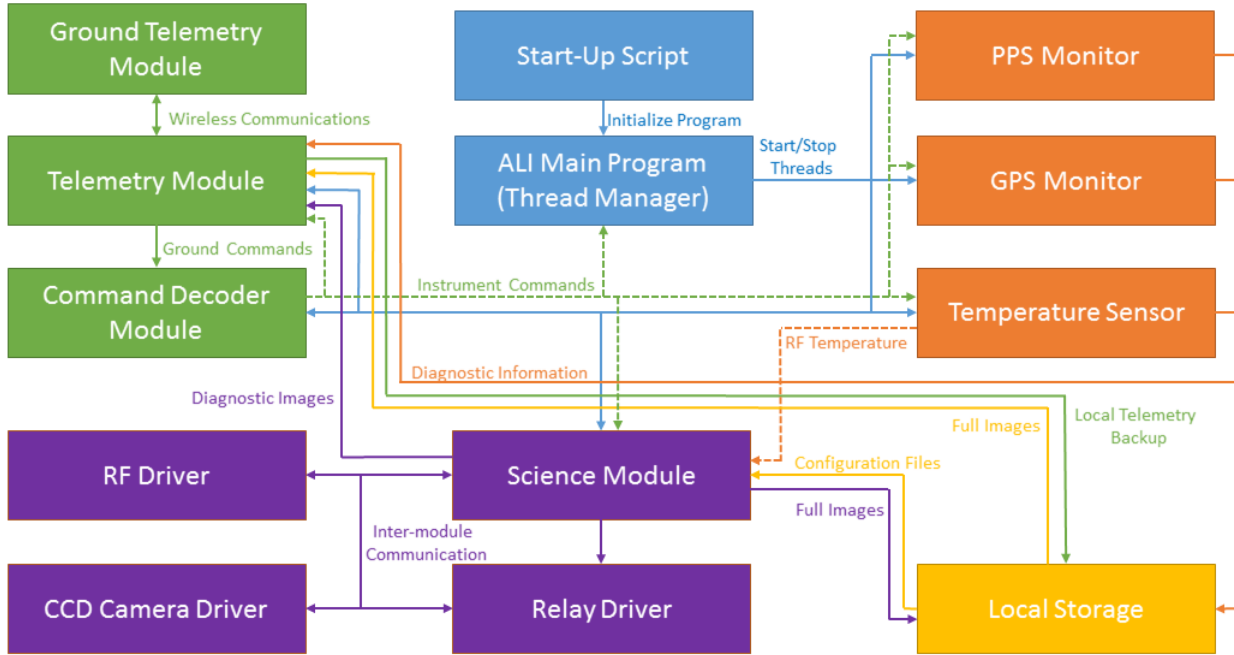


Figure 3-28: A complete flow diagram showing interaction between all the of ALI software modules on the on board ALI flight computer.

The main module consists of a bash script which initiates the ALI C++ flight program during startup and can be restarted from the ground upon a software failure. Once the main program has been started by the script, the thread manager initializes all of the individual threads for the other processes and then waits for a terminate command to close the ALI flight software.

The first module started by the thread manager is the communications module which operates the telemetry or communication between other modules as well interactions with the ground control software. The module sends and receives all data packets that are outgoing and incoming through UDP protocol as required by the CSA and CNES specifications. Also, data rate limits were imposed on the instruments to avoid one instrument using all the bandwidth to transfer data from the gondola. For ALI the limit was 100,000 bits per second. The communication module was responsible for verifying that this limit was obeyed when encoding into packets and sending them to the ground. Also, uploaded commands are decoded and sent to the command decoder which

takes all the incoming commands from the ground, parses the information, and sends the commands to the proper modules.

The diagnostic module manages the Global Positioning System (GPS), pulse per second, and the temperature sensors. The GPS monitor records the current location and height of the instrument from the front of ALI optical instrument. The pulse per second is a signal that is sent out from the gondola's SIREN module (a device used for the gondola's communications and telemetry system) every second. It is a constant signal between all instruments on board to correlate each systems data to each other. Lastly, the temperature sensor module reads all of the temperature sensors from a one line temperature sensing device, where all temperature sensors are on a single line and are connected with a simple RS-232 connection. The locations of the temperature sensors can be seen in Table 3-5 and the locations attempt to achieve a complete temperature profile of the instrument. All information gathered by the diagnostic module is sent to the telemetry system so the ground user can determine the state of the system and make any required changes. The data is also stored on the local hard drive (solid state) onboard ALI for use when ALI is recovered after the flight.

Table 3-5: Location of ALI temperature sensors.

Number	Sensor Location
1	Aluminum wall of electronics case
2	Cooling plat of RF Driver
3	OCELOT CPU heatsink
4	Aluminum wall of power supply case
5	5 V power supply transducer
6	12 V power supply transducer
7	Front of ALI baffle just inside system
8	On the CCD camera

The science module operated the ALI instrument, the acquisition of data, and directly controls the relay to the RF driver, the QSI CCD camera, and the RF driver. The science module loads program defaults upon startup from local storage. or program settings can be altered from ground

control. Each of the modes for data acquisition has its own configuration files and the supported modes are a calibration mode, an aerosol mode, an H₂O mode, an O₂ mode, a constant exposure time aerosol mode, and a custom mode. The details for these mode can be found in appendix B.2.

When the science operations are enabled ALI will load in an operational mode as specified from the ground. The science mode will control all of the hardware and process the imaging cycle and two types of images are created. Full images that contain the entire image are sent to local storage due to bandwidth considerations and diagnostic images are transmitted to the ground that contain the needed housekeeping measurements and five vertical image profiles in case the local solid state data is not recoverable after the balloon flight. When the mode is completed the same modes are repeated unless ALI has received a command to stop acquiring images or is queued to start another mode.

A diagnostic image is sent down for every image during the mission. Each diagnostic image contains five complete vertical columns of measurements with statistics on the entire image, including percentages of saturated and under-saturated pixels, as well as the location and time of the measurement and the current state of ALI. There are two reasons to include diagnostic images. First, having diagnostics on every image gives the users real time information if the measured data is saturated or under exposed and adjustments can be made during the mission. The second reason is there is no guarantee that when the gondola lands ALI will survive. It can land in water and the data be lost or crash land destroying the stored data. In case of the occurrence of such events, some data is sent down for every image so analysis and results can still be acquired from the ALI mission and can be used to verify the feasibility of the technology. Lastly, any extra bandwidth that is not allocated to other processes is used to transmit complete images down to the ground for complete horizontal and vertical verifications of the ALI instrument.

3.6 ALI Calibrations and System Test

A series of pre-flight laboratory calibrations were performed on ALI. The instrument was characterized as a complete system to provide calibrated radiance and estimate flight exposure times. Furthermore, complete system tests were performed to assess the full system in operation and address any issues or concerns. The following calibration measurements were performed on ALI:

- Exposure time determination
- DC offset removal
- Dark current correction
- Stray light calibration
- Relative flat-fielding correction
- Full system testing

3.6.1 Exposure Time Determination

A test for ALI was performed to determine exposure times for the stratospheric balloon flight as well as the entrance pupil size of the system. On July 12, 2014 from 13:00 to 16:00, during clear conditions, ALI was placed on the roof of a building (52.13°N 106.63°W) pointing approximately 90° in the azimuth from sun and measurements were recorded with variety of exposure time (0.01 to 120 seconds) and wavelengths (600 to 1000 nm). The exposure times that would achieve a three quarter full well on the ground were determined for each wavelength. However, the exposure times were needed for the balloon geometry, not on the ground, where the change in altitude greatly changes the spectral radiance which will alter the exposure times.

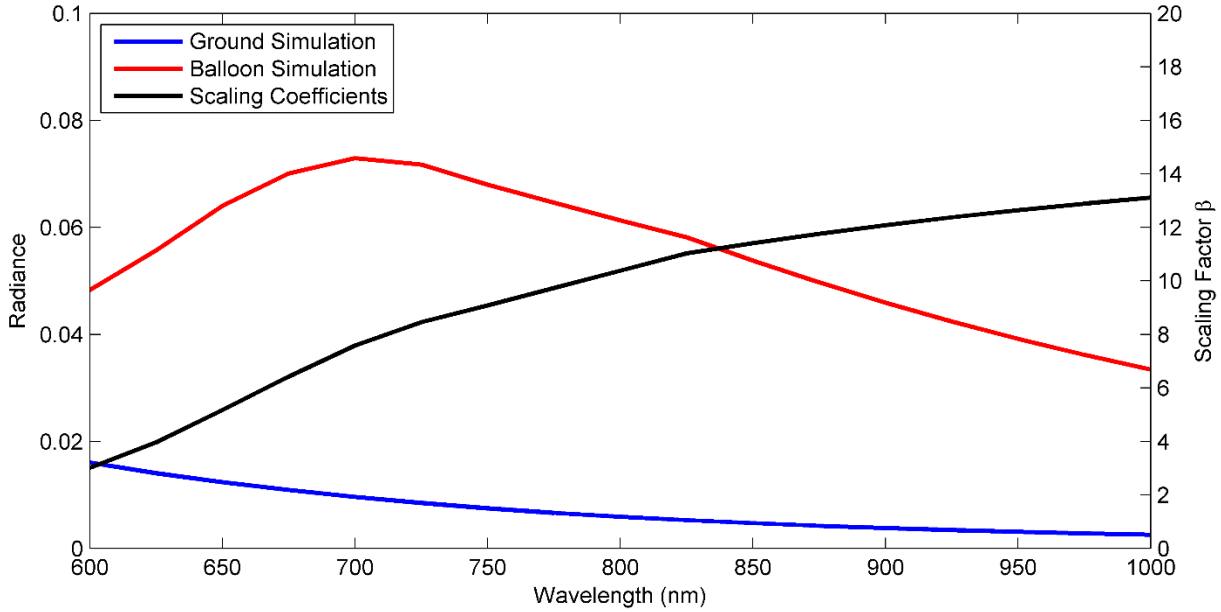


Figure 3-29: Simulated scalar radiances from the SASKTRAN-HR in blue and red with the radiance on the left side and the scaling factor in black with the value on the right side.

In order to address this issue a radiative transfer model is needed. A radiative transfer model has been developed at the University of Saskatchewan over the past 15 years. Using the scalar SASKTRAN-HR (Bourassa *et al.*, 2008; Zawada *et al.*, 2015) radiative transfer model, discussed in detail in section 2.4.5, radiance profiles were simulated from a ground-based geometry and a simulated balloon flight geometry. The simulated radiance profiles for the ground based and balloon flight geometry are seen in Figure 3-29. Radiance profiles based on the ratio of the ground based and balloon based geometries were used as a scaling factor, β . The scaling factor can be used in combination with the ground based determined integration times, t_g in the following

$$t_b = t_g \beta = t_g \frac{I_b}{I_g}, \quad (3.41)$$

where t_b is the integration time from the balloon platform, and I_b and I_g are the simulated scalar radiances from the balloon and ground respectively. The scaling factor can be observed in Figure 3-29 and the estimated balloon geometry exposure times are located in Table 3-6.

Table 3-6: Estimated balloon flight exposure times.

Wavelength (nm)	Exposure Time (s)
650	2.00
675	2.00
700	1.39
725	0.38
750	0.10
775	0.10
800	0.10
825	0.33
850	0.47
875	0.48
900	1.00
925	2.00
950	2.00

The exposure times determined were designed to be on the order of a second during the flight; however, there was some uncertainty with the final determined exposure times. The radiances used from the SASKTRAN-HR model were scalar since the vector model was still in development. ALI is a polarized instrument so the effect polarization would have on the scaling factors was unknown. To account for the unknown effect from the lack of simulated polarized radiances, the software was designed to be able to change the exposure time curve during the mission as required.

3.6.2 DC Offset Removal

The DC offset is a bias that is applied to the analogue to digital converter inside the CCD camera that causes a bias in the final count values for the image and needs to be removed in order to be able to get the pure measurement counts from the instrument. It is usually assumed that the DC offset for a CCD is a constant across the operating temperatures and exposure times of the device; however, the DC offset for the camera used in ALI exhibited a temperature dependence. Dark images were acquired in the laboratory to be used in the calibration. Additionally, a calibration mode was used on the ascent of the balloon during the campaign that acquired dark images which

were used to determine the DC offset. All of the dark images were taken with the shortest possible exposure time of 0.01 s to reduce any dark current contribution from the images. The mean value of the counts for each image was determined and was used to determine the DC offset. The standard deviation of the counts for each image ended up being approximately 2% of the average value. Using this data, a curve was fit to determine the DC offset with respect to temperature. The curve is in the form of

$$\text{DC offset} = 0.00659T^3 - 0.09202T^2 - 3.5368T + 64305127 \pm 2\%, \quad (3.42)$$

where T is the temperature of the detector in degrees Celsius and is plotted in Figure 3-30.

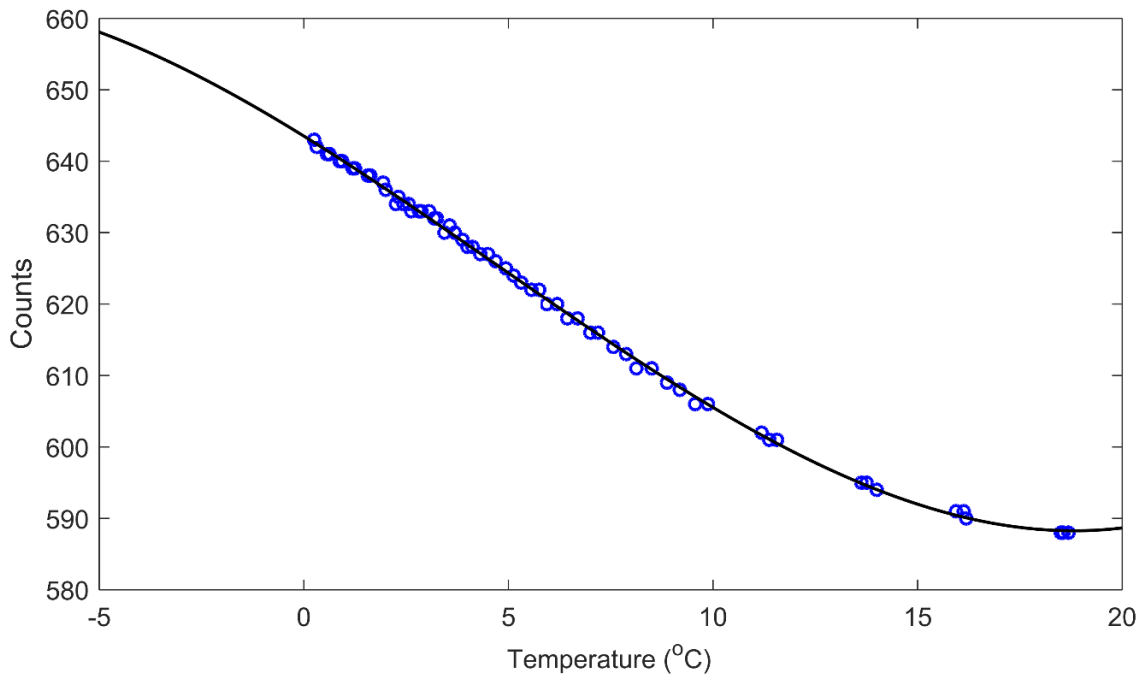


Figure 3-30: The DC offset curve (Equation 3.42) is seen in black where the lab and flight calibration data is shown in blue. The counts on the vertical axis are the counts that need to be removed to account for the DC offset.

3.6.3 Dark Current Correction

The dark current is thermal energy that builds up in the CCD detector. It grows linearly with exposure time and nonlinearly with temperature. By using images taken in darkness with a variety of exposures time, the dark current can be determined by looking at the residual after the DC offset

has been removed using the curve developed in the previous section. The residual of the counts for the calibration dark image can be seen in Figure 3-31. During the campaign, the operating temperature of the camera was less than 10°C throughout the entire flight and most exposure times were less than five seconds (shown in blue) leading a very small dark current contribution in the measurement images. The seven count dark current was small compared to the DC offset and was considered to be an addition noise source added to the error for the radiances.

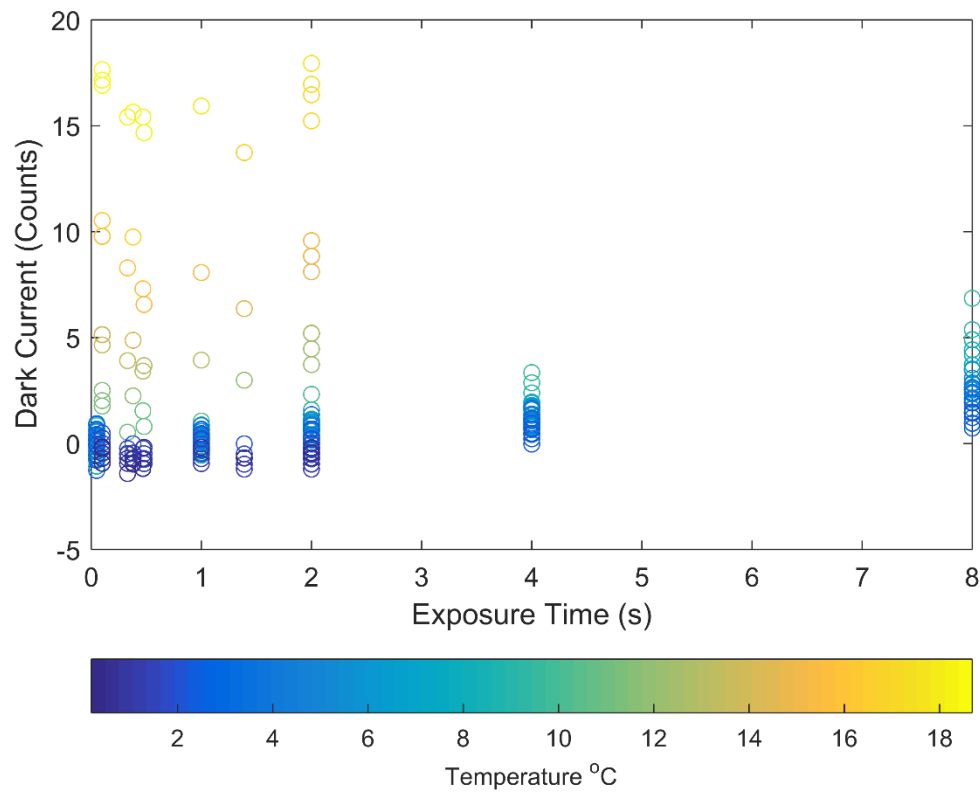


Figure 3-31: The dark current from the calibration images over a series of camera temperatures and exposure times.

3.6.4 Stray Light Calibration

A laboratory experiment to characterize the stray light in the ALI system was performed. Two types of stray light exist; the first is out-of-field stray light, i.e. signal that enters the optical path that originates outside of the field of view. The second is internal stray light, which is caused by

scattering, reflections or other imperfections in the optical elements. As mentioned above, stray light removal is critical for limb scatter measurements.

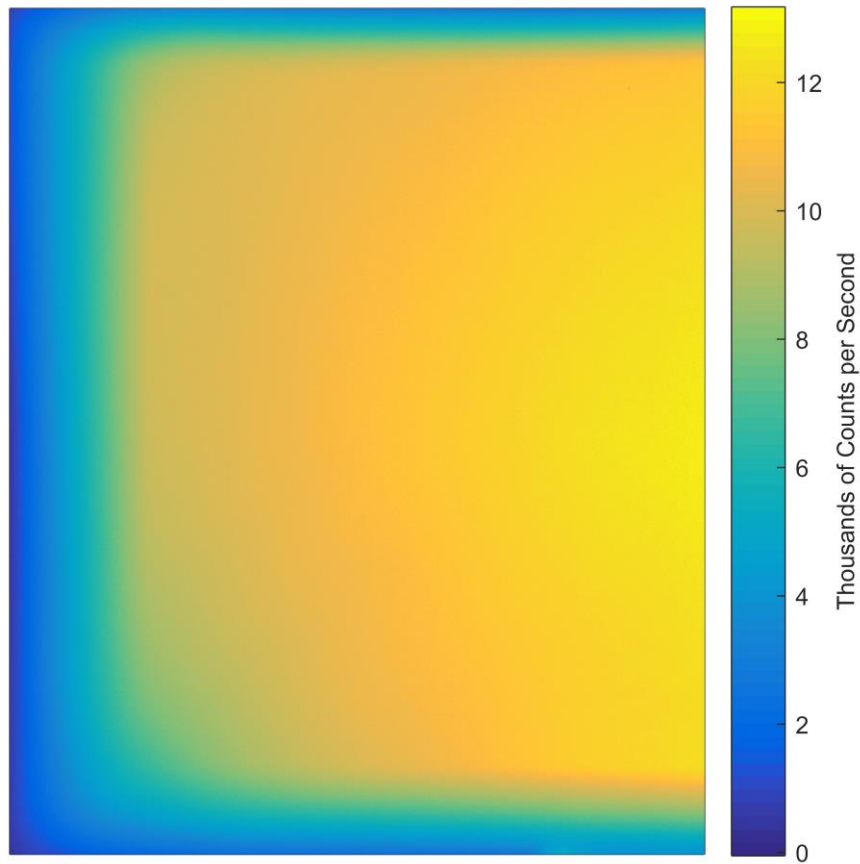


Figure 3-32: A calibration image after stray light removal has been performed where the measured wavelength is 750 nm with a 1 second exposure time. Vignetting can be seen as moving away from center of the image. Additionally the last 1° of the horizontal field of view is on the right side is lost due to strong contamination from reflections within the system.

The use of the AOTF has potential to increase the amount of internal stray light due to the fact that the undiffracted beam and the unmeasured polarization also propagate through the system. However, the diffraction interaction only occurs when the acoustic wave signal is applied, so without the acoustic wave the recorded measurement only contains the stray light in the system. Using this characteristic, the stray light of the system was measured in the laboratory. A 250 W quartz-tungsten light source was passed through a dispersing screen and onto the entrance aperture of ALI, effectively filling the entire aperture and all angles within the FOV. Using a variety of

exposure times, ranging from 0.1 to 60 s and wavelengths from 650 to 950 nm in 25 nm intervals, this diffuse source was imaged twice, once with the AOTF in its off state, with no driving acoustic wave, and once with the AOTF in its on state, with the acoustic wave applied. For each pair of measurements the image with the “AOTF-off” only contains stray light in the system, and the “AOTF-on” image contains the stray light combined with the image of the diffuse source. Subtracting the “AOTF-off” image from the “AOTF-on” image yields a final image that contains only the image of the diffuse source. A typical example of a resulting image is shown in Figure 3-32. The observed vignetting is caused by the aperture of the AOTF, expected from the ray tracing model, and light entering the AOTF outside the acceptance angle. Note that this method also partially removes dark current associated with the detector. This two-image method was used operationally during the balloon measurement campaign such that images captured had a corresponding “AOTF-off” image immediately obtained with the same exposure time. For the calibration images an average stray light to signal ratio of $2.5 \cdot 10^{-2}$ was noted.

3.6.5 Relative Flat-Fielding Correction

By using a simple optical layout as chosen for the prototype, light gets blocked by the AOTF's aperture causing a vignetting on the images. As the FOV is increased, so is the vignetting. Furthermore, the extreme range of the FOV, approximately the last half degree in each direction, is outside the acceptance angle of the AOTF which causes a loss of diffraction efficiency. Both of these effects will also need to be calibrated out of the measurements to achieve final radiances. The flat-field calibration corrects optical and detector level differences in the system across the FOV such that a calibrated image of a perfectly diffuse source yields a constant value across the image. The resulting images from the diffuse source described above were used to determine the flat fielding corrections for ALI. These were determined in two steps: spatial and spectral.

The experimental measurements from the stray light calibration mentioned above was also used to perform the relative flat-fielding calibration. For the spatial correction, for each image at a given wavelength, each pixel was scaled to the mean value of the center 25x25 pixels. A series of images was used to determine the mean flat fielding coefficient for each wavelength which had no more than a 4% standard deviation.

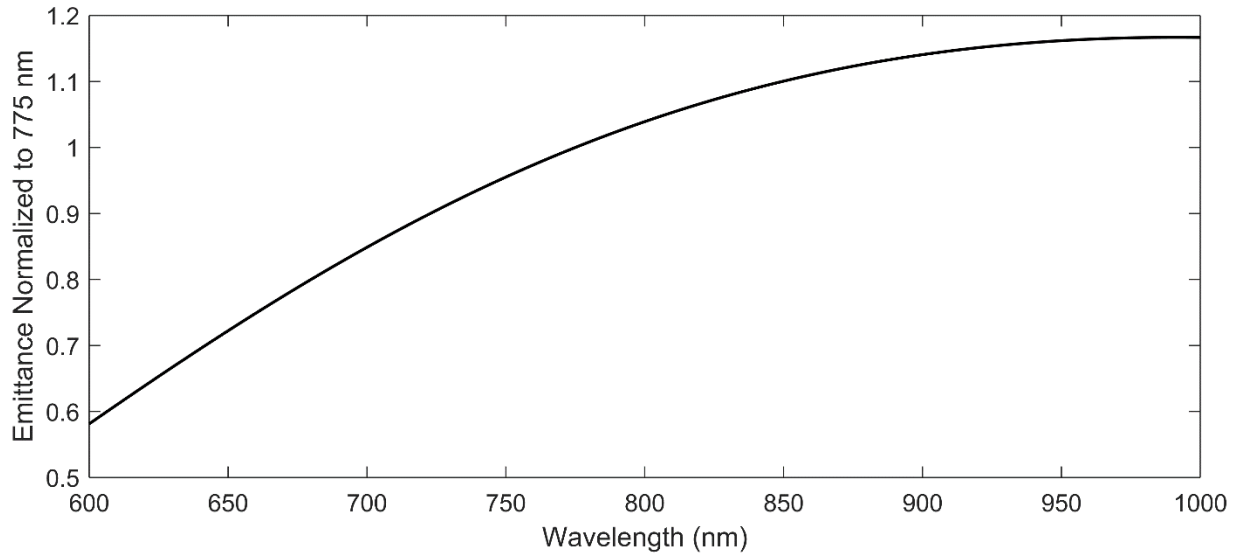


Figure 3-33: The blackbody emittance curve from Equation 3.43 normalized to 775 nm.

For the spectral calibration, ALI is most sensitive at 775 nm so this wavelength was chosen as the reference wavelength of a relative spectral calibration. All flat-fielding corrections were then scaled to the blackbody curve of a tungsten halogen bulb normalized to 775 nm assuming an operating temperature, T , of 3300 K using a method by *Kosch et al.* (2003). The blackbody emittance, $E(\lambda, T)$, of a filament bulb is given by

$$E(\lambda, T) = \varepsilon(\lambda, T) \frac{2\pi c}{\lambda^4} \frac{1}{\exp\left(\frac{hc}{\lambda kT}\right) - 1}, \quad (3.43)$$

where $\varepsilon(\lambda, T)$ is the emissivity of the tungsten filament, c is the speed of light, h is Planck's constant, and k is Boltzmann's constant. The emissivity values for tungsten were acquired by work

done by *Forsythe and Worthing* (1925) and used to compute the spectral emittance of the bulb normalized to 775 nm seen in Figure 3-33.

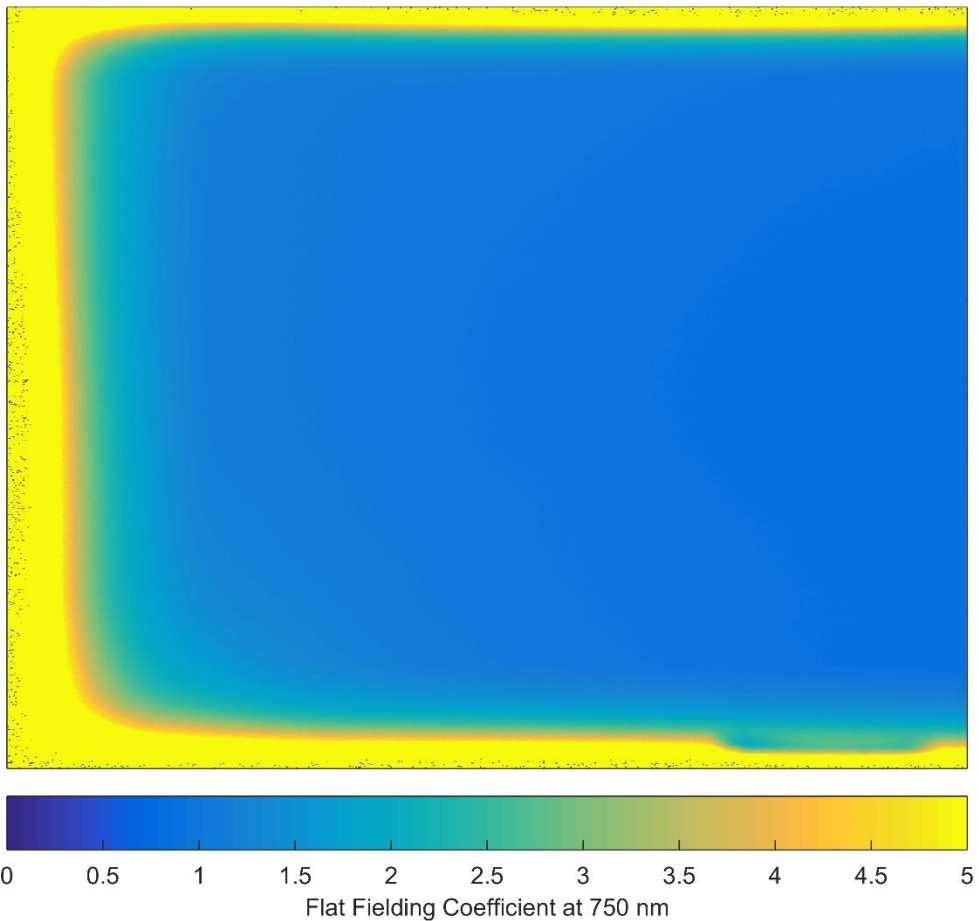


Figure 3-34: The flat fielding coefficients for 750 nm.

An example of the flat fielding coefficients for 750 nm can be seen in Figure 3-34. A majority of the coefficient for the central FOVs are near unity which should yield good sensitivity throughout most of the image. However, due to the vignetting and the loss of diffraction efficiency near the edges of the image, the flat fielding values in these regions are larger than the more central field of views. It should be noted that the relative flat-fielding is the final calibration for ALI and the final radiances will be relative to 775 nm. No absolute calibration was performed due to lack

of availability of an appropriately calibrated source. For a future iteration of ALI, an absolute calibration would be strongly suggested to be performed.

3.6.6 Integrated Testing

With the completion of the ALI instrument, including the optical chain, power and electronics hardware, and system software, a full system test was performed. All of the individual components of the system have been tested and verified but a complete integrated test was required to assure no undesired cross-communications occurs. ALI was set up in a flight configuration to simulate the launch of the balloon. During the test, ALI was completely controlled from a ground station computer over a local area network to simulate the gondola's communication interface. All commands were sent to ALI from the ground station and the simulation performed a full but shortened mission plan, which including pre-flight checks, launch, science measurement acquisition, and mission termination. During the simulation, the temperature and pressure during the flight could not be simulated.

The full integration testing occurred on August 12, 2014, along with a second instrument, the OSIRIS development model (*Kozun 2015; Taylor, 2015*) which was flown alongside ALI during the Timmins campaign. OSIRIS development model was connected to the same local network, as would be the case during the flight, to be a further test for both ALI and OSIRIS to locate any cross communication problems between multiple instruments.

The testing suite for ALI consisted of testing the pre-flight commands to verify full systems operation, ascent operational mode, science operational mode, and systems power down. Each mode tested the various states of ALI during the balloon mission. Further, all of the possible commands for ALI were also tested to verify no issues with their operation.

The full integration test found a few minor software bugs that were not found prior, but no major problems were noted with ALI itself or any cross communication problems with the OSIRIS

development model. The minor software issues were patched and tested on ALI before a final stable version of the software was loaded onto both the ground and flight computer systems and were considered to be the final flight version for the mission.

CHAPTER 4

THE SENSITIVITY TO POLARIZATION IN STRATOSPHERIC AEROSOL RETRIEVALS FROM LIMB SCATTERED MEASUREMENTS

4.1 Introduction

Stratospheric aerosols, which are micron-sized spherical liquid droplets of sulfuric acid, cause a cooling effect by scattering the incoming solar irradiance and therefore have an important radiative effect on climate. This effect depends strongly on the aerosol concentration and also the particle size distribution (*Kiehl and Briegleb*, 1993; *Stocker et al.*, 2013). Recent studies have proposed a link between the so-called global warming hiatus and an increase in the stratospheric sulfate aerosol layer. (*Solomon et al.*, 2011; *Haywood et al.*, 2014; *Fyfe et al.*, 2013). The increase in stratospheric aerosol over the last decade was primarily caused by a series of somewhat minor, mostly tropical volcanic eruptions (*Vernier et al.*, 2011) although the impact of anthropogenic pollution sources continues to be studied (*Neely et al.*, 2014). As noted in the recent review paper by *Kremser et al.* (2015) there is a distinct need for continued monitoring with global coverage of aerosol, particularly extending down to tropopause altitudes.

Stratospheric aerosol distributions have been monitored on a global scale since the 1970s with satellite instruments using a variety of remote sensing techniques. The first satellite aerosol extinction profile retrievals were from limb sounding solar occultation measurements, most notably from the NASA SAGE missions (*Russell and McCormick*, 1989; *Thomason and Taha*, 2003). The solar occultation technique has provided a robust and reliable method to retrieve aerosol by directly measuring the atmospheric optical depth. However, the global sampling of occultation measurements is somewhat limited due the necessity of a sunrise or sunset and typically requires months to cover a large range of latitudes. Limb scatter measurements, such as

from OSIRIS (*Llewellyn et al.*, 2004), SCIAMACHY (*Bovensmann et al.*, 1999), and most recently by OMPS (*Rault and Loughman*, 2013), have better coverage by only requiring the sunlit conditions at the tangent point, but the retrieval of aerosol is more complex requiring computationally heavy forward modelling and inversion compared to occultation (*Bourassa et al.*, 2007; *Bourassa et al.*, 2012b; *Rieger et al.*, 2014). It is worthwhile to note the success of limb scatter aerosol measurements: the combination of the SAGE II and OSIRIS datasets have recently been used to successfully create a single long term merged time series depicting the evolution of the stratospheric aerosol layer (*Rieger et al.*, 2015), and OSIRIS measurements have been used as one of primary extension of the stratospheric aerosol record for the CMIP6 study (*Thomason et al.*, in preparation).

OSIRIS, SCIAMACHY, and OMPS measure the spectral radiance of the scattered sunlight from the limb and use non-linear inversion techniques to retrieve aerosol extinction profiles (*Bourassa et al.*, 2012b; *Ernst et al.*, 2012, *Rault and Loughman*, 2013). For these retrievals, some assumptions regarding particle size distributions and/or composition are always required in the forward model. Most importantly for this study, currently none of these retrievals account for any polarization sensitivity in their respective measurements. However, these instruments have been specifically designed to measure the total radiance by minimizing the instrument sensitivity to polarization. Recently proposed new instruments with the capability to measure aerosol using limb scattering include the Belgium instrument Atmospheric Limb Tracker for the Investigation of the Upcoming Stratosphere (ALTIUS) (*Dekemper et al.*, 2012) and the Aerosol Limb Imager (ALI), a Canadian endeavour. Both instruments image the limb and use acousto-optic tunable filters to select the measured wavelength. The use of the acousto-optic filter inherently means that the measured image is of the linearly polarized radiance. Although it has been previously shown that

the retrieval of stratospheric aerosol extinction profiles from polarized scattered sunlight measurements are possible (*McLinden et al.*, 1999), the full impact of the polarized measurement has not been systematically studied. In this work we perform an analysis with simulated polarized measurements to determine first if there are any clear advantages or disadvantages to making the linearly polarized measurement. Further, we investigate which linear polarization and viewing geometries have the largest sensitivities to aerosol, and how the polarized measurements affect the accuracy and precision of the retrieved aerosol product.

4.2 Background and Forward Model

In order to investigate the effect of polarization on the sensitivity to aerosol, an accurate model of the polarized limb radiance must be employed. Additionally, a large number of scenarios, including various atmospheric states and viewing geometries, are required to fully probe the solution space. In this section, the basic background describing the polarization state of the limb signal is developed, and the SASKTRAN-HR model and the various model scenarios used for the analysis are described. Based on the useful spectral range for limb scatter observations of stratospheric aerosol, we have limited our discussion to wavelengths from 500-1500 nm.

4.2.1 Polarized Scattered Sunlight and Stratospheric Aerosols

All full description of scattering interactions within the atmosphere can be found in section 2.4.2 to 2.4.4. This section will briefly cover the theory and then use it to analyze the polarization state of earth's atmosphere in regards to look direction.

The polarization state of electromagnetic waves can be fully defined by the Stokes vector formulation. The Stokes vector is given by a column matrix

$$\mathbf{I} = \begin{bmatrix} I \\ Q \\ U \\ V \end{bmatrix}. \quad (4.1)$$

where the terms of the Stokes vector, defined in a reference frame, are measures of the total radiance, I , the difference between horizontal polarization to vertical polarization, Q , the difference between $+45^\circ$ diagonal polarization to -45° polarization, U , and the difference between the counter clockwise circular polarization to clockwise polarization, V . Using a reference frame where the x-axis is defined to be the horizontal polarization leads to the following definition for the Stokes parameters

$$\begin{aligned} I &= \langle E_x \rangle^2 + \langle E_y \rangle^2 \\ Q &= \langle E_x \rangle^2 - \langle E_y \rangle^2 \\ U &= 2\text{Re}(\langle E_x \rangle \langle E_y^* \rangle) \\ V &= -2\text{Im}(\langle E_x \rangle \langle E_y^* \rangle). \end{aligned} \quad (4.2)$$

To model the scattering for an incident ray propagating in a given direction the ray undergoes a rotation into the Stokes reference frame and is then multiplied by the phase matrix for the scattering process. After the multiplication the resulting ray is then rotated back into the ray's initial coordinate system through the following operation,

$$\mathbf{I}^{\text{sca}} = \mathbf{L}(\theta_2)\mathbf{P}(\Theta)\mathbf{L}(\theta_1)\mathbf{I}^{\text{inc}}. \quad (4.3)$$

The outgoing, or scattered, and incoming radiances are represented 4 by 1 matrices, *i.e.* Stokes column vectors, given by \mathbf{I}^{sca} and \mathbf{I}^{inc} , the rotation matrices are given by \mathbf{L} and rotate the incoming ray and scattered ray by rotation angles θ_1 and θ_2 . The phase matrix is a 4 by 4 represented by $\mathbf{P}(\Theta)$ and is related to the probability that an incoming ray will be scattered at a scattering angle, Θ . It also describes the change in polarization state through the elements of the matrix.

For this work, two primary scattering interactions induce and/or modify the polarization state of the light propagating in the atmosphere. These are scattering by the molecular air density and by stratospheric sulfate aerosols. The molecular atmosphere interaction is referred to as Rayleigh

scattering, and has a phase matrix that is determined from the Rayleigh-Gans approximation (*Mishchenko et al.*, 2002) given by

$$\mathbf{P}(\Theta)_{\text{ray}} = \frac{3}{4} \begin{bmatrix} 1 + \cos^2 \Theta & -\sin^2 \Theta & 0 & 0 \\ -\sin^2 \Theta & 1 + \cos^2 \Theta & 0 & 0 \\ 0 & 0 & 2\cos\Theta & 0 \\ 0 & 0 & 0 & 2\cos\Theta \end{bmatrix} \quad (4.4)$$

where Θ is the scattering angle.

For randomly orientated or spherical particles, such as stratospheric aerosol, only six elements of the phase matrix are required (*van de Hulst*, 1957) which are the following

$$\mathbf{P}(\Theta) = \begin{bmatrix} P_{11}(\Theta) & P_{12}(\Theta) & 0 & 0 \\ P_{12}(\Theta) & P_{22}(\Theta) & 0 & 0 \\ 0 & 0 & P_{33}(\Theta) & P_{34}(\Theta) \\ 0 & 0 & -P_{34}(\Theta) & P_{44}(\Theta) \end{bmatrix} \quad (4.5)$$

Additionally, for spherical particles like stratospheric aerosol only four unique terms are required since $P_{11} = P_{22}$ and $P_{33} = P_{44}$. Spherical aerosol scattering at visible and near-infrared wavelengths is fully described by Mie theory (*Mie*, 1908), for which several standard codes have been developed to calculate scattering cross sections and phase matrices based on the particle size distribution and index of refraction (e.g. *Wiscombe*, 1980). A full derivation can be found in *van de Hulst* (1957).

The basic polarization state of the scattered light in the earth's atmosphere can be understood by first considering a single scattering event of the unpolarized incoming sunlight in a molecular atmosphere. It can be easily seen from the form of the Rayleigh phase matrix (Equation 4.4) that a single scattering event causes the sky to develop a distinct polarization at a solar scattering angle (SSA) of 90 degrees from the incoming solar beam. The scattered sunlight is linearly polarized in the horizontal orientation, which is parallel to the horizon. The degree of polarization gradually decreases at scattering angles greater than or less than 90 degrees (broadly referred to as back-

scatter and forward-scatter geometries, respectively). In this single scattering scenario, the radiance is completely unpolarized at solar scattering angles of 0 and 180 degrees. If multiple scattering events are taken into account, the degree of polarization is decreased at 90 degrees SSA, and conversely does not become completely unpolarized at SSAs of 0 and 180 degrees. Simulations with the SASKTRAN-HR radiative transfer model, which is described below, using an atmosphere of molecular air density show that at 90 degrees SSA, the degree of linear polarization of the limb radiance is approximately 95% for a wavelength of 750 nm. This linear polarization effect is strongest at longer wavelengths (*i.e.* approaching 1500 nm) and decreases, on average by 10%, as the wavelength become shorter (*i.e.* down to 500 nm). This is directly related to the greater contribution from multiple scattering at shorter wavelengths. As the SSA increases from 90 degrees, the degree of linear polarization decreases. It is approximately 20% for a back scatter geometry of 180 degrees, and 30% for a scattering angle of 45 degrees. The ratio of the horizontal polarization over the total radiance and the vertical polarization over the total radiance is shown in the top of Figure 4-1. The strong polarized nature can be noted around SSA of 90 degrees where the radiance is almost complete horizontally polarized.

For an atmosphere that contains both the molecular air density as well as a typical background state of stratospheric sulfate aerosol, both Rayleigh and Mie scattering occur in a weighted fraction according to the optical depth of air and aerosol. Compared to the pure Rayleigh scattering case, the addition of aerosol causes a decrease in the degree of linear horizontal polarization for wavelengths shorter than approximately 750 nm. The bottom two panels of Figure 4-1 show the difference in the ratio of the polarized over the total radiance for the atmosphere with aerosol and one without, this effect has a weak dependence on solar scattering angle, with the most depolarization occurring in forward scatter geometries for short wavelengths. Interestingly, for

longer wavelengths in back-scatter geometries, the opposite occurs. This is due to the changing fraction of scattering from the molecular air density and aerosol because the Rayleigh scattering cross section falls off much more quickly with wavelength than the aerosol cross section. The magnitude of the observed change in linear polarization from a pure Rayleigh atmosphere to that with typical background aerosol is approximately 5-10%, but it obviously varies depending on aerosol loading and the microphysical parameters of the aerosol.

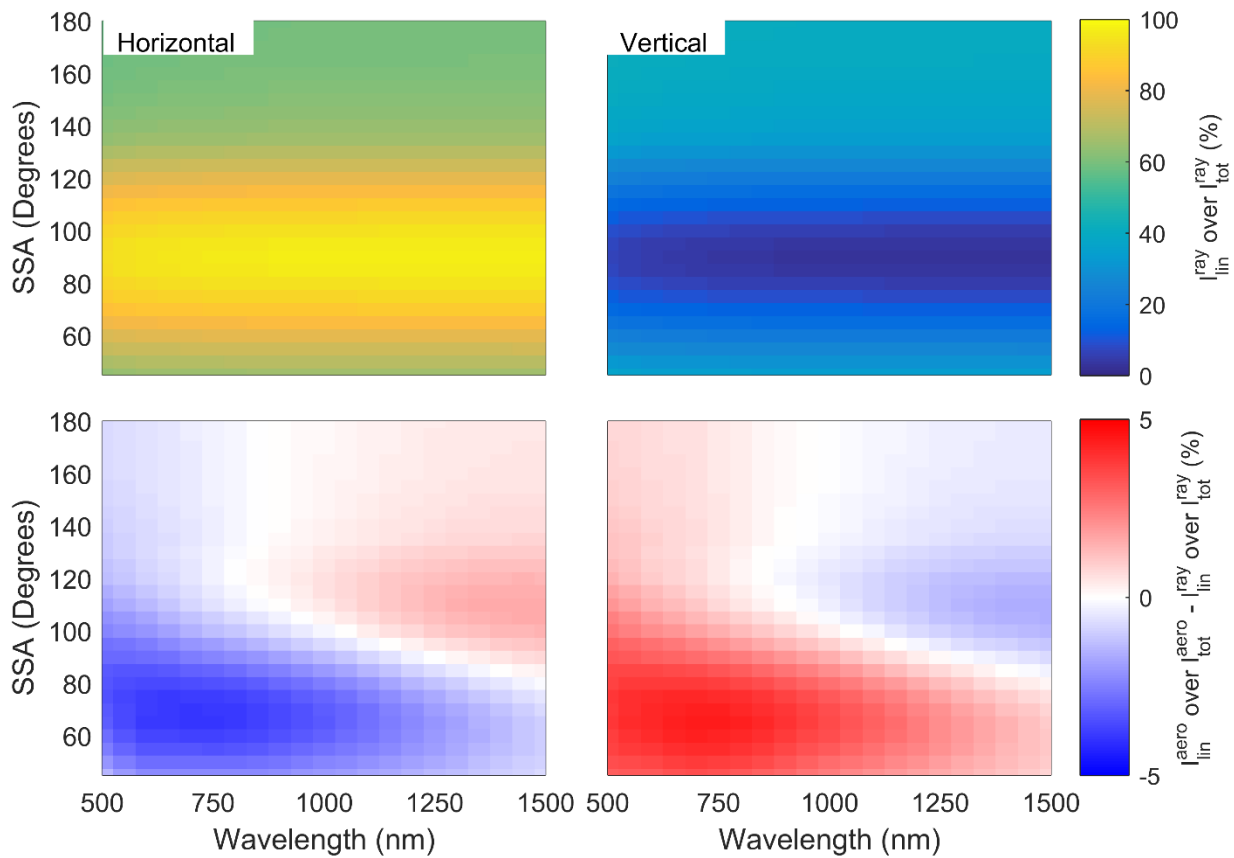


Figure 4-1: (Top) The fraction of a linear polarization (left is horizontal and right is vertical) over the total radiance for molecular air density. (Bottom) The change in linear polarization between an atmosphere that contains aerosol and one with only molecular air density.

4.2.2 SASKTRAN-HR Model

The model used for this work is the SASKTRAN-HR radiative transfer model discussed in section 2.4.5 and a brief overview will follow. The High Resolution module of the SASKTRAN radiative transfer framework (*Bourassa et al.*, 2007; *Zawada et al.*, 2015) was used in this study. The SASKTRAN framework handles built-in and user-specified atmospheric species optical properties and number density profiles, and uses a fully 3D spherical geometry to solve the radiative transfer equation. The High Resolution module uses a successive orders of scattering technique, and solves either the scalar or vector (polarized) radiative transfer equations to arbitrarily many orders of scatter. In this study, the HR module is set to handle the first two orders of scattering in a fully polarized sense, and to handle all scattering into the observer line of sight in a polarized sense. Three orders of scattering into the instrument line of sight are therefore handled in a fully polarized sense. For higher orders of scatter, the higher-than-second orders of scatter are handled in a scalar sense and the polarization state is assumed to be random before the final (polarized) scatter into the observer line of sight. This “pseudo-polarized” approximation has been shown, through comparison against the highly accurate and fully polarized Monte Carlo module of the SASKTRAN framework (*Dueck et al.*, 2016), to be sufficiently accurate for the wavelengths and geometries of interest of this work. All calculations performed with SASKTRAN-HR in this study assume randomly polarized sunlight, and dry air and Mie (H_2SO_4) scattering events only to model the interaction with the molecular air density and stratospheric aerosol, respectively. Scattering events from the Earth’s surface are assumed to be Lambertian and fully depolarizing.

4.2.3 Model Scenarios

The impact of using polarized radiance measurements on stratospheric aerosol retrievals is systematically studied with the radiative transfer model by exploring a set of distinct cases that

approximately cover the expected range of aerosol parameters, including both particle size and concentration (or extinction) profiles, and viewing geometries. Viewing geometry is an important parameter as even in the case of the total radiance measurements, the geometry can have a substantial effect on the sensitivity of the measurement to aerosol due to asymmetry of the Mie scattering phase function, i.e. element $P_{11}(\theta)$ of the phase matrix (*Rieger et al.*, 2014). There is strong aerosol scattering in the forward direction and so this results in a weaker relative aerosol signal in the back scatter direction.

To probe the space of possible aerosol measurement scenarios, two aerosol extinction coefficient profiles and four particle size distributions were used. The two extinction profiles, nominally specified at 750 nm, correspond to a background aerosol case, typical of the volcanically quiet period of the early 2000's (*Deshler et al.*, 2003), and a volcanically enhanced case which was taken from OSIRIS measurements two months after the Nabro eruption in 2012 (*Bourassa et al.*, 2012c). Both profiles are shown in Figure 4-2. The four particle size distributions were also chosen to represent typical background and volcanically enhanced cases. The background cases are both single mode lognormal distributions with somewhat different, but still typically observed, size parameters. A bi-modal lognormal particle size distribution was used for the volcanically enhanced cases, with one fine mode and one coarse mode, each comprising an equal fraction of the total extinction. All of the parameters of the size distributions are detailed in Table 4-1. These selected distributions are based on in-situ balloon particle counter measurements from Laramie, Wyoming (*Deshler et al.*, 2003). The size distributions were used for translating the extinction profiles, which are specified at 750 nm, to other wavelengths by scaling the extinction by the ratio of the Mie scattering cross sections corresponding to the size distribution at the two wavelengths.

To probe the range of possible viewing geometries from low earth orbit, a range of Solar Zenith Angles (SZAs) and Solar Scattering Angles (SSA) were selected. The ranges give representative selections of the possible geometries of a limb scatter instrument in low earth orbits at a range of local times. The selected values for SZA are 15°, 45°, and 75° and for SSA of 30°, 60°, 90°, 120°, 150°, and 180°.

Simulated measurements were performed at wavelengths of 500, 750, 1000, 1250, 1500 nm, which approximately cover for the spectral range commonly used for aerosol retrievals from limb instruments. For example, OSIRIS and SCHIAMACHY aerosol products use the ratio of 750 nm to 470 nm for the aerosol retrieval (*Bourassa et al.*, 2012b; *Ernst et al.*, 2012). Additional longer wavelengths have been shown to provide particle size information from limb scatter measurements (*Rieger et al.*, 2014) and so the 1000-1500 nm wavelength range was also included in this study. Finally, we also performed simulations for Earth surface albedo values of 0 and 1 in order to cover the full range of potential impact.

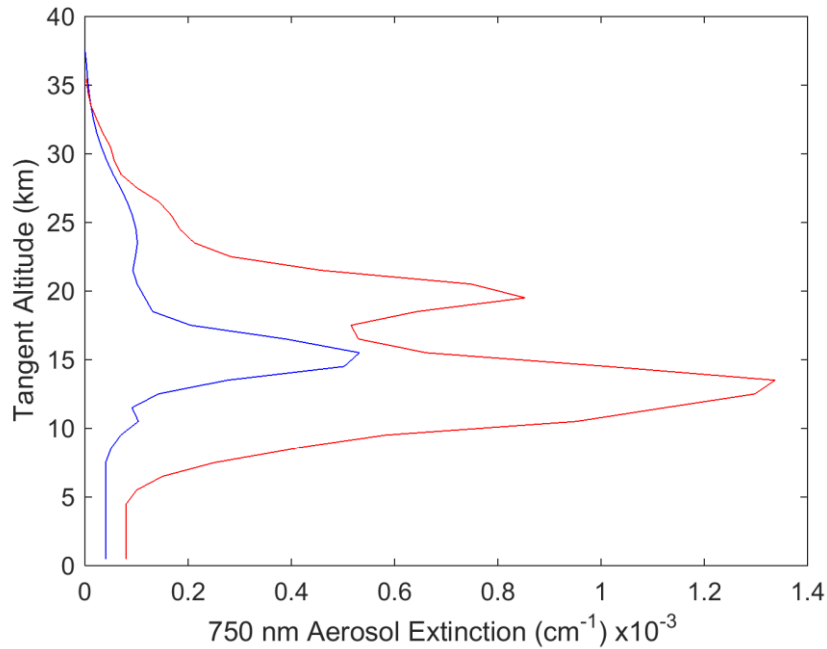


Figure 4-2: The two aerosol profiles used in this study. The blue is a background aerosol extinction levels, and the red curve is a representative aerosol profile after the Nabro eruption.

Table 4-1: Different particle size distributions used to test the sensitivity of the aerosol retrieval.

Particle size distributions	Fine mode radius (μm)	Fine mode width	Coarse mode radius (μm)	Coarse mode width	Percent extinction coarse mode (%)
1	0.04	1.8	--	--	0
2	0.12	1.25	--	--	0
3	0.04	1.8	0.30	1.15	50
4	0.12	1.25	0.30	1.15	50

To probe the range of possible viewing geometries, a range of Solar Zenith Angles (SZAs) and Solar Scattering Angles (SSA) were selected. The ranges give representative selections of the possible geometries of a limb scatter instrument in low earth orbit. The selected values for SZA are 15° , 45° , and 75° and for SSA of 30° , 60° , 90° , 120° , 150° , and 180° . The simulations were performed at wavelengths of 500, 750, 1000, 1250, 1500 nm, which approximately cover for the spectral range commonly used for aerosol retrievals from limb instruments. For example, OSIRIS and SCIAMACHY aerosol products use the ratio of 750 nm to 470 nm for the aerosol retrieval (Bourassa *et al.*, 2012b; Ernst *et al.*, 2012). Further near infrared wavelengths have been shown to provide particle size information from limb scatter measurements (Rieger *et al.*, 2014) and so the 1000-1500 nm wavelength range was also important to include in this study. The other important input parameter is the albedo of the Earth's surface and for this study we use both values of 0 and 1 in order to cover the full range of potential impact.

4.3 Methodology

For the purposes of this study, we have assumed an instrument capable of measuring only the linearly polarized radiance with either a vertical or horizontal orientation. This is representative of newly proposed instruments like ALTIUS (Dekemper *et al.*, 2012) and ALI that use an AOTF and by nature only measure one orientation of linearly polarized radiance. We want to answer the question: if the linear polarization is measured, is this an advantage or a disadvantage over a

measurement of the total radiance for aerosol retrievals? Further, is there a preferred orientation of linear polarization?

The polarization states used here are defined as the following: the linearly polarized radiance aligned with the horizon is referred to as the horizontal polarization, and the linearly polarized radiance that is perpendicular to the horizon is referred to as the vertical polarization. We also use the total radiance, or alternatively the scalar radiance, as the reference case. Note that the scalar radiance is not precisely equal to the total radiance. For the work presented here the term “total radiance” refers to the first term in the Stokes vector, which is calculated by the SASKTRAN model when solving the vector radiative transfer equation. The term “scalar radiance” refers to the radiance calculated by the SASKTRAN model when solving the scalar transfer equation. Using the Stokes parameter formulation, the horizontal polarization is given by $0.5(I + Q)$ and the vertical polarization is given by $0.5(I - Q)$, which can be easily shown from the definitions given in Equation 4.2.

Our study further breaks down this problem into three questions. First, how does the fraction of the limb scatter signal that is due to aerosol vary with aerosol load and viewing geometry for both scalar and polarized measurements? Secondly, does the polarized measurement increase sensitivity to assumptions in the retrieval algorithm and therefore increase potential for biased results? And finally, how does the polarized measurement effect the uncertainty estimate of the retrieved profile?

To explore the first question, simulated measurements were calculated with SASKTRAN using the scenarios described in section 4.2.3, including various wavelengths, geometries, aerosol loading and particle size distributions. These simulated measurements are then used to determine the approximate fraction of the limb signal that is due to aerosol. In each case the model is run

with a nominal atmosphere that consists of molecular air density, and climatological ozone and nitrogen dioxide profiles.

The fraction of the limb signal due to aerosol is determined by calculating the radiance without aerosol in the model atmosphere, *i.e.* that due to Rayleigh scattering only, I_R , and the radiance including aerosol, I_A . To find the fraction, δ , in percentage, of the signal that is attributed to aerosol, the following formulation is used:

$$\delta = \frac{I_A - I_R}{I_A} * 100\%. \quad (4.6)$$

Due to non-linearities from multiple scattering, it is not strictly true that this is the fraction of the signal due to aerosol; however, at most stratospheric tangent altitudes, the wavelengths under study are quite optically thin and this simple percent difference provides an intuitive approximation of the fraction of the signal due to aerosol.

We explore the second question about the effect of the polarized measurement on the aerosol retrieval using simulated measurements and a retrieval method that is essentially similar to that developed by *Bourassa et al.* (2012b) for OSIRIS. A minor change to the algorithm is made where the measurement vector for this study is not normalized by a shorter wavelength. We have made this change as the results from *Rieger et al.* (2014) shows this actually decreases sensitivity to particle size distributions. Although it is advantageous in a retrieval scenario to limit sensitivity to particle size, for this study we explore the worst case scenario under possible limitations of future technology, given that not all instruments may cover a wide enough spectral range for short wavelength normalization.

The limb radiance is calculated using SASKTRAN, again with climatological ozone and NO₂ profiles, for each of the scenarios listed in section 4.2.3. This is taken as a simulated measurement and is then used to retrieve aerosol extinction profiles using the *Bourassa et al.* (2012b) technique.

This is done similarly for the total radiance and for each orientation of the linearly polarized radiance. Additionally, a retrieval is performed with the scalar SASKTRAN-HR model to see if there is any substantial difference between using the scalar radiance and the total radiance from the vector model. For each aerosol retrieval, the ozone, NO², and albedo are fixed to the values used in the simulation of the measurement. All four particle size distributions from Table 4-1 are used in the simulations, but following *Bourassa et al.* (2012b), the aerosol particle size is fixed in the retrieval to a single mode log-normal with 0.08 μm mode radius and mode width of 1.6. The assumption of a fixed particle size distribution is common in limb scatter retrieval algorithms and this is used to explore sensitivity of the polarized measurements to particle size distributions, and test if the uncertainty in this assumption greatly effects the retrieved extinction.

Lastly, to answer the third question, an uncertainty estimate is performed on these retrievals in order to check the precision of the retrieved aerosol profile. The precision is determined by mapping the covariance of the measurement vector, \mathbf{S}_ϵ through the gain matrix, \mathbf{G} , which describes the sensitivity of the retrieval to the measurement and the respective noise through the following (*Rodgers*, 2000)

$$\mathbf{S}_{\text{aero}} = \mathbf{G} \mathbf{S}_\epsilon \mathbf{G}^T. \quad (4.7)$$

where \mathbf{S}_{aero} is the co-variance matrix for the retrieved aerosol profile. However, the direct calculation of the gain matrix is computationally intensive and numerically requires a retrieval for each measured altitude. A method presented by *Bourassa et al.* (2012a) uses the Jacobian, \mathbf{K} , to approximate the gain matrix by assuming the problem is linear near the solution state, which is largely a good assumption for limb scatter aerosol retrievals. Using these assumptions, the gain matrix can be determined simply through the inverse of the Jacobian,

$$\mathbf{G} \cong \mathbf{K}^{-1}. \quad (4.8)$$

Rather than specifying an assumed measurement co-variance to study the behavior of the retrieval precision, we simply replace the measurement co-variance in Equation 4.7 with the identity matrix. Thus the resulting terms of \mathbf{S}_{aero} are not absolute quantities but are related to the amplification of the measurement noise when mapped to the retrieved state (*i.e.* the larger the values of \mathbf{S}_{aero} the larger the uncertainty for the retrieval). The square root of the elements of the diagonal of the aerosol covariance, typically used to represent the error bars on the retrieved profile, are taken as the amplification of the measurement noise.

This method assumes that the radiance measurements regardless of polarization state have exactly the same signal to noise performance, *i.e.* all measurements have the same co-variance. We also consider the case where the instrument is not compensated such that the magnitude of the various polarization states directly scales the signal to noise performance, *i.e.* the instrument is not compensated to equalize the measurement co-variance when the signal drops due to the measured polarization state. In this scenario the above method must be modified by replacing the identity matrix with the matrix, \mathbf{R} , to represent the change in signal strength for the various polarizations relative to the scalar case. This matrix is defined as

$$R_{ij} = \begin{cases} \frac{I_{ref,i}}{I_{pol,i}} & \text{for } i = j \\ 0 & \text{for } i \neq j \end{cases} \quad (4.9)$$

The diagonal of the R matrix is effectively scaled by the inverse of the magnitude of ratio of the polarized radiance, $I_{pol,i}$, to the reference scalar case, $I_{ref,i}$, for the measurement altitude, i .

4.4 Analysis

4.4.1 Difference in Scalar Retrievals using a Scalar or Vector Model

First, we investigate if there is any significant difference between the use of the scalar radiance and the total radiance for retrievals on measurements of the total radiance. As mentioned above,

retrieval algorithms for current limb scatter data sets such as OSIRIS and SCIAMACHY use a scalar radiative transfer model with general success; however, as the total radiance is not strictly equal to the scalar radiance, this may lead to biases in the retrieved extinction profile under certain scenarios. Accounting for the vector component in the model alters the overall total radiance from the scalar solution due to multiple scattering interactions between the various polarization states of each successive order of scattering.

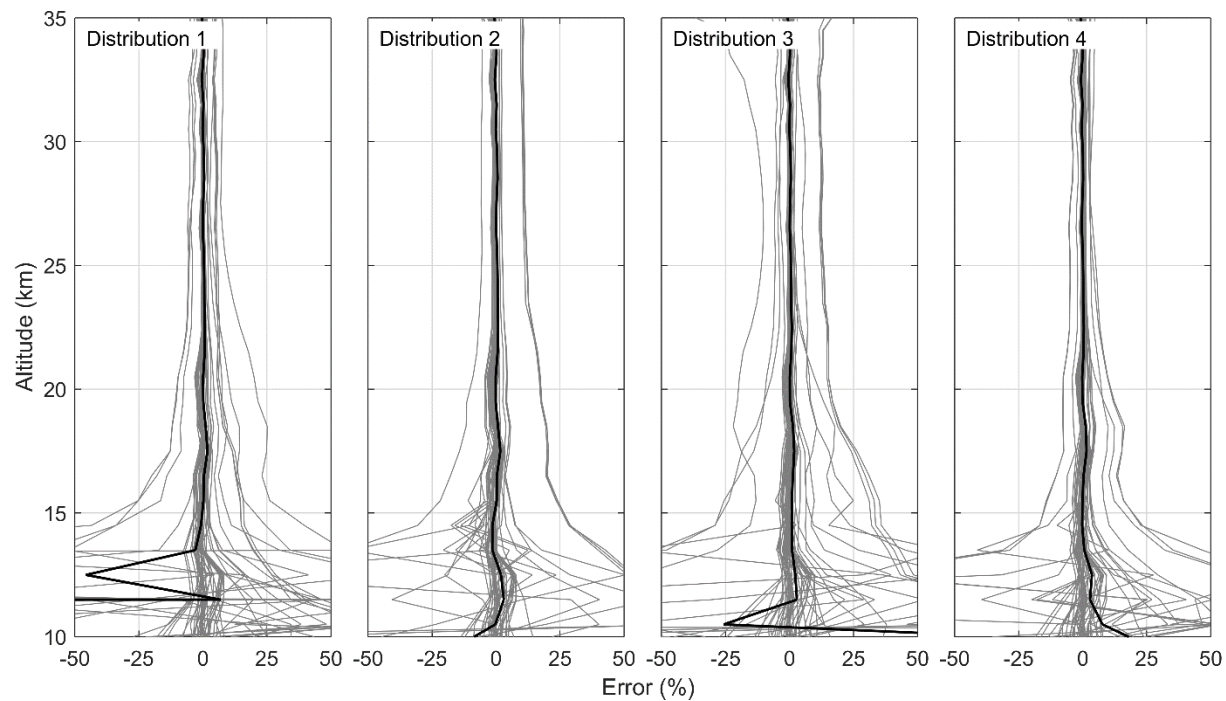


Figure 4-3: Percent differences between the vector retrieved aerosol extinction profiles and the scalar retrieval from simulated total radiance measurements. Each column represents a different particle size distribution (see Table 4-1).

The total radiance was simulated with SASKTRAN in vector mode for the full set of wavelengths and viewing geometries, and for the range of aerosol loading scenarios. These were used as input measurements to the retrieval algorithm, which was then performed using both the scalar and vector models. A case-by-case comparison between the retrieved extinctions for the scalar and vector models was performed using a simple percentage difference at each retrieved

altitude a can be seen as the grey lines in Figure 4-3. Furthermore, the mean of the bias for each particle size distribution is shown in solid black. These results, given in Figure 4-3, show that across all wavelengths, the mean percent difference is less than 2% from 15 to 37 km. A small number of outlier cases occur where the difference between the retrievals is greater than 7%. All of these cases occur for back scatter geometries and short wavelengths. The reason for this discrepancy is not well understood, although it certainly arises from the differences between the scalar and total radiance due to polarization interactions from the relatively larger contribution of multiply scattered light at shorter wavelengths. Generally, however, any differences between the use of the scalar and vector model for the retrieval are negligible. In fact, any form of discrepancy essentially vanishes for wavelengths past 1000 nm. Since the use of the vector model can increase calculation times by a factor of at least two, it is certainly justifiable to use the scalar model for the overwhelming majority of scenarios. For the rest of the work presented, any reference to the radiance will only refer to the total radiance, I , from the vector model.

4.4.2 Fraction of Limb Signal due to Aerosol

For a typical background aerosol state, the fractional contribution to the total limb radiance from aerosol was calculated from modelled radiances over a series of stratospheric tangent altitudes using the background aerosol profile and particle size distribution #1, given in Table 4-1. Figure 4-4 shows the percent change in this fraction for horizontally and vertically polarized measurements compared to the total radiance. The viewing geometry, which is a typical low earth orbit scenario, is SZA=45° and SSA=60°, and the albedo is 0. The top of Figure 4-4 shows the percentage of signal that is contributed to aerosol for both horizontal and vertical linear polarizations. As can be seen from the bottom of Figure 4-4, most of the change in the aerosol fraction of the polarized limb signal compared to the total radiance occurs for wavelengths between 500-1000 nm. At these wavelengths the horizontal polarization has a smaller fraction of signal due

to aerosol and the vertical polarization has a larger fraction due to aerosol. Overall the change is small and essentially limited to less than 10%.

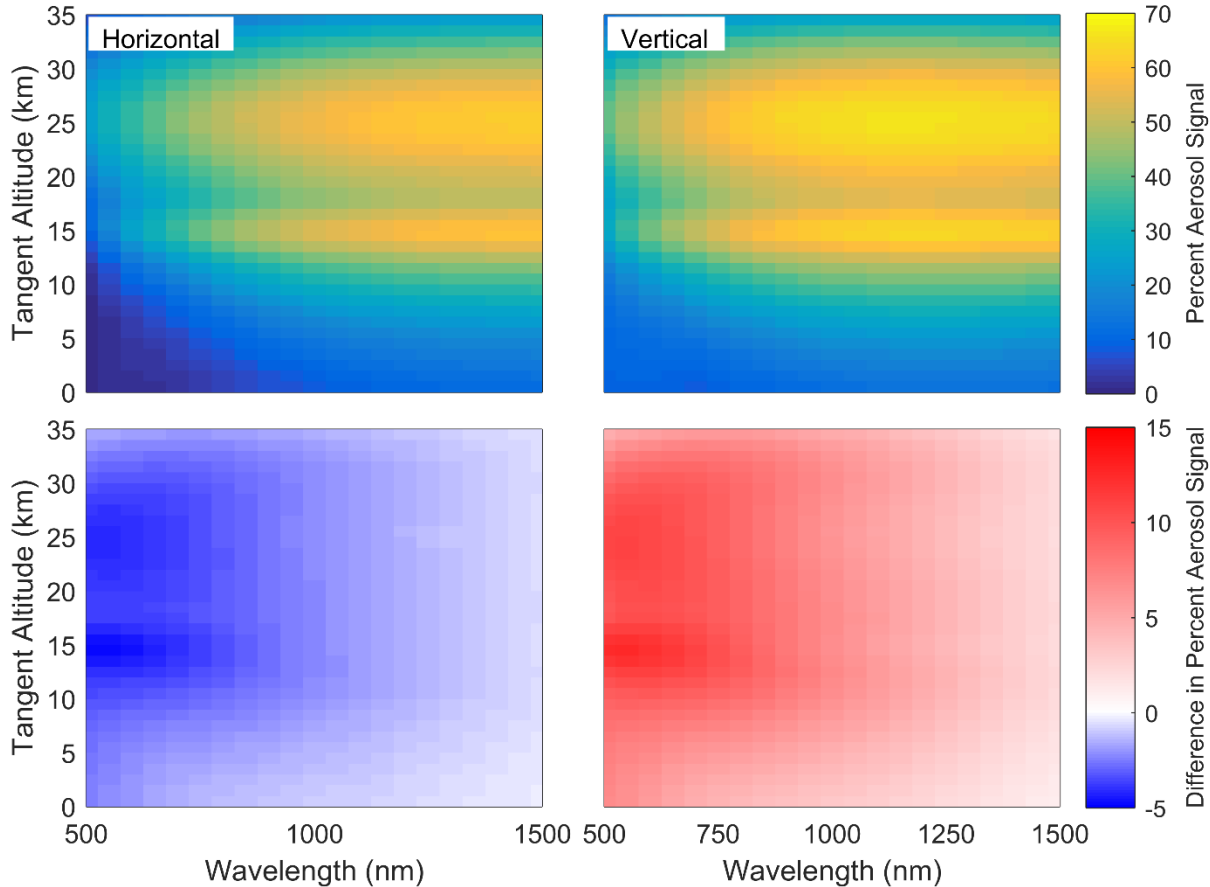


Figure 4-4: (Top) For a horizontal (left) or vertical (right) linear polarization the percent of the signal that is attributed to aerosol. (Bottom) The change in the fraction of the limb signal due to aerosol when compared to the total radiance for the horizontal (left) and vertical (right) polarization. The simulation uses a geometry of SZA=45° and SSA=60°, with the albedo being 0 and the aerosol state the background profile with particle size distribution #1.

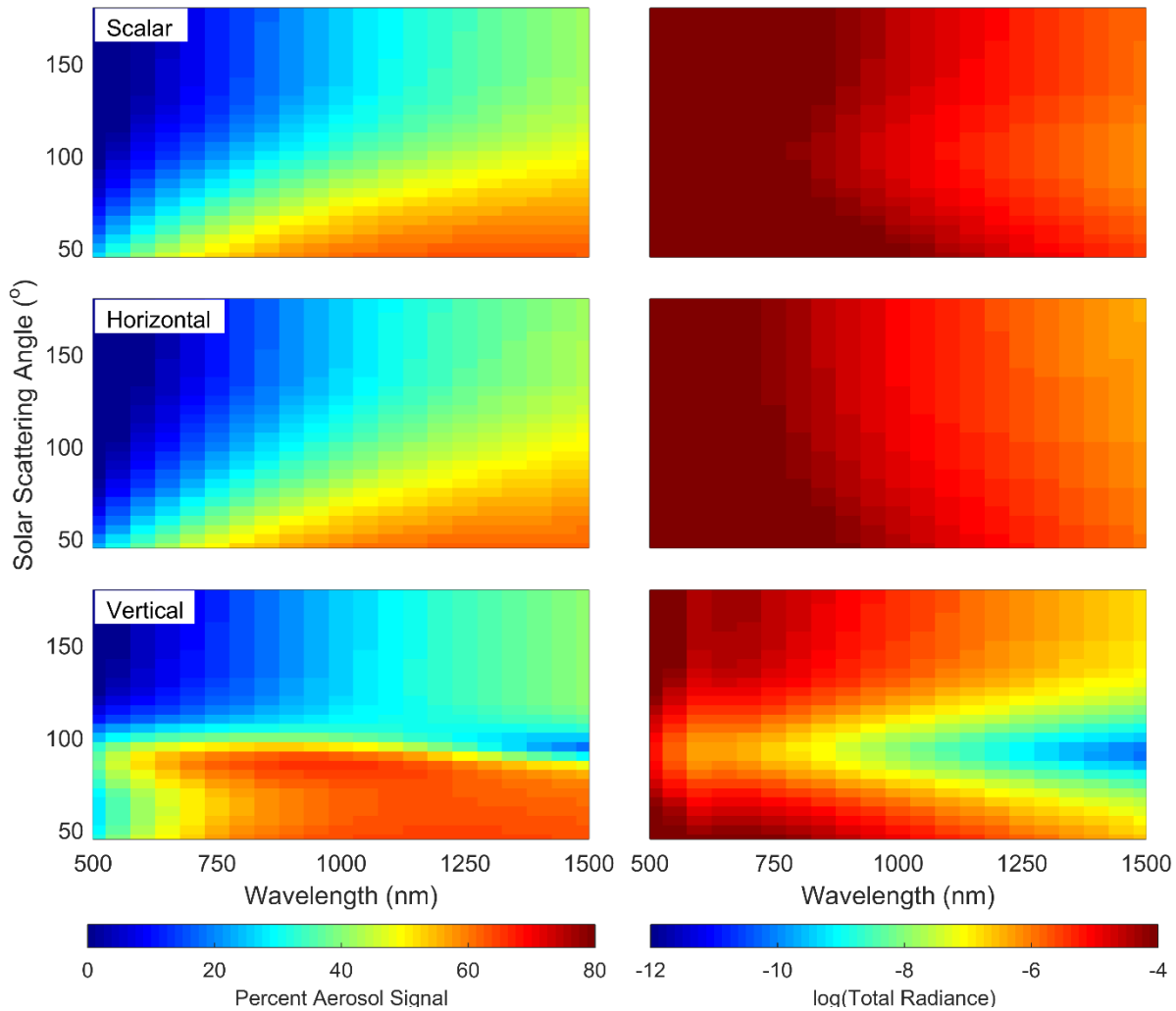


Figure 4-5: Dependence of the fraction of the limb spectra due to aerosol on solar scattering angle (left panels) for total radiance (top), horizontal polarization (middle) and vertical polarization (bottom), and the magnitude of the radiance for each case (right panels). Note the low signal near SSA of 90 degrees for the vertical polarization which would be problematic for terminator orbits.

Similar calculations were performed for the range of viewing geometries using the same atmospheric state. Figure 4-5 shows the fraction of limb signal due to aerosol for the total radiance, and both orientations of the linearly polarized radiance. This calculation was performed for 15 km tangent altitude, and other stratospheric tangent altitudes show very similar patterns. An important difference is noted between the forward and back scattering geometries. Remembering the horizontal polarization is given by $0.5(I + Q)$, the total and horizontal polarization cases have a

similar dependence on viewing geometry, with the strongest aerosol signal from long wavelengths in the forward scatter direction. The vertical polarization, given by $0.5(I - Q)$, has a strong aerosol signal contribution for forward scattering directions, especially at visible wavelengths, in comparison to the total and horizontal polarization cases. For back scattering geometries, somewhat less aerosol signal is observed. For reference, the magnitude of the limb radiance in each case is shown in the right hand column of Figure 4-5 taking note that the high end of the scale is saturated to emphasize the smaller values. It is important to note that the vertical polarization has a very low magnitude at scattering angles near 90 degrees. This makes this combination of viewing geometry and polarization very difficult to use reliably.

We performed these same calculations for the full range of SZAs and found that the SZA only effects the fraction of the signal due to aerosol by less than 1%. Also, when the albedo is changed from 0 to 1, the aerosol signal decreases for all polarizations and wavelengths thus reducing overall sensitivity to aerosol as albedo increases in all cases. Note, however, that the SASKTRAN-HR model assumes that all ground reflection is randomly polarized; the addition of a BRDF model may change the sensitivity to aerosol with higher albedo.

This same analysis was also performed for two other additional polarization orientations, the +45 degree and -45 degree linear polarizations (*i.e* $0.5(I + U)$ and $0.5(I - U)$) to investigate sensitivity to aerosol. It was found that these two polarization orientations had similar aerosol contribution to the total radiance case with approximately a loss of a third of the overall signal.

In general, the contribution to the limb radiance from aerosol for the horizontally polarized and total radiance cases is approximately the same. The vertical polarization has more asymmetry in aerosol signal between forward and back scattering geometries with very low signal magnitude near 90 degrees scattering angle. Given that essentially all low earth orbit scenarios will cover

forward and backward scattering angles, including 90 degrees scattering angle, it is clear that the horizontal orientation overall shows a more favorable response to aerosol. This is particularly true for a terminator orbit such as that for OSIRIS.

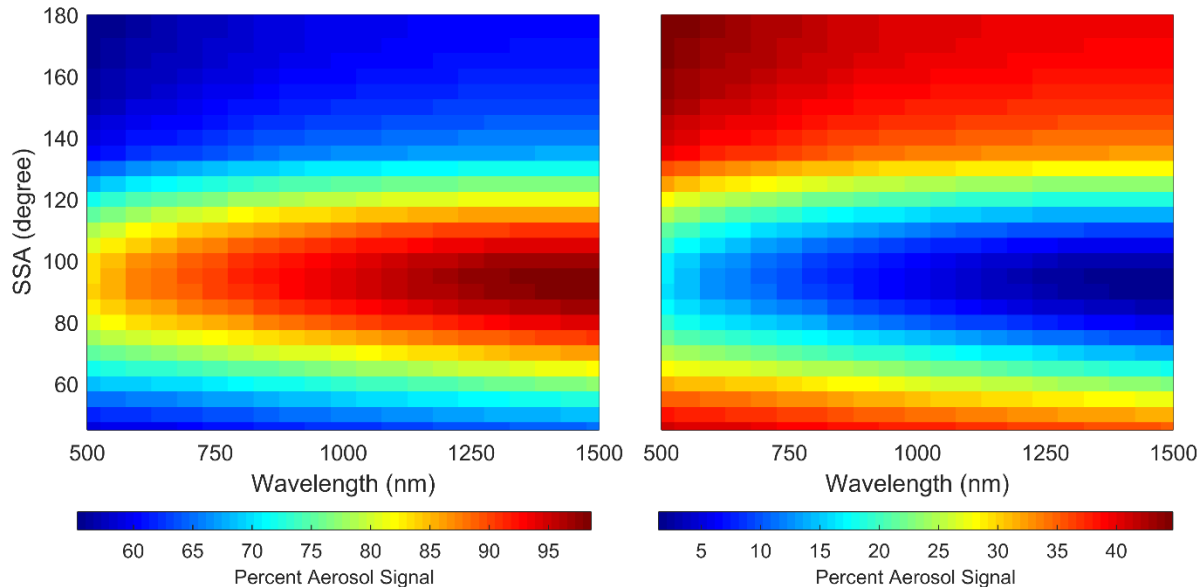


Figure 4-6: The ratio of the linearly polarized radiance to the total radiance for horizontal (left) and vertical (right) orientations. Note that the scale for each plot is different. The simulation was performed with a SSA of 60 degrees with volcanic aerosol loading for a tangent altitude of 20 km.

A distinct disadvantage of measuring a linear polarization rather than the total radiance is the loss of overall signal magnitude. In Figure 4-6, the ratio of the polarized radiance to the total radiance is shown for a series of SSAs for a tangent altitude of 20 km, but in this case using the volcanic aerosol extinction profile, which serves to enhance the fraction of signal due to aerosol. Measuring the horizontal polarization results in observing signal levels approximately one half to two thirds of the total radiance, with the greatest effect at the shorter wavelengths. The other forward scatter geometries are similarly affected. For back scatter geometries, the signal levels are also approximately half of the total radiance, but with less spectral dependence. For solar scattering angles near 90°, the horizontal polarization encompasses a large fraction of the total radiance resulting in signals of 80-95% of the total. Across the full parameter space of viewing geometries,

wavelengths, and aerosol loading scenarios, the magnitude of the horizontal polarization is on average 60-70% of the total radiance.

Although the vertical polarization shows a relatively larger fraction of the signal due to aerosol particularly in forward scatter geometries, the overall signal levels are substantially lower. For forward scatter geometries, the magnitude of the vertically polarized radiance is only approximately one third of the total radiance across the spectral range. Back scatter geometries are only slightly better with slightly less than half of the total radiance. Again, near solar scattering angles of 90° the limb radiance is almost fully horizontally polarized and the vertically polarized signal is only 5-20% of the total. On average across the entire parameter space, the vertical polarization is on 30-40% of the total signal.

It is clear from this relatively simplistic analysis of the aerosol signal in polarized limb radiance that there are trade-offs between viewing geometries and polarization orientation, and changing sensitivity across the spectral range. While there is not an overwhelming case to be made for one particular option over the wide range of scenarios that can be considered, the overall response of the horizontally polarized radiance is essentially similar to the total radiance, but with somewhat reduced magnitude that can most likely be mitigated through instrument design considerations. The vertical polarization has much more widely varying sensitivity to aerosol with very low signal levels near 90 degrees scattering angle, and is a much more challenging choice in terms of instrument performance for aerosol measurements.

4.4.3 Potential for Retrieval Bias

In this section we directly explore the effect of the polarized measurement on the results of a typical retrieval algorithm through application of the algorithm to simulated measurements across the full parameter space.

We explore the potential of an effect of polarization on the bias in retrieved extinction caused by uncertainty in the assumed particle size distribution. The set of radiances for all cases across the parameter space were again used as simulated input measurements to the retrieval algorithm. This time, retrievals were performed on the horizontally polarized radiance, the vertically polarized radiance, and the total radiance. The radiance calculations in the iterations of the retrieval were set to match the polarization states of the input radiance, but the total solution was used to approximate the total radiance. In all cases, the retrieval was performed using an assumed particle size distribution, which was log-normal with a mode radius and width of 0.08 μm and 1.6 respectively. Note that this assumed size distribution is different than all four of the size distributions used as the “true” state for the simulated input radiances. For the total radiance case, this uncertainty is well known to cause biases of up to 20-30% in retrieved extinction (*Rieger et al.*, 2014). A summary of the differences between the retrieved and true aerosol extinction for 750 nm and 20 km altitude is shown in Figure 4-7. Errors bars on each point represent one standard deviation of the variability in the results for the range of viewing geometries. These results are representative of the level of agreement also found for other wavelengths and altitudes. There is no substantial difference between the results for the background and volcanic extinction profiles. It should be noted that cases with solar scattering angle of 90° have been removed for the vertical polarization due to the very low values of signal, which manifests as a large dependency on the particle size distribution and a highly biased retrieval. This large bias is very sensitive to scattering angle and is nearly eliminated for even 85° or 95°.

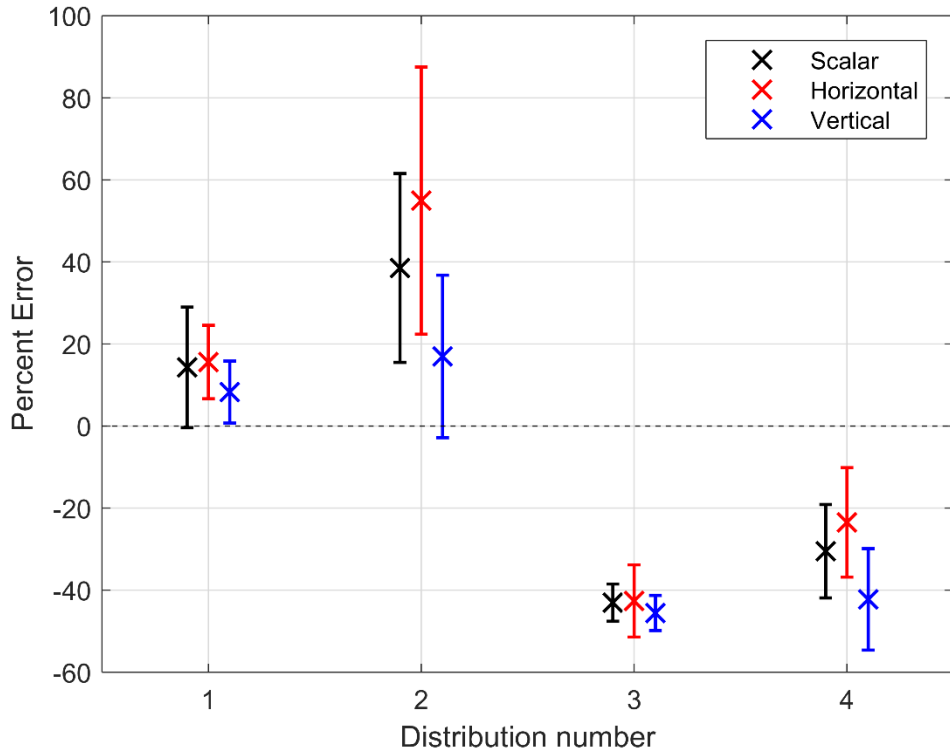


Figure 4-7: The mean percent difference between the retrieved aerosol extinction profile with an assumed particle size distribution and the true state corresponding to the indicated particle size distribution (see Table 4-1). Error bars represent one standard deviation of the variability across all viewing geometries. Results shown are for 750 nm and 20 km altitude.

It is clear that the major element of observed bias is simply the difference between the true and assumed particle size distribution. In all four cases there is some difference between the solutions for the various polarization states; however, for each particle size distribution the biases between the polarization states are essentially the same within the variability observed across the various viewing geometries. Neither of the linearly polarized states perform consistently better than the total radiance case; however, they do not perform any worse either (excepting the vertical polarization near 90 degree solar scattering angle), which is an equally important result.

4.4.4 Precision analysis

Finally, we study the effect of the polarized measurement on the performance of the retrieval in terms of the precision of the results. We again use simulated measurements across the full range

of input parameters as input to the standard retrieval algorithm. Following the methodology outlined in section 4.3, using SASKTRAN-HR the Jacobian matrices were calculated for each retrieved state and used determine the gain matrices, which were then applied as in Equation 4.7 to determine the retrieval precision. It should be noted that not all of the Jacobian matrices could be inverted due to negative sensitivity of the lower tangent altitudes (see discussion in *Bourassa et al.*, 2007) and these were removed from the data set (approximately 9% of total cases). This affected a large fraction of the 500 nm cases, so this wavelength was removed from this section of the analysis. As discussed in section 4.3, we approach this problem from two perspectives: (1) an instrument that is compensated in design and/or operation such that measurements regardless of polarization state or geometries have the same signal to noise ratio, and (2) an uncompensated instrument such that the changing signal level with polarization state and viewing geometry affects the signal to noise ratio of the observation.

For the first case, where the signal to noise ratio is compensated such that it is equal for all cases, the measurement co-variance matrix in Equation 4.7 is replaced with the identity matrix, and the relative size of the square root of the diagonal of the resulting aerosol co-variance represents the amplification of the measurement noise. To compare the performance of the various polarization states, the resulting retrieval co-variances for the linearly polarized measurements were normalized by the retrieval co-variances from the total radiance case. The dependence of the results on the various input parameters, such as wavelength and viewing geometry were examined. Very little altitude dependence was observed and so the results were averaged across the retrieved altitude range.

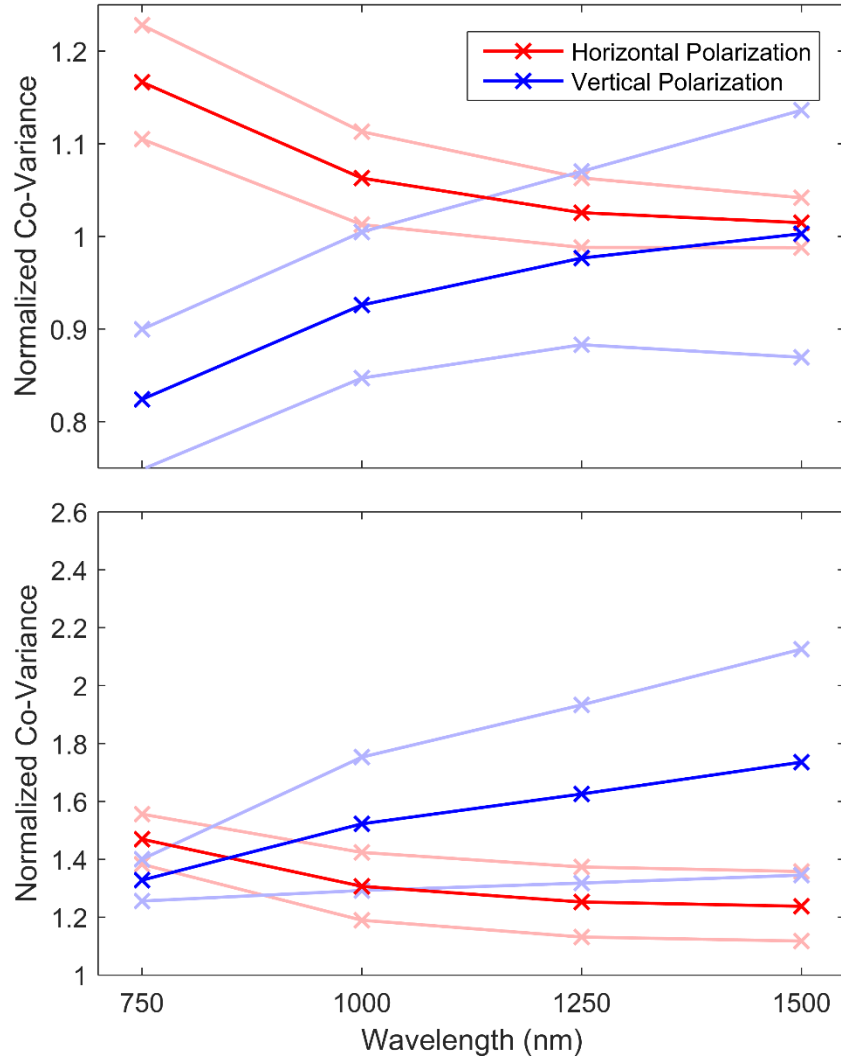


Figure 4-8: The wavelength dependence of the co-variance for the horizontal and vertical polarization retrievals normalized to the total radiance case. The faded line represent one standard deviation of the variability encountered across all input parameters. The top panel is for an instrument design and/or operation that compensates for changing signal levels with polarization and viewing geometry, and the bottom panel is for uncompensated measurements.

In Figure 4-8 the normalized co-variance cases were sorted by wavelength using all geometries and atmospheric states. These bins were then averaged for each wavelength shown with by the red and blue points for the horizontal and vertical polarization respectively. The fainted colours are one standard deviation from the mean. Each of the means in Figure 4-8 contains between 186 to

229 unique data points and values less than one represent co-variance better than the total radiance case and the opposite for values larger than one.

The resulting normalized co-variances have a substantial dependence on wavelength. The situation where the signal to noise ratio is compensated such that it is equal for all cases is shown in the top panel of Figure 4-8, where the vertical polarization has a smaller co-variance, i.e. better precision, by approximately 20% at the shorter wavelengths than the total radiance retrieval. As wavelength increases to 1500 nm, the precision of the vertical polarization case is approximately equal to that of the total radiance case. The horizontal polarization essentially mirrors the vertical case with higher co-variances than total radiance at short wavelengths and approximately equal at 1500 nm. Recall, however, that the vertical polarization has significantly lower magnitude signal levels and in order for the measurement to be compensated to obtain equal signal to noise levels, an increase in instrument sensitivity or exposure time would be required.

Table 4-2: The SSA dependence of the normalized co-variance for the horizontal and vertical polarization retrievals. The given numbers are the mean with the standard deviation for each geometry across all wavelengths. Note that the SSA of 90° for the vertical polarization has been removed due to the poor signal in this region.

Polarization	60°	90°	120°	150°	180°
Horizontal (Compensated)	1.072±0.051	1.090±0.082	1.047±0.078	1.027±0.048	1.023±0.042
Vertical (Compensated)	0.861±0.084	--	0.968±0.157	0.977±0.063	0.980±0.051
Horizontal (Uncompensated)	1.289±0.075	1.225±0.158	1.261±0.165	1.341±0.098	1.360±0.085
Vertical (Uncompensated)	1.576±0.167	--	1.852±0.559	1.527±0.170	1.490±0.130

Across the range of solar scattering angles, the vertical polarization has slightly lower covariance than the other two cases, except at 90 degrees, which is due to the lack of sensitivity in this region noted previously. Table 4-2 shows the calculated means and standard deviations across SSA for the horizontal and vertical polarizations, note the SSA of 90° is missing due to the poor signal, and retrieval quality noted in previous sections which results in poor co-variances for this

geometry. Furthermore, the variability of the result across all of the other input parameters increases dramatically as the scattering angle approaches 90 degrees. The precision of the retrieval shows very little dependence on the other input parameters such as solar zenith angle, albedo, particle size distribution, and extinction level. On average across all parameters, the retrieved co-variance from the vertical polarization is approximately 15% smaller than the horizontally polarized retrieval.

In the case of an uncompensated instrument, for example where a linear polarizer is added to the optical chain with no other changes in observation, the scaling of the diagonal of the measurement co-variance is used as outlined in section 4.3. Due to the larger magnitude of the signal in the horizontal polarization compared to the vertical polarization, the horizontal cases generally have lower retrieval co-variance, and this effect increases with longer wavelength as seen in the lower panel of Figure 4-8. Note that in this uncompensated case, since the linear polarizations are always some fraction of the total radiance, the co-variance is always larger than the total radiance case (i.e. the normalized co-variances are always greater than 1). Once again very little dependence on solar zenith angle, albedo, size distribution or extinction level was observed. There was also little dependence on solar scattering angle, except for vertical polarization at 90 degrees. On average across all parameters, vertical and horizontal polarizations have approximately a 60% and 30% larger uncertainty than the total radiance case, respectively.

This analysis shows that the main driver of retrieval precision is the signal to noise level of the observation, as would be expected. Again, this leads to instrument design and/or operational considerations in order to maintain retrieval precision at the same level as the total radiance measurement. A main scientific goal of both the ALI and ALTIUS instruments is obtaining high spatial resolution observations, both vertically and horizontally along, and across, the satellite

track. This generally means that images must be collected rapidly and long exposure times are not an affordable luxury. Once more, the relatively higher magnitude signal levels of the horizontal polarization point to this as the more appealing choice of orientation; however, compared to the total radiance case the decreased precision is exaggerated at shorter wavelengths.

4.5 Conclusions

We have attempted to address the question of whether or not the measurement of linearly polarized radiance rather than total limb radiance is an advantage or disadvantage with respect to retrievals of stratospheric aerosol. The sensitivity of the polarized limb radiance to aerosol is complex with respect to many parameters, and there are trade-offs in the orientation of the polarization and the orbital viewing geometry. One important point is the very low magnitude of signal observed in the vertical polarization for scattering angles near 90 degrees, which are encountered for a large fraction of observations in low earth orbit, particularly sun-synchronous near-terminator orbits such as for OSIRIS. More generally, it is important to consider the overall lower magnitude of the linearly polarized radiance, which by definition is a fraction of the total radiance. The horizontal polarization has, on average, higher signal levels than the vertical polarization. It also has a weaker dependence on solar scattering angle that is more similar to the total radiance than the vertical polarization, which is more strongly skewed in the forward scatter direction.

One critical bias in limb scatter retrievals of stratospheric aerosol is that due to uncertainty in particle size parameters. We tested four different particle size distribution scenarios, representing background and volcanically perturbed conditions, over a large range of other parameters such as wavelength, viewing geometry, and extinction level and found that there is no significant change in the observed bias for polarized or total radiance measurements. So, with respect to this bias, the polarized measurement is neither an advantage or a disadvantage.

The polarized measurement can have an effect on the precision of the retrieval, where again the main driver is the magnitude of the signal. The polarization can either increase or decrease the precision and there is an apparent trade-off between signal levels and performance of the vertical or horizontal polarization. This is mostly important at shorter wavelengths since at longer wavelengths the differences are negligible.

In conclusion, we have found no clear advantage to the linearly polarized measurement over the total radiance for aerosol retrievals; however, there are also no clear disadvantages assuming the somewhat lower overall signal levels can be handled in the instrument design or operation. With careful choice of the orientation of the measured polarization with respect to the orbital geometry and desired coverage, an instrument such as ALI or ALTIUS is fully capable of obtaining retrieved aerosol products of very similar quality to an equivalent instrument that measures the total radiance.

CHAPTER 5

STRATOSPHERIC BALLOON FLIGHT AND AEROSOL RETRIVALS

5.1 Stratospheric Balloon Flight

After the completion of the ALI system tests on August 18, 2014, the instrument was transported to Timmins, Ontario and preparations were underway for the balloon launch from August 25, 2014 until September 18, 2014. During this balloon campaign, there were seven balloon launches with ALI being a part of the seventh balloon. The flight of ALI took place on September 19, 2014.

5.1.1 Preflight Preparations

The Canadian Space Agency (CSA) balloon launch facility in Timmins, Ontario is located at the Victor M. Power Airport (48.47°N 81.33°W). ALI arrived at the base on August 25, 2014 with a launch window from September 8 to 14, 2014. In between the arrival of ALI and the balloon launch, ALI had to be verified to have survived transportation, a seal within the CCD needed to be removed, thermal insulation needed to be added, and finally, ALI needed to be integrated onto the Centre National d'Etudes Spatiales (CNES) CARMEN-2 gondola.

ALI was unpacked and set up on a test bench at the launch facility. A visual inspection occurred to verify that no obvious damage occurred to the instrument during transportation. Once completed, ALI was connected to its electronics and power boxes and was powered on. A ground station computer was used to connect to ALI and perform a system check, including verification of automated startup, establishment of telemetry connection, ensuring that the system powered on correctly with no errors and that the science operation program functioned. With this test it was verified that no functional problems occurred to the device during transportation, and all

temperature and voltage sensors, GPS module, and CCD camera were reporting valid diagnostic values.

Once the ALI system was verified to be operational, an imaging check was performed to check that no optical components suffered damage or slippage during transportation. An EIA 1956 resolution target was illuminated by a 250 W tungsten halogen light source and was imaged by ALI to verify the optical layout. The recorded images were very similar to the ones taken in the laboratory before leaving Saskatoon.

Following the successful test of ALI, final preparations were needed prior to beginning integration with CARMEN-2. First, the CCD used by ALI had a sealed chamber that was in a vacuum state designed to be at atmospheric pressure and would be required to be unsealed before the flight. The unsealing is done in order to not develop a strong pressure gradient between the CCD chamber and the low pressure of a 35 km environment which could cause permanent catastrophic damage to the CCD detector. At the launch facility, ALI was taken to a semi-clean area to unseal the CCD chamber. A panel was removed on the side of the camera and the seal to be removed can be seen in Figure 5-1. The orange o-ring was removed with associated sealing components and the vacuum seal was broken. The chamber panel was replaced and ALI was moved back to the integration hall and another set of test resolution targets were taken to verify the correct operation of ALI. All resolution targets were similar with the set before the chamber was unsealed except there was approximately a 5% drop in counts which may have been caused by unsealing the chamber or a change in the lighting conditions of the resolution target.



Figure 5-1: Side of the QSI CCD with the panel that contains the vacuum seal opened. The orange o-ring seen in the cavity is removed from the chamber to open the vacuum seal to the camera's CCD chip.

The next step before ALI could be integrated was to add thermal shielding in order to protect ALI from the thermal environment at approximately 35 km. The first thermal concern was the instrument temperature falling to a point where the electronics were too cold to function. The instrument would have to be in complete darkness during the ascent which would result in little to no solar heating. Furthermore, ALI will pass through the tropopause where temperatures can be as cold as -70°C. Insulation, in the form of foam, was added around the exterior of the instrument to give ALI thermal isolation from the cold environment. The second concern was once CARMEN-2 was at float altitude, ALI would have to be able to survive the direct heating from the sun's radiation which could cause overheating. The impact of the sun's energy was reduced on ALI by

adding a thermal reflector to the outside of the thermal insulation which would reflect a portion of the incoming solar radiation away from ALI.

With the completion of the thermal management, ALI was ready to be mounted onto the CARMEN-2 gondola. ALI can be seen mounted on the CARMEN-2 gondola in Figure 5-2 and ALI used the power and communication subsystems of CARMEN-2. Testing was performed with collaboration from the CARMEN-2 team to verify that there were no issues between ALI and CARMEN-2's systems. A problem was found in the communication module, named Siren, between ALI and the ground station computer. With assistance from the CARMEN-2 team, the correct Ethernet settings were determined and a patch to the ALI operation code was applied.

During the integration phase, it should be noted that several instruments were also being verified with the CARMEN-2 systems alongside ALI for integration onto the gondola including four other Canadian instruments, such as the OSRIS development model (*Kozun, 2015; Taylor, 2015*) and SHOW which measures water vapour.

The CNES gondola is an actively pointed gondola with azimuthal pointing precision better than $1'$ with the use of an onboard star tracker. ALI was orientated so it would be maintained at 90° from the azimuthal direction of the sun, with an overall southern field of view during the mission.



Figure 5-2: The ALI instrument is mounted on board the CARMEN-2 gondola (top shelf on the right). ALI located next to SHOW, another Canadian instrument with collaboration between ABB, York University, and the University of Saskatchewan. ALI has its red tag cover over the optical entrance to protect the instrument from dust and other contaminates. Thermal insulation has been added to the instrument and during the flight sun side will be on the side of SHOW. Some of the reflective layer was blacked out to not cause additional stray light into SHOW optical path.

5.1.2 Balloon Flight

The flight plan for the CARMEN-2 gondola was once float altitude was reached and the sun had risen ALI, OSIRIS, and SHOW would perform their operational missions for the first four hours of the campaign. The operational objectives for ALI included a dark imaging suite for calibration purposes and an aerosol imaging suite for aerosol measurements. A secondary goal was to test the sensitivity to aerosol of ALI with respect to SSA by recording images at various azimuth directions as well as attempt an O₂ and water vapour imaging suite. After the end of the ALI mission, the instrument was to be powered off and other instruments on CARMEN-2 were to gather measurements.

The flight of CARMEN-2 was delayed past its launch window of September 8 to 14, 2014 due to poor weather conditions. On September 19, 2014 at 05:35 UTC (01:35 local time) ALI was launched as part of the Nimbus 7 mission from the CSA Timmins balloon launch facility. During the launch, the sky was clear with light winds allowing for a safe and uneventful launch. The ascent of the gondola occurred in darkness and reached its flight altitude of 36.5 km at 8:17 UTC. First light was observed by ALI at 9:39 UTC and spectral images were recorded until 14:42 UTC. ALI was powered off at 17:15 UTC.

A visualization of the flight path with major landmarks noted can be found in Figure 5-3a. Temperature profiles for the ambient atmosphere and instrument are shown in Figure 5-3b. The black curve is the ambient atmospheric temperature at the gondola altitude and location during the flight as obtained from ECMWF reanalysis (*Dee et al.*, 2011). The blue, green, and red are from temperature sensors onboard ALI located on the baffle, camera, and RF driver respectively. The baffle temperature sensor was attached just on the inside of ALI right by the entrance aperture for the system and monitors the temperature at the front of the system. The camera sensor is attached to the back of the CCD camera and the RF driver sensors measures the surface temperature of the RF driver. ALI was thermally insulated to keep the system warm whereas the baffle temperature sensor is relatively uninsulated from the extreme cold of the tropopause. The effect of the cold tropopause can be seen on the gondola at approximately 6:00 UTC. The cooling effect can even be seen on the interior CCD and RF driver sensors which are isolated from the exterior temperature. After the internal temperature drop, the system reaches an equilibrium temperature until the sun rises and solar radiation comes into contact on the instrument at approximately 10:00 UTC at which point there is an increase in the system's temperature. The temperature of the system are kept within operating range with the aid of the reflective material during the flight.

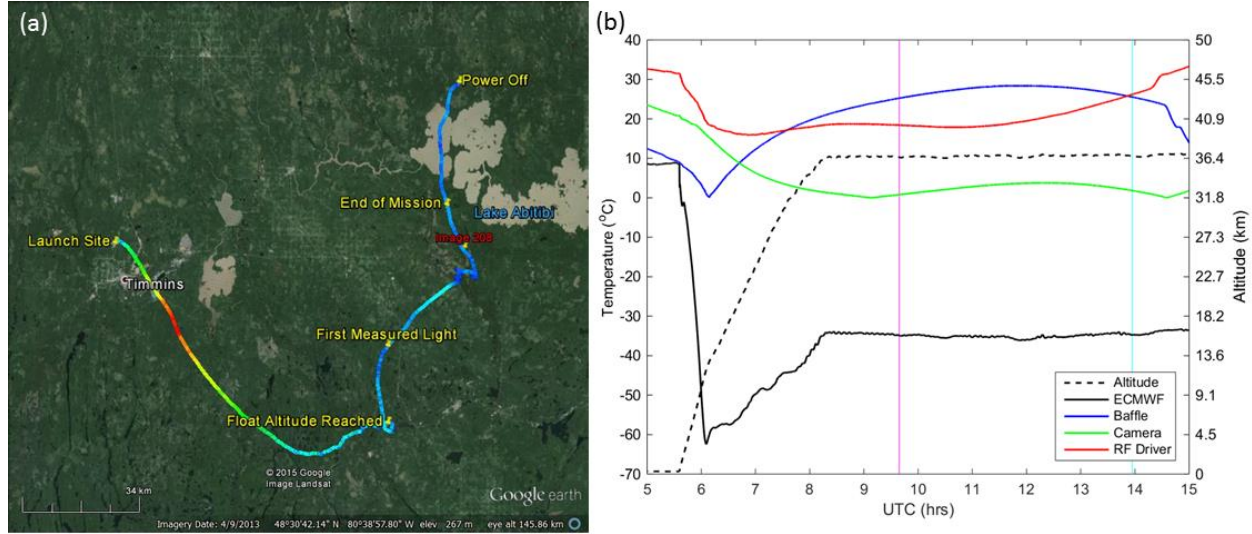


Figure 5-3: (a) The GPS data from ALI during the Nimbus 7 mission generated via Google Earth. The colour of the line represents the absolute speed of the gondola during the mission and the blue, green, red colours represent speeds of approximately 10, 70, and 140 km/h.. Important landmarks are noted on the image. The end of mission represents the end of the primary aerosol mission. No GPS data was collected from ALI after power down. The location of image 208 is the red label. (b) The temperature and altitude profiles from the Nimbus 7 flight. The time of image 208 is shown by the cyan vertical line and first light measured by ALI occurs at the magenta vertical line.

During the mission, ALI operated in two primary acquisition modes, a calibration mode and an aerosol imaging mode. The first mode, the calibration mode, was primarily used during ascent when the gondola was in darkness and intermittently between the aerosol mode during sunlit conditions. During this mode, the filtering of the AOTF was not enabled and the system imaged essentially only dark current during the ascent in darkness and stray light during sunlit conditions. Eight exposures are taken in the calibration mode with 0.05, 0.1, 0.5, 1, 2, 3, 5, 10 second exposure times.

The second operational mode, the aerosol mode, recorded measurements in a cycle that contained 13 pairs of images across the spectral range (650-950 nm every 25 nm), the pairs being a calibration image with the “AOTF-off” and an image of the limb. Each cycle took approximately 10 minutes with each measurement set taking approximately 40 seconds to acquire with initial exposure times shown in Figure 5-4 in blue, which were the exposure times determined during the

roof testing of ALI (see section 3.6.1). However, during the flight it was determined that the calculated exposure times were not long enough and the images were underexposed. The underexposure is believed to be caused by the initial exposure time calibration curves being calculated with simulated scalar radiance since the SASKTRAN-HR polarization module had not yet completed development. So the exposure time curve was recalibrated during the flight using the image statics that were sent down with the house keeping. A comparison of the two exposure time curves with the percent increase can be seen in Figure 5-4. The percent increase is given by

$$\text{Percent Difference} = \frac{t_c - t_u}{t_c} * 100\%, \quad (5.1)$$

where t_c is the exposure time for the original calibration and t_u are the updated exposure times calculated from the flight.

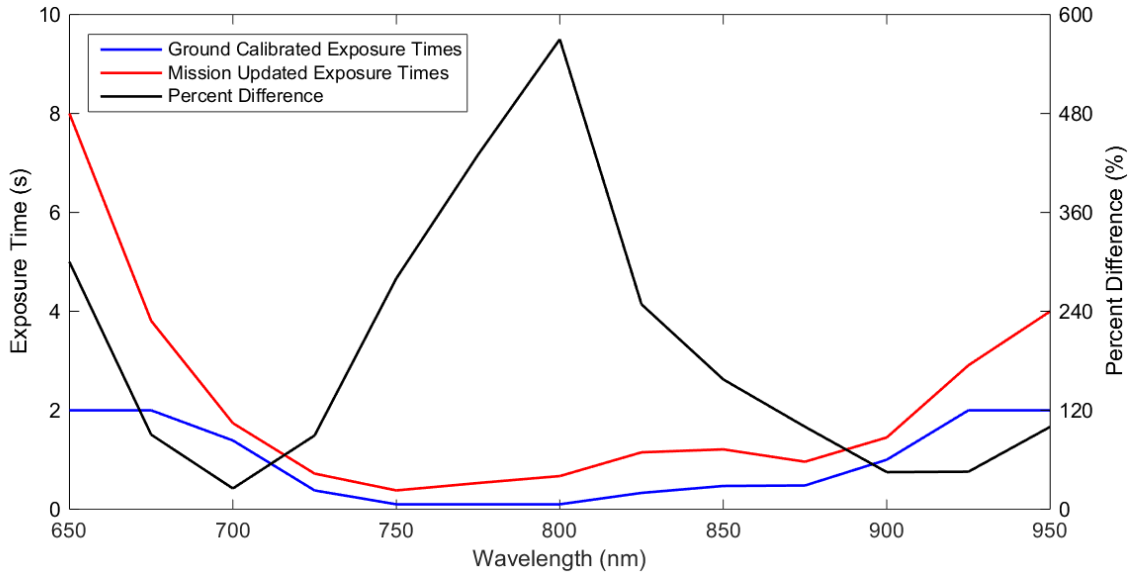


Figure 5-4: During the flight the calibrated exposure times was updated. The blue curve represents the exposure times from the ground calibration and the red curve is the recalibration during the flight. The black curve is the percent change in between the pre-flight calibrated results and the during flight calibration.

The Nimbus 7 flight lasted for 16 hours 19 minutes with a successful landing at 21:54 UTC. During the flight, ALI successfully gathered 216 aerosol images. The gondola landed 70 km from

Amos, Quebec or approximately 250 km from the launch facility. CARMEN-2 was recovered by the balloon recovery team and was returned to base on September 21, 2015. ALI was removed from the gondola, repacked and transported back to Saskatoon, Saskatchewan where the measurements could be verified and processed.

5.2 Limb Measurements

After the successful post-flight recovery, ALI was unpacked and checked for any damages in Saskatoon, SK on September 25, 2014. No obvious damage had occurred to ALI from the flight and the instrument was functioning correctly. 216 raw aerosol mode image pairs were obtained from the flight and calibration was performed including pointing alignment and the calibrations as detailed in section 3.3.

The images needed to have complete pointing information added since the raw images only had position and altitude information from the onboard GPS. The azimuth and zenith directional information needed to be added to the images as they are needed to determine the line of sight of each pixel on the CCD. The CNES team supplied the Solar Azimuth Angle (SAA) information from the flight and was correlated to the images using GPS time. However, no information was supplied about the zenith direction of the gondola, we were just notified that the gondola was zenithally stable throughout the majority of the flight. So some manual calibration of the zenith angle occurred. ALI was tilted at 3° so the zenith was assumed to be 93° for ALI. This starting guess and was not accurate enough since features in the radiance profiles did not retain the same altitude over the course of a few images. To determine a more precise zenith angle, the zenith angle was varied from 92° to 94° in 0.1° intervals and the tangent altitude was calculated for each case. Then the radiance profiles for each zenith angle was compared to find zeniths where the features were aligned. The zenith angle with the optimal alignment was determined to be 92.6° with an uncertainty of 0.1° .

The calibration techniques discussed in section 3.3 were then applied to the raw images to find the final radiances. As an example, image number 208 is used to demonstrate the steps in the calibration on a flight image. Image 208 is recorded with a wavelength of 750 nm and taken at 13:57 UTC with a SZA and SSA of 63° and 98° respectively. The dark current and DC offset have been removed from image 208 using the Equation 3.42. Next, the stray light is removed by using the “AOTF-off” or calibration image and removing it from the “AOTF-on” or measurement image. The result of this procedure can be seen in Figure 5-5. In the first panel, abnormal bright spots are noticed in the right side and the top right of the measurement. These same features are noticed in the stray light image. By subtracting the AOTF-off image from the measurement image, a final smooth measurement image is seen. Finally, a flat fielding calibration is performed (see section 3.6.5) and a final calibrated image can be seen in Figure 5-6a. Remember that no absolute calibration was performed on ALI, so the radiance are relative radiance in arbitrary units to the 775 nm laboratory calibration. The error, ϵ , on a given pixel for the radiance measurements were given by

$$\epsilon^2 = \epsilon_{read}^2 + \epsilon_{DC}^2 + \epsilon_{dark}^2 + \epsilon_{stray}^2 + \epsilon_{ff}^2, \quad (5.2)$$

where ϵ_{read} is the readout uncertainty from the CCD, which is 15 counts at worst, ϵ_{DC} is the error in the DC offset calibration, ϵ_{dark} is the error from the dark current in the CCD, ϵ_{stray} is the error in the stray light calibration, and ϵ_{ff} is the error in the flat field corrections.

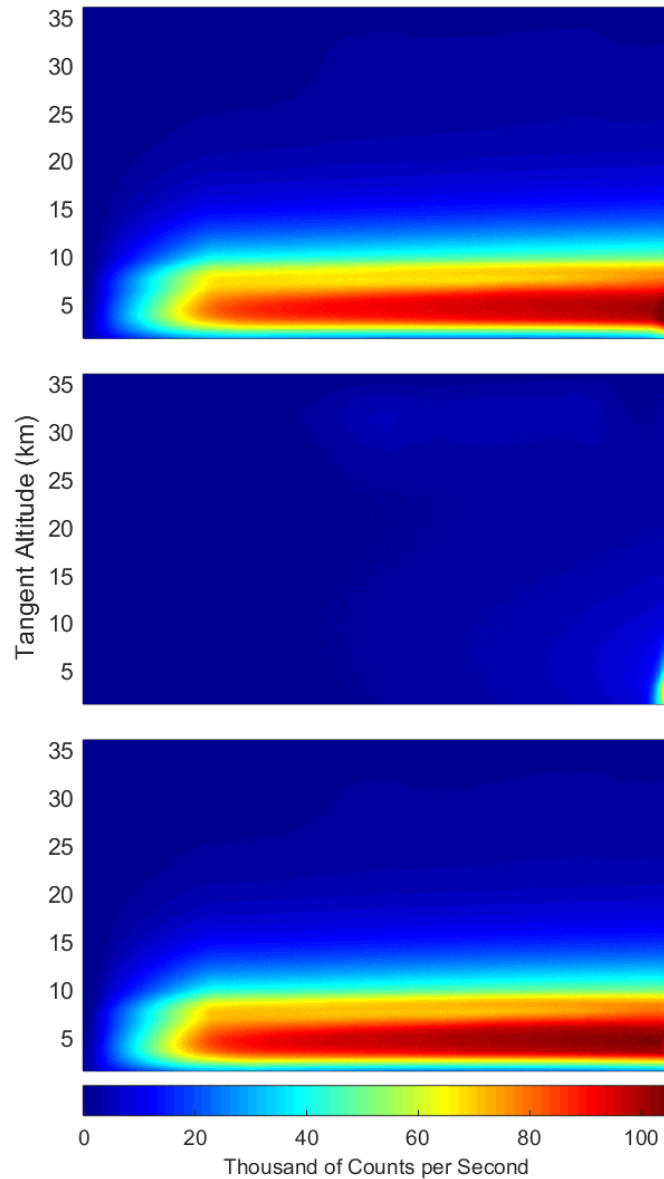


Figure 5-5: Stray light removal technique is performed using image 208 which is a 750 nm measurement. The top panel is the image after the DC offset has been removed from the measurement. The middle panel is the associated AOTF-off image and stray light features are seen in the upper right of the image as well as light being registered in the entire right side of the image. The final panel is the first panel minus the second panel and the abnormal gradient has been removed from the final image, leaving a cleaner radiance profile.

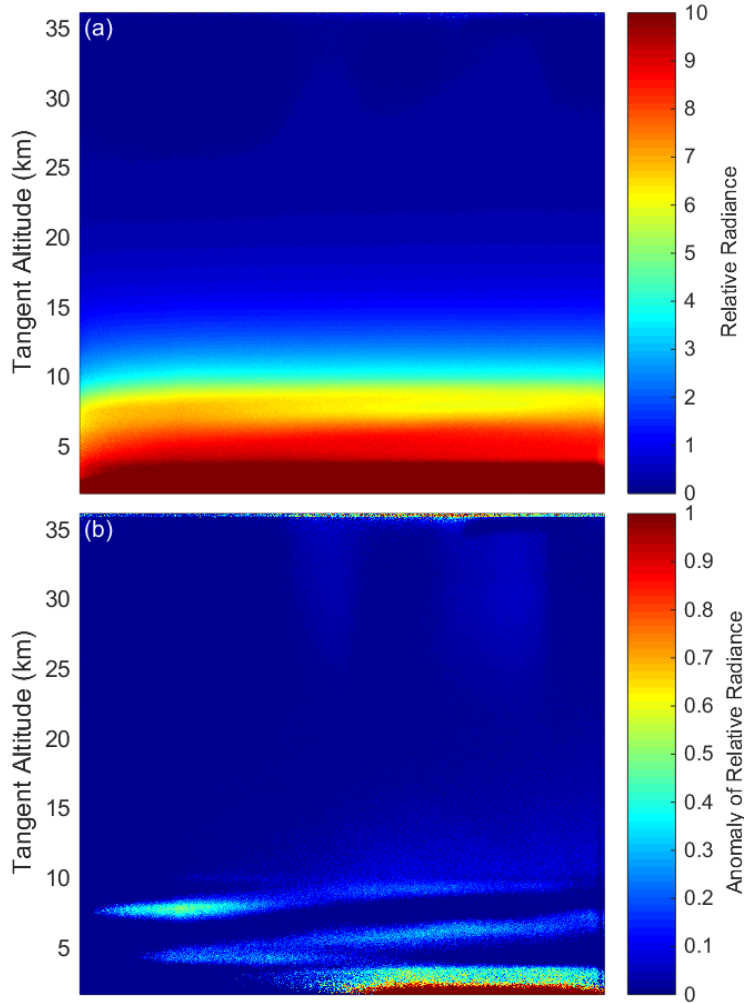


Figure 5-6: (a) Final calibrated 750 nm image, taken at 13:57 UTC located at 48.55°N , 80.00°W with a SZA and SSA of 63° and 98° respectively. (b) The same 750 nm image with the mean of the profile removed from the image leaving the residual signal that shows thin clouds in the troposphere.

From image 208, the horizontal structure across the image is nicely revealed by calculating the mean radiance profile across the image and then removing it from each profile. This is shown in Figure 5-6b, where thin clouds (2 km vertical extent or less) are clearly seen near and below the tropopause level, with substantial variation in tangent altitude across the horizontal field of view. These clouds were also observed from other instruments on board the gondola during the mission (B. Solheim, private communication, 2014). A brief check on the CALIPSO quick-look plots also

shows clouds at a maximum height of approximately 13 km from measurements taken at 08:40 UTC at 47.24°N, 95.25°W, the nearest measurement point to the ALI location and time. Although these images only have a 35 km extent in the horizontal direction, there is also some indication of horizontal variation in radiance significantly above the cloud level, possibly due to real atmospheric variability in the aerosol layer. It should also be noted that some high altitude stray light is also visible in this mean residual image that was not observed in the laboratory tests. For the high altitudes in the range of 27 to 20 km the expected ratio of signal to stray light was estimated to be inbetween 2-3 but for the campaign the ratio of signal to stray light for some regions dropped down to slightly below one. This may be due to contamination from scattering from a baffle vein or a nearby component of the gondola, although the true cause is unknown at this point.

For ease of further analysis, and to increase the precision of the measurements to a minimum of 0.6 MTF, the images were averaged into cells of 25 pixels horizontally and averaged vertically onto a 1 km tangent altitude grid. The errors for the averaged radiances, E , is given by

$$E = \left(\frac{1}{(N-n)(M-m)} \sum_{i=n}^N \sum_{j=m}^M (\epsilon_{i,j})^2 \right)^{\frac{1}{2}}, \quad (5.3)$$

where the errors for each pixel, $\epsilon_{i,j}$, are summed in vertical, i , and horizontal, j , directions from the starting pixel, n for the vertical and m for the horizontal, to the final pixel in the average, N for the vertical and M for the horizontal. The radiance profiles from the center column of the images for all measurements obtained during the flight are shown in Figure 5-7. The first set of profiles, the dashed lines, which start near zero and move toward larger values, are the measurements that were recorded near and during sunrise so the gradual increase is therefore expected. Measurements obtained for SZAs less than 90° are represented by the solid lines. These

radiance profiles follow a similar and expected exponential shape, with some variability at tangent altitudes below 12 km corresponding largely to changing cloud conditions.

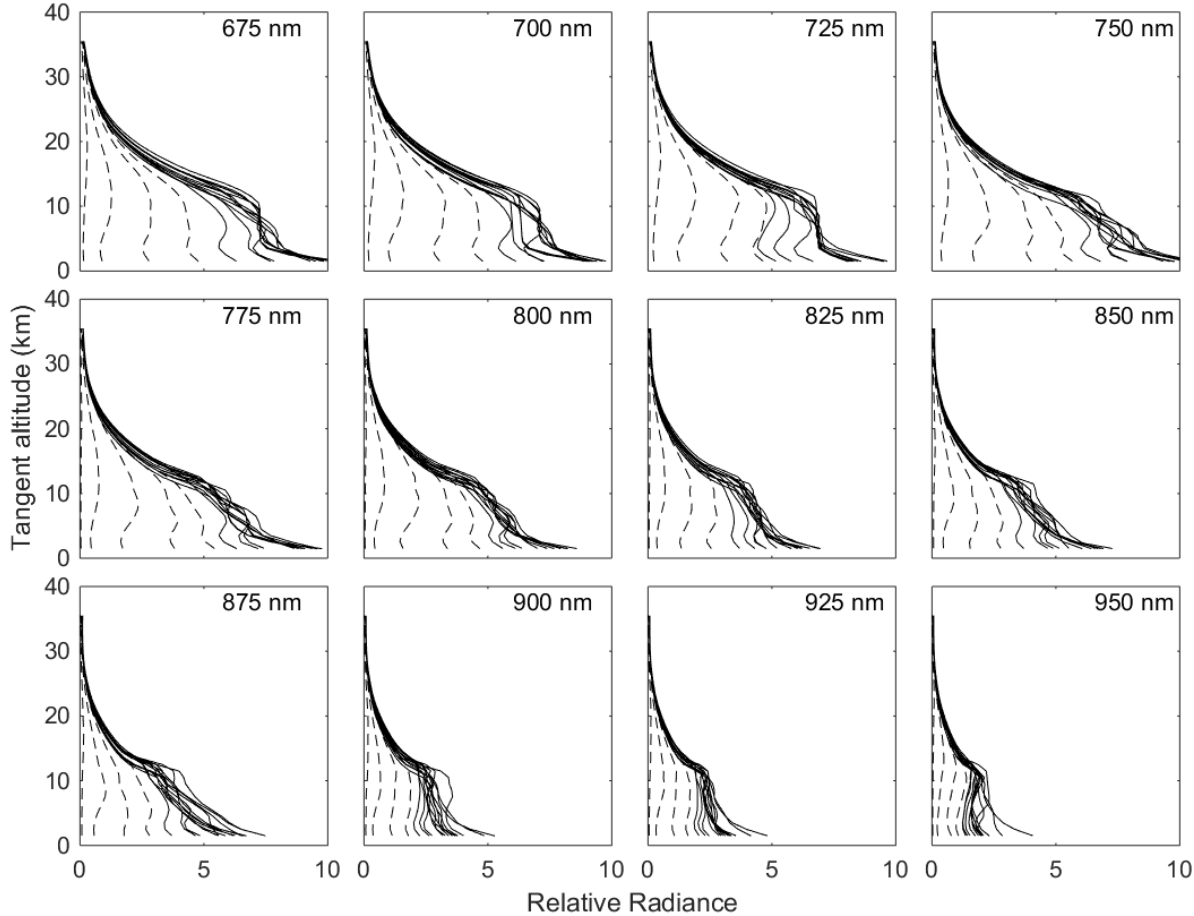


Figure 5-7: Averaged ALI relative radiance vectors from 12 of the 13 wavelengths from the Nimbus 7 flight. Each panel presents the radiance vectors from a different wavelength measured which is denoted in the top right corner. The dashed lines are radiance profiles where the SZA is greater than 90° and solid lines are profile where the SZA is less than 90° .

A full cycle of 13 spectral images (numbers 204-216) were used in Figure 5-8 to show the spectrum of relative calibrated radiances at selected tangent altitudes. The estimated uncertainty in the radiance is represented by the shading and was calculated using Equations 5.2 and 5.3. The uncertainty is approximately five percent from 5 to 20 km and increases up to eight percent from 20 to 35 km. The spectra displays the expected and relatively smooth fall off in intensity with

increasing wavelength with Chappuis ozone absorption seen at the lower wavelengths; however, the reason for the peak in the spectra at 875 nm is not known and may be due to an inconsistency in the pre-flight calibration.

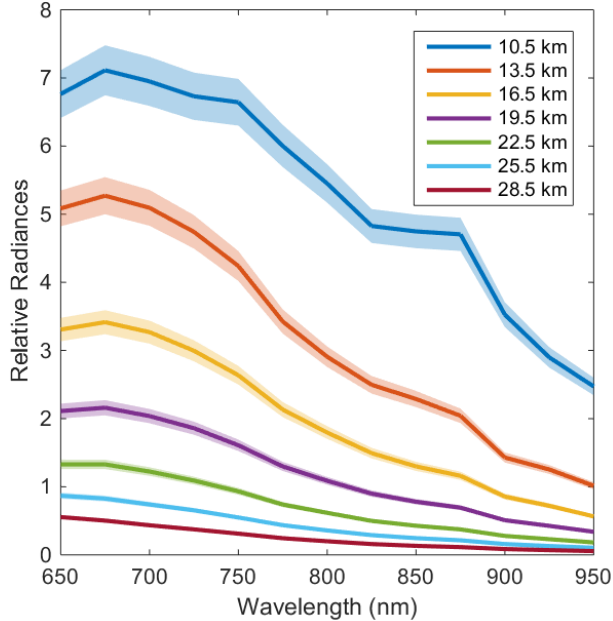


Figure 5-8: Relative radiances spectrally from 650 nm to 950 nm as measured from ALI at approximately 14:20 UTC consisting of images number 204 to 216 looking 90° in the azimuth from the sun facing southwards. These spectral profiles are presented at several tangent altitudes with a horizontal look direction of 0°. The shading represents the error on the radiances.

5.3 Aerosol Retrievals

From the successful mission, radiance measurements from ALI needed to be used to determine aerosol parameters. The following sections will describe the Multiplicative Algebraic Reconstruction Technique (MART) retrieval method used to determine aerosol. The retrieved aerosol profile from ALI using the MART method will be presented and will be compared to the OSIRIS version 5.07 aerosol extinction product. Following, a cycle of aerosol measurements will be used to determine a particle size distribution estimate and will be contrasted with particle size parameters from other instruments.

5.3.1 Aerosol Extinction Retrieval Methodology

A measurement inversion technique is a method used on a measured value and can be converted into a wanted usable physical quantity via an iterative method. A measurement vector, \mathbf{y} , is constructed that has sensitivity to a desired physical state and is computed with a forward model, \mathbf{F} , with an input state, \mathbf{b} , and a wanted physical parameter, \mathbf{x} . The measurement vector is then calculated with the model and is yielded by

$$\mathbf{y} = \mathbf{F}(\mathbf{x}, \mathbf{b}) + \boldsymbol{\epsilon}, \quad (5.4)$$

where $\boldsymbol{\epsilon}$ is the noise on the measurement vector.

The inversion of the ALI radiances used a Multiplicative Algebraic Reconstruction Technique (MART), specifically we have applied a slightly modified version of the standard OSIRIS stratospheric aerosol extinction retrieval (*Bourassa et al.*, 2007; 2012b). This inversion algorithm, which is applied from the tropopause to 30 km altitude, assumes log-normal distributed hydrated sulphuric acid droplets (see Equation 2.1) in order to calculate the aerosol scattering cross section from the Mie scattering solution. The modeled radiances for the nonlinear inversion were computed with the SASKTRAN-HR radiative transfer engine using the newly developed vector module for polarization (*Bourassa et al.*, 2008; *Zawada et al.*, 2015; *Dueck et al.*, 2016). The output of SASKTRAN-HR gives the Stokes vectors for the radiance in the model reference frame, which are then rotated into the instrument's coordinate system (see section 2.4.5). Once rotated, the polarization signal required to match the ALI measurement is the vertical polarization given by

$$I_v = \frac{1}{2}(I - Q), \quad (5.5)$$

where I and Q are Stokes parameters defined by $I = \langle E_x^2 \rangle + \langle E_y^2 \rangle$ and $Q = \langle E_x^2 \rangle - \langle E_y^2 \rangle$. The variables E_x and E_y are the horizontal and vertical component of the electric field in the instrument reference frame.

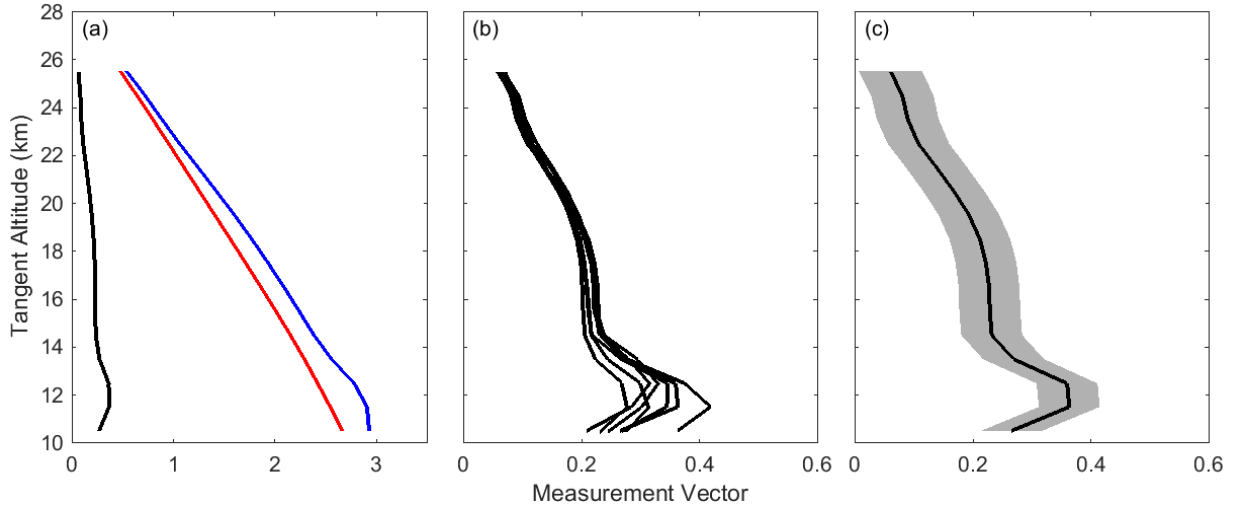


Figure 5-9: (a) The black, blue, red curves represent the measurement vector, first term of Equation 5.6, and second term of Equation 5.6 using image 208 (b) A collection of all of the measurement vectors at 750 nm during the mission with a SZA greater than 90°. (c) Image 208 measurement vector with associated error represented by the shading.

The relative radiance measurements from ALI are used to create measurement vectors, \mathbf{y} , as specified in *Bourassa et al.* (2012b) in the form,

$$\mathbf{y} = \log\left(\frac{\mathbf{I}_v(\mathbf{z}, \lambda)}{I_v(z_{ref}, \lambda)}\right) - \log\left(\frac{\mathbf{I}_{v,ray}(\mathbf{z}, \lambda)}{I_{v,ray}(z_{ref}, \lambda)}\right), \quad (5.6)$$

where $\mathbf{I}_v(\mathbf{z}, \lambda)$ is the measured relative radiance from ALI and $I_v(z_{ref}, \lambda)$ is the relative radiance at a high reference tangent altitude where there is little aerosol contribution. For the ALI measurements, the highest possible tangent altitude where the signal is above the noise threshold is approximately 30 km tangent height and typical values for z_{ref} were between 27 and 30 km. The second term in Equation 5.6 uses modeled radiances from SASKTRAN-HR with only the molecular atmosphere to approximately remove the Rayleigh signal. This is done to improve the speed of the convergence of the retrieval (*Bourassa et al.*, 2012b). Figure 5-9a shows the

measurement vector from a 750 nm image (number 208) from the center of the CCD. The final measurement vector, \mathbf{y} , is shown in the black, with the first term of Equation 5.6 in blue and the second term in red. Removing the Rayleigh component of the signal from the measurement vector increases the sensitivity to aerosol which increases the speed of convergence of the solution. All of the measurement vectors for the 750 nm images from the mission can be seen in Figure 5-9b.

An initial guess state, \mathbf{x} , for the aerosol extinction and an assumed particle size distribution profile are set in the SASKTRAN-HR model. The forward model vector is then constructed similarly to the measurement vector, and used in combination with the measurement vector to update the aerosol extinction coefficient profile using the MART algorithm,

$$x_i^{n+1} = x_i^n \sum_j \frac{y_j}{F(z_j)} W_{ij} \quad (5.7)$$

where x_i is the aerosol extinction at each model altitude, i and j denotes a tangent altitude from the measurements. W_{ij} is the weighting matrix that relates the importance of each element of the measurement vector to each shell altitude. It should be noted that this inversion technique is computationally efficient as it allows for the updating of the atmospheric state without calculating the Jacobian (Degenstein *et al.*, 2009). This iterative process is run until the solution has converged and the value of the summation is approximately one and the final aerosol state is determined.

In order to determine the precision on the retrieved aerosol profiles, an error estimate on the measurement vector is performed. To yield the error on the measurement vector at a specific tangent altitude, j , Equation 5.6 is differentiated and summed in quadrature yielding the following result

$$\delta y_j^2 = \left(\frac{\delta I_v(z_j, \lambda)}{I_v(z_j, \lambda)} \right)^2 + \left(\frac{\delta I_v(z_{ref}, \lambda)}{I_v(z_{ref}, \lambda)} \right)^2 + \left(\frac{\delta I_{v,ray}(z_j, \lambda)}{I_{v,ray}(z_j, \lambda)} \right)^2 + \left(\frac{\delta I_{v,ray}(z_{ref}, \lambda)}{I_{v,ray}(z_{ref}, \lambda)} \right)^2. \quad (5.8)$$

However, the only error that is considered is due to the instrument measurement and calibrations, inaccuracies in the SASKTRAN-HR model are ignored. Since the Rayleigh components are modeled, they are dropped from the error, simplifying the above result to

$$\delta y_j^2 = \left(\frac{\delta I_v(z_j, \lambda)}{I_v(z_j, \lambda)} \right)^2 + \left(\frac{\delta I_v(z_{ref}, \lambda)}{I_v(z_{ref}, \lambda)} \right)^2 \quad (5.9)$$

An example of the error on a measurement vector for image 208 is located on Figure 5-9c.

The error on the measurement vector is used to determine the error on the retrieved aerosol profile. Once a retrieval has been completed for a measured radiance profile, the result is then used to estimate the error in the retrieved extinction. For each altitude, a gain matrix is defined as

$$\mathbf{G} = \frac{d\mathbf{x}}{d\mathbf{y}} \quad (5.10)$$

where $d\mathbf{x}$ is the change in the retrieved aerosol extinction and $d\mathbf{y}$ is the change in the measurement vector. The gain matrix is calculated through successive numerical perturbation of the measurement vector and re-retrieval (*Rodgers*, 2000). A much faster method to use the Jacobian to determine the uncertainty has been performed (*Bourassa et al.*, 2012a), as used in the analysis for chapter 4, but makes an assumption that the gain matrix is equal to the inverse of the Jacobian, as typically the averaging kernel is close to the identity matrix. However, this method adds additional uncertainty to the error estimate and was deemed unsuitable for the balloon campaign. Instead, with a limited set of balloon data, it is feasible to calculate the gain matrix directly. The error at each retrieved altitude is then given by

$$\mathbf{E} = \mathbf{G}\mathbf{S}_\epsilon\mathbf{G}^T \quad (5.11)$$

where \mathbf{S}_ϵ is the covariance matrix of the measurement vector and \mathbf{E} is the covariance of the retrieved aerosol profile (*Rodgers*, 2000). The covariance matrix is given by

$$\mathbf{S}_\epsilon = \begin{pmatrix} S_{11} & S_{12} & \cdots & S_{1n} \\ S_{21} & S_{22} & \cdots & S_{2n} \\ \vdots & \vdots & \ddots & \vdots \\ S_{m1} & S_{m2} & \cdots & S_{mn} \end{pmatrix} \quad (5.12)$$

where the individual terms are given by

$$S_{\epsilon,ij} = \begin{cases} \left(\frac{\delta I_\nu(z_j, \lambda)}{I_\nu(z_j, \lambda)} \right)^2 + \left(\frac{\delta I_\nu(z_{ref}, \lambda)}{I_\nu(z_{ref}, \lambda)} \right)^2 & i = j \\ \left(\frac{\delta I_\nu(z_{ref}, \lambda)}{I_\nu(z_{ref}, \lambda)} \right)^2 & i \neq j. \end{cases} \quad (5.13)$$

The reported precision for ALI aerosol extinction retrievals is the square root of the diagonal of \mathbf{E} .

Ideally, the ALI measurements would be used independently to also retrieve ozone in the Chappuis band (600-700 nm range for ALI). However, due to the spectral range of the prototype, only a small fraction of the long wavelength side of the absorption band was captured. For this analysis, we have not retrieved the ozone profile but have set the ozone profile in SASKTRAN-HR to an average of the five closest coincident ozone profiles measured by OSIRIS at the ALI location and time. The ozone cross sections were determined by *Burrows et al.* (1999). The surface albedo used is also from the OSIRIS scans since the two instruments share a similar measurement method and should determine a similar albedo for the cloudy conditions. Preferably, albedo would be determined from ALI following the method of *Bourassa et al.*, 2012b, however due to the lack of an absolute calibration this was not possible.

5.3.2 Aerosol Extinction Retrievals

The complete mission consisted of 216 images that were recorded in illuminated conditions. The MART retrieval method was run on a select complete cycle for the purpose of the analysis, specifically the set of images from 650 to 950 nm consisting of images 204-216. For the purpose of the retrieval an *a priori* for particle size distribution was used with a mode radius of 0.08 μm

and a mode width of 1.6 (*Thomason*, 1991). A sample of the retrievals can be observed in Figure **5-10** which highlights the 750, 850, and 950 nm retrievals. The left panels show the measurement vector from ALI in black with the forward model radiance profile from SASKTRAN-HR in blue. For each of the wavelengths, the algorithm determines altitudes where the value of the measurement vector is less than the known noise and does not allow aerosol to be retrieved in those regions. Instead, the scaling factor, α , given by the summation term in Equation 5.7 is scaled to the aerosol profile above and below the last retrieved point to keep the aerosol profile smooth, as discontinuities are nonphysical and can lead to a nonphysical result in the MART algorithm. The middle panel shows the convergence between the measurement vector and the forward model result. The right column of Figure 5-10 is the received aerosol profiles in blue with the associated error calculated using the method described in the previous section.

The retrieved aerosol extinction profiles for the analysis cycle can be seen in the left panel of Figure 5-11, note the log scale. For the full range of wavelengths, a difference of less than 2% between the measurement vector and forward model is seen throughout the retrieval altitude from approximately 13 to 29 km. Note the behavior of decreasing extinction with increasing wavelength as expected due to the dependence of the cross section with respect to particle size.

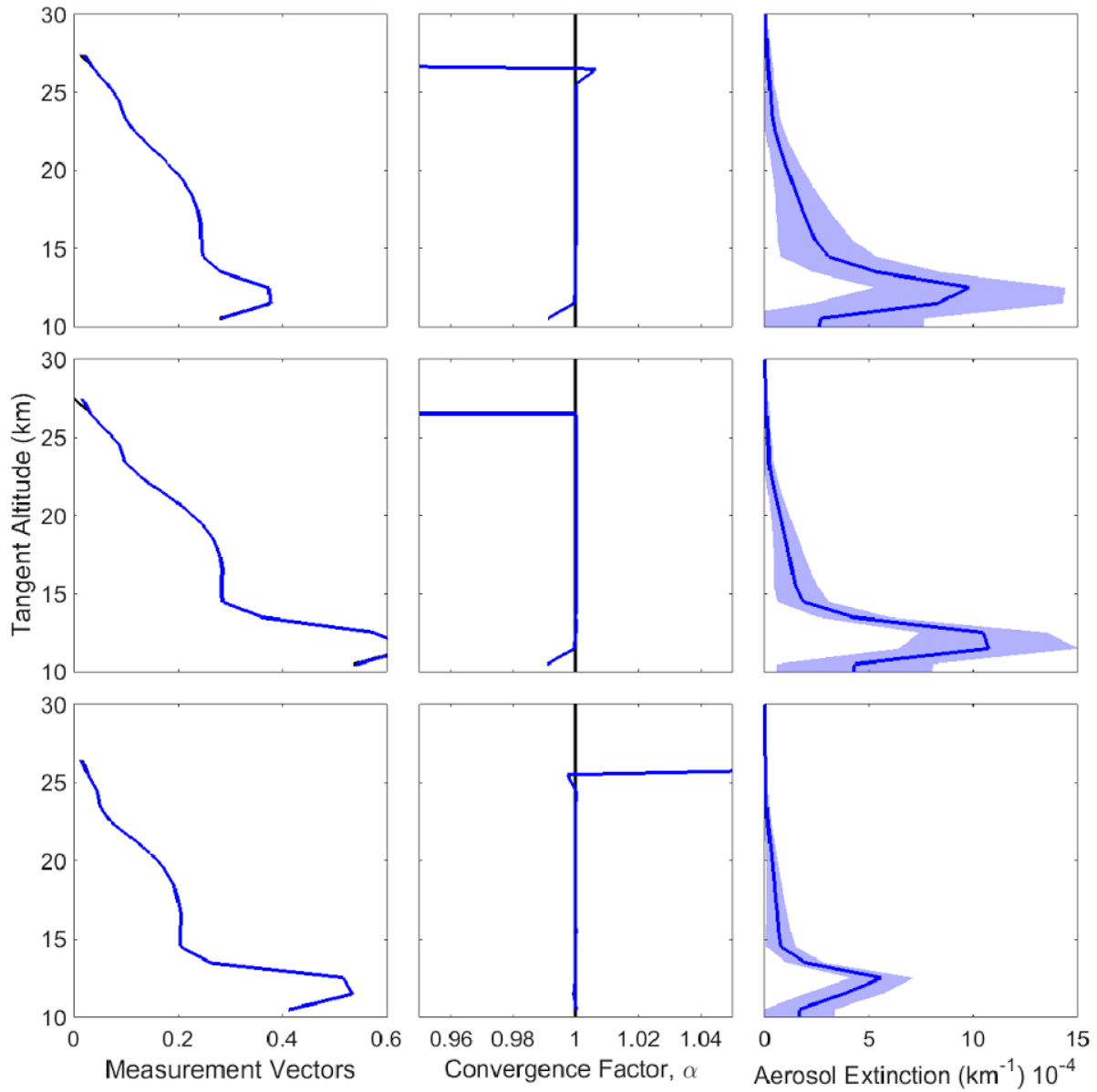


Figure 5-10: An example of three aerosol retrievals from images 206, 208, and 214, with center wavelengths of 750, 850, and 950 nm respectively are vertically displayed in the figure from top to bottom. The left column shows the measurement vector, \mathbf{y} , in black with the retrieved forward model, \mathbf{F} , in blue. The center column shows the ratio of the measurement vector over forward model known as α and is the convergence factor between the ALI measurement and the forward model. For both of the first two columns, the black line is barely viable due to the very good agreement of the forward model. The final column is ALI aerosol extinction in blue with the associated error represented by the light blue shading.

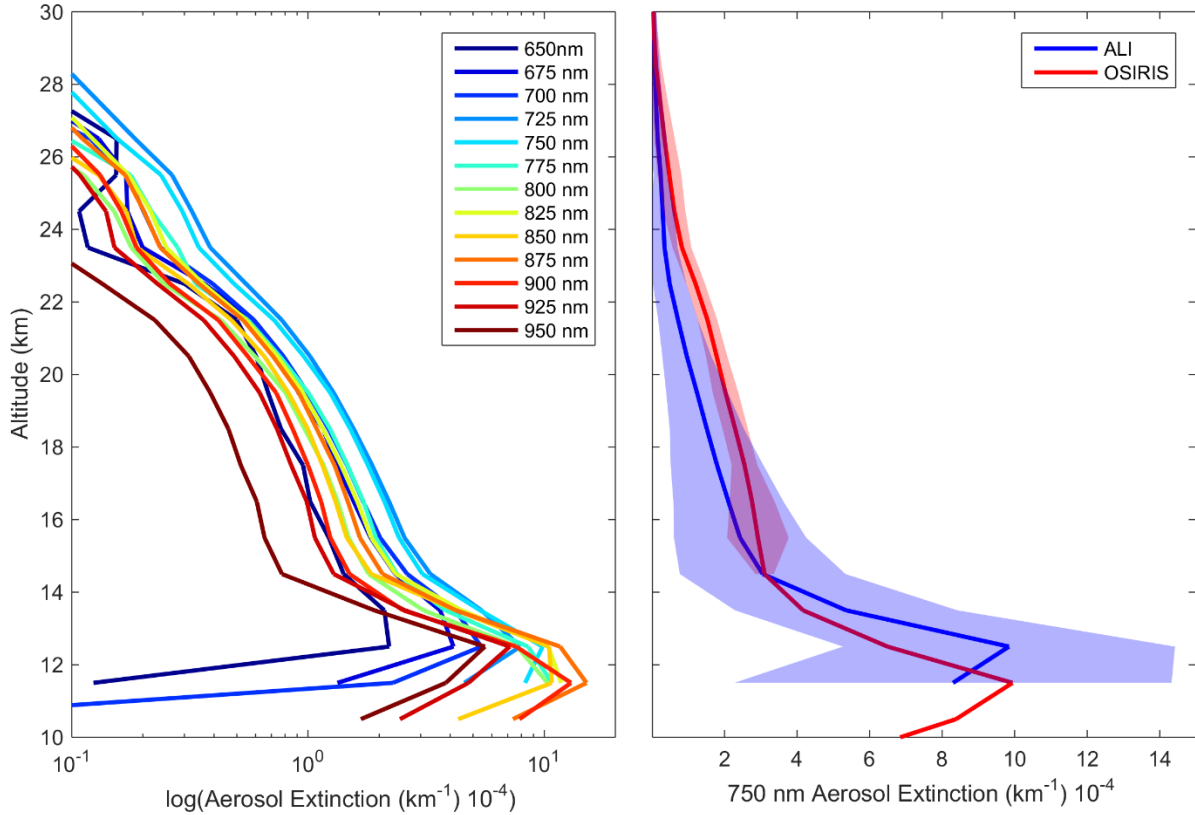


Figure 5-11: Left is the retrieved aerosol extinction profiles from the last complete imaging cycle consisting of images 205 to 216 from the 0.0° horizontal line-of-sight. Right is the 750 nm ALI aerosol extinction in blue with its error represented by the shading compared to the 750 nm extinction measured by OSIRIS in red with its error represented by the shading.

The ALI 750 nm aerosol extinction profile is shown in the right panel of Figure 5-11 with the shading representing the precision of the retrieval. The error is strictly based on measurement and instrument uncertainty and neglects any model and atmospheric state uncertainties as previously outlined. The red curve is the average 750 nm aerosol extinction profiles of the same five coincident OSIRIS scans used for the ozone profile. The retrieved extinction profiles from ALI and OSIRIS are within the total retrieval uncertainty. It is encouraging, however, that the instruments follow the same overall profile shape including the stratospheric layer and the steep increase below 15 km. Aerosol is notoriously difficult to validate in remote sensing with various technique and instrument geometries, and yet the SAGE II, SAGE III and OSIRIS differences are

generally below 20-30% up to 30 km (*Bourassa et al.*, 2012b; *Rieger et al.*, 2015) There are also several possible systematic errors not accounted for in the inversion including the choice of retrieval altitude ranges, particle size composition and distributions, stray light, and the high altitude aerosol load.

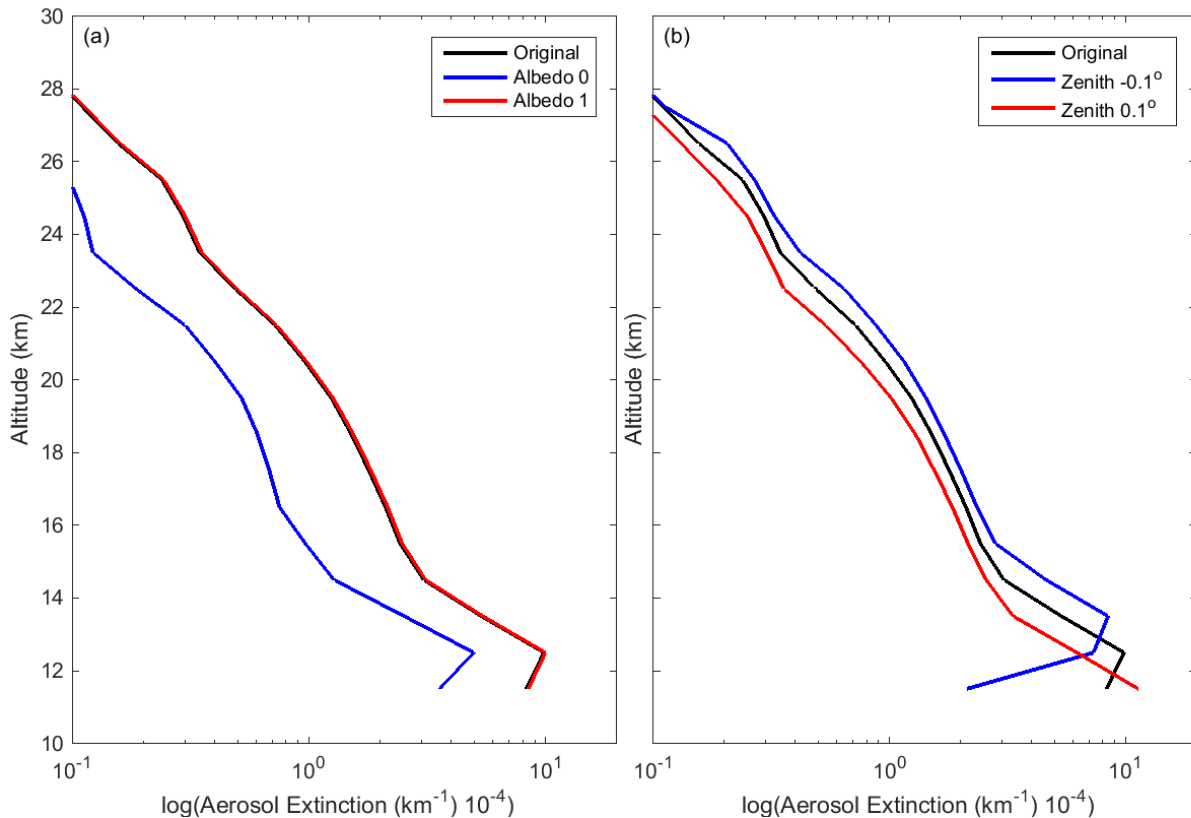


Figure 5-12: (a) Image 208 (750 nm) re-retrieved using an albedo of 0 and 1 compared to the original albedo used from OSIRIS. (b) Using the determined zenith pointing error from section 5.2, image 208 is retrieved again using the maximum possible pointing error compared to the original.

As a further note, other issues may have resulted in the disagreement between OSIRIS and ALI, mainly the estimation of the albedo and the pointing inaccuracies. For the albedo, vertically linear polarized aerosol retrievals have a much larger sensitivity to albedo. For a scalar retrieval, changing the albedo from zero to one results in approximately a 30% increase in the aerosol extinction, but for a linear polarized measurement this change in albedo can be as large as a 100% increase. Image 208 from the ALI campaign was rerun using an albedo of zero and one and the

outcome of the retrieval can be seen in Figure 5-12a. Once again, note the log scale, the albedo used from OSIRIS was 0.79. It should be noted that increasing the albedo higher than the OSIRIS values does not greatly increase the aerosol extinction. A similar rerun was performed using the error in the zenith pointing discussed in section 5.2. The results of the alteration of the pointing can be seen in Figure 5-12b. From decreasing the zenith angle, the aerosol extinction is increased which could account for the largest discrepancies between the OSIRIS and ALI results at the 20 km range but moves the aerosol peak to a higher altitude causing a further discrepancy with OSIRIS at lower tangent altitudes. However, due to a lack of pointing information from the gondola this is the best estimation that could be performed. Furthermore, there may be further issues to explore with the polarized measurements and forward model. Regardless, the results are encouraging.

5.3.3 Particle Size Retrieval Methodology

Work done by *Rieger et al.* (2014) has shown that different particle size distributions can affect the aerosol measurement vectors to yield some sensitivity. In his study, he uses an OSIRIS geometry and calculates the respective measurement vectors for a series of particle sizes which can be seen recreated in Figure 5-13. In panel A, three different log-normal distributions are used to calculate the measurement vector using a simulated atmosphere through SASKTRAN. The three profiles are: a single fine mode particle size distribution with a mode radius and width of 0.08 μm and 1.6 respectively shown in blue, bimodal particle size distribution that simulates volcanic conditions with the mode radius and width of 0.08 μm and 1.6 for the fine mode and 0.4 μm and 1.2 for the coarse mode which is shown in black, and lastly red is a representative size distribution with mode radius and width of 77 μm and 1.75. Panel B shows the measurement vectors calculated with the three distributions across a series of wavelengths. The third panel, panel C, shows the difference of the measurement vectors compared to the bimodal distribution. Sensitivity to particle size is only seen past 800 nm measurements but great sensitivity does not occur until measurement

are recorded out to 1200 nm. Furthermore, a 1% error in the radiance yields a relative error in the bimodal distribution measurement vector shown by the gray shading.

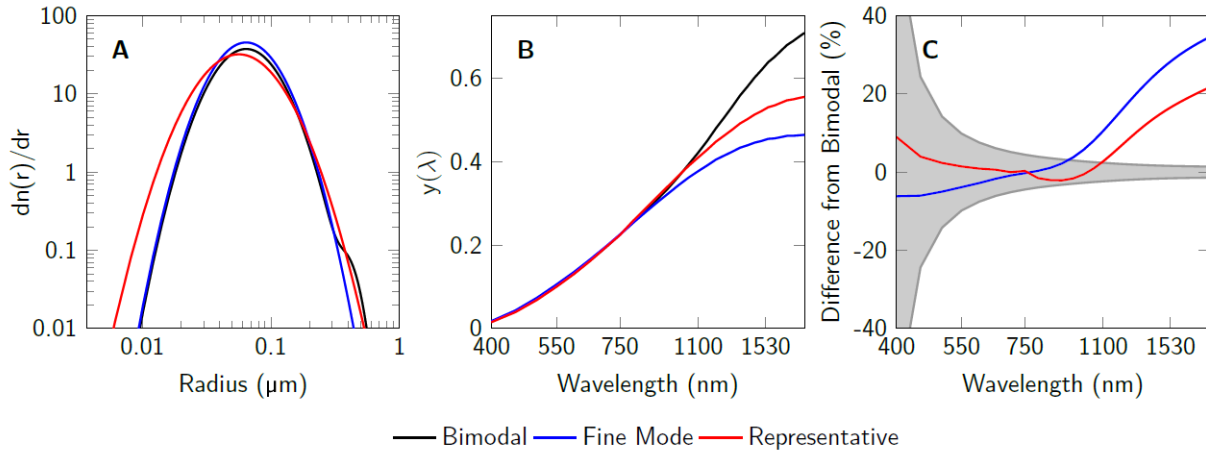


Figure 5-13: Reproduced from Figure 4 of *Rieger et al. (2014)*. For OSIRIS scan 6432001 aerosol measurement vectors were calculated at 22.5 km. (A) The three size distributions used in the study. (B) The measurement vectors calculated via the SASKTRAN simulation (C) The relative percent difference of the fine and representative distributions with respect to the bimodal distribution. A 1% error in the radiance yields an uncertainty in the bimodal measurement vector shown by the grey shading.

For ALI, measurements were only gathered between 650 and 950 nm in wavelength, due to the low sensitivity of the CCD camera in the NIR. ALI only has sensitivity to particle size from the longer wavelengths and only a small amount. As such, it will not be possible to determine both the mode radius and mode width. Instead, the data from ALI will be used to determine an Angström exponent. The Angström exponent is an approximation to Mie scattering since the value of the Angström exponent, α , is an analogy to particle size. The scattering cross section for aerosol is dependent on the particle size distribution since the number density must be a constant across wavelength, as such the extinction value changes with a change in cross section. From

$$\frac{n\sigma}{n_0\sigma_0} = \left(\frac{\lambda}{\lambda_0}\right)^{-\alpha}, \quad (5.14)$$

the particle size profile from a series of wavelengths can be determined from the Angström exponent. Lower Angström exponents correspond to larger particle sizes and vice versa for small particle sizes. The differences between extinction ratios at the different wavelengths can be used to gather an understanding of aerosol particle size in the form of Equation 5.14 where n is the aerosol concentration, and σ is the scattering cross section. Since the measurements observe relatively the same atmosphere over the time of one complete aerosol cycle. For the 750 nm wavelength, the Mie scattering cross section was calculated for a variety of mode radii and widths and a change in the cross section can be observed in Figure 5-14.

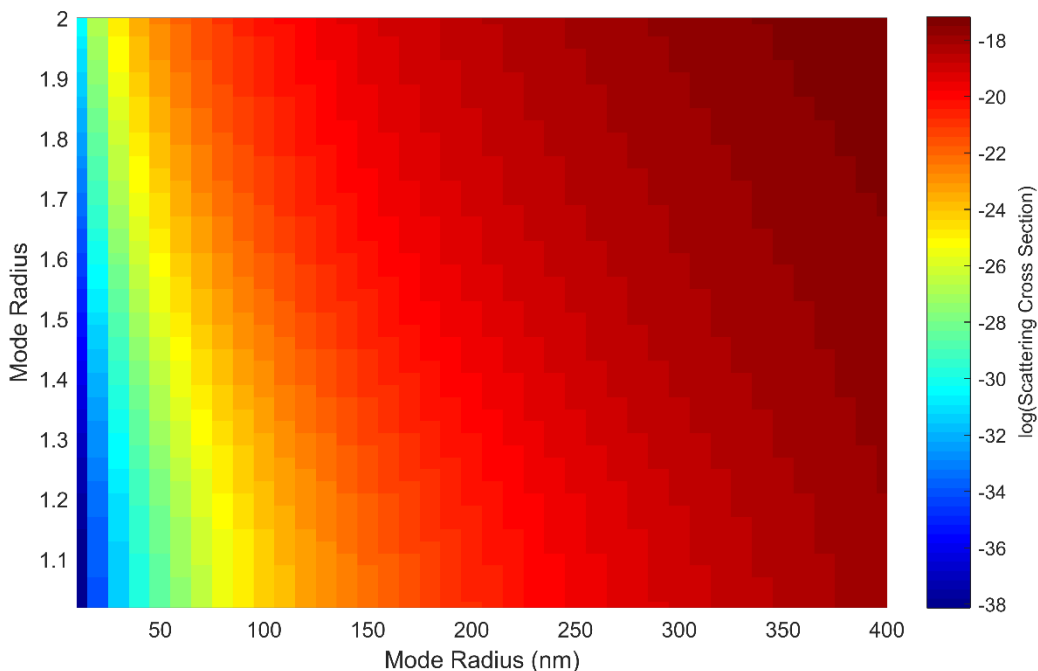


Figure 5-14: Computed with the optical properties of the SASKTRAN engine. This variation of the cross section with respect to the mode radius and width allows for some determination of the particle size distribution through the Angström exponent.

The Angström exponent can be determine by fitting a line through a series of spectral points by rearranging Equation 5.14 into the following

$$\alpha = -\frac{\log(n\sigma) - \log(n_0\sigma_0)}{\log(\lambda) - \log(\lambda_0)}. \quad (5.15)$$

The rearranging demonstrates that the Angström exponent is the simple slope of the log of the extinction over the log of the wavelengths.

Using the retrieved extinction profiles for the complete spectral range, we have attempted a determination of the Angström exponent using a method similar to that outlined by *Rault and Loughman* (2013) for the OMPS-LP analysis. In this method, the independently retrieved extinction profiles at each wavelength and altitude are fit with a straight line in log-wavelength, log-extinction space using a least squares fit. The slope of this line corresponds to the Angström exponent. This is then used to find the best match to the spectral dependence of the Mie scattering cross section in order to update the particle size distribution. With only one piece of information, the mode-width of the log-normal distribution is fixed to 1.6 and the mode radius is updated. The extinction retrievals are then performed again at each wavelength and the process is iterated until the Angström exponent, corresponding to the determined mode radius, converges.

A precision estimate was also required and since a least squares fit was used to determine the Angström exponent, the method to determine the error from the fit was also used. Assuming no uncertainty in the measurement points, the error in the slope is given by

$$\delta\alpha = \frac{s}{SS_{xx}}, \quad (5.16)$$

where s is

$$s = \sqrt{\frac{SS_{yy} - \alpha SS_{xy}}{n - 2}}, \quad (5.17)$$

and SS_{xx} , SS_{yy} , and SS_{xy} are the sum of squares of the wavelength, aerosol extinction, and cross term between the wavelength and aerosol extinction and n is the number of points. However, there is an associated error with each aerosol extinction profile as outlined in section 5.3.1. So to determine the precision of the Angström exponent, accounting for the uncertainty in the aerosol

extinction, a Monte Carlo method was used. The uncertainty of the Angström exponent was calculated millions of times and for each calculation a random amount of the error from the known range was added to the extinction. Finally, the mean from all of the uncertainty calculations of all of the least squares fits was used as the precision estimate on the Angström exponent.

5.3.4 A Sample Particle Size Retrieval

The particle size method outlined above was also applied to this measurement set consisting of images 204 to 216. The retrieved extinction at a given altitude was rejected from the straight line fit if the converged forward model radiance at that altitude was not within 2% of the measurement vector. In the case shown in Figure 5-15, at the 14.5 km altitude point, only 10 of the 13 possible wavelengths contributed to the determination of the Angström exponent. The first panel of Figure 5-15 shows the median Angström exponent that was determined after each iteration and convergence can be seen after a couple iterations. The results are shown in the second panel of Figure 5-15, where the Angström exponent is between 2 and 3 throughout the altitude range from 13 to 22 km. Assuming a mode width of 1.6 yields a median mode radius of 0.077 μm . In comparison to typical levels of background aerosol from the Laramie, Wyoming OPC data (*Deshler et al.*, 2003), the retrieved particle size parameters are certainly within an expected range, although there is a relatively large error bar on the retrieved value, limiting the usefulness of the retrieved particle size information for background aerosol. However, with these error bars, even this limited spectral range would have the sensitivity to detected particle size changes as seen by OSIRIS and SAGE II over recent decades due to small volcanic perturbations (*Rieger et al.*, 2014).

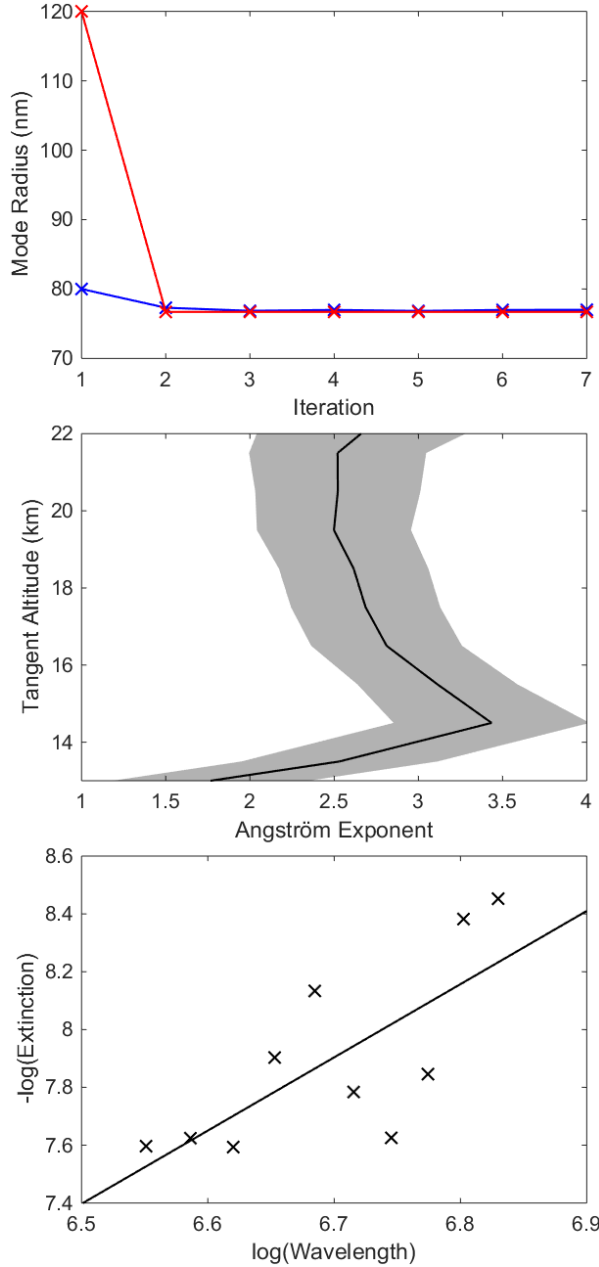


Figure 5-15: The top panel shows the convergence of two sample particle size retrievals, blue and red represent an initial state of 0.08 and $0.12\text{ }\mu\text{m}$ mode radius respectively. Both initial states converge to the same value over approximately 3 iterations in the particle size retrieval method. The middle panel shows the final Angström exponents determined from images 204-216. The shading represents the error associated with the least squares fit. The bottom panel shows a typical least squares fit of the retrieved extinction values over wavelength to determine the Angström exponent at model altitude of 14.5 km .

5.4 Results and Future Improvements

The ALI prototype, which is a telescopic acousto-optic imager, has been used to successfully measure two dimensional spectral images of the atmospheric limb from a stratospheric balloon. The observed radiances appear to be of high quality and show both vertical and horizontal features of the cloud and aerosol layers. Aerosol extinction coefficient profiles were retrieved from the ALI data that show reasonable agreement with OSIRIS satellite measurements. Furthermore rudimentary particle size microphysics information was also retrieved from the ALI mission. Due to the limited spectral range of the prototype these retrieval was noisy but would still yield sensitivity to large particle size perturbation seen after a volcanic eruption similar to OSRIS or SAGE products and with the extended wavelength range into the NIR the precision could be increased. A satellite version of the ALI instrument would be able to supply global distribution of aerosol extinction and microphysics and assist in continuing the global aerosol record.

No large scale issues were found with the instrument performance; however, some future changes would be recommended. First, an absolute calibration of the instrument would allow ALI to determine the effective of albedo directly, as is done with OSIRIS. This would remove some of the uncertainly in the model inputs and likely yield higher quality results. This is simply a matter of having access to the calibration equipment and preforming the necessary experiments. Also, even with the baffle and the robust method of removing stray light with the cycling of the AOTF, some stray light was still observed in the obtained images. Impact and mitigation of this should be tacked in future iterations of the instrument. An issue to be tackled in a second generation instrument is added a telescope back end to the imager to be able to help remove reflection the zero order beams from contaminating the final image from internal stray light as occurred in the prototype version of ALI. Also to further reduce this problem Glan-Taylor prism polarizer should replace the nanoparticle linear polarizers. The advantage to the Glan-Taylor prism is rather than

attenuate the unwanted polarization have unabsorbed it is reflected though total internal reflection approximately 90 degrees from the optical axis where it can be absorbed away from imaging plane reducing the stray light contamination improving the imaging quality.

Apart from aerosol future iteration of ALI could be used to possibly measure additional atmospheric species with modifications to the possible wavelength range. The current version of ALI was able to measure from 650-950 nm, and expanding out to the NIR and selecting an AOTF with a narrower bandpass the possibility of retrieving a water vapour profile using the water absorption bands around 930 nm. Further if the AOTF is replaced with a dual octave filter the wavelength range of the device could be expanded, for example 450-1800 nm, and replace the camera with an extended InGa array would allow the addition of an ozone retrieval while still maintaining the ability to retrieve high quality aerosol profiles. Furthermore, the addition of an ozone retrieval has an effect on aerosol retrievals at the shorter wavelengths which would improve the aerosol product at these wavelengths. Lastly, using an extended range AOTF would also allow a short wavelength normalization to the measurement vector like OSIRIS and SCIAMACHY for easier and consistent comparison between various instruments.

CHAPTER 6

CONCLUSION

Measurements of aerosol have been used for decades from in-situ measurements through the use of balloons and sondes and globally through the use of satellites. These datasets have been used to determine radiative forcing changes on the earth such as the recent global warming hiatus inferred from the record. However, current generation instruments are aging and operating well beyond their lifetimes. New instrumentation to continue the long term global aerosol dataset is required to continue to monitor climate change. This work has been focused on developing a prototype instrument to capture images of polarized radiance from a limb scatter geometry in order to determine aerosol profiles in two dimensions. ALI is the proposed prototype instrument and was designed as an engineering test to be launched from a stratospheric balloon to determine aerosol extinction and microphysics.

ALI was designed and developed using an AOTF to spectrally filter measured radiance from 650 to 950 nm in two dimensional images with exposure times on the order of seconds. A simple three lens linear optical system using a telescopic layout consisting of the telescope for the FEO and a focusing lens for the BEO to resolve the image was used for ALI. The system had a large FOV of 6° to image from a tangent point on the ground to float altitude (approximately 35 km). This resulted in significant aberrations being present in the last degree of the FOV, which was also partially outside of the acceptance angle of the AOTF. From testing and simulations in Code V optical design software the optical resolution of the instrument was a nominal 210 m both in the vertical and horizontal directions. ALI was calibrated accounting for DC offset, dark current, stray light, flat fielding, and relative spectral calibrations.

With the completion of ALI, a simulation study was underwent to determine if there was any advantage or disadvantage to measuring a linear polarization over the total radiance. Overall it was

determined that there is no distinctive advantage to measuring a linear polarization over the total radiance. However, a polarized measurement only observes a fraction of the signal compared to the total radiance case which would need to be mitigated in the optical design or operation. One exception to poor instrument performance is measuring the 90 degree SSA with the vertical polarization due to the extremely low signal levels.

The test flight for ALI occurred in Timmins, Ontario from the CSA balloon launch facility. ALI was mounted on board the CNES CARMEN-2 gondola and the launch of the stratospheric balloon occurred at 05:35 UTC on September 19, 2014 and had a flight duration of 16 hours and 14 minutes. Float altitude was 36.5 km and ALI captured aerosol images for five hours resulting in 216 measurements. These images were used to compute one dimensional aerosol extinction profiles from the flight which agreed well to the nearest OSIRIS scans but had some large discrepancies in extinction values from 20-25 km. This may have been from unaccounted for systematics in the retrieval or the SSA being relatively close to 90° at 98° which is known to yield systematics in the retrieval. Overall, however the results are promising and work on a second iteration of the instrument has already begun. Furthermore, the particle size retrievals agree with accepted values for the background stratospheric aerosol. A large error bar is associated with the determine particle size since the wavelength range is limited. Even with this limitation, ALI in its current state could notice large particle size trends in the stratosphere, such as the effect of a volcanic eruption. A satellite version of ALI would be able to accurately model aerosol trends on a global basis and be able to continue the global aerosol dataset.

This first prototype ALI instrument has allowed for the measurement of stratospheric aerosol through polarized images and with the continuation of the ALI project some recommendations for future work are suggested. First, an azimuth scan occurred during the flight to test the sensitivity

of the measurement to aerosol and provide some verification for the simulation study. These measurements should be analyzed to better understand the correct orientation for the second generation of ALI. A future iteration of ALI that is vertically polarized should be orientated so that the SAA is in between 45-60° to avoid the problematic scattering angles of 80-100° that causes a bias in the retrieved aerosol profile or reorientate the instrument to measure the horizontal polarization instead to avoid this problem.

During the mission, unknown stray light was noted in some of the images and a back end telescopic chain should be added to help further reduce internal stray light from the rejected polarization. Replacing the back end polarizer with a Glan-Taylor prism would allow the unwanted polarization to be reflected off axis and help reduce this stray light issue. Additionally the addition of a back end telescope between the AOTF and the camera could further be used to help separate the desired diffracted signal from the undesired outputs in space to remove more stray light. Lastly, the addition of an absolute calibration would allow the direct determination of albedo which would help improve the retrievals due to the highly dependent nature between polarized albedo and retrieved aerosol extinction.

Some recommendation are for the camera could also improve the quality of the measurements. The addition of a shutter or masked pixels on the CCD would be useful to calibrate DC offset and dark current changes during the flight due to temperature changes. Also an extended range camera and/or AOTF could be used to measure radiances from 500-1500 nm to allow for short wavelength normalization and added particle size sensitivity.

For an additional improvement, to be able to test the platform in a low earth orbit satellite geometry as well as a functional test for a balloon geometry, a zoom lens could be added to the front of a future iteration to allow the verification of both geometries with a single flight. Addition

the adaptation of a folded optics design will be required for a space platform and should be tacked in a future iteration. All of these improvements would help to improve the image quality of the next generation instrument.

LIST OF REFERENCES

- Andersson, S. M., B. G. Martinsson, J.-P. Vernier, J. Friberg, C. A. Brenninkmeijer, M. Hermann, P. F. van Velthoven, and A. Zahn (2015), Significant radiative impact of volcanic aerosol in the lowermost stratosphere, *Nature communications*, 6.
- Andrews F. G. (1987), *Middle atmospheric dynamics*, Academic Press Inc.
- Angstrom, A. (1964), The parameters of atmospheric turbidity, *Tellus*, 16(1), 64 – 75.
- Barth, C. A., D. W. Rusch, R. J. Thomas, G. H. Mount, G. J. Rottman, G. E. Thomas, R. W. Sanders, and G. M. Lawrence (1983), Solar Mesosphere Explorer - Scientific objectives and results, *Geophysical Research Letters*, 10, 237-240, doi:10.1029/GL010i004p00237.
- Berthet, G., J.-B. Renard, C. Brogniez, C. Robert, M. Chartier, and M. Pirre (2002), Optical and physical properties of stratospheric aerosols from balloon measurements in the visible and near-infrared domains. i. Analysis of aerosol extinction spectra from the AMON and SALOMON balloonborne spectrometers, *Applied optics*, 41, 7522-7539.
- Beuttell, R. G., and A. W. Brewer (1949), Instruments for the measurement of the visual range, *Journal of Scientific Instruments*, 26, 357.
- Bickel, W. S., and W. M. Bailey (1985), Stokes vectors, Mueller matrices, and polarized scattered light, *American Journal of Physics*, 53, 468-478 (1985), doi:<http://dx.doi.org/10.1119/1.14202>
- Bingen, C., D. Fussen, and F. Vanhellemont (2004), A global climatology of stratospheric aerosol size distribution parameters derived from sage ii data over the period 1984-2000: 1. methodology and climatological observations, *Journal of Geophysical Research*, 109.
- Boucher O. (2015), *Atmospheric Aerosols: Properties and Climate Impacts*, Springer.
- Bourassa, A. E., D. A. Degenstein, R. L. Gattinger, and E. J. Llewellyn (2007), Stratospheric aerosol retrieval with optical spectrograph and infrared imaging system limb scatter measurements, *Journal of Geophysical Research*, 112, D10217, doi:10.1029/2006JD008079.
- Bourassa, A. E., D. A. Degenstein, and E. J. Llewellyn (2008), SASKTRAN: A spherical geometry radiative transfer code for efficient estimation of limb scattered sunlight, *Journal of Quantitative Spectroscopy and Radiative Transfer*, 109, 52-73, doi:10.1016/j.jqsrt.2007.07.007.

- Bourassa, A. E., C. A. McLinden, A. F. Bathgate, B. J. Elash, and D. A. Degenstein (2012a), Precision estimate for Odin-OSIRIS limb scatter retrievals, *Journal of Geophysical Research: Atmospheres*, 117, D04303, doi:10.1029/2011JD016976.
- Bourassa, A. E., L. A. Rieger, N. D. Lloyd, and D. A. Degenstein (2012b), Odin-OSIRIS stratospheric aerosol data product and SAGE III intercomparison, *Atmospheric Chemistry & Physics*, 12, 605{614, doi:10.5194/acp-12-605-2012.
- Bourassa, A. E., A. Robock, W. J. Randel, T. Deshler, L. A. Rieger, N. D. Lloyd, E. T. Llewellyn, and D. A. Degenstein (2012c), Large volcanic aerosol load in the stratosphere linked to Asian monsoon transport, *Science*, 337, 78-81.
- Bourassa, A. E., A. Robock, W. J. Randel, T. Deshler, L. A. Rieger, N. D. Lloyd, E. Llewellyn, and D. A. Degenstein (2013), Response to comments on "large volcanic aerosol load in the stratosphere linked to Asian monsoon transport", *Science*, 339, 647-647.
- Bovensmann, H., J. Burrows, M. Buchwitz, J. Frerick, S. Noël, V. Rozanov, K. Chance, and A. Goede (1999), SCIAMACHY: Mission objectives and measurement modes, *Journal of the Atmospheric Sciences*, 56, 127-150.
- Brasseur G. P. and S. Solomon (2005), *Aeronomy of the Middle Atmosphere: Chemistry and Physics of the Stratosphere and Mesosphere*, 3rd edition, Springer.
- Brock, C. A., P. Hamill, J. C. Wilson, H. H. Jonsson, and K. R. Chan (1995), Particle Formation in the Upper Tropical Troposphere: A Source of Nuclei for the Stratospheric Aerosol, *Science*, 270, 1650-1653, doi:10.1126/science.270.5242.1650.
- Canty, T., N. Mascioli, M. Smarte, and R. Salawitch (2013), An empirical model of global climate—Part 1: A critical evaluation of volcanic cooling, *Atmospheric Chemistry and Physics*, 13(8), 3997–4031.
- Chang, I. C. (1977), Noncollinear tunable acousto-optic filter. Patent.
- Charlson, R. J., N. Ahlquist, H. Selvidge, and P. MacCready Jr (1969), Monitoring of atmospheric aerosol parameters with the integrating nephelometer, *Journal of the Air Pollution Control Association*, 19, 937-942.
- Chazette, P., C. David, J. Lefrere, S. Godin, J. Pelon, and G. Mégié (1995), Comparative lidar study of the optical, geometrical, and dynamical properties of stratospheric postvolcanic

aerosols, following the eruptions of el chichon and mount pinatubo, *Journal of Geophysical Research*, 100, 23-195.

Chuang, T., P. Burns, E. B. Walters, T. Wysocki, T. Deely, A. Losse, L. Le, B. Drumheller, T. Schum, M. Hart, K. Puffenburger, B. Ziegler, and F. Hovis (2013), Space-based, multi-wavelength solid-state lasers for NASA's Cloud Aerosol Transport System for International Space Station (CATS-ISS), *Proc. SPIE*, 8599, 85990N. doi:10.1117/12.2005545.

Cisewski, M., J. Zawodny, J. Gasbarre, R. Eckman, N. Topiwala, O. Rodriguez-Alvarez, D. Cheek, and S. Hall (2014), The stratospheric aerosol and gas experiment (SAGE III) on the international space station (ISS) mission, *Proc. SPIE*, 9241, 924,107-924,107-7, doi:10.1117/12.2073131.

Clarisso, L., P.-F. Coheur, N. Theys, D. Hurtmans, and C. Clerbaux (2014), The 2011 Nabro eruption, a SO₂ plume height analysis using IASI measurements, *Atmospheric Chemistry and Physics*, 14, 3095-3111, doi:10.5194/acp-14-3095-2014.

Crutzen, P. J. (1976), The possible importance of CSO for the sulfate layer of the stratosphere, *Geophysics Research Letters*, 3, 73-76.

Damadeo, R. P., J. M. Zawodny, L. W. Thomason, and N. Iyer (2013), SAGE version 7.0 algorithm: application to SAGE II, *Atmospheric Measurement Techniques*, 6, 3539-3561, doi:10.5194/amt-6-3539-2013.

Dee, D. P., S. M. Uppala, A. J. Simmons, P. Berrisford, P. Poli, S. Kobayashi, U. Andrae, M. A. Balmaseda, G. Balsamo, P. Bauer, P. Bechtold, A. C. M. Beljaars, L. van de Berg, J. Bidlot, N. Bormann, C. Delsol, R. Dragani, M. Fuentes, A. J. Geer, L. Haimberger, S. B. Healy, H. Hersbach, E. V. Hlm, L. Isaksen, P. Kllberg, M. Khler, M. Matricardi, A. P. McNally, B. M. Monge-Sanz, J.-J. Morcrette, B.-K. Park, C. Peubey, P. de Rosnay, C. Tavolato, J.-N. Thpaut, and F. Vitart (2011), The ERA-interim reanalysis: configuration and performance of the data assimilation system, *Quarterly Journal of the Royal Meteorological Society*, 137, 553-597, doi:10.1002/qj.828.

Degenstein, D. A., A. E. Bourassa, C. Z. Roth, and E. J. Llewellyn (2009), Limb scatter ozone retrieval from 10 to 60 km using a multiplicative algebraic reconstruction technique, *Atmospheric Chemistry and Physics*, 9, 6521-6529.

Dekemper, E., N. Loodts, B. V. Opstal, J. Maes, F. Vanhellemont, N. Mateshvili, G. Franssens, D. Pieroux, C. Bingen, C. Robert, L. D. Vos, L. Aballea, and D. Fussen (2012), Tunable

acousto-optic spectral imager for atmospheric composition measurements in the visible spectral domain, *Applied Optics*, 51, 6259-6267, doi:10.1364/AO.51.006259.

Deshler, T., M. Hervig, D. Hofmann, J. Rosen, and J. Liley (2003), Thirty years of in situ stratospheric aerosol size distribution measurements from Laramie, Wyoming (41 N), using balloon-borne instruments, *Journal of Geophysical Research*, 108.

Deshler T. (2008), A review of global stratospheric aerosol: Measurements, importance, life cycle, and local stratospheric aerosol, *Atmospheric Research*, 90, 2–4, 223-232.

Dueck, S., A. E., Bourassa, and D. A. Degenstein (2016), Polarization Additions SASKTRAN Radiative Transfer Model, In Preparations.

Ernst, F., C. von Savigny, A. Rozanov, V. Rozanov, K.-U. Eichmann, L. A. Brinkho, H. Bovensmann, and J. P. Burrows (2012), Global stratospheric aerosol extinction profile retrievals from SCIAMACHY limb-scatter observations, *Atmospheric Measurement Techniques*, 5, 5993-6035, doi:10.5194/amtd-5-5993-2012.

Fairlie, T. D., J.-P. Vernier, M. Natarajan, and K. M. Bedka (2014), Dispersion of the Nabro volcanic plume and its relation to the Asian summer monsoon, *Atmospheric Chemistry and Physics*, 14, 7045-7057, doi:10.5194/acp-14-7045-2014.

Fischer, R. E., B. Tadic-Galeb, and P. R. Yoder (2008), *Optical System Design*, 2nd ed., McGraw-Hill.

Fiocco, G., and G. Grams (1964), Observations of the aerosol layer at 20 km by optical radar, *Journal of the Atmospheric Sciences*, 21, 323-324.

Forsythe, W. E., and Worthing, A. G. (1925). The properties of tungsten and the characteristics of tungsten lamps. *The Astrophysical Journal*, 61, 146, doi:10.1086/142880.

Fromm, M., G. Nedoluha, and Z. Charvt (2013), Comment on "large volcanic aerosol load in the stratosphere linked to Asian monsoon transport", *Science*, 339, 647, doi:10.1126/science.1228605.

Fromm, M., G. Kablick, G. Nedoluha, E. Carboni, R. Grainger, J. Campbell, and J. Lewis (2014), Correcting the record of volcanic stratospheric aerosol impact: Nabro and sarychev peak, *Journal of Geophysical Research*, 119, 10,343-10,364, doi:10.1002/2014JD021507.

Fyfe, J. C., N. P. Gillett, and F. W. Zwiers (2013), Overestimated global warming over the past 20 years, *Nature Climate Change*, 3, 767-769.

- Gass, P. A., and J. R. Sambles (1991), Accurate design of a non-collinear acousto-optic tunable filter, *Optics Letters*, 16, 429-431, doi:10.1364/OL.16.000429.
- Gilbert, K., D. Turnbull, K. Walker, C. Boone, S. McLeod, M. Butler, R. Skelton, P. Bernath, F. Chateauneuf, and M.-A. Soucy (2007), The onboard imagers for the Canadian ACE SCISAT-1 mission, *Journal of Geophysical Research*, 112.
- Guenther, R. (1990), *Modern Optics*, 1st edition ed., Wiley and Sons, Inc.
- Hamill P., E. J. Jensen, P. B. Russell, and J. J. Bauman (1997), The Life Cycle of Stratospheric Aerosol Particles, *Bulletin of the American Meteorological Society*, 78, 1395–1410.
- Hansen, J. E., and L. D. Travis (1974), Light Scattering in Planetary Atmospheres, *Space Science Reviews*, 16(4), 527-610.
- Hansen, J., R. Ruedy, and M. Sato (1996), Global surface air temperature in 1995: Return to pre-Pinatubo levels, *Geophysical Research Letters*, 23(13), 1665-1668.
- Harris, S. E., and R. W. Wallace (1969), Acousto-Optic Tunable Filter, *Journal of the Optical Society of America* (1917-1983), 59, 744.
- Haywood, J. M., A. Jones, and G. S. Jones (2014), The impact of volcanic eruptions in the period 2000-2013 on global mean temperature trends evaluated in the HadGEM2-ES climate model, *Atmospheric Science Letters*, 15, 92-96, doi:10.1002/asl2.471.
- Hofmann D. J. and J. M. Rosen (1983), Stratospheric sulfur acid fraction and mass estimate for the 1982 volcanic eruption of El Chichon, *Geophysical Research Letters*, 10(4), 313-316.
- Hofmann, D., J. Barnes, M. O'Neill, M. Trudeau, and R. Neely (2009), Increase in background stratospheric aerosol observed with lidar at Mauna Loa observatory and Boulder, Colorado, *Geophysical Research Letters*, 36, doi:10.1029/2009GL039008, 115808.
- Hoinka, K. (1997), The tropopause: Discovery, definition and demarcation, *Meteorologische Zeitschrift*, 6, 281-303.
- Holton, J. R., P. H. Haynes, M. E. McIntyre, A. R. Douglass, R. B. Rood, and L Pfister (1995), Stratosphere-troposphere exchange, *Review of Geophysics*, 33, 403–439, DOI: 10.1029/95RG02097.

Jäger, H., and D. Hofmann (1991), Midlatitude lidar backscatter to mass, area, and extinction conversion model based on in situ aerosol measurements from 1980 to 1987, *Applied optics*, 30, 127-138.

Junge, C. E., C. W. Chagnon, and J. E. Manson (1961), Stratospheric aerosols, *Journal of Atmospheric Science*, 18, 81–108.

Kettle, A. J., U. Kuhn, M. von Hobe, J. Kesselmeier, M. O. Andreae, (2002) The global budget of atmospheric carbonyl sulfide: Temporal and spatial variations of the dominant sources and sinks, *Journal Geophysical Research*, 107, D22, 4658, doi:10.1029/2002JD002187.

Kiehl, J. T., and B. P. Briegleb (1993), The relative roles of sulfate aerosols and greenhouse gases in climate forcing, *Science*, 260, 311-314, doi:10.1126/science.260.5106.311.

Kosch, M., S. Mäkinen, F. Sigernes, and O. Harang (2003), Absolute optical calibration using a simple tungsten light bulb: Experiment, *Proceedings of the 30th Annual European Meeting on Atmospheric Studies by Optical Methods*, 50-54.

Kvilakam, M., and T. Deshler (2015), On the accuracy of stratospheric aerosol extinction derived from in situ size distribution measurements and surface area density derived from remote SAGE II and HALOE extinction measurements, *Journal Geophysical Research Atmospheres*, 120, 8426–8447, doi:10.1002/2015JD023303.

Kozun M. N. (2015), *Optical Pointing System For Stratospheric Balloon-Borne Multi-Slit OSIRIS-DM*, Master's Thesis, University of Saskatchewan.

Kremser, S., L. W. Thomason, M. von Hobe, M. Hermann, T. Deshler, C. Timmreck, M. Toohey, A. Stenke, J. P. Schwarz, R. Weigel, S. Fueglstaler, F. J. Prata, J.-P. Vernier, H. Schlager, J. E. Barnes, J.-C. Antuña-Marrero, D. Fairlie, M. Palm, E. Mahieu, J. Notholt, M. Rex, C. Bingen, F. Vanhellemont, A. Bourassa, J. M. C. Plane, D. Klocke, S. A. Carn, L. Clarisse, T. Trickl, R. Neely, A. D. James, L. Rieger, J. C. Wilson, and B. Meland (2015), Stratospheric aerosol—Observations, processes, and impact on climate, *Rev. Geophys.*, 54, doi:10.1002/2015RG000511.

Lacis, A., J. Hansen, and M. Sato (1992), Climate forcing by stratospheric aerosols, *Geophysical Research Letters*, 19, 1607–1610.

Llewellyn, E., N. D. Lloyd, D. A. Degenstein, R. L. Gattinger, S. V. Petelina, A. E. Bourassa, J. T. Wiensz, E. V. Ivanov, I. C. McDade, B. H. Solheim, J. C. McConnell, C. S. Haley, C. von Savigny, C. E. Sioris, C. A. McLinden, E. Grifoen, J. Kaminski, W. F. J. Evans, E. Puckrin, K. Strong, V. Wehrle, R. H. Hum, D. J. W. Kendall, J. Matsushita, D. P. Murtagh, S.

- Brohede, J. Stegman, G. Witt, G. Barnes, W. F. Payne, L. Piche, K. Smith, G. Warshaw, D. L. Deslauniers, P. Marchand, E. H. Richardson, R. A. King, I. Wevers, W. McCreathe, E. Kyrölä, L. Oikarinen, G. W. Leppelmeier, H. Auvinen, G. Megie, A. Hauchecorne, F. Lefevre, J. de La Noe, P. Ricaud, U. Frisk, F. Sjoberg, F. von Scheele, and L. Nordh (2004), The OSIRIS instrument on the Odin spacecraft, *Canadian Journal of Physics*, 82, 411-422, doi:10.1139/p04-005.
- McLinden, C. A., J. C. McConnell, C. T. McElroy, and E. Griffioen (1999), Observations of Stratospheric Aerosol Using CPFM Polarized Limb Radiances, *Journal of the Atmospheric Sciences*, 56:2, 233-240, doi:10.1175/1520-0469(1999)056<0233:OOSAUC>2.0.CO;2.
- McCormick, M. P., and T. J. Swissler (1983), Stratospheric aerosol mass and latitudinal distribution of the El Chichon eruption cloud for October 1982, *Geophysical Research Letters*, 10(9), 877–880, doi:10.1029/GL010i009p00877.
- McCormick, M. P. and R. E. Veiga (1992), SAGE II measurements of early Pinatubo aerosols, *Geophysical Research Letters*, 19(2), 155-158.
- McCormick, M. P., L. W. Thomason, and C. R. Trepte (1995), Atmospheric effects of the Mt Pinatubo eruption, *Nature*, 373(6513), 399-404.
- McElroy, C. T., C. R. Nowlan, J. R. Drummond, P. F. Bernath, D. V. Barton, D. G. Dufour, C. Midwinter, R. B. Hall, A. Ogyu, A. Ullberg, D. I. Wardle, J. Kar, J. Zou, F. Nichitiu, C. D. Boone, K. A. Walker, and N. Rowlands (2007), The ACE-MAESTRO instrument on SCISAT: description, performance, and preliminary results, *Applied Optics*, 46, 4341-4356, doi:10.1364/AO.46.004341.
- Mie, G. (1908), Considerations on the optics of turbid media, especially colloidal metal solutions, *Ann. Phys. (Leipzig)*, 42, 377.
- Mishchenko, M. I., L. D. Travis, and A. A. Lacis (2002), *Scattering, Absorption, and Emission of Light by Small Particles*, 3rd edition, Cambridge, UK: Cambridge University Press.
- Murphy, D. M., K. D. Froyd, J. P. Schwarz, and J. C. Wilson (2014), Observations of the chemical composition of stratospheric aerosol particles, *Quarterly Journal of the Royal Meteorological Society*, 140, 1269-1278, doi:10.1002/qj.2213.
- Neely, R. R., P. Yu, K. H. Rosenlof, O. B. Toon, J. S. Daniel, S. Solomon, and H. L. Miller (2014), The contribution of anthropogenic SO₂ emissions to the Asian tropopause aerosol layer, *Journal of Geophysical Research*, 119, 1571-1579, doi:10.1002/2013JD020578.

- Notholt, J., Z. Kuang, C. P. Rinsland, G. C. Toon, M. Rex, N. Jones, T. Albrecht, H. Deckelmann, J. Krieg, C. Weinzierl, H. Bingemer, R. Weller and O. Schrems (2003), Enhanced Upper Tropical Tropospheric COS: Impact on the Stratospheric Aerosol Layer, *Science*, 300, 307-310.
- Oikarinen, L., E. Sihvola, and E. Kyrölä (1999), Multiple scattering radiance in limb-viewing geometry, *Journal of Geophysical Research*, 104, 31,261-31,274.
- Plumb, R. A. and J. Eluszkiewicz, (1999), The Brewer–Dobson Circulation: Dynamics of the Tropical Upwelling, *Journal of Atmospheric Science*, 56, 868–890.
- Rault, D. F., and R. P. Loughman (2013), The OMPS limb profiler environmental data record algorithm theoretical basis document and expected performance, *Geoscience and Remote Sensing, IEEE Transactions on*, 51, 2505-2527.
- Ridley, D. A., S. Solomon, J. E. Barnes, V. D. Burlakov, T. Deshler, S. I. Dolgii, A. B. Herber, T. Nagai, R. R. Neely, A. V. Nevezorov, C. Ritter, T. Sakai, B. D. Santer, M. Sato, A. Schmidt, O. Uchino, and J. P. Vernier (2014), Total volcanic stratospheric aerosol optical depths and implications for global climate change, *Geophysical Research Letters*, 41, 7763-7769, doi:10.1002/2014GL061541, 2014GL061541.
- Rieger, L. A., A. E. Bourassa, and D. A. Degenstein (2014), Stratospheric aerosol particle size information in Odin-OSIRIS limb scatter spectra, *Atmospheric Measurement Techniques*, 7, 507-522, doi:10.5194/amt-7-507-2014.
- Rieger, L. A., A. E. Bourassa, and D. A. Degenstein (2015), Merging the OSIRIS and SAGE II stratospheric aerosol records, *Journal of Geophysical Research*, doi:10.1002/2015JD023133, 2015JD023133.
- Rodgers, C. (2000), *Inverse Methods for Atmospheric Sounding: Theory and Practice, Series on atmospheric, oceanic and planetary physics*: 1999, World Scientific, River Edge, NJ, USA.
- Rogers, R. R., C. A. Hostetler, J. W. Hair, R. A. Ferrare, Z. Liu, M. D. Obland, D. B. Harper, A. L. Cook, K. A. Powell, M. A. Vaughan, and D. M. Winker (2011), Assessment of the CALIPSO lidar 532 nm attenuated backscatter calibration using the NASA LARC airborne high spectral resolution lidar, *Atmospheric Chemistry and Physics*, 11, 1295-1311, doi:10.5194/acp-11-1295-2011.
- Rosen J. M. (1971), The Boiling Point of Stratospheric Aerosols, *Journal of Applied Meteorology*, 10, 1044–1046.

Russell, P., and M. McCormick (1989), SAGE II aerosol data validation and initial data use: An introduction and overview, *Journal of Geophysical Research*, 94, 8335-8338.

Saito K., A. W. and T. Yano (1976), Acousto-optic filter. Patent.

Sawamura, P., J. P. Vernier, J. E. Barnes, T. A. Berko, E. J. Welton, L. Alados-Arboledas, F. Navas-Guzmn, G. Pappalardo, L. Mona, F. Madonna, D. Lange, M. Sicard, S. Godin-Beckmann, G. Payen, Z. Wang, S. Hu, S. N. Tripathi, C. Cordoba-Jabonero, and R. M. Ho (2012), Stratospheric AOD after the 2011 eruption of Nabro volcano measured by lidars over the northern hemisphere, *Environmental Research Letters*, 7, 034,013.

Schutz, B., H. Zwally, C. Shuman, D. Hancock, and J. DiMarzio (2005), Overview of the ICESat mission, *Geophysical Research Letters*, 32.

Sioris, C. E., C. D. Boone, P. F. Bernath, J. Zou, C. T. McElroy, and C. A. McLinden (2010), Atmospheric chemistry experiment (ACE) observations of aerosol in the upper troposphere and lower stratosphere from the Kasatochi volcanic eruption, *Journal of Geophysical Research*, 115, doi:10.1029/2009JD013469, d00L14.

Smith, W. J. (2000), *Modern Optical Engineering*, New York: McGraw-Hill.

Sneep, M., and W. Ubachs (2005), Direct measurement of the Rayleigh scattering cross section in various gases, *Journal of Quantitative Spectroscopy and Radiative Transfer*, 92(3), 293-310, doi:10.1016/j.jqsrt.2004.07.025.

Soden, B. J., R. T. Wetherald, G. L. Stenchikov, and A. Robock (2002), Global cooling after the eruption of Mount Pinatubo: A test of climate feedback by water vapor, *Science*, 296(5568), 727–730, doi:10.1126/science.296.5568.727.

Solomon, S., D. Qin, M. Manning, Z. Chen, M. Marquis, K. B. Averyt, M. Tignor, and H. L. Miller (2007), Contribution of Working Group I to the Fourth Assessment Report of the Intergovernmental Panel on Climate Change, *Tech. rep.*

Solomon, S., J. S. Daniel, R. R. Neely, J.-P. Vernier, E. G. Dutton, and L. W. Thomason (2011), The persistently variable background stratospheric aerosol layer and global climate change, *Science*, 333, 866-870, doi:10.1126/science.1206027.

Stocker, T. F., D. Qin, G.-K. Plattner, M. M. Tignor, S. K. Allen, J. Boschung, A. Nauels, Y. Xia, V. Bex, and P. M. Midgley (2013), *Climate Change 2013 The Physical Science Basis*.

Suhre, D. R., L. J. Denes, and N. Gupta (2004), Telecentric confocal optics for aberration correction of acousto-optic tunable filters, *Applied Optics*, 43, 1255-1260, doi:10.1364/AO.43.001255.

Taylor B. J. A. (2015), *The Upgrade, Calibration, and Evaluation of the Multi-Slit OSIRIS-DM for Stratospheric Balloon Flight*, Master's Thesis, University of Saskatchewan.

Thomason, L. W. (1991), A diagnostic stratospheric aerosol size distribution inferred from SAGE II measurements, *Journal of Geophysical Research*, 96(D12), 22,501-22,508.

Thomason, L. W., and G. Taha (2003), SAGE III aerosol extinction measurements: Initial results, *Geophysical Research Letters*, 30.

Thomason, L. W. and T. Peter (2006), Assessment of Stratospheric Aerosol Processes (ASAP), *World Climate Research Program*, 1–322.

Thompson, D. W., J. M. Wallace, P. D. Jones, and J. J. Kennedy (2009), Identifying signatures of natural climate variability in time series of global-mean surface temperature: Methodology and insights, *Journal of Climate*, 22(22), 6120–6141.

Thomason, L. W., and J.-P. Vernier (2013), Improved SAGE II cloud/aerosol categorization and observations of the Asian tropopause aerosol layer: 1989-2005, *Atmospheric Chemistry and Physics*, 13, 4605-4616, doi:10.5194/acp-13-4605-2013.

Uchida, N. (1971), Optical properties of single-crystal paratellurite (TeO_2), *Physics Review B*, 4, 3736-3745, doi:10.1103/PhysRevB.4.3736.

Van de Hulst, H. C. (1962), *Light Scattering by Small Particles*, New York: Wiley and Sons Inc.

Vanhelmont, F., C. Tetard, A. Bourassa, M. Fromm, J. Dodion, D. Fussen, C. Brogniez, D. Degenstein, K. L. Gilbert, D. N. Turnbull, P. Bernath, C. Boone, and K. A. Walker (2008), Aerosol extinction profiles at 525 nm and 1020 nm derived from ACE imager data: comparisons with GOMOS, SAGE II, SAGE III, POAM III, and OSIRIS, *Atmospheric Chemistry and Physics*, 8, 2027-2037, doi:10.5194/acp-8-2027-2008.

Vernier, J.-P., L. Thomason, and J. Kar (2011a), CALIPSO detection of an Asian tropopause aerosol layer, *Geophysical Research Letters*, 38.

- Vernier, J.-P., L. W. Thomason, J.-P. Pommereau, A. Bourassa, L. Blanot, C. Trepte, D. Degenstein, and F. Vargas (2011b), Major influence of tropical volcanic eruptions on the stratospheric aerosol layer during the last decade, *Geophysical Research Letters*, 38, L12807, doi:10.1029/2011GL047563.
- Vernier, J.-P., L. W. Thomason, T. D. Fairlie, P. Minnis, R. Palikonda, and K. M. Bedka (2013), Comment on "Large volcanic aerosol load in the stratosphere linked to Asian monsoon transport", *Science*, 339, 647, doi:10.1126/science.1227817.
- Volk, C. M., J. W. Elkins, D. W. Fahey, G. S. Dutton, J. M. Gilligan, M. Loewenstein, J. R. Podolske, K. R. Chan, and M. R. Gunson (1997), Evaluation of source gas lifetimes from stratospheric observations, *Journal of Geophysical Research*, 102(D21), 25543–25564, doi:10.1029/97JD02215.
- Voloshinov, V. (1996), Spectral and polarization analysis of optical images by means of acousto-optics, *Optics Laser Technology*, 28, 119-127, doi:10.1016/0030-3992(95)00079-8.
- Voloshinov, V. B., and J. C. Mosquera (2006), Wide-aperture acousto-optic interaction in birefringent crystals, *Optics and Spectroscopy*, 101, 635-641, doi:10.1134/S0030400X06100225.
- Voloshinov, V. B., K. B. Yushkov, and B. B. J. Linde (2007), Improvement in performance of a TeO₂ acousto-optic imaging spectrometer, *Journal of Optics A: Pure and Applied Optics*, 9, 341-347, doi:10.1088/1464-4258/9/4/006.
- von Savigny, C., F. Ernst, A. Rozanov, R. Hommel, K.-U. Eichmann, V. Rozanov, J. P. Burrows, and L. W. Thomason (2015), Improved stratospheric aerosol extinction profiles from SCIAMACHY: validation and sample results, *Atmospheric Measurement Techniques*, 8, 8353-8383, doi:10.5194/amtd-8-8353-2015.
- Wang, P.-H., M. P. McCormick, T. J. Swissler, M. T. Osborn, W. H. Fuller, and G. K. Yue (1989), Inference of stratospheric aerosol composition and size distribution from SAGE II satellite measurements, *Journal Geophysical Research*, 94(D6), 8435–8446, doi:10.1029/JD094iD06p08435.
- Winker, D. M., W. H. Hunt, and M. J. McGill (2007), Initial performance assessment of CALIOP, *Geophysical Research Letters*, 34.
- Wiscombe, W. J. (1980), Improved Mie scattering algorithms, *Applied Optics*, 19, 1505-1509.

Xu, J., and R. Stroud (1992), *Acousto-optic devices: principles, design, and applications*, Wiley-Interscience.

Young, S. A., and M. A. Vaughan (2009), The retrieval of profiles of particulate extinction from cloud-aerosol lidar infrared pathfinder satellite observations (calipso) data: Algorithm description, *Journal of Atmospheric and Oceanic Technology*, 26, 1105-1119.

Zawada, D. J., S. R. Dueck, L. A. Rieger, A. E. Bourassa, N. D. Lloyd, and D. A. Degenstein (2015), High resolution and Monte Carlo additions to the SASKTRAN radiative transfer model, *Atmospheric Measurement Techniques*, 8, 3357-3397, doi:10.5194/amtd-8-3357-2015.

APPENDIX A

ALI HARDWARE COMPONENTS

The section will list and give specifications for all of the major ALI hardware components.

Each section will have a brief description followed by a table of the specifications.

A.1 Optical Components

A.1.1 Optical Lenses

All lenses used in the ALI system were purchased from Newport and were coated with anti-reflective coating AR.16 which covers 650-1000 nm range with an average reflectance of 0.5% and a maximum of 1.5%. All the lens in the system were made from N-BK7 glass and the specification and model number of each lens is located in Table A-1.

Table A-1: Lens used in ALI and their specifications.

Model Number	Effective Focal Length (mm)	Diameter (mm)	Center Thickness (mm)	Radius (mm)	Type of Lens
KPX100AR.16	150.0±1.5	25.4+0/-0.1	4.0±0.1	77.520	Plano-Convex
KPX187AR.16	100.0±1.0	50.2+0/-0.1	9.7±0.1	51.680	Plano-Convex
KBX052AR.16	50.2±0.5	25.4+0/-0.1	6.2±0.1	50.806	Bi-Convex

A.1.2 Polarizers

ALI needed two linear polarizers to help remove unwanted signal and reduce stray light in the system. These polarizers required a high extinction ratio over the range of the CCD sensitivities. The polarizers chosen were model number LPVIS100 from Thorlabs. The extinction ratios and transmission of the device can be seen in Figure A-1.

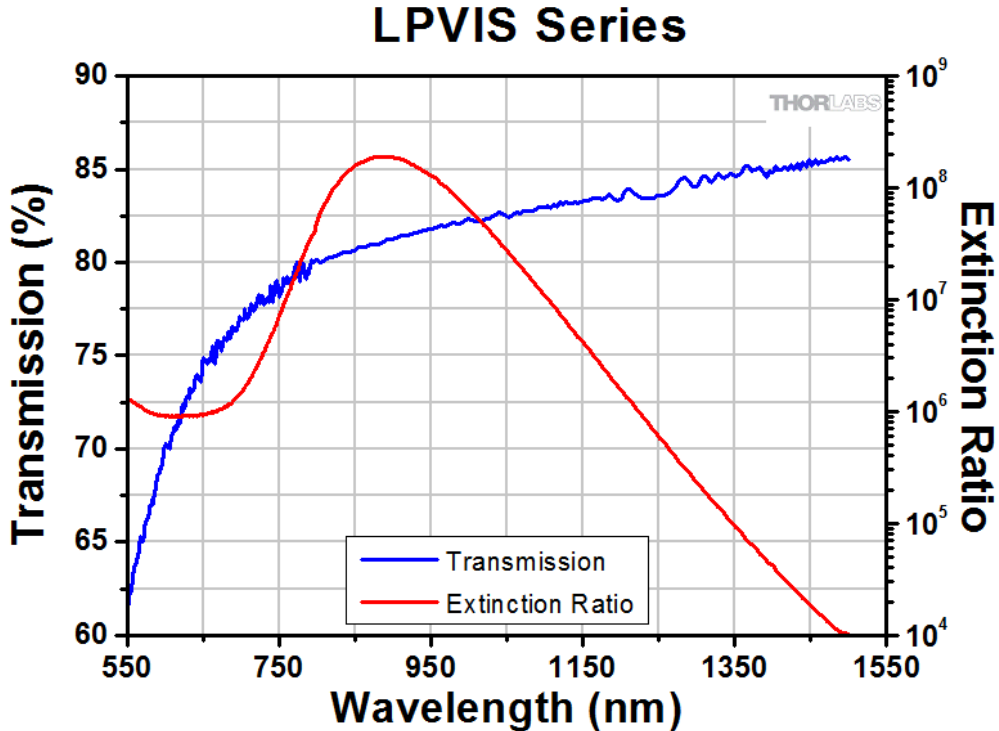


Figure A-1: The transmission and extinction ratios of the LPVIS100 used in ALI.

A.1.3 AOTF

The AOTF in ALI is made by Brimrose of America (model number TEAFI10-0.6-1.0-MSD).

The specifications of the device can be seen in Table A-2. The separation angle is defined as the angle between the input source and the desired refracted polarization and the acceptance angle is measured from the normal of the face of the crystal.

Table A-2: AOTF Specifications.

Parameter	Value	Parameter	Value
Material	TeO ₂	Polarization	Linear vertical
RF Range (Mhz)	75-156	Tunable Range (nm)	600-1200
Optical Aperture (mm)	10x10	Angular Aperture (°)	5-6
Acceptance Angle (°)	3.0	Separation Angle (°)	2.7
RF Power (W)	2.0	Damage Threshold (W)	5.0

A.2 Opto-Mechanical and Electrical Components

A.2.1 RF Driver

The driver for ALI is made by Gooch and Housego (model number 64020-200-2ADMDFS-A). It had no internal control mechanism and required additional control hardware to operate the device. In order to pick the frequency, a 30-bit digital value is inputted into the device to pick a frequency as well as manage several control lines to the device. The control word is used to determine a specific frequency which is given by

$$K_{10} = \frac{F2^{n+1}}{F_{clk}} \quad (\text{A.1})$$

where K_{10} is the 30-bit control word in base 10 rounded to the nearest integer, F is the desired RF to be outputted by the driver, F_{clk} is the internal clock of the driver which is 1000.059 MHz for ALI, and n is the number of bits in the control word for ALI (*i.e.* $n = 30$). The control word is converted to binary and sent to the device to get the desired RF.

A.2.2 QSI CCD Camera

The CCD camera was a QSI 616s with a Kodak KAP-1603ME sensor with a mechanical shutter and a 16-bit digital readout. The spectral response of the device can be seen in Figure 3-10 and the camera specification can be seen in Table A-3.

Table A-3: QSI CCD camera specifications.

Parameter	Value	Parameter	Value
Imager Size (mm)	13.8 x 9.2	Imager Size (pixels)	1536 x 1024
Pixel Size (μm)	9 x 9	Read Noise RMS (electrons)	15
Mass (kg)	0.95	Power Consumption (W)	24
Operating Temperature ($^{\circ}\text{C}$)	-20 to 30	Full Well Depth (electrons)	100,000

A.2.3 OCELOT Computer

The on board computer for the ALI instrument was the Ocelot VL-EPMs-21 computer made by VersaLogic. Its architecture is based on the Intel Atom Z5 processor and had 2 GB of DDR2

memory. It had low power draw and fanless operation. It had a temperature range of -40 to 85 °C.

The system run a bare-bone version of Debian Linux.

A.2.4 Opto-Mechanical Pieces

In this section is a brief list of all the opto-mechanical components used within the final version of ALI. Listed is the model number of the components and the quantity in the design with a short description. All components were purchased from Thorlabs.

Table A-4: Opto-mechanical components used in ALI

Model Number	Quantity	Description
XT95SP-1000	1	1000 mm length optical rail, 95 mm width
XT95P11/M	4	95 mm width optical rail drop-on carriage
RS2P4M	2	Pedestal post, 50 mm long, 25.4 mm width, metric, M4
RS2P/M	2	Pedestal post, 50 mm long, 25.4 mm width, metric, M6
RS2M	2	Pedestal post spacer, 2 mm long, 25.4 mm width
RS7M	2	Pedestal post spacer, 7 mm long, 25.4 mm width
LCP01B	2	60 mm cage clamp
CP02T/M	1	30 mm cage plate, 1" lens holder, square, metric
CP07	3	60 mm cage plate, 1" lens holder, round, metric
LCP01/M	1	60 mm cage plate, 2" lens holder, square, metric
LCP02/M	4	30 mm to 60 mm cage converter, metric
ER1-P4	3	Cage assembly rod, 1" long, 4 pack
ER2-P4	2	Cage assembly rod, 2" long, 4 pack
ER4-P4	1	Cage assembly rod, 4" long, 4 pack
ER8-P4	2	Cage assembly rod, 8" long, 4 pack
LC1A/M	1	Swivel mount, 60

APPENDIX B

ALI SOFTWARE COMMANDS

B.1 List of Commands for ALI Software

Following is a list of the commands that can be used in the ALI software for operational control during flight through the ground based communication program. A complete list will be presented then a description of each function will follow, all are case sensitive.

- `EnableScience`
- `DisableScience`
- `EnableRF`
- `DisableRF`
- `EnableAutoSendStats`
- `DisableAutoSendStats`
- `SetScienceMode`
- `ReloadConfig`
- `LdCusCnf`
- `LdCusExp`
- `GetFile`
- `EndCurrentScienceCycle`
- `SetExposureScaleFactor`
- `UpdateExposureTimeCurve`
- `EnableCheckRfTemps`
- `DisableCheckRfTemps`
- `ResetHousekeeping`

- `DumpConfig`
- `SetBitsPerSecond`
- `EnableAutomation`
- `DisableAutomation`
- `SetAutomationTimeout`
- `EnableGps`
- `DisableGps`
- `EnablePulse`
- `DisablePulse`

B.1.1 EnableScience

Full Command: `EnableScience`

This command enables science data acquisition and enables the RF driver. If the current mode is invalid, the system reports the error to the user. By default, science mode data acquisition is disabled and must be enabled.

B.1.2 DisableScience

Full Command: `DisableScience`

This command disables science data acquisition at the end of the current science mode cycle. This mode does not disable the RF driver. Disabling the RF driver only pauses the cycle and does not terminate it. By default, science data acquisition is disabled.

B.1.3 EnableRF

Full Command: `EnableRF`

This command turns on the RF driver by enabling the relay that controls the power to the device. It has a heavy power draw and by default is disabled.

B.1.4 DisableRF

Full Command: **DisableRF**

Disables the RF driver during science mode acquisition. This only pauses the science acquisition cycle mode and will continue once the driver is enabled again. By default, the RF driver is disabled due to the high power draw.

B.1.5 EnableAutoSendStats

Full Command: **EnableAutoSendStats**

Enables the sending of statistics for each image taken and includes five vertical columns of measured data and housekeeping information. By default, this is enabled.

B.1.6 DisableAutoSendStats

Full Command: **DisableAutoSendStats**

Disables the sending of statistics for each image taken. It is not recommended to disable sending the statistics. .

B.1.7 SetScienceMode

Full Command: **SetScienceMode scienceMode,exposureMode**

Parameter: **scienceMode** is a numerical value of the science mode to be run.

Parameter: **exposureMode** is a numerical value of the science mode to be run.

Allows the user to change science mode and exposure modes that ALI is performing. The science mode is a predetermined cycle of images to perform a specific scientific goal and Table **B-1** contains a list of all of the modes available and a complete description of each cycle is presented in section B.2. The exposure mode is a predetermined exposure time length to be used for each wavelength and Table B-6 contains a list of all of the modes available and a complete description of each mode is presented in section B.3. The next mode will be loaded once the current mode is complete. By default the program is set in Invalid Mode.

B.1.8 ReloadConfig

Full Command: **ReloadConfig**

Upon completion of the current science cycle, the science mode cycle will be reloaded from the configuration files.

B.1.9 LdCusCnf

Full Command: **LdCusCnf IsOneExp,NumExp,wavelength,RFPower...**

Parameter: **IsOneExp** is either a 0 or a 1. A 0 states that the exposure time will be scaled to the calibration curve. A value of 1 states the exposure time will be constant.

Parameter: **NumExp** is the number of images in the custom science mode.

Parameter: **wavelength,RFPower...** is a pair of values for each image in the cycle as defined by **NumExp** consisting of a wavelength in nanometers and a RF power ranging from zero to one.

This function uploads values for a custom science mode. The first value is whether a constant or varying exposure time is to be used for the cycle followed by the number of exposures. For each exposure, a pair of values that consists of a wavelength in nanometers and RF power are required for the specifications. There is no check on the values of the wavelength and RF powers and the user must verify that the wavelength range is in between 600 and 1000 nm and the RF power is between zero and one.

B.1.10 LdCusExp

Full Command: **LdCusExp numTimes,time...**

Parameter: **numTime** is the number of exposure times to be entered.

Parameter: **time...** is a series of times in seconds separated by commas to match the number of exposure times loaded into the custom mode.

This function uploads values for a custom exposure time series. The first value is the number of exposure times followed by a series of time in seconds. If custom exposure time is used, the number of exposures must match the number of exposure times or an error is sent to the user.

B.1.11 GetFile

Full Command: **GetFile filename**

Parameter: **filename** is the image file to be downloaded from ALI with the full path.

Sends a filename into the queue to be downloaded from ALI if the filename exists. This entered file is added to the top of the queue.

B.1.12 EndCurrentScienceCycle

Full Command: **EndCurrentScienceCycle**

Ends the current science operation mode immediately.

B.1.13 SetExposureScaleFactor

Full Command: **SetExposureScaleFactor scaleFactor**

Parameter: **scaleFactor** is a number greater than zero that scales the default calibrated exposure time curve seen in Table 3-6.

Sets a scaling factor for the exposure times. Value must be greater than zero or an error is returned. Default is 1.0.

B.1.14 UpdateExposureTimeCurve

Full Command: **UpdateExposureTimeCurve time...**

Parameter: **time...** is a series of 13 times separated by commas with minimum values of 0.05 seconds and a maximum of 60 seconds. The 13 values correspond to exposure times for wavelengths from 650-950 nm in 25 nm intervals.

This function changes the default values in the calibrated exposure time curve. Default values can be seen in Table 3-6.

B.1.15 EnableCheckRfTemps

Full Command: `EnableCheckRfTemps`

Enables a check to verify that the RF driver is not operating outside its rated temperature range.

At 0 degrees Celsius the RF driver is powered on and at 50 degrees it is powered off. By default the check is enabled.

B.1.16 DisableCheckRfTemps

Full Command: `DisableCheckRfTemps`

Disables the temperature check for the RF driver. By default the check is enabled and it is not recommended to disable the check unless an issue with the temperature sensors arises.

B.1.17 ResetHousekeeping

Full Command: `ResetHouseKeeping`

Resets the housekeeping module to reacquire the voltage and temperature sensors. To only be used if there is a problem occurs with the housekeeping module.

B.1.18 DumpConfig

Full Command: `DumpConfig`

Prints the current configuration loaded into the science module. It is used for debugging purposes.

B.1.19 SetBitsPerSecond

Full Command: `SetBitsPerSecond bitsPerSecond`

Parameter: `bitsPerSecond` is the value to change the download speed during operation in bits per second.

Changes the bitrate limit for the ALI operation program. Minimum value is 32000 bits per second and the default is 50000 bits for second.

B.1.20 EnableAutomation

Full Command: **EnableAutomation**

Enables the automatic timeout process in case of a loss of communication during the launch.

Enabled by default and after 90 minutes of inactivity it puts the system in aerosol mode.

B.1.21 DisableAutomation

Full Command: **DisableAutomation**

Stops the process that automatically starts ALI in an aerosol mode science operation after 90 minutes. This process should be disabled if the user has control of the system at float altitude.

B.1.22 SetAutomationTimeout

Full Command: **SetAutomationTimeout time**

Parameter: **time** is the new time in minutes to set the timeout value.

Changes the default timeout time to the time given in minutes. Default is 90, minimum is 5 and maximum is 240 minutes.

B.1.23 EnableGps

Full Command: **EnableGps**

Starts the GPS process if it is not already started.

B.1.24 DisableGps

Full Command: **DisableGps**

Stops the GPS process if it is not currently running.

B.1.25 EnablePulse

Full Command: **EnablePulse**

Starts the pulse per second process if it is not already started.

B.1.26 DisablePulse

Full Command: **DisbalePulse**

Stops the pulse per second process if it is not currently running.

B.2 List of ALI Science Modes

The following section will give a brief description of each of the programmed science operational modes that exist on the ALI platform. A complete table of the modes can be seen in Table B-1.

Table B-1: ALI operational science modes.

Mode Number	Mode Name
0	Invalid Mode
1	Calibration Mode
2	Aerosol Mode
3	H ₂ O Mode
4	O ₂ Mode
5	Custom Mode
6	Aerosol Constant Exposure Time Mode

B.2.1 Invalid Mode

This mode is a nonexistent mode that has no operational function and will not allow the science module to operate. No images in the mode.

Mode Number: 0

Number of Images: N/A

B.2.2 Calibration Mode

This mode runs with the shutter opened and the AOTF off. The scaling factor does not work on this function and the values are hard coded into the system. This mode does not use any wavelength values and the RF power is set at 0.

Mode: 1

Number of Images: 8

Table B-2: ALI calibration science mode specifications.

Image Number	Exposure Time (s)	Image Number	Exposure Time (s)
1	0.05	5	2.00
2	0.10	6	3.00
3	0.50	7	5.00
4	1.00	8	10.00

B.2.3 Aerosol Mode

This mode runs with the standard aerosol mode. An AOTF off image is taken between each exposure. Custom exposure times and scale factor can be used. Exposure time is based off the standard calibration curve which can be seen in Table 3-6.

Mode Number: 2

Number of Images: 26

Table B-3: ALI aerosol science mode specifications.

Image Number	Wavelength (nm)	RF Power	Image Number	Wavelength (nm)	RF Power
1	650	0.0	14	800	1.0
2	650	1.0	15	825	0.0
3	675	0.0	16	825	1.0
4	675	1.0	17	850	0.0
5	700	0.0	18	850	1.0
6	700	1.0	19	875	0.0
7	725	0.0	20	875	1.0
8	725	1.0	21	900	0.0
9	750	0.0	22	900	1.0
10	750	0.9	23	925	0.0
11	775	0.0	24	925	1.0
12	775	0.9	25	950	0.0
13	800	0.0	26	950	1.0

B.2.4 H₂O Mode

This mode is used to measure water vapor lines. An AOTF off image is taken at the start and end of each cycle. Custom exposure times can be used, as well as a scale factor can be used. Exposure times are based off of the standard calibration curve for the first wavelength of the cycle and is constant for every image.

Mode Number: 3

Number of Images: 28

Table B-4: ALI H₂O science mode specifications.

Image Number	Wavelength (nm)	RF Power	Image Number	Wavelength (nm)	RF Power
1	920	0.0	15	946	1.0
2	920	1.0	16	948	1.0
3	922	1.0	17	950	1.0
4	924	1.0	18	952	1.0
5	926	1.0	19	954	1.0
6	928	1.0	20	956	1.0
7	930	1.0	21	958	1.0
8	932	1.0	22	960	1.0
9	934	1.0	23	962	1.0
10	936	1.0	24	964	1.0
11	938	1.0	25	966	1.0
12	940	1.0	26	968	1.0
13	942	1.0	27	970	1.0
14	944	1.0	28	970	0.0

B.2.5 O₂ Mode

This mode is used to measure O₂ lines. An AOTF off image is taken at the start and end of each cycle. Custom exposure time and scale factor can be used. Exposure times are based off of the standard calibration curve for the first wavelength of the cycle and are constant for every image.

Mode Number: 4

Number of Images: 20

Table B-5: ALI O₂ science mode specifications.

Image Number	Wavelength (nm)	RF Power	Image Number	Wavelength (nm)	RF Power
1	755	0.0	11	764	1.0
2	755	1.0	12	765	1.0
3	756	1.0	13	766	1.0
4	757	1.0	14	767	1.0
5	758	1.0	15	768	1.0
6	759	1.0	16	769	1.0
7	760	1.0	17	770	1.0
8	761	1.0	18	771	1.0
9	762	1.0	19	772	1.0
10	763	1.0	20	772	0.0

B.2.6 Custom Mode

This mode lets the user upload a configuration to an extra configuration file on the ALI platform. The command is sent up via the `LdCusCnf` command. Details can be located in section B.1.9.

Mode Number: 5

Number of Images: N/A

B.2.7 Aerosol Constant Exposure Time Mode

This function is the same as the aerosol science mode (section B.2.3) except the exposure time has been set to two seconds for all exposures. The scaling factor is applied to this mode. A table of the specifications can be seen in Table B-3.

Mode Number: 6

Number of Images: 26

B.3 List of ALI Exposure Modes

ALI had two usable exposure modes during the campaign, a calibrated mode and a custom mode which can be configured by the user. An automatic exposure mode was planned but due to time constraints was never implemented. A brief description of the modes will follow.

Table B-6: ALI operational exposure time modes.

Mode Number	Mode Name
0	Invalid Mode
1	Calibrated Exposure Mode
2	Automatic Exposure Mode (<i>Not Implemented</i>)
3	Custom Exposure Mode

B.3.1 Invalid Mode

This mode is a nonexistent mode that has no operational function and will not allow the science module to operate. No exposure times are associated with this mode.

Mode Number: 0

B.3.2 Calibrated Exposure Mode

Using the method outlined in section 3.6.1, a table of calibrated exposure times were determined for a stratospheric balloon geometry. Table 3-6 contains the calibrated exposure times. For any wavelength requested that is between two of the calibrated wavelengths, the exposure time is linearly interpolated between the two wavelength's exposure times. For wavelengths less than 650 nm the exposure time for 650 nm is used, and for wavelengths greater than 950 nm the exposure time for 950 nm is used.

Mode Number: 1

B.3.3 Custom Exposure Mode

This mode lets the user upload a series of exposure times on the ALI platform to be used instead of the calibrated exposure mode. The command is sent up via the LdCusExp command. Details can be located in section B.1.10.

Mode Number: 3